國立臺灣大學生物資源暨農學院生物機電工程學系

碩士論文

Department of Biomechatronics Engineering
College of Bioresources and Agriculture
National Taiwan University

Master's Thesis

應用病患專屬數位分身模擬髕骨運動軌跡：外側支持帶鬆解術之影響

Simulation of patellar tracking using a patient-specific digital twin: Effects of lateral retinacular release

雷尚勤

Sean Aldrich Rebuyas

指導教授：顏炳郎 博士, 王建凱 博士

Advisors: Ping-Lang Yen, Ph.D., Chien-Kai Wang, Ph.D.

中華民國 114 年 7 月

July 2025

doi:10.6342/NTU202503673

Acknowledgements

I would like to express gratitude to my adviser, Prof. Ping-Lang Yen, for his guidance throughout the course of my master's studies. His guidance on novel and standardized methodologies in the scientific community always challenged me to raise the quality of my research. His formative critiques and support enabled me to accomplish the many tasks of this thesis within a span of just two years.

I am equally grateful to my co-adviser, Prof. Chien-Kai Wang, for providing me with the Ansys Academic Research license for my thesis.

I also wish to thank my family and my late grandmother, to whom I dedicate this research, for their encouragement and support. It was difficult to pursue master's studies in a demanding field. Their guidance helped me to persevere throughout the two years.

Lastly, I give my thanks to the Divine Providence for all the blessings bestowed upon me, especially for granting me the opportunity to pursue this academic endeavor.

doi:10.6342/NTU202503673

中文摘要

本研究建立一套病患專屬的膝關節數位分身系統，用以預測髕股關節在韌帶鬆解術後的運動反應，並著重於外側支持帶鬆解。此數位分身系統整合了新穎的二維至三維重建方法、統計形狀建模（SSM）、有限元素（FE）分析以及機器學習，旨在提升針對髕股關節不穩定與運動異常（maltracking）的手術技術。子集式配準（SBR）為一種新穎方法，可將三維模型與已標註之二維 X 光影像對齊。本研究結合 SBR 與 SSM 形變技術，以重建病患專屬的三維解剖模型。並以屍體實驗作為驗證依據。研究結果顯示，針對性鬆解比起擴大鬆解範圍更能有效改善運動異常。在膝關節彎曲小於 60°時，對上外側支持帶（LR）進行約 25%的部分鬆解，所達成的髕骨偏移修正效果幾乎與正常狀況一致；反之，進行較大範圍或完全（75–100%）的 LR 鬆解則導致過度修正。若同時搭配施行 25–50%的內側支持帶（MR）鬆解，則可進一步改善髕骨的偏移與傾斜校正。屍體實驗亦支持有限元素模擬的預測結果，顯示若進行雙側完全鬆解，會導致髕骨傾斜活動度增加，指出關節不穩定的風險。然而，髕骨偏移的量測結果與正常運動軌跡吻合度不佳，主因可能為骨標記的遺失所致。在未進行鬆解的情況下，髕骨屈曲延遲達 30–50%；在 LR 鬆解情境下則達 60–75%，皆顯著低於常見的正常值，顯示實驗中存在誤差。在有限元素分析中，LEPL 束，尤其是上外側髁髕韌帶（sLEPL），對於恢復正常髕骨傾斜具有良好效果。機器學習分析亦指出，sLEPL 是影響髕骨傾斜與偏移最具影響力的參數，具有應用於針對性鬆解決策輔助的潛力。本研究成功建立並驗證了病患專屬數位分身系統中各個獨立模組於髕骨運動模擬中的可行性，提供術前外側支持帶鬆解決策之輔助依據。未來若能納入更多術前與術後的臨床資料，將有助於提升此數位分身系統之普遍適用性。

關鍵詞：數位分身；髕股關節；二維–三維重建；統計形狀建模；有限元素分析；外側支持帶釋放

doi:10.6342/NTU202503673

Abstract

This study created a patient-specific digital twin system of the knee joint to predict the kinematic response of the patellofemoral joint following ligament release, focusing on lateral retinacular release. The digital twin aimed to improve the surgical technique for patellofemoral instability and maltracking by integrating a novel 2D–3D reconstruction method, statistical shape modeling (SSM), finite element (FE) analysis, and machine learning. Subset-based registration (SBR) is a novel method to align 3D models to annotated 2D X-rays, used here with SSM deformation to reconstruct a patient-specific 3D model. A cadaver study served as a validation benchmark. Results showed that targeted release corrected maltracking better than increasing release extent. Partial (~25%) release of the superior lateral retinaculum (LR) achieved shift correction nearly identical to normal below 60° flexion. Larger or full LR release (75–100%) caused over-correction. Combining 25–50% medial retinacular (MR) release with LR release improved shift and tilt correction. Cadaver study results supported FE predictions in that full bilateral release increased patellar tilt mobility, indicating instability. Shift measurements poorly matched normal tracking due to bone marker loss. Patellar flexion lagged 30–50% in no-release and 60–75% in LR release—lower than commonly observed normal values, indicating experimental inaccuracies. The LEPL bundle, particularly the superior lateral epicondylopatellar ligament (sLEPL), showed good restoration of normal patellar tilt in the FE analysis. Machine learning analysis also identified sLEPL as the most influential parameter affecting patellar tilt and shift—useful for targeted release decision support. This study successfully developed and validated the individual systems of the patient-specific digital twin system for patellar tracking for preoperative lateral retinacular release decision support. Large clinical datasets of preoperative and postoperative data could improve the generalizability of the digital twin system.

Keywords: digital twin; patellofemoral joint; 2D–3D reconstruction; statistical shape modeling; finite element analysis; lateral retinacular release.

doi:10.6342/NTU202503673

Table of Contents

doi:10.6342/NTU202503673

doi:10.6342/NTU202503673

doi:10.6342/NTU202503673

doi:10.6342/NTU202503673

doi:10.6342/NTU202503673

doi:10.6342/NTU202503673

doi:10.6342/NTU202503673

List of Abbreviations

Abbreviation	Full Term
ACL	Anterior Cruciate Ligament
ACS	Anatomical Coordinate System
AP	Anterior-Posterior
BF	Biceps Femoris
BM	Bone Marker
BMF	Bone Marker (Femur)
BMP	Bone Marker (Patella)
BMT	Bone Marker (Tibia)
DRR	Digitally Reconstructed Radiograph
FE	Finite Element
FEA	Finite Element Analysis
FEM	Finite Element Model
FM	Fiducial Marker
GPA	General Procrustes Analysis
HJC	Hip Joint Center
ICP	Iterative Closest Point
IS	Inferior-Superior
ITB	Iliotibial Band
LEPL	Lateral Epicondylopatellar Ligament
LPFL	Lateral Patellofemoral Ligament
LPML	Lateral Patellomeniscal Ligament
LPTL	Lateral Patellotibial Ligament
LR	Lateral Retinaculum
LRR	Lateral Retinacular Release
LTL	Lateral Transverse Ligament
MBD	Multibody Dynamics
MBS	Multibody System
ML	Mediolateral
MPFL	Medial Patellofemoral Ligament
MR	Medial Retinaculum
MRR	Medial Retinacular Release
PCA	Principal Component Analysis
PCL	Posterior Cruciate Ligament
PCSA	Physiological Cross-Section Area
PC	Principal Component

doi:10.6342/NTU202503673

PD	Proximal-Distal
PF	Patellofemoral
PFP	Patellofemoral Pain
PFPS	Patellofemoral Pain Syndrome
PL	Patellar Ligament
PR	Probe Tracker Reference Frame
RF	Rectus Femoris
SBR	Subset-Based Registration
SI	Superior-Inferior
SM	Semimembranous
SSM	Statistical Shape Model
SVD	Singular Value Decomposition
TEA	Transepicondylar Axis
TPS	Thin-Plate Spline
VI	Vastus Intermedius
VL	Vastus Lateralis
VLO	Vastus Lateralis Obliquus
VM	Vastus Medialis
VMO	Vastus Medialis Obliquus
iLEPL	Inferior Lateral Epicondylopatellar Ligament
iLTL	Inferior Lateral Transverse Ligament
iMPFL	Inferior Medial Patellofemoral Ligament
mLTL	Middle Lateral Transverse Ligament
mMPFL	Middle Medial Patellofemoral Ligament
pACS	Patellar Anatomical Coordinate System
sLEPL	Superior Lateral Epicondylopatellar Ligament
sLTL	Superior Lateral Transverse Ligament
sMPFL	Superior Medial Patellofemoral Ligament

doi:10.6342/NTU202503673

Explanation of Symbols

$\boldsymbol{s}_i \in \mathbb{R}^3$ 3D anatomical landmark point with coordinates (x_i, y_i, z_i)

$\boldsymbol{S} = \{\boldsymbol{s}_1, \boldsymbol{s}_2, \ldots, \boldsymbol{s}_N\}$ Full set of N anatomical landmarks in the 3D shape

$I(\boldsymbol{s}_i)$ Identifier of landmark $\boldsymbol{s}_i$ (e.g., anatomical name)

$\boldsymbol{T}^{(k)} \subseteq \boldsymbol{S}$ Subset of landmarks visible in 2D X-ray for the k-th view

M_k Number of matched landmarks in subset $\boldsymbol{T}^{(k)}$

$\bar{\boldsymbol{s}}^{(k)}, \bar{\boldsymbol{t}}^{(k)}$ Centroids of source and target landmarks in subset k

$\boldsymbol{S}_c^{(k)}, \boldsymbol{T}_c^{(k)}$ Centered landmark sets with centroid subtracted

$\boldsymbol{H}$ Covariance matrix used for rigid alignment

$\boldsymbol{R}$ Optimal rotation matrix computed from SVD

$\boldsymbol{t}$ Optimal translation vector

$\boldsymbol{s}_{aligned}^{(k)}$ Aligned source landmark after rigid registration

$\Delta \boldsymbol{s}_j$ Displacement vector between source and target landmarks

$\boldsymbol{s}_{new,j}^{(k)}$ Re-projected 3D point using 2D displacements and original depth

$\boldsymbol{X} = \in \mathbb{R}^{N\times 3}$ 3D shape defined by N ordered landmarks

$\{\boldsymbol{X}^{(i)}\}_{i=1}^{M}$ Set of M aligned shapes used to build the SSM

$\boldsymbol{X}_{mean} \in \mathbb{R}^{\boldsymbol{N}\times \boldsymbol{3}}$ Mean shape from the aligned dataset

$\Delta \boldsymbol{X}^{(i)}$ Shape deviation from mean $\boldsymbol{X}^{(i)} - \boldsymbol{X}_{mean}$

$\boldsymbol{C}$ Covariance matrix of shape deviations

doi:10.6342/NTU202503673

$\boldsymbol{P} \in \mathbb{R}^{3N\times K}$ Matrix of principal components (eigenvectors)

$\Lambda \in \mathbb{R}^{K\times K}$ Diagonal matrix of eigenvalues

$\boldsymbol{b} \in \mathbb{R}^{K\times 1}$ Deformation coefficients used to fit new shape

$\boldsymbol{s}_{mean} \in \mathbb{R}^{3N\times 1}$ Flattened mean shape vector

$\boldsymbol{s}_{deformed} \in \mathbb{R}^{3N\times 1}$ Flattened deformed shape

$\boldsymbol{X}_{deformed} \in \mathbb{R}^{N\times 3}$ Deformed shape reshaped to 3D form

$\boldsymbol{D} \in \mathbb{R}^{N\times 3}$ Displacement vectors between deformed and mean shape

$f: \mathbb{R}^3 \to \mathbb{R}$ Thin Plate Spline (TPS) interpolation function

$\phi(r) = r^2 \log r$ TPS kernel, where r is the Euclidean distance

$\widehat{\boldsymbol{D}} \in \mathbb{R}^{N\times 3}$ Interpolated displacements from TPS

$\widehat{\boldsymbol{X}} \in \mathbb{R}^{N\times 3}$ Final reconstructed patient-specific 3D shape

doi:10.6342/NTU202503673

Chapter 1: Introduction

1.1 Background

The patellofemoral (PF) joint plays a critical role in enhancing the efficiency of the quadriceps during knee extension, increasing the extension force, which generates substantial reactive forces ranging from 2.5 to 7.6 times body weight during daily activities. The patella also distributes these forces across a larger surface area, centralizing the load on the extensor mechanism and minimizing stress on individual components [1]. Beyond its load distribution function, the patella acts as a dynamic lever, increasing the moment arm of the quadriceps, particularly in early knee flexion, to allow for efficient force transmission between the quadriceps and the patellar tendon. As the knee moves through flexion and extension, the patella's position changes. The distribution of force is affected by this change, and individual patellar tracking patterns can vary significantly [2]. Patellar stability is further maintained by the balanced interaction of the articular geometry, muscle forces, and passive soft-tissue restraints, with the medial patellofemoral ligament being the primary passive restraint against lateral displacement during knee flexion [3].

The presence of a tight lateral retinaculum can lead to the generation of a tilting moment and lateral force exerted on the patella. The degree of the strain contribution caused by a tight lateral retinaculum is sufficient to lead to the onset of patellar

doi:10.6342/NTU202503673

maltracking [4]. The compressive force on the patellar facets increases during patellar maltracking, causing anterior knee pain [5]. Arthroscopic lateral retinacular release is one of the surgical techniques to improve PF biomechanics and alleviate anterior knee pain, prevent patellar dislocation and relieve tension in the PF joint. The release is done by making a sufficiently long incision on the lateral retinaculum [6]. However, the outcome of surgery is still unpredictable [7]. Furthermore, excessive release risks post-surgical iatrogenic medial patellar instability [8].

Modeling the contribution of the ligaments is important for understanding how the patella stays stable, especially because structures like the MPFL provide most of the static stability [9], [10], [11], [12]. On the other hand, soft tissue structures like the iliotibial band can also influence patellar tracking, depending on the loading condition. If the lateral retinaculum is over-released during procedures like lateral retinacular release (LRR), it can increase the patellar mobility too much and risk patellar instability [13], [14]. So, being able to model and assess these soft tissue contributions more accurately is important to avoid destabilization and make sure the surgery has the desired effect.

Lateral retinacular release (LRR) is a commonly used surgical intervention for treating patellofemoral disorders, particularly when there is confirmed tightness of the lateral retinaculum. The LRR surgical procedure can be effective in relieving patellofemoral pain and correct maltracking. However, the outcomes of LRR is variable. Over-correction such

doi:10.6342/NTU202503673

as excessive release of the soft tissues can lead to high patellar mobility, which introduces the risk of patellar instability. Therefore, personalized preoperative assessment and planning are important to decide the extent of release and which other structures should be released or preserved. It is difficult to predict the kinematic response of release extent without any guidance tools or patient-specific simulations, which may contribute to inconsistent surgical outcomes [13], [14].

The current process for deciding on treatment for patellar maltracking has some limitations. Most of the time, clinical decisions depend heavily on patient history and radiographic imaging. However, relying only on these may not always capture the full picture—especially when it comes to complex anatomical problems like trochlear dysplasia or other subtle shape abnormalities, even if the standard measurements seem normal [15], [16]. Another issue is that decisions made during surgery often come down to trial-and-error and the surgeon's experience, which can lead to different outcomes from case to case and might result in less-than-ideal results [16]. Since there's no personalized, real-time biomechanical feedback available during surgery, it's hard to know for sure if the chosen intervention will work well for that specific patient. Because of these challenges, there is a need for newer, more advanced tools—such as digital twins—that can help improve accuracy, predict surgical outcomes, and support more personalized treatment planning.

doi:10.6342/NTU202503673

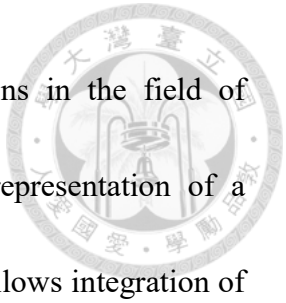

Digital twins have shown successful and promising applications in the field of orthopedics. A digital twin in orthopedics refers to the virtual representation of a biological system of an actual patient such as the knee joint, which allows integration of real-time data that helps in personalized treatment planning, surgical simulation, and precision medicine [17], [18]. These advanced biomechanical models use machine learning, artificial intelligence, and imaging data such as CT and MRI scans to improve pre-operative planning, optimize surgical interventions, and predict post-surgery outcomes. As a tool in personalized healthcare, digital twins allow personalized surgical strategies by simulating the biomechanical responses of the individual patient, which supports data-driven decision-making [19], [20], [21]. The goal of this approach in orthopedics is to increase the accuracy of surgical procedures, minimize complications, and provide more patient-centered and efficient care.

Simulation-based tools like Statistical Shape Models (SSMs), Finite Element (FE) modeling, and Machine Learning are becoming more common in the planning of patellofemoral joint surgeries. These tools help move towards more personalized and data-driven treatment decisions. SSM-based registration can reconstruct patient-specific bone shapes using only limited imaging data like 2D X-rays. This helps reduce the need for full 3D scans and also saves computation time while still keeping the anatomical variation between patients [22]. FE modeling can simulate joint biomechanics and

doi:10.6342/NTU202503673

surgical procedures like MPFL reconstruction or lateral release, giving insights on things like joint stability, stress distribution, and contact pressures without needing to test directly in the patient [4], [23], [24]. These simulations can be used during preoperative planning for repeated testing of different surgical scenarios. The implementation of machine learning technology enables automation of relevant tasks for patellofemoral joint modeling: prediction of tissue properties, assignment of ligament properties, and suggesting possible surgical release strategies. It can also make quick predictions during planning, which helps guide more personalized treatment decisions. All of these techniques combined aim to make surgery safer, more accurate, and better suited to each individual patient.

1.2 Research Problem

Despite LRR being the commonly used surgical technique to correct patellar maltracking and manage patellofemoral pain, the decision-making process remains subjective. There is limited study on quantitative assessment of the extent of surgical release and the kinematic response of LRR—and other combinations to improve LRR—on patellofemoral biomechanics such as patellar shift and tilt. Specifically, there is limited research that uses patient-specific knee joint models with simulation tools to predict the outcomes of different surgical release scenarios for treating patellar instability or maltracking. Furthermore, to the best of the researcher's knowledge, there is no existing

doi:10.6342/NTU202503673

digital twin framework specifically designed to simulate patellar tracking following progressive ligament release. This presents a research gap in the application of state-of-the-art technologies such as digital twins, finite element analysis, patient-specific imaging and modeling, and machine learning to support preoperative planning and improve predictability of surgical outcomes for lateral retinacular release.

1.3 Research Objectives

This study aims to develop and evaluate a patient-specific digital twin of the knee joint that is capable of simulating patellar tracking under different ligament release scenarios, focusing on LRR. The digital twin system integrates statistical shape modeling, a novel 3D shape reconstruction method, and finite element analysis to reconstruct a patient-specific model and simulate patellofemoral biomechanics using limited fluoroscopy images. To achieve this, the study proposes the following specific objectives:

1. To construct a patient-specific digital twin framework of the knee joint by the integration of the following techniques: statistical shape model (SSM); novel registration technique for aligning 3D models to 2D X-ray landmarks; and 2D-3D reconstruction using the novel technique and SSM deformation
2. To simulate normal (baseline) and maltracking patellar trajectories using a finite element model of the knee joint
3. To simulate and analyze the biomechanical impacts of different progressive LRR

doi:10.6342/NTU202503673

4. To train and implement machine learning models that enable rapid personalization and optimization of soft tissue release strategies
5. To validate the predictive capabilities of the digital twin by conducting a cadaver study

doi:10.6342/NTU202503673

Chapter 2: Review of Related Literature

2.1 Patellofemoral Joint Biomechanics

2.1.1 Biomechanical Role of the Patella

The patella is a sesamoid bone embedded in the extensor mechanism tendon of the knee joint. As the patella increases the magnitude of the quadriceps muscles forces, flexion and extension can thus be achieved by exerting a smaller force magnitude. The patella is integral to the flexion-extension motion as the quadriceps alone cannot exert the necessary forces to achieve motion especially during higher intensity activities [25], [26]. The patella acts as a fulcrum and increases the force of the quadriceps muscles by increasing the moment arm of the patellar ligament. Beyond the augmentation of the force magnitude exerted by the quadriceps muscles, the patellofemoral joint also provides a control strategy during maneuvers such as jumping by reducing the burden on the joint [9], [25]. The quadriceps and the patellar tendon generate the primary forces in the patellofemoral joint [25], [26]. While in motion, the forces exerted by the patellofemoral joint is converted to compressive forces upon engaging with the trochlea of the femur. Depending on the activity, the magnitude of these forces can vary from 0.5-20 times the bodyweight of an individual. The compressive force of up to 20 times the bodyweight is distributed over a large area for a brief period of time. Thus, the patellofemoral joint can

doi:10.6342/NTU202503673

tolerate such compressive force magnitudes without damaging the cartilage [25].

2.1.2 Patellar Tracking Mechanics and Contact Dynamics

During flexion, the patella optimizes the distribution of compressive forces by changing the contact area. The contact area increases linearly from 20°-60°, then becomes stable beyond this point. As the knee flexes, the patella progressively engages with the trochlea of the femur. The patella is most vulnerable during the early phases of flexion, where the engagement is still incomplete. In normal patellar tracking the patella is positioned slightly lateral from the center of the trochlear groove in the femur during early phases of flexion, eventually centering as the knee further flexes. Establishing a patellar coordinate system ensures an objective basis for consistent measurements of mediolateral displacement [25], [26]. The patella is capable of translation and slight tilting motion to accommodate dynamic activities such as walking and climbing stairs [25]. Mediolateral displacement and patellar tilt (inferosuperior axis rotation) are of particular significance in patellar tracking. For the patellar tilt in normal patellar tracking, slight lateral tilt can be observed. Once the patella centers in the trochlear groove the slight tilt reduces. According to the study, a marker of diagnosing patellar malalignment is the noticeable patellar tilt that does not decrease as the knee enters further flexion [26]. Patella alta is a condition where the patella is positioned more superior than normal. This results in a delayed patella engagement with the trochlear groove of the femur until higher degrees

doi:10.6342/NTU202503673

of knee flexion. A delayed engagement with the trochlea causes more instability in the knee joint [9].

2.1.3 Patellofemoral Stability: Anatomical and Biomechanical Factors

Patellar instability is a multifactorial pathology of the patellofemoral joint. The widely regarded critical factors influencing patellar stability are the following: trochlear shape, patella alta, and patella infera [15]. Patellar tracking is influenced by the restraints in the form of soft tissues and the geometry of the articular surfaces of the knee patellofemoral joint [26]. The morphology of the patella and trochlear groove [27] greatly influences stability, especially around 30° of knee flexion [15]. Patella alta or high-riding patella has increased risk in patellar instability, especially when the engagement of the patella with the trochlear groove is delayed. Patella infera or low-riding patella is generally associated with stability issues [15].

The stability of the lateral patellofemoral joint relies on bony contours, static soft-tissue structures, and dynamic muscle forces. These lateral structures balance the medial forces for proper patellar tracking during movement. For soft tissue restraints, the medial retinaculum, most importantly the medial patellofemoral ligament (MPFL), is critical in resisting lateral displacement of the patella, more so at early stages of knee flexion (<30°). The lateral retinaculum stabilizes the lateral edge of the patella. However, when the lateral retinaculum is cut during lateral release, the patella stability decreases [15].

doi:10.6342/NTU202503673

There are two main layers in the lateral soft-tissue structures: superficial retinacular layer and deep retinacular layer. The superficial retinacular layer is composed of fibers from the iliotibial band (ITB), direct fibers that have attachment originating from Gerdy's tubercle and connects to the patella and the patellar tendon, and the vastus lateralis obliquus (VLO) quadriceps muscle, which is directly underneath the ITB and is attached to the proximal and superficial lateral patella. The deep retinacular layer is formed by deeper fibers from the superficial retinacular layer. The key ligaments in the deep retinacular layer are the following: (a) lateral patellofemoral ligament (LPFL), which connects the superolateral patella to the lateral femoral epicondyle; (b) lateral patellomeniscal ligament (LPML), which extends from the lateral patella to the lateral meniscus; and (c) lateral patellotibial ligament (LPTL), which connects the lateral patella to Gerdy's tubercle [28]. The associated superficial and deep ligaments during LRR include the patellofemoral, patellotibial, and lateral transverse ligaments [29].

The quadriceps muscles, vastus medialis and vastus lateralis, serve as active stabilizers to the patella. Other factors affecting patellofemoral stability include tibia rotations, which affect tension in the muscles and soft tissue structures thereby influencing patellar stability during extension [30]. These factors affecting patella kinematics include the morphology of the trochlear groove, the balancing of soft tissue structures (the influence of which is lesser compared to the muscle loading of the vastus medialis and vastus

doi:10.6342/NTU202503673

lateralis of the quadriceps), and tibiofemoral rotations, specifically rotations about the SI and AP axes rotations [9]. Generally, imbalances in the passive and active stabilizers lead to increased tension in the lateral retinaculum. Over time, the increased tension can lead to lateral patellar dislocation. Specifically, the common cause of patellar instability is the increased tension in the lateral retinaculum and a decreased muscle activity in the vastus medialis [30]. Passive structures such as ligaments and active structures such as muscles influence patellar tilt. While not a unique cause, tightness in lateral retinaculum is a contributing factor to patellar tilt maltracking [9] and tilt lateralization [29]. Issues with the vastus lateralis and vastus medialis are shown to negatively affect patellar tilt, causing maltracking. [9]. Prior to surgical intervention, rehabilitation is usually prescribed to strengthen weakened muscles to restore balance. Once rehabilitation fails, this becomes a factor that leads to a patient being a candidate for LRR [30].

2.1.4 Patellar Tracking Patterns in Cadaveric Knee Studies

A study by Nagamine et al investigated the differences in patella kinematics between normal cadaveric knee and abnormal cadaveric knees [31]. The abnormal knees were classified by having patellar tracking significantly different from the majority of the cadaveric knee specimens. The primary cause of abnormal patellar tracking was attributed to the abnormal morphology of the bones with no mention of soft tissue imbalance. For normal patellar shift, early knee flexion stages showed a medial shift before shifting

doi:10.6342/NTU202503673

laterally, continuing towards the end of knee flexion at 90°. For abnormal patellar shift, the medial shift is more pronounced and continued shifting medially to a much later stage than that of the normal patella trajectory. As the abnormal patellar shifted laterally, however, it eventually plateaued in the latter stages of knee flexion. For normal patellar tilt, a gradual increase to 10° medial tilt was observed from 0°-20° knee flexion angle. Beyond this point, no observable variation in patellar tilt was noted. For abnormal patellar tilt, the patella has small variations in lateral tilt until a 45° knee angle. A gradual increase in lateral patellar tilt was observed until the end of the knee flexion [31]. Tibial rotation about the SI axis is approximately 12° during knee flexion angle between 0°-90°, when the tibia is torque-loaded pointing internally. Tibial rotation is approximately 17° when the tibia is torque-loaded pointing externally. The influence of an internally-directed torque is a more medial patellar shift and tilt below 45° knee flexion angle, while an externally-directed torque results in a more lateral patellar shift and tilt below 45° knee flexion angle. The patellar shift and tilt are not significantly affected at deeper knee flexion angles beyond 45° [31]. In the cadaveric study by Amis et al [32], the common patterns of patellar tracking during knee flexion showed that the patellar shifts medially until 20° as the patella engages with the trochlear groove. Then, the patella progressively shifted laterally until the end of the knee flexion. No notable patterns were identified with the patellar rotations aside from the restrictive, small variable patterns throughout the

doi:10.6342/NTU202503673

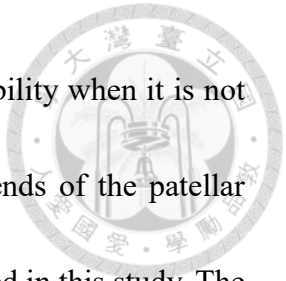

entire knee flexion. It was observed that the patella had the least stability when it is not engaged with the trochlear groove. The differences between the trends of the patellar tracking during knee flexion and knee extension were also investigated in this study. The common trends during knee extension showed that the patellar tracking was more stable. Less patellar tilt and rotation were observed during knee extension. The stability of the patella was attributed mainly by the soft tissue structures such as the medial retinaculum and the medial patellofemoral ligament. At near and full knee extension, the tension of the medial soft tissue restraints is tightest, significantly influencing patella stability [32]. The trochlear groove guides the path of the patella during knee flexion and extension, resulting in different patellar tracking trajectories in each phase [32].

2.2 Patellar Malalignment and Maltracking

2.2.1 Association of Patellar Maltracking with Patellofemoral Pain Syndrome (PFPS)

There are no significant differences observed between the patellar kinematics of individuals with patellofemoral pain syndrome (PFPS) and those without. This implies that abnormal patellar tracking is not a consistent feature of PFPS. One study found that in the PFPS group there was an observed 2.25 mm shift more lateral than the healthy group. However, there are large overlaps in individual values, implying that patellar

doi:10.6342/NTU202503673

maltracking is not a reliable marker for diagnosing PFPS. The study further recommends investigating other causes such as neurogenic factors [33]. It is hypothesized by other studies that great compressive forces on the patellofemoral joints leads to patellofemoral pain syndrome. The condition is further aggravated by patellar malalignment due to causing increased compressive forces. It is held that patellar malalignment is one of the major contributors to patellofemoral pain syndrome (PFPS). However, the quantification of the patellofemoral biomechanics of patellar malalignment has not yet been investigated and is unclear [9]. The study by MacIntyre et al [33] challenges the commonly held primary factors that cause PFPS. While aspects of their methods lack objectivity, these limitations also highlight the necessity of objective methods and techniques to identify factors causing abnormal patella kinematics. The study also notes that force distribution over a contact area varies per individual regardless of similarities in patellar kinematics. [33].

The association of patellar malalignment and patellofemoral pain syndrome is controversial as there has not been a widely accepted evidence correlating the two, suggesting further investigation is needed. This study used four methods of measuring patella height: Caton-Deschamps, Blackburne-Peel, Insall-Salvati, and Modified Insall-Salvati. From this study, results show that patella alta has a strong correlation with patellofemoral pain syndrome. The difference in methods to determine patella height

doi:10.6342/NTU202503673

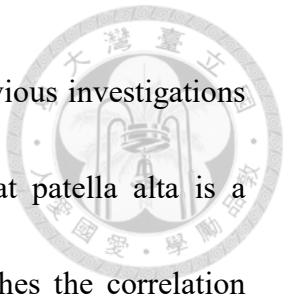

makes it impossible to compare the results from this study with previous investigations on patella alta. Therefore, in their population the study states that patella alta is a contributing factor to patellofemoral pain [34]. This study establishes the correlation between the vastus medialis (VM) activation delay as an instigating factor in patellofemoral pain. It is found that VM activation delay only causes patellofemoral pain in patients with both abnormal patellar tilt tracking and bisect offset—a measurement of patellar lateral displacement relative to the trochlear groove center. There is a strong relationship between VM activation delay and patellar maltracking. There is otherwise no observable relationship with VM activation delay and patellofemoral pain in individuals without patellar maltracking [35].

2.2.2 Definitions and Characteristics of Patellar Malalignment and Maltracking

Patellar malalignment is defined as the abnormal spatial orientation of the patella. It pertains to both the static spatial relationship between the patella and the trochlea at any spatial plane, and the interrelationship among the femur, patella, and tibia [36]. Patellar tracking is defined as the dynamic spatial orientation of the patella throughout knee movement. Consequently, patellar maltracking is the abnormal dynamic spatial orientation of the patella [36].

doi:10.6342/NTU202503673

Patellar malalignment associated with patellofemoral pain is difficult to define as abnormal measurements can also be found in patients not experiencing symptoms of pain. The commonly diagnosed types of patellar malalignment include rotational malalignment (abnormal lateral patellar tilt) and patella alta (high-riding) or baja (low-riding) [36]. Recent studies using dynamic MRI show the correlation between patellar maltracking and patellofemoral pain syndrome (PFPS). It was noted that patients with PFPS have increased patellar shift and tilt lateralization. A patella that is less stable (i.e., more mobile) was also found to have a strong correlation with patellofemoral pain [37].

2.2.3 Biomechanical Risk Factors and Muscular Influence

The cause of patellofemoral pain syndrome (PFPS) is multifactorial. The primary contributors include overuse and abnormal anatomy. As a consequence, load-bearing activities are impaired for patients experiencing PFPS [38]. Load-bearing activities such as squatting, running, and climbing the stairs are risk factors for patellofemoral pain syndrome (PFPS) and intensify the pain experienced [39].

The orientation of the resultant muscle force of the quadriceps is represented by the Q-angle. Normal Q-angle can vary from 6°-27°. Higher Q-angle values tend to be abnormal and result in an increased lateral force acting on the patella, which results in pain due to increased contact pressure [40]. A lateral orientation of the quadriceps also results in a lateralization of the patella during knee flexion. It is commonly held that

doi:10.6342/NTU202503673

patellar malalignment and maltracking are attributed to anterior knee pain. Patellar maltracking causes greater compressive force exerted on the lateral trochlear groove during flexion, inducing pain and wear to the articular cartilage [40].

The normal mean of Q-angle for men is 14°, while the normal mean for women is higher at 17°. The lateral forces acting on the patella is linear with the Q-angle [39]. Due to the linear relationship between Q-angle and lateral forces on the patella, it is commonly held that abnormal Q-angles causes anterior knee pain or patellofemoral pain syndrome (PFPS) [39]. The consensus for the contribution of Q-angle to patellofemoral pain syndrome (PFPS) is still contested as some studies support that abnormal (high) Q-angle puts athletes at higher risk of knee injuries while some studies did not find strong correlations to associate Q-angle and PFPS [37]. Recent studies show that an abnormal Q-angle is not the primary cause of patellofemoral pain syndrome (PFPS) [39].

It is unclear if abnormal vastus lateralis and the vastus medialis of the quadriceps are primary contributors for patellar maltracking. However, it has been observed that muscle activation imbalance between the vastus lateralis and medialis is associated with patellofemoral pain in patients when climbing stairs [37].

2.2.4 Influence of Soft Tissue and Bone Morphology

Due to the significant influence of the joint loading conditions on patellar tracking, it is important to control the variables of magnitude and direction of factors such as the

doi:10.6342/NTU202503673

muscles and soft tissues structures [9]. It is held that the medial patellofemoral ligament (MPFL) has a major contribution to patellar lateral stability [9]. Specifically, MPFL is a major contributor to the static stability of the patella [11]. Among the quadriceps muscles, the vastus medialis obliquus (VMO) is a major contributor to the dynamic stability of the patella [11]. Besides muscles, loading conditions from the soft tissue structure, the iliotibial band, is also known to affect patellar tracking. The relationship between the iliotibial band tension and patellar shift and tilt is found to be linear from 60°-75° knee flexion range [9].

Advances in biomechanics research has improved the understanding and modeling of the ligament structures, particularly during knee motion. Soft tissue restraints such as the ligaments provide patella stability and prevent abnormal motion [12]. The knee ligaments maintain their tension during movement, effectively acting as the fulcrum for the knee joint axes of motion [12]. Passive knee motion, i.e., non-loaded knee motion, is primarily guided in tandem by the articular bone geometry and soft tissue structures [12].

2.2.5 Variability and Diagnosis Challenges

The major limitations in studies that found no correlation between patellar kinematics and PFPS are disregarding full weight-bearing loads affecting patellar kinematics and subjective classification of patellar alignment. Thereby compromising reliability [33]. Furthermore, there is currently no unified and objective characterization of normal

doi:10.6342/NTU202503673

patellofemoral kinematics as inter-patient as well as inter-study variability of patellar kinematics is great [9]. These limitations highlight the necessity of objective methods and techniques to identify factors causing abnormal patella kinematics [33].

It is generally held that patellar malalignment is one of the major contributors to patellofemoral pain syndrome (PFPS). However, the quantification of the patellofemoral biomechanics of patellar malalignment has not yet been investigated and is unclear. Although no universally defined normal patellar tracking trajectory exists, many studies have identified trends and implications in normal patellar tracking. Patellar flexion is found to lag 60-70% behind the current knee flexion angle (Figure 2-1). For patellar tilt (Figure 2-2), it is difficult to define trends in normal patellar tilt dynamics. Some studies report small changes of total variation around 2°. Other studies report total variation as high as 14.5°. There are also other studies that report a medial tilt after knee flexion angle of 90°. The common implication regarding trends in patellar tilt across different studies is that the patellar tilts laterally during knee flexion angle up to 90°. Similar to patellar tilt, normal patellar rotation has varying trends across multiple studies (Figure 2-3). A common trend during knee flexion angle of up to 30° shows that the patellar rotation has a range of -1° to 2°. Beyond 30° knee flexion angle, the trajectory of the normal patellar rotation is different per study. For normal patellar shift (Figure 2-4), it is common to observe a medial shift during the early stages of knee flexion (10°-30°) before shifting

doi:10.6342/NTU202503673

laterally. It is difficult to analyze patellar shift trends at deeper knee flexion angles (i.e., exceeding 90°), due to a limited number of studies investigating this range [9].

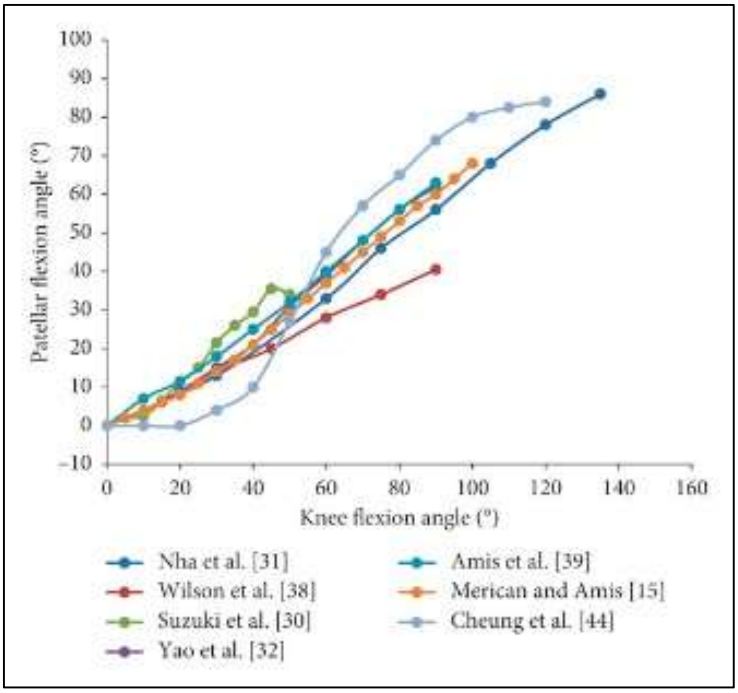

Figure 2-1. Comparison of normal patellar flexion trajectories based on data from multiple studies. Adapted from [9].

doi:10.6342/NTU202503673

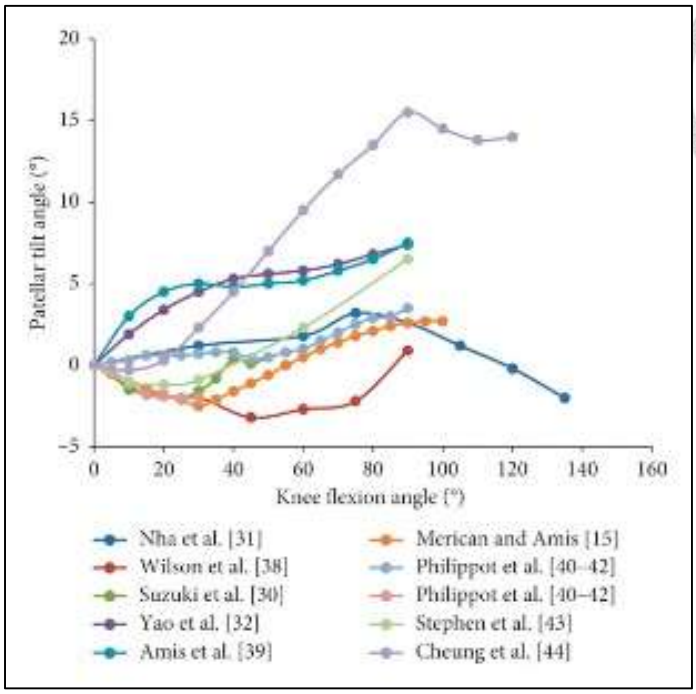

Figure 2-2. Comparison of normal patellar tilt trajectories based on data from multiple studies. Adapted from [9].

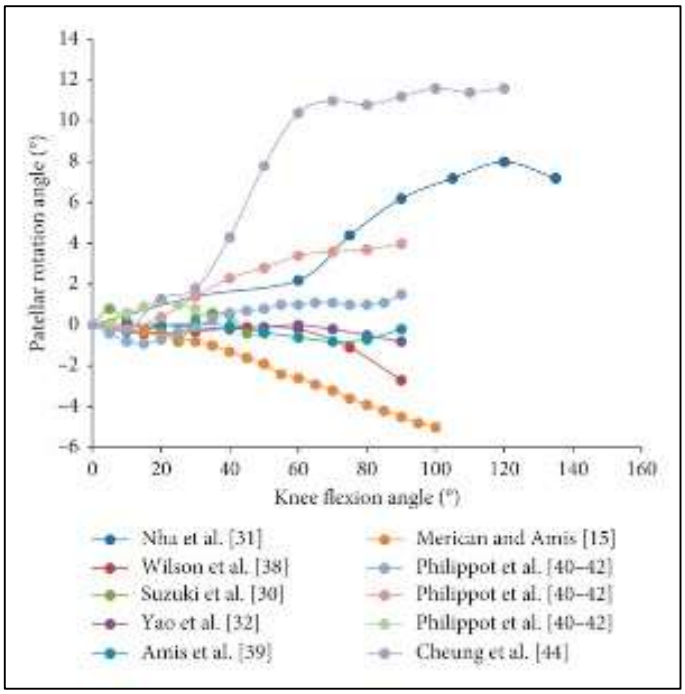

Figure 2-3. Comparison of normal patellar rotation trajectories based on data from multiple studies. Adapted from [9].

doi:10.6342/NTU202503673

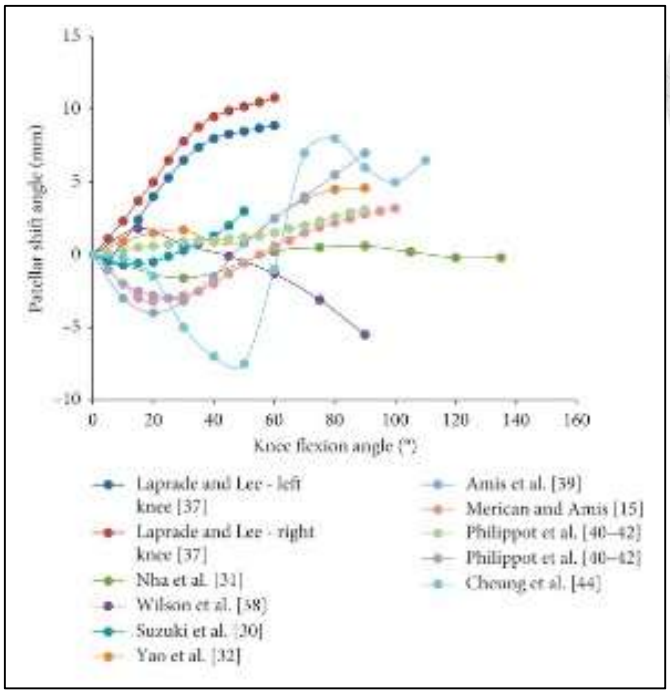

Figure 2-4. Comparison of normal patellar shift trajectories based on data from multiple studies. Adapted from [9].

2.3 Anatomical and Measurement Frameworks for Patellar Kinematics

2.3.1 Anatomical Coordinate Systems

For femoral coordinate systems, it is conventional to use the anatomical or the mechanical axes to define the superior-inferior (SI) axis or the proximal-distal (PD) axis. The transepicondylar axis (TEA) or the line that passes through the epicondyles of the femur or the posterior condyle line are commonly defined as the mediolateral (ML) axis. The anteroposterior (AP) axis is conventionally the cross product of the ML and PD axes. The irregular morphology of the patella complicates establishing its anatomical coordinate system. There is no singular, widely-accepted technique on determining the

doi:10.6342/NTU202503673

patellar anatomical coordinate system. As a consequence, diverse strategies exist. One strategy is by bounding box, in which the center of the bounding box is determined as the coordinate system origin. Another is by performing an initial determination of the patella center before using the femur coordinate system as the basis for the patellar coordinate system axes [9]. The conventional definitions of the 6DOF and the sign convention of the patella are shown in Figure 2-5. Patellar flexion is defined as the rotation about the ML axis. Patellar tilt is defined as the rotation about the SI axis. Patellar rotation is defined as the rotation about the AP axis. Patellar shift is defined as the translation about the ML axis. Patella translations about the AP and PD axis are also defined, but are not as significant in analyzing patellar tracking. The patellar rotation parameters are expressed in degrees, while the patella translation parameters are expressed in distance [9].

doi:10.6342/NTU202503673

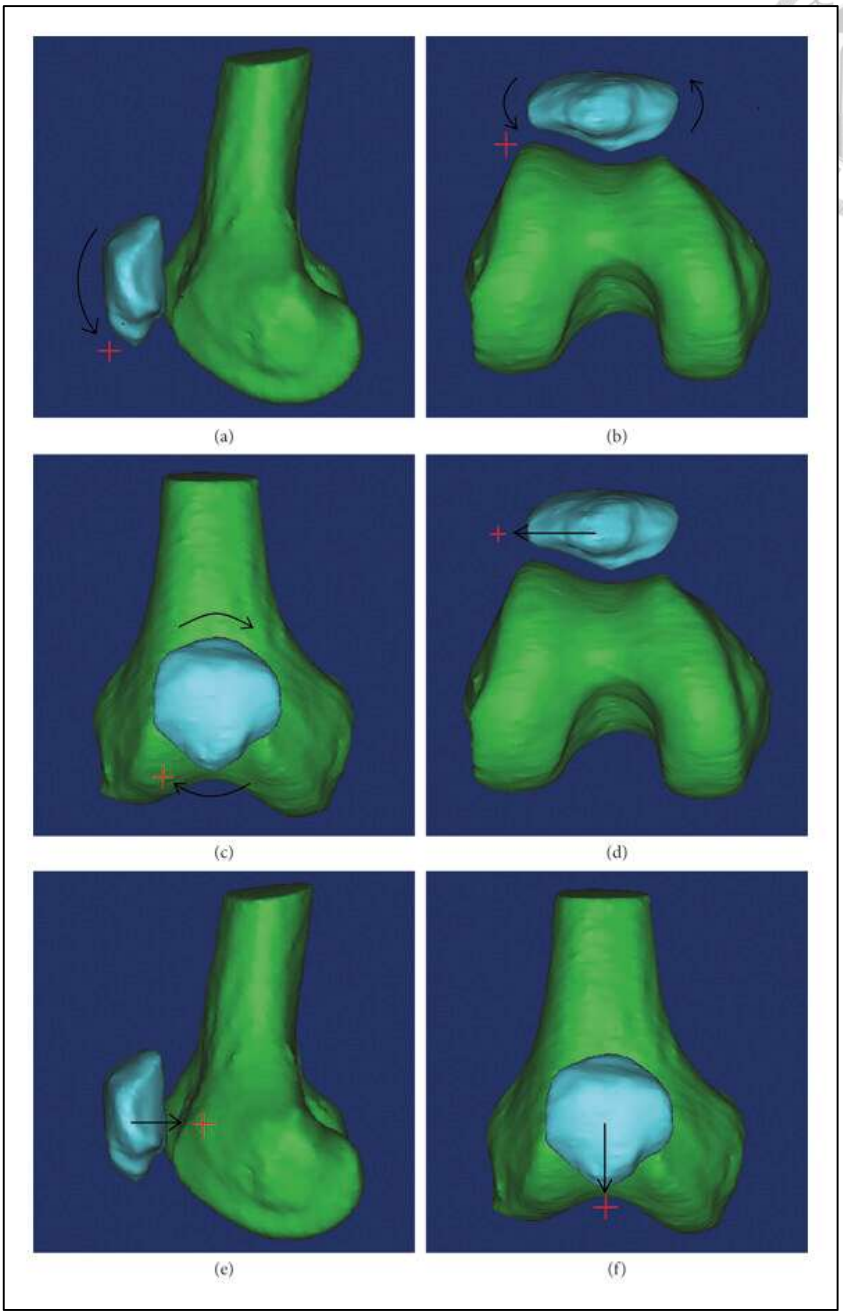

Figure 2-5. Definitions of 6DOF patella motion with sign conventions. Adapted from [9].

2.3.2 Influence of Loading and Reference Frames

A standardized method for loading conditions and coordinate system has not been developed, resulting in no generalizable model of normal patella kinematics being defined

doi:10.6342/NTU202503673

[9]. Joint loading conditions have a profound influence during complete knee extension by causing the patella to tilt and shift laterally. Both magnitude and direction of the muscle loading force affect patellar tilt and shift. A 175 N force is the commonly used loading force for the quadriceps muscles due to the load being the minimum force that extends the knee against gravity, e.g. standing from a seated position [9]. Choosing different coordinate systems for the bones in the knee joint will result in significant deviations in patellofemoral kinematics results. The error can reach 26% for patellar flexion angle data and ten times the error for patellar shift data. inter-frame relative motion is the primary cause for the measurement errors in patellofemoral kinematics data [9].

2.3.3 Imaging Modalities and Evolution of Kinematic Modeling

Contemporary imaging modalities such as MRI facilitated the shift from the instant center of motion model to a fixed axes model. The advancement of imaging modalities not only improved analysis of patella kinematics but also enhanced prosthetic design. Earlier knee joint kinematics models such as the instant center of motion model assumes that knee flexion is restricted in the 2D sagittal plane. Fixed and independent anatomical axes can be defined using anatomical landmarks, e.g., posterior condylar axis and longitudinal axis [12].

doi:10.6342/NTU202503673

2.4 Surgical Treatment Strategies for Patellar Instability

2.4.1 Diagnostic Criteria for Patellar Instability

Patellar instability is defined as present if an individual has a history of recurrent patellar dislocations or there is a probability of reoccurrence of patellar dislocations after the first instance [16]. Patellar instability is a common, multifactorial disorder of the patellofemoral joint [27]. Often, multiple risk factors contribute to joint instability[27].

Patient history is the primary clinical assessment to distinguish patellar instability from other knee issues [15]. Clinical assessment using radiographs usually involve specific radiographic views: AP view, true lateral with slight knee flexion, and a skyline or axial view with 20°-30° degrees of knee flexion. Then, the patella height can be calculated using established measurement methods such as Insall-Salvati, Blackburn-Peel, and Caton-Deschamps ratios. However, even after obtaining normal ratio measurements using these methods does not exempt the possibility of patella alta or if the trochlear groove morphology issues will cause patella instability. Therefore, the additional utility of taking a skyline view is for identifying important anatomical factors such as trochlear morphology and dysplasia features, which is indicative of abnormal trochlear developments [15].

In a study by Dejour et al [41], pathological thresholds are formally defined. Establishing quantitative pathological thresholds improves the sensitivity and specificity

doi:10.6342/NTU202503673

of diagnosing patellar instability. Patellar tilt is classified as pathologic once it exceeds the 20° threshold. Lateral displacement is classified as pathologic once it exceeds the 3 mm threshold. Patellar tracking showing lateralization exceeding 3 mm or patellar tilt exceeding 20° is considered maltracking [41].

2.4.2 Lateral Retinacular Release (LRR): Overview

Lateral retinacular release (LRR) is a commonly performed surgical procedure for patients with confirmed lateral retinaculum tightness and are experiencing patellofemoral pain [13]. LRR addresses patellofemoral disorders such as anterior knee pain, patellar instability, chondropathy, and osteoarthritis [30]. LRR is reserved for patients where nonoperative measures, i.e., physical therapy, fail [42]. LRR has been in use for a long time as a part of patellofemoral joint surgery. The earliest applications were for treating recurrent patellar dislocation. LRR has since increased in popularity after the procedures shifted from open surgery to being performed arthroscopically [43]. LRR has evolved from being the standard for treating patellar maltracking to understanding that multiple factors beyond simple lateral retinacular tightness affect conditions that lead to patellar maltracking. This is due to LRR primarily addressing isolated lateral retinacular tightness and may not resolve all underlying issues for patellar maltracking and patellofemoral pain [14].

The purpose of LRR is to reduce the lateral forces and the lateralization of the patella.

doi:10.6342/NTU202503673

This process relieves the compressive force and alleviates patellofemoral issues such as pain and pathological malalignment. However, the risks of LRR especially after over-release is an increase of patellar mobility, which may lead to patella instability. The effectiveness of LRR is variable, with success rates from different studies varying from 14%-99%. The high success rate variability suggests that LRR is not universally effective and is appropriate only on specific patellar pathology. However, a recent study reports that LRR generally maintains satisfactory long-term results for patients with stable patella. Notably, patients with patellar instability experience deterioration in post-surgical outcomes in the long-term [13].

Medial retinacular release (MRR) is often combined with LRR to balance the soft tissues. The two main strategies for MRR are medial soft-tissue realignment and distal bony realignment of the tibial tubercle. LRR as a standalone surgical treatment and LRR combined with MRR are both considered minimally-invasive and effective treatments for patients without significant malalignment. However, LRR alone can sometimes worsen patella stability due to imbalances in medial and lateral forces. This indicates that LRR and MRR results in more satisfactory post-surgical outcomes. The medial patellofemoral ligament is the primary restraint in preventing lateral dislocation of the patella. The lateral retinaculum also influences stability [42].

doi:10.6342/NTU202503673

2.4.3 Lateral Retinacular Release (LRR): Surgical Procedure

The procedure of the LRR surgical technique is as follows: anesthesia, arthroscopic evaluation, LRR technique, and assessment of patellar tracking after LRR [13]. The LRR surgical procedure begins with anesthesia, either under general, epidural, or peripheral nerve block anesthesia [13]. A pneumatic tourniquet can also be used to control bleeding during surgery. To prepare the patient for hemostasis, exsanguination is performed then a tourniquet is applied on the proximal thigh, typically at a pressure of around 300 mmHg [44]. A thorough preoperative examination is conducted with the patient under anesthesia to examine the knee in full extension. The specific tests include evaluation of the tightness of the lateral retinaculum by palpation. Lateral retinaculum tightness is confirmed based on the inability of the patella to be pushed medially by less than one quadrant. Alternatively, the presence of lateral retinacular thickening and tightening also confirms tightness [44].

Figure 2-6 shows the medial-push test or patellar-glide test as part of the preoperative examination during LRR. Lateral tightness is confirmed if the medial displacement does not exceed one quadrant of motion, while lateral laxity—loose lateral tissues—are confirmed if medial displacement exceeds three quadrants. Patellar glide test is performed at different knee angles including full extension [45].

doi:10.6342/NTU202503673

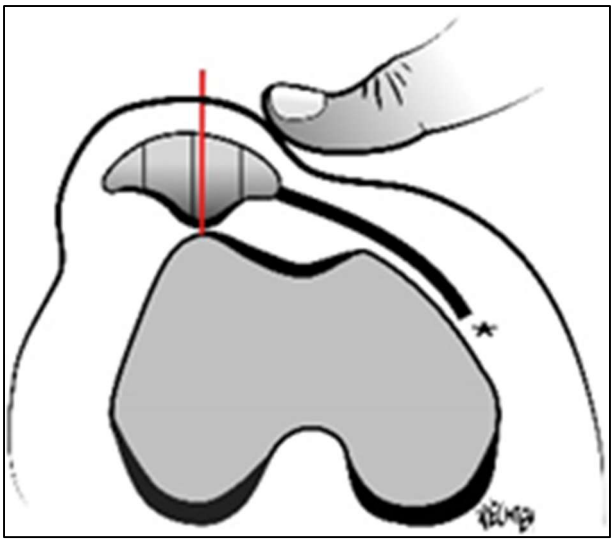

Figure 2-6. Diagram of the patella glide test. Adapted from [45].

Figure 2-7 shows the patellar tilt test, in which the patella is held by the hand and pressure is applied on the anterior medial border to assess lateral elevation. Normal patellar tilt is 15°–20° elevation from neutral position. Lateral tightness is confirmed if elevation is zero. Greater than 20° elevations are also pathological, indicating laxity. Patellar tilt test is performed at full knee extension [45].

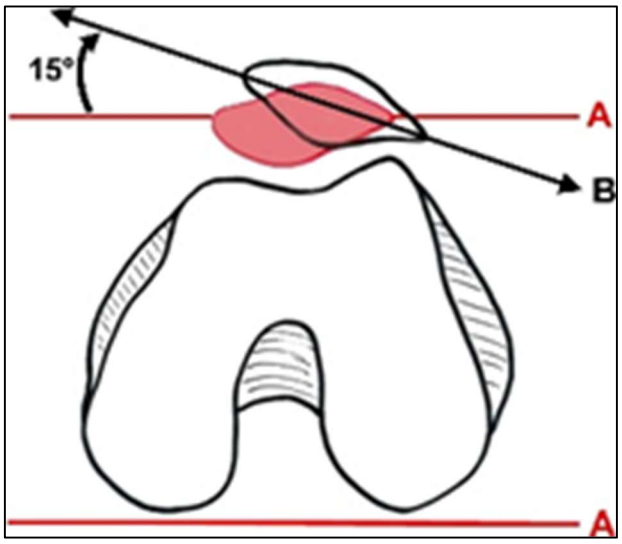

Figure 2-7. Diagram of the patellar tilt test. Adapted from [45].

doi:10.6342/NTU202503673

Following arthroscopic evaluation is performing the LRR technique [13]. The approach for the release uses Metcalf's method: an effective and safe release of the tight lateral structures around the patella [13]. From the inferolateral portal, blunt dissection is made through subcutaneous tunnel. The surgeon carefully makes an incision on all three layers of the lateral retinaculum: superficial, middle, and deep layers [13]. Then, surgical entry points or "portals" are made into the joint through which the arthroscope and surgical instruments are inserted for examination [13]. Superolateral and inferolateral portals are usually used for comprehensive assessment of patellar tracking and chondromalacia—the softening, damage, or deterioration of the articular cartilage (posterior side) of the patella [13]. The anterior inferolateral portal is used for visualization, while the superolateral portal is the entry point of surgical instruments [29]. The anatomical location and the extent of LRR starts from the superior patella—approximately 2 cm proximal to the superior pole—and continues down to Gerdy's tubercle (Figure 2-8) [46].

doi:10.6342/NTU202503673

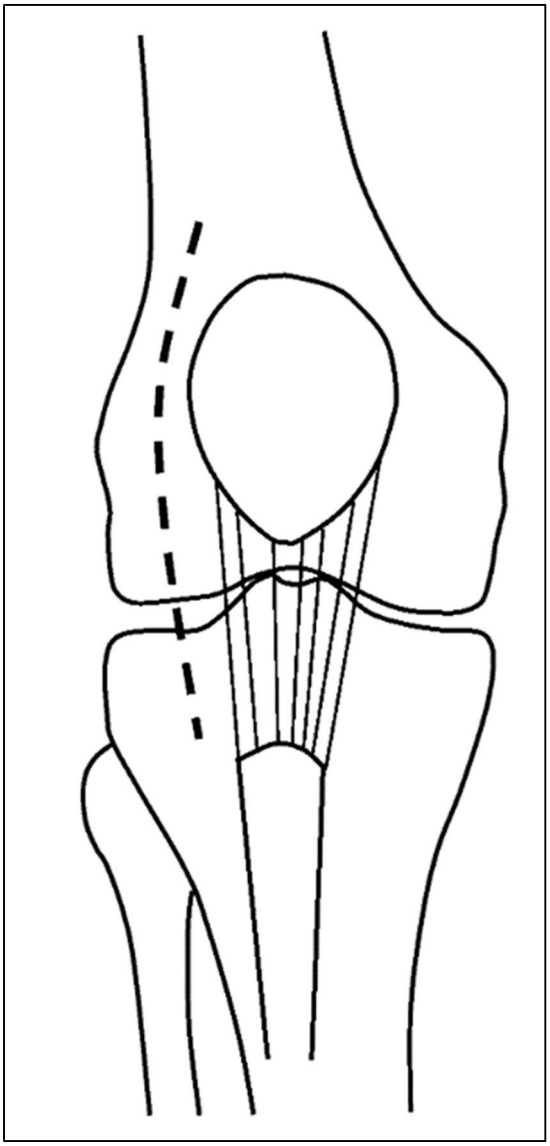

Figure 2-8. Diagram showing the extent of LRR. Adapted from [46].

Subcutaneous arthroscopically controlled release is a type of LRR which involves placing the arthroscope on either the medial or lateral side. Then a cutting instrument will be inserted from the lateral side, from outside the joint. The visualization of the release is done arthroscopically. This type of LRR has a 10.2% complication rate [43]. Entirely arthroscopic technique is another type of LRR which involves inserting the arthroscope through the medial portal while the cutting instrument is inserted through the opposite or

doi:10.6342/NTU202503673

lateral portal. The entire procedure is performed within the joint cavity. This type of LRR has a lower complication rate (4.6%) and is considered safer [43].

Post-surgical assessment is performed arthroscopically. The release is deemed adequate when the lateral border of the patella could be tilted upward with its medial aspect touching the intercondylar notch [13]. Then, the tourniquet will not be removed until elastic bandage with foam padding is applied to prevent hemarthrosis. Patients will undergo physical therapy for at least 6 months afterwards [13].

2.4.4 Lateral Retinacular Release (LRR): Postoperative Changes

The patellar shift dynamics of patients with healthy knees are observed to decrease from 0°-30° knee flexion but increase significantly at later stages of knee flexion. In preoperative patients for LRR treatment, patellar shift increases throughout entire flexion, indicating abnormal patellar shift trajectory. In postoperative patients, patellar shift slightly increases in the 0°-30° range but decreases significantly at 90° flexion, which shows some improvement and normalization of patellar shift [14].

The patellar tilt dynamics of patients with healthy knees are observed to slightly increase from 0°-30° knee flexion, then significantly increase at 90° flexion. In preoperative patients, there is no observable increase in the 0°-30° knee flexion range. In postoperative patients, there is a reduction in patellar tilt throughout the entire knee flexion, especially at 30° knee flexion. Postoperative patients also have a higher patellar

doi:10.6342/NTU202503673

tilt than healthy patients in the 0°-30° knee flexion range, indicating persistent abnormalities [14].

Overall, LRR is effective at improving patellofemoral kinematics in carefully selected patients. Postoperative improvements include a reduction in abnormal lateralization of patellar shift, improved patellar tilt angles, increased patella contact area, and even correction of tibiofemoral kinematics. However, LRR is not effective in improving patellar shift and tilt dynamics at early stages of knee flexion, 0°-30°. Furthermore, despite improvements, complete restoration of patellar tracking and alignment cannot be achieved [14].

2.4.5 Lateral Retinacular Release (LRR): Considerations

LRR must be performed with great care. The joint anatomy, biomechanics, and specific patellar pathology must be considered as extensive releases can lead to increased medial patellar instability, which may cause medial patellar dislocation. The lateral retinaculum contributes to approximately 10% of lateral stability. However, when the tension in the lateral retinaculum is increased, it can cause patellar malalignment and maltracking [30]. Modern surgical treatment procedures of patella instability are shifting away from standalone LRR. Performing LRR alone introduces imbalance in the patellar forces and reduces the restraining lateral forces, causing the patella to be at risk of lateral dislocation [15].

doi:10.6342/NTU202503673

Better clinical outcomes from LRR are observed when patellofemoral pain is experienced due to tight lateral tissues. Furthermore, combining LRR with other procedures such as cartilage debridement to improve pain and patellofemoral function, especially in osteoarthritic patients. The effectiveness of LRR is decreased when patellofemoral pain is due to cartilage damage, malalignment, or abnormalities in bone morphology. Over-release can also lead to complications and therefore reduce effectiveness of LRR [28].

A novel technique has been designed specifically for athletes that also combines LRR with another technique. It is common for athletes to exert significantly high compressive forces on their patellofemoral joints, the magnitude of which can reach at least five times their body weight. The surgical procedure designed for athletes with recurrent patellar instability and dislocations includes LRR and a modified Fulkerson osteotomy—moving the tibial tubercle to a more anterior and medial position). This surgical technique is tailored for athletes, allowing a safe return to intense physical demands on their knees [47].

2.5 Computational Modeling Approaches in Knee Biomechanics

2.5.1 Ligament and Bone Modeling Strategies

Using literature data for ligament stiffness and reference strain values for use in a computational model are not universally applicable but serve as useful starting points for

doi:10.6342/NTU202503673

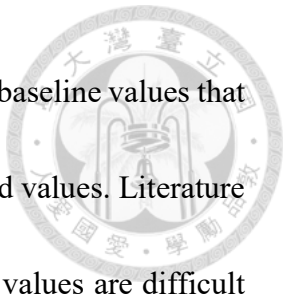

patient-specific computational models. The literature data are used as baseline values that are meant to be refined later instead of being treated as exact and fixed values. Literature data also serves a practical purpose as direct measurements of these values are difficult in-vivo, as opposed to using known physiological data that are based on realistic measurements [48]. Recent studies show that the FE model outcomes are highly sensitive to parameters such as ligament material properties, ligament prestretch, ligament stiffness and cartilage contact properties. This highlights the importance of careful calibration of these parameters rather than using literature values. The importance of a parameter in one model may not be the same for another model. Therefore, using literature values for the parameters may not be appropriate for all cases. Understanding the sensitivity of the model response is important to calibrate the parameters to be better suited for patient-specific deployment of the finite element model (FEM). It is recommended to conduct sensitivity analysis for each FE model as it is useful in determining the most influential parameters for personalized clinical applications [49]. Furthermore, parameters with small influences are still important as these influences accumulate and can still affect the FE model results from the simulations [49].

The ligament model selection depends on the purpose of the study. Using spring models for the ligaments is a simple method that is computationally efficient. The spring models are effective in use for movement predictions. Another ligament model is the

doi:10.6342/NTU202503673

hyperelastic model, which is better suited for detailed analysis of tissue stress and strain as it considers interaction between the soft tissue structures. Using a rigid body model for the bones is adequate as it reduces computational cost and simplifies calculations made by the FEA software [50]. Modeling the bones as rigid bodies is found to be accurate for calculating tibiofemoral contact under loading conditions of one body weight (around 800 N force load). The simplification of the assumptions for the bones do not compromise accuracy in this context [51].

Soft tissue such as ligaments in traditional FEM are often modeled as 1D springs for computational efficiency. These springs have nonlinear tensile response properties for realism, although most spring models neglect ligament wrapping. Spring models, while efficient, can be sensitive to geometric assumptions. These assumptions include ligament origin and insertion points and number of element representation of each ligament. Representing ligaments with fewer than three elements is found to result in the FEM being highly sensitive to geometric variations. Furthermore, spring models in knee joint FEM models tend to suffer from poor contact pressure predictions, especially at higher degrees of knee flexion [52]. Some studies model knee ligaments as 3D structures to address ligament wrapping and modeling complex physical properties. These knee models are more realistic in predicting knee joint motion but are computationally expensive. This is due to the physical property of ligaments being highly anisotropic and hyperelastic, which

doi:10.6342/NTU202503673

is difficult to simulate [52].

2.5.2 Contact Mechanics and Joint Constraints

It is difficult to simulate accurate contact friction between articular surfaces in FEM studies. The actual coefficient of friction in the knee joint is low and many FEM studies simply assume frictionless contact to simplify calculations. Using low coefficients of friction is computationally expensive and may not result in solution convergence [50]. Simulating realistic joint motion requires application of realistic rotational constraints and not constraining the degrees of motion such as applying compressive loads that inhibit rotational motion, limiting the knee flexion—particularly the femur movement—in the sagittal plane, and constraining tibia rotation about the AP axis [51].

2.5.3 Soft Tissue Mechanics and Load Response

FE knee models enable simulation of complex biomechanics of the knee joint, particularly important for understanding the interactions of soft tissues during dynamic activities. FE knee models provide a realistic 3D analysis of load distributions and the tension in the tissues such as the patellar tendon which is more engaged in high-impact movements. Stress measures such as von Mises stress is critical for predicting the deformation of the knee joint soft tissues under complex loads during load-bearing activities. These detailed stress measures help identify the mechanism of injury and guide

doi:10.6342/NTU202503673

injury prevention or treatment strategies [53]. The integration of musculoskeletal models into the FE model creates a more patient-specific knee model that increases the accuracy of biomechanical assessments and help create personalized treatment strategies. [53]. An innovation of FE modeling techniques is integrating dynamic imaging like the dual fluoroscopic imaging system to capture actual knee joint motion at different time points. The resulting representations of the knee joint motion and the tissue behavior throughout the movement cycle are more realistic [53].

2.5.4 Soft Tissue Modeling and Cutting Simulation

The central role of modeling soft tissues for realistic surgical simulation is generating insights from deformation and cutting. The challenge is achieving a balance between realism and computational efficiency during real-time interactive simulations. Soft tissue modeling can be classified into three main groups according to contemporary FEM research: mesh-based methods, meshfree-based methods, and hybrid methods [17]. Tissue models must replicate complex biomechanical behaviors to achieve effective surgical training in a virtual setting [54]. Mesh-based methods refer to the context of traditional FEM by the discretization of geometries into finite meshes for detailed simulation and tissue deformation. A key limitation of this method is the computational intensity that limits its use in real-time surgical simulations, despite the high model outcome accuracy. However, the mesh-based method is still widely used and is favored

doi:10.6342/NTU202503673

for its accuracy and realism. The trend of mesh-based methods showing greater prevalence in research highlights the importance of improving the method (e.g., reducing computational load by using explicit dynamic schemes, model-order reduction techniques to speed up simulations, and using adaptive mesh refinement to focus on critical regions while maintaining efficiency) for improved feasibility for real-time use [17]. Mesh-based methods such as traditional FEM are highly accurate and are suitable for internal structures. The challenge with using this method is the high computational cost which limits applications for real-time simulations [54]. Meshfree-based methods model soft tissues using discrete points instead of meshes which is particularly useful for large deformation and complex geometries. Mass-spring system is a type of meshfree-based method used for its simplicity and computational efficiency. However, simpler model behaviors in this method prohibit accurate modeling of material properties without increasing computational cost. Another meshfree-based method is the emerging position-based dynamics method. This method directly works with positions instead of forces. With this, the technique boasts simple implementation, model stability, and real-time applications with applications in brain deformation and cardiac beating dynamics. However, similar to the mass-spring system method, the position-based dynamics is unable to model physical properties in detail. Meshfree-based methods can handle real-time simulation of large deformations but are greatly limited in capturing detailed

doi:10.6342/NTU202503673

material properties, i.e., the method struggles with physical realism. Therefore, more researchers are focused on improving mesh-based methods for real-time simulations due to its accuracy and realism [17]. Meshfree-based methods create models that are flexible but struggle with accurate representation of tissue properties [54]. Hybrid methods attempt to integrate the individual strengths of different techniques under the mesh-based and meshfree-based methods to improve accuracy while maintaining computational efficiency. For example, the combination of FEM with mass-spring modeling has the advantage of near-realistic replication of material behavior. Achievements and limitations of hybrid modeling methods include reduction of computational costs but despite the advantages of the hybrid methods, the challenge persists for achieving real-time simulation for more complex models [17]. Hybrid methods include techniques such as chainmail algorithms and mass-spring models with FEM. These hybrid methods balance realism with computational efficiency but have difficulties in representing tissue behavior and smooth incisions, which is a key feature of traditional FEM [54].

Traditional FEM can be used to model soft tissue deformation during cutting. FEM can replicate tissue response from experimental force-displacement data. To achieve suitable real-time simulation capabilities, models made using FEM typically requires reducing the number of elements, nodes, and other FEM model assumptions [55]. The mechanism for simulating cutting operations in traditional FEM is through an application

doi:10.6342/NTU202503673

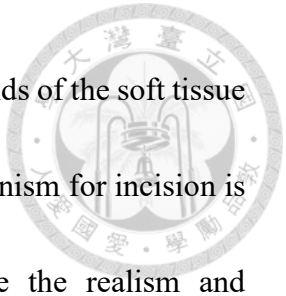

of external force, e.g., surgical instruments, that exceed stress thresholds of the soft tissue causing deformation and eventually bisection. This traditional mechanism for incision is computationally heavy. Modeling through Bezier curves enhance the realism and smoothness while maintaining simplified overall calculations [56]. The eXtended Finite Element Method or XFEM is capable of capturing local discontinuities such as voids and heterogeneity without remeshing, a significant feature and advantage over traditional FEM. Most XFEM applications are focused on blade-based cutting with successful cutting scenario applications such as arterial dissection, brain resection, and other blades-based surgery Most recent XFEM models are powerful for accurate simulations of complex incisions while keeping the mesh unchanged for high fidelity. Complex incision shapes and tissue discontinuities are better captured as this method does not rely on deleting mesh elements. By eliminating the need for mesh modifications and local refinement, XFEM is more efficient and robust in simulating soft tissue deformation and cutting. However, material property assumptions are still simplified for this method. XFEM models assume that tissues are linearly elastic which may cause error propagation especially during large deformations [57].

2.5.5 Model Validation and Clinical Use

Capturing the patient-specific anatomical features enables personalized assessment of knee kinematics. Validating the FE model outcomes with real data—ideally in-vivo—

doi:10.6342/NTU202503673

enhances confidence in the predictive accuracy of the model for clinical applications [58]. FE knee models can be used for evaluating severity of a patient's injury, rehabilitative treatment planning, and preventing further complications such as osteoarthritis. The potential of FE knee models hinges on analyzing knee joint function beyond insights obtained from static imaging alone [58].

2.5.6 Cadaver Study vs Simulation

Cadaveric studies are more straightforward and easier to understand than simulations. However, the disadvantages of conducting cadaver experiments significantly hinder in-depth research. Acquisition, preservation, and complex joint articulations are the greatest challenges in cadaver experiments. The development of finite element analysis (FEA) software overcomes the disadvantages of cadaveric studies by several factors: FEA enables non-invasive kinematic response simulation of tissues provides low-cost and low-risk biomechanical analysis, and enables repeated trials using the finite element model (FEM) [50].

2.5.7 Use Cases and Gaps in FEM Studies

The common application of FEM studies includes bone defect treatment, osteoarthritis and joint replacement, soft tissue injury, and knee rehabilitation. There are almost no FEM studies performed for improving surgical release, particularly for the lateral and medial

doi:10.6342/NTU202503673

retinacular release surgical technique [50].

2.6 Patient-Specific Modeling and Digital Twins in Orthopedics

2.6.1 Concept and Applications

The origin of digital twin systems application was in the industry and in aerospace. Over time, it has since expanded across different fields such as engineering, manufacturing, and healthcare. Digital twins are enabled by technologies such as machine learning, artificial intelligence, augmented reality, and large datasets. These technologies affect the accuracy and capability of a digital twin system [19]. The term digital twin is formally defined as a virtual representation of a physical system that is capable of real-time data output. In the medical field, the role of digital twins are tools that help personalize treatment planning, surgical simulation, and decision making input. The common areas of application are in cardiology, trauma surgery, and orthopedics [17]. Digital twins as dynamic virtual models that are updated with real-time data have ab emerging role in orthopedics by transforming practices, although the application in orthopedics is currently limited compared to other fields [18]. A proposed extension of the digital twin concept in orthopedics is presented by Bjelland et al. The concept is specifically for arthroscopic surgery, creating a patient-specific, virtual model of the knee joint. The digital twin proposed would incorporate real-time intraoperative data for a dynamic virtual modeling of joint biomechanics during specific procedures. The

doi:10.6342/NTU202503673

integration of novel procedures into the digital twin concept would innovate surgical planning and develop enhanced personalized treatment strategies [17]. The application of digital twins in surgical planning and simulation lies in the virtual model being built on patient-specific imaging such as CT or MRI. These personalized virtual models enhance preoperative planning, especially for complex cases (e.g., multiligamentous knee injuries). Digital twins also assist training for surgeons by rehearsing surgeries, optimize techniques, and explore alternatives before actual surgery. [18]. Digital twins also have applications in postoperative outcome prediction. Through continuous integration of postoperative data, digital twins are able to develop generalizable and personalized care [18]. Digital twins in medicine can serve as valuable tools for surgical training, planning, simulation, outcome prediction, and personalized rehabilitation. The digital twin framework is further enhanced by integrating real-time sensing, intraoperative data, and machine learning technologies [17]. Digital twins are the replicas of physical objects or systems that benefit from data-driven simulations. Digital twin systems have applications in various fields including healthcare for precision medicine. Despite the application of digital twin in medicine being relatively new and developing, digital twins in medicine is high potential [59]. The application of digital twins in orthopedics help optimize implant design, personalize surgical procedures, and improve monitoring post-surgery. The fundamental role of FEA in a digital twin framework is the prediction of material and structure

doi:10.6342/NTU202503673

response to various physical stimuli such as force during surgery. The ability of FEA to predict the behavior of intricate biological structures such as the knee joint is useful for cases in biomedical engineering such as: stress-strain response analysis for optimal implant design, prediction of tear progression in tendons, and simulation of surgical release. Outcome-predicting digital twins also have the capability of anticipating future health problems or treatment responses of a patient, whether the recovery patterns follow expected normal functioning [59].

2.6.2 Training and Surgical Planning

The necessity of surgical simulation systems has evolved to a necessity for safe and effective training for junior surgeons. Patient-specific simulators are becoming a promising future direction for enabling surgeons to simulate specific procedures preoperatively and develop core skills even outside a clinical setting [17]. Machine learning and computer-assisted surgery technologies have the potential to obtain valuable insights, guide surgical planning, and therefore improve surgical outcomes [17].

2.6.3 Data and Imaging for Digital Twin

The digital twin system must rely on high-quality, detailed 3D imaging data to represent accurate individual anatomy. CT is valuable for bone reconstructions while MRI excels in soft tissue detail. The imaging modality selection affects the quality of the digital

doi:10.6342/NTU202503673

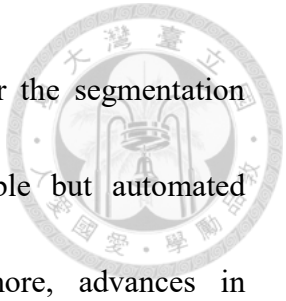

twin but the choice may depend on the purpose of the study. For the segmentation techniques for 3D reconstruction, manual techniques are possible but automated segmentation techniques are essential for efficiency. Furthermore, advances in convolutional neural networks greatly enhances efficiency by significantly reducing segmentation time without compromising accuracy during rapid model generation. After segmentation, converting voxel data into surface meshes commonly use algorithms such as marching cubes or dual contouring. Alternatively, volumetric meshing techniques such as Delaunay tetrahedralization prepares the model for FEA. However, for simulating rigid body models a surface mesh should suffice. Soft tissue properties (e.g., in-vivo stiffness data) can be obtained through magnetic resonance elastography and shear-wave elastography. The combination of techniques in imaging, segmentation, meshing, and tissue material property estimation creates a comprehensive and personalized digital twin [17]. A successful creation of digital twin relies heavily on large quantities of high-quality datasets. The demand for large datasets, e.g., imaging, clinical outcomes, and postoperative data, is integral to developing and validating digital twin simulations [18]. Effective digital twins combine macro-scale patient-specific imaging data (e.g., CT and MRI scans) with microstructural details (e.g., bone microarchitecture), and reconstructed using advanced AI techniques. A multi-scale approach enhances realism and predictions made using the digital twins. The microstructural details simulate pathological changes

doi:10.6342/NTU202503673

and the mechanical response, providing quantitative assessments and aiding decision-making [60].

2.6.4 FE Modeling in Digital Twin

Traditional FEM discretizes geometries into finite elements for precise analyses. This proves involves complex processing which makes it computationally intensive, therefore its usability to intraoperative application is limited. Therefore, traditional FEM is primarily used in preoperative planning and implant design optimization due to demands in computational intensity [61].

Patient-specific digital twins modeled using FEM can simulate different treatment options precisely for an individual patient, tailored specifically to their unique bone structure, fracture details, and force-loading conditions during activities. FEM-based digital twin models are unlikely to be feasible for real-time intraoperative decision-making. These digital twins are more suitable for preoperative planning than live guidance. Despite these limitations, FEM-based digital twins provide insights in biomechanical behavior, stability, and stress distribution. This type of digital twins are powerful tools for surgical planning, optimizing surgical strategies, and predicting long-term postoperative outcomes [62].

doi:10.6342/NTU202503673

2.6.5 Multibody Dynamics Modeling in Digital Twin

Multibody Dynamics (MBD) is a promising alternative approach for modeling digital twins of a knee joint. MBD is computationally efficient, enables real-time feedback for intraoperative simulations, and surgical optimization. However, MBD suffers from accurately modeling contact and collision detection with more complex geometries. Using MBD requires further integration of collision detection algorithms that provide rapid results to maintain intraoperative applications. Therefore, optimizing traditional FEM for faster predictions is more favorable [61].

2.6.6 Digital Twins in Personalized Medicine and Precision Healthcare

The complexity and variability of the biological systems of every patient necessitates personalized treatment approaches such as precision medicine, which is a holistic medical treatment approach by considering genetic, environmental, and even lifestyle differences. Developments in digital twin technologies are increasingly used to realize precision medicine and personalized care approach [20]. Current personalized healthcare approaches have limitations in effective personalization of healthcare. Existing AI-based approaches rely on regression techniques which are limited in scope, disease-specific, and often produces high rates of false negative predictions. A generic approach neglects individual differences and leads to suboptimal outcomes for personalized healthcare [63]. Recent developments of digital twins have seen a departure from a disease care

doi:10.6342/NTU202503673

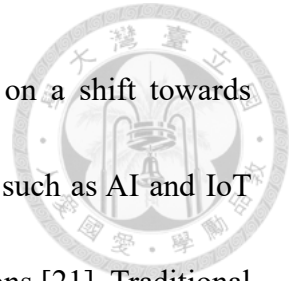

perspective to a personalized and preventive healthcare, focusing on a shift towards becoming person-centric. The integration of advanced technologies such as AI and IoT enables the modern digital twin to provide tailored healthcare solutions [21]. Traditional healthcare systems is facing significant resource shortages, rising cost, and inefficiencies brought upon and highlighted during the COVID-19 pandemic. Due to this crisis, there is an urgent need for innovative solutions to improve efficiency, outcomes, and efficient resource utilization [64].

The increase of prevalence in musculoskeletal diseases due to aging populations emphasize the growing medical need for advanced diagnostic and treatment methods. A key factor in understanding musculoskeletal disease development is analyzing biomechanical changes. Conventional biomechanical research methods have limitations in analyzing dynamic kinematic response and modeling individual variability. The complexity of the human musculoskeletal system makes accurate modeling difficult. In-vivo methods for modeling face difficulties in technical and safety limitations such as sensor size and battery safety. In-vitro methods have difficulties replicating microenvironments, and availability of cadavers are limited by ethical issues. Digital twins have high potential for transforming diagnosis, treatment, and recovery monitoring. High-resolution digital twins could provide high precision, real-time monitoring, and personalized treatment for musculoskeletal diseases [19]. Highly detailed and real-time

doi:10.6342/NTU202503673

biomechanical modeling are advantages of digital twins in musculoskeletal applications. The first digital twin of a human lumbar spine is an example of these advantages. Furthermore, dynamic simulations enhance understanding of biomechanical changes such as biomechanical performance and disease progression. Through digital twins, personalized treatment planning and continuous monitoring transforms treatment of musculoskeletal diseases [19].

2.6.7 Applications and Capabilities of Digital Twins

Digital twins in medicine, particularly in orthopedics and biomechanics, can be applied to monitor spinal biomechanics, and assist in post-operative assessment and monitoring [20]. Digital twins are more comprehensive in representing an individual virtually by integrating diverse dataset sources, enabling detection of subtle patterns that are beyond human recognition. The applications of digital twins in personalized healthcare include drug development, lifestyle recommendations, disease prevention by early warning, and surgical planning. With real-time and personalized insights, digital twins can accurately model individual health status and future risks, resulting in proactive healthcare. High-fidelity digital twins improve synchronization between the individual and their digital twin [63]. The key features of digital twins in healthcare are: accurate digital representations of their physical system counterparts; incorporation of all processes and operations related to the physical entity; synchronization and constant, real-time, updating

doi:10.6342/NTU202503673

of data; and simulation of the behaviors of the physical twin, enabling analysis and decision-making support [21]. The role of digital twins in healthcare is expanded by its capability of providing a dynamic platform for running theoretical scenarios, aiding in diagnosis, treatment planning, and understanding complex biological systems. The digitization of scenarios such as patient experience like sensations of pain, early disease detection like identifying genomic and epigenomic changes, and vaccine testing are some of the advantages of digital twins for safe, cost-effective, and reliable hyper-realistic testbeds [64].

2.6.8 Implementation Requirements and Challenges

Successful digital twin implementation requires three core requirements: real-time data aggregation, integration and interoperability, and fidelity. There must be a fast and reliable health data collection and updating from diverse sources. Seamless cooperation with other systems is a core requirement for digital twins, requiring mechanisms for data exchange. Lastly, a digital twin is as accurate as the data used. Therefore, data quality affects how the digital twin reflects complex biological structures and functions [65]. The current state of personalized digital twin in healthcare is still in the early development stages. Its development and innovation require further research and standardization [21]. The future potential of digital twins in healthcare is towards a smart and personalized healthcare industry through integration of digital twins with existing advanced

doi:10.6342/NTU202503673

technologies for patient-centered care, rapid diagnosis, and personalized treatment [21]. The present challenges of digital twins in personalized healthcare is its reliance on non-individualized data—dataset sources range from cadaveric or previous studies. Using non-individualized data, digital twins rely on the generalizability of these datasets. Furthermore, real-time data acquisition, in-vivo or intraoperatively, is difficult. This factor may lead to gaps between digital twins and actual physical systems [19].

2.7 Methods for 2D-3D Shape Reconstruction in Patient-specific Modeling

2.7.1 2D-3D Reconstruction Methods and Challenges

Personalized 3D bone models are invaluable for disease diagnosis, surgical planning, and surgical intervention guidance [66]. Acquisition of 3D models using conventional methods such as CT and MRI are costly and expose the patient to high radiation doses [22]. Using conventional methods for acquiring 3D models are also limited in providing assessment of physiological functions. This limitation is due to the information from CT or MRI are static conditions of the bones [66]. An alternative to reconstructing 3D models is by using 2D images such as X-ray or C-arm radiographs but requires solving related challenges [22]. 2D-3D reconstruction from limited 2D X-rays such as biplanar X-rays is one of the emerging techniques. A successful approach uses contour extraction from planar or biplanar X-rays. Then, the corresponding points are aligned to create a 3D point cloud from the matching points. Mesh reconstruction is typically achieved using

doi:10.6342/NTU202503673

established methods such as Poisson-based techniques [66]. 3D modeling reconstruction techniques can be categorized into the following: generic model deformation methods, statistical shape models (SSMs), and hybrid methods [22].

An example of a process for reconstructing 3D models with the SSM method involves using digitally reconstructed radiographs (DRRs) with the SSM. A DRR is a simulated 2D projection of the 3D model, flattening the 3D model to mimic the appearance of a 2D X-ray. For each candidate 3D shape generated by the SSM, a DRR is created. Iterative optimization algorithms adjust the DRR to minimize the difference between actual radiographs of the patient. Once a satisfactory match between the DRR and the patient radiograph is obtained, the deformed SSM is considered the 3D model representation of the patient's anatomy [67].

2.7.2 Statistical Shape Models (SSMs) Fundamentals

SSMs such as point distribution models are effective in representing anatomical variations. SSM-based 3D reconstruction is particularly valuable in surgical planning. An example is total hip arthroplasty where the patient-specific 3D models of the pelvis and femur are reconstructed from limited 2D images for implant design and planning [22]. SSMs have the fundamental principle of capturing the morphological variability. SSMs are built from a collection of 3D surface models of anatomical structures such as bones. These datasets are called training shapes and represent the normal and pathological

doi:10.6342/NTU202503673

variations of different individuals [67].

The construction of SSMs involve the following processes: shape representation methods, correspondence establishment, shape alignment, and statistical modeling. Shapes can be described using various features such as landmark points, distance maps, and deformation fields. The most common method is using landmark points. Modern approaches to this method uses thousands of densely clustered landmarks for high detail modeling. To compare shapes, each point must correspond to the same anatomical feature across all other samples or shapes. Achieving correspondence usually involve methods such as iterative closest point (ICP) algorithm, coherent point drift, and robust point matching. Without correspondence, no meaningful statistical analysis can be made [68].

Correspondence techniques are categorized into the following: mesh-to-mesh registration, mesh-to-volume registration, and volume-to-volume registration. Mesh-to-mesh registration refers to the direct registration of one mesh surface to another. The algorithms commonly used is ICP. This method requires a template shape to which all other training shapes are registered—this may introduce bias. The limitations of this method is that it assumes similarity between the training shapes, and large deformities may lead to incorrect correspondences. Non-rigid registration approaches like B-splines and thin-plate splines can be used to handle these large shape variations, but will require manual landmark placement. Mesh-to-volume registration refers to correspondences

doi:10.6342/NTU202503673

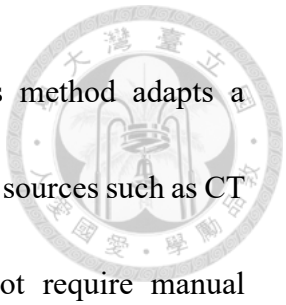

derived from the final vertex positions after surface fitting. This method adapts a deformable surface model, the mesh, to volumetric data from imaging sources such as CT and MRI. If the template model is robust, this method does not require manual segmentation. Volume-to-volume registration refers to the alignment of volumetric datasets directly using atlases. These atlases are used to propagate landmarks to training shapes through deformation fields. Many techniques can be used for registration in this method such as B-splines and quasi-affine registration. This method also does not require manual segmentation and can be directly applied to grayscale images. However, this method relies on high-quality images and similarity between samples—this may also introduce bias [69]. MDL is a method that evaluates the quality of shape correspondences by capturing shape variability across all training shapes. Specifically, MDL calculates the bit-length—the encoding cost of the shape model and the training shapes. A good correspondence means shorter and compact descriptions lengths. MDL uses optimization algorithms such as genetic algorithms or gradient descent to iteratively search for the correspondence setup that minimizes description length. The iteration procedures under MDL makes it computationally expensive and usually requires significant processing time. SPHARM is a method that describes and compares shapes by mapping their surfaces onto a sphere. The core process in SPHARM is spherical parametrization, a process in which each shape is mapped onto a sphere with as little distortions as possible.

doi:10.6342/NTU202503673

The unique features of each training shape are then represented through spherical harmonic coefficients. Then, correspondence is achieved by using conformal mapping to align spherical parametrizations. Conformal mapping preserves angles and ensures consistent shape comparison. The limitations in SPHARM for 3D correspondence is that the method is restrictive in the possible training shapes that can be handled (e.g., no holes in topology of shapes). Furthermore, the computational costs for conformal mapping and calculating spherical harmonic coefficients are high [70].

Alignment of shapes requires all training shapes be aligned in a common coordinate frame. Alignment is necessary for accurately modeling shape variability. The standard method is using GPA, which removes any shape differences caused by translation, rotation, and scaling. GPA minimizes the mean squared distances between the training shapes and then aligning them to a mean shape. Establishing accurate shape correspondences across all the training shapes in the dataset is critical in modeling shape statistics. The quality of correspondence determines the accuracy and usefulness of the SSM [69]. 3D correspondence is particularly difficult due to complex and nonlinear shape variations. Traditional 3D shape correspondence methods rely on landmarks but these may not correspond to anatomical points. Existing state-of-the-art methods for 3D shape correspondence are minimum length description (MDL) and spherical harmonics (SPHARM). These two 3D correspondence methods are widely used but each approaches

doi:10.6342/NTU202503673

the problem differently and has its own limitations [70].

After alignment using GPA, shape variations are then modeled statistically. Principal component analysis (PCA) is another widely used technique that can be applied to find the main modes of variation by calculating the eigenvectors. These eigenvectors are ordered to display the most significant modes that explain the most variance [68]. Using techniques like PCA, main modes of variation in the SSM training dataset can be identified. These modes or PCs describe shape variations like physical dimensions, bony contours, and specific deformities [67]. The SSM is constructed by the combination of all the PCs, which are weighted for the cumulative explained variance. A mean shape also serves as the approximate of the overall shape of the SSM [68]. The choice of shape representation in SSM is the most fundamental step and therefore influences all subsequent modeling steps. The most common method for shape representation is landmark-based point distribution models. This method places points on the surface of a shape, the coordinates of these points form a shape vector. The distribution of points can be anatomical features or simply arbitrary placement. The landmark-based shape representation method is the most popular due to its simplicity, ease of use and visualization, and simple implementation compared to more complex methods like spherical harmonics (SPHARM) [69].

SSMs can be validated for model quality using the following metrics: compactness,

doi:10.6342/NTU202503673

specificity, and generality. Compactness is another metric that indicates the effectiveness of the SSM to represent shape variability with only a limited number of principal components. Specificity refers to the measure of realism in the generated shapes, i.e., whether or not the shapes are similar to the training data (sample shapes). Lastly, generality refers to the capacity of the SSM to generate shapes not in the training set for scalability and generalizability. In general, a good balance of the model quality metrics is essential for creating high-quality SSMs. Specifically, a balance must be achieved between specificity (shape realism) and generality (handling new shapes). Overfitting occurs when there is high specificity but low generality, which is undesirable [68].

2.7.3 Modern Techniques for SSM-based 2D-3D Registration

Modern techniques for 2D-3D reconstruction are emphasizing SSM-based deformations through non-rigid registration of 2D X-ray images to 3D models, allowing for personalized reconstruction of anatomical features. The key process of 2D-3D registration is that once the registration has successfully aligned the 3D models with the 2D images, the patient-specific anatomy can be estimated [22]. There are emerging techniques for 2D-3D registration based on the intensity of limited 2D images. Such emerging techniques generally fall under two main categories: single template-based methods and SSM-based methods. The single template-based method requires more parameters and optimization due to the reliance on a specific template derived from either

doi:10.6342/NTU202503673

CT scans or visual hulls. Using SSMs as a basis for 2D-3D reconstruction have the advantages of being more robust and reducing computational complexity by constraining deformations to variations based on statistics [22]. Using B-spline has a successful application for SSM deformation. The deformed SSM using this method effectively captures the mean and variability of known deformations. With the use of prior statistical anatomical information, the warps made to the SSM is constrained to the most statistically plausible shapes. This approach reduces the number of parameters needed for registration [22].

2.7.4 3D Bone Reconstruction from 2D X-ray Imaging

Existing methods for 3D bone reconstruction using 2D X-rays use planar or biplanar X-rays to morph the SSM against the contour lines of the anatomy in the 2D X-rays. These methods require calibration of X-ray images and benefits from deep learning techniques to reconstruct 3D images. Furthermore, these methods may face difficulties when parts of the anatomy such as bones are missing (e.g., result of major trauma) or incomplete (e.g., FOV limitations from imaging). Using SSMs bridge the gaps and restore missing parts to enable analysis of joint kinematics and accurate surgical planning. Some studies have integrated regression models with SSMs for better estimation of parameters such as bone length from incomplete bones [71]. Prevalent techniques for 3D shape and pose estimation from 2D X-ray images can be categorized into the following: intensity-

doi:10.6342/NTU202503673

based methods and edge-based methods. Intensity-based methods optimize similarities between X-ray images and DRRs. These methods often require modeling tissue density. Edge-based methods simply minimize distances between image edges and model silhouettes. These methods are found to be more robust in clinical applications. Furthermore, the edge-based approach method is more suitable when the edges of the bones are clearly visible, allowing semi-automated or automated edge detection. Overall, edge-based methods are less computationally intensive than using DRR [72]. Edge-based methods have been developed with automated approaches to successfully reconstruct 3D bony anatomy, specifically the distal femur. The inputs use two or more calibrated X-ray images, a prior SSM, and a 3D distance-based objective function on Canny edges. Minimal manual input is one of the advantages of this technique and can perform well in realistic conditions. Specifically, applications to cadaveric study in-vivo show high accuracy. Error propagation is attributed to limitations in the SSM and image quality. However, the limitations of this technique assumes that the bones are healthy. The technique may not perform well for pathological bones. Furthermore, the technique was only used for distal femur applications. The reliability of the technique in other applications such as considering the entire knee joint as a whole (e.g., femur, patella, and tibia) is unclear [72]. A technique has been successfully developed for achieving 2D-3D shape reconstruction using fluoroscopic images through a two-stage reconstruction

doi:10.6342/NTU202503673

process. The first stage is optimal position and orientation estimation within the 2D fluoroscopic images. This stage involves the use of the level set method for registration. The second stage is the estimation of the shape parameters to best fit the silhouettes observed in the fluoroscopic images [73]. Reconstructing 3D shapes from 2D fluoroscopic images is highly desirable due to the practicality and minimal radiation exposure acquired from this imaging modality [73].

Using low-dose 2D X-ray data for 3D model reconstruction addresses the issues associated with CT scans. However, this process necessitates prior statistical information such as the use of SSM [72]. Multi-object SSMs that incorporate shape and pose are more realistic in representing complex biological systems that have multiple bones such as the knee joint. Multi-object SSMs outperform isolated-object or single-object models by being able to better capture anatomical proximity and the interaction of the bones [74]. Bones such as the femur have universal shape patterns and can be modeled statistically. These patterns, once modeled using SSMs, can be used to reconstruct patient-specific 3D shapes even from minimal 2D data [73].

2.8 Computational Surgical Simulations Using Patient-Specific Models

2.8.1 Computational Modeling in Patellofemoral Surgery

The limitations in relying on cadaveric studies alone is that cadaveric data may not accurately represent in-vivo conditions such as patellar subluxation or anatomical

doi:10.6342/NTU202503673

variations. It is difficult to reproduce pathological patellar conditions with a cadaver specimen, and since differences in individual knee anatomy are important for influencing surgical outcomes a limited number of cadaveric specimens cannot represent a wide range of anatomical variability [75]. Use of cadaveric data lacks applicability to living patients. Dynamic neuromuscular control, particularly observed in active, younger individuals is not possible to simulate in cadaveric studies. Although possible, joint forces and full-leg alignment—factors influencing patellar stability in-vivo—is difficult to simulate in cadaveric studies [76]. Computational simulations such as FE modelling for surgical procedures allows detailed and controlled analysis of individual factors affecting patellar stability. The accuracy of simulated results is found to be within a single standard deviation from cadaveric data. Modeling the knee joint in a virtual environment overcomes the limitations of in-vivo experiments, primarily variability and ethical constraints. Precise and reproducible measurements of contact pressures, areas, and kinematics overcome limitations of static imaging-based studies [77].

Computer models created using digitized cadaver data or in-vivo imaging are considered valuable for assessment of surgical procedures in a virtual environment and optimizing procedures tailored to individual anatomy. 3D models created from patient data captures unique joint topography and pathology for a more realistic surgical outcome. Computer models in surgical planning is a shift towards patient-specific surgical planning

doi:10.6342/NTU202503673

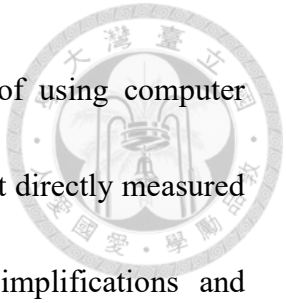

that optimizes outcomes and reduces variability. The limitations of using computer models include estimation of muscle and soft tissues properties if not directly measured [75]. The limitations of using computational models include simplifications and assumptions of material properties and anatomy not directly measured. It is common to derive material properties from literature for simplicity when developing computational models. However, the results may not be patient-specific in this specific regard. Careful considerations must also be made when simplifying joint biomechanics as factors from muscular influences influence patellar stability [77].

2.8.2 FE Modeling for Patellofemoral Joint

FEA as a computational tool has evolved from applications in bone mechanics analysis to understanding complex biomechanical behaviors of tissues at cellular levels. Modern FE modeling in a surgical context can provide real-time analysis based on a single model for rapid evaluation. Measurements and visualizations of maximum stress areas has made FE modeling valuable for decision-making support and implant design [23]. FE models allow in-silico analysis of different types of surgical procedures such as MPFL reconstruction and lateral retinacular release before actual surgery. These virtual surgeries enable assessment of the influence of each surgical procedure on joint biomechanics, stability, and contact pressures. These measurements are difficult to measure directly in-vivo [69]. FE models have successful applications in simulating the complex joint

doi:10.6342/NTU202503673

biomechanics of the patellofemoral joint and simulating different surgical conditions. FE models used in this area help predict the biomechanical effects of surgical procedures like lateral retinacular release [24]. FE modeling of knee surgeries also have successful applications in assisting meniscectomy, meniscal repair, ACL and PCL reconstruction, and MPFL reconstruction [23].

FE models can also replicate pathological states such as increased tibial tubercle and trochlear groove (TT-TG) distance, ligament lesions, and retinacular tightening. Simulating pathological conditions provide insights into their biomechanical impacts and the mechanical responses to different surgical procedures while maintaining a controlled and reproducible environment [69]. FE models of the knee joint for surgical simulations can incorporate specific biomechanical parameters such as physiological loads and ligament stiffness values based on literature to represent realistic tissue behavior. Further adjustments can be made to the model parameters simulate personalized conditions as well as simulation of pathology and surgical release procedures [24].

FE models for knee joints rely on high-quality 3D imaging data like CT and MRI scans for creating and conversion into analysis-ready formats, usually STL files. Soft tissue structures such as ligaments are modeled with nonlinear, tension-only springs elements to mimic the behavior of their physical counterparts efficiently. Other soft tissues such as cartilage and menisci are modeled as having isotropic, elastic material properties to better

doi:10.6342/NTU202503673

capture the complex tissue behavior. Hard tissues such as bones are typically treated as completely rigid, nondeformable bodies due to their high stiffness. Realistic joint mechanics rely on contact interactions and in FE modeling it is possible to use frictionless contact formulations. The physiological loads such as quadriceps muscle forces are based on biomechanical data, which is sufficient to replicate in-vivo conditions. The distribution of physiological loads from the muscles enhances the relevance of the FE model. Kinematic constraints such as axis definitions can adopt widely-used biomechanical conventions for accuracy [69].

Surgical simulation of lateral release can be performed by disabling spring elements that represent lateral soft tissues with abnormal tension. The release of excessive tension mimics surgical release, allowing simulation of how the patellofemoral joint respond upon reduced lateral retinacular constraints. Simplified representations, such as using spring elements for ligaments allows, for realistic yet computationally efficient simulations, practical for surgical planning [69]. It is a common practice in FE modeling of knee joints to simulate soft tissue structures like the MPFL and the lateral retinaculum as spring elements. Then, for surgical release simulation, the spring elements for the lateral retinaculum can be simply deactivated. Alternatively, deactivating spring elements can also simulate injury, e.g., MPFL tear [24].

doi:10.6342/NTU202503673

2.8.3 FE Modeling Limitations

A limitation when using healthy knee imaging data in surgical simulations using FE models is that these models may not accurately simulate or incorporate multiple risk factors of patellar instability such as patella alta, trochlear dysplasia, or lateralization of the tibial tubercle [24]. Limitations of FE modeling in a surgical context include the requirement of expertise in FEA. FEA is complex and labor-intensive. Without image-based models, it will be difficult to analyze changes of material properties over time [23].

doi:10.6342/NTU202503673

Chapter 3: Materials and Methods

3.1 Digital Twin System Overview

The overall architecture of the digital twin system and its subsystems is shown in Figure 3-1. The system is designed to replicate patient-specific knee joint biomechanics using non-invasive clinical imaging as input. Routine preoperative X-rays are the imaging input used. Using these X-rays acquired during the preoperative phase limits the radiation exposure of the patient. The X-rays must be anteroposterior (AP), mediolateral (ML), and Merchant views for optimal usage in the proposed digital twin system. 2D anatomical landmarks are extracted from the X-rays using manual methods. The accuracy of the obtained landmarks depends largely upon the expertise of the annotator. The list of landmarks to be identified is consistent for every patient. Using the novel technique of Subset-Based Registration (SBR) method, the 2D anatomical landmarks are then processed via SBR to reconstruct 2.5D landmark positions. These 2.5D landmarks are used to deform an existing statistical shape model (SSM) using an SBR-based deformation technique with thin-plate splines, resulting in a patient-specific 3D mesh of the knee joint. The reconstructed geometries obtained from deforming the SSM include the femur, tibia, patella, and fibula. The geometry of these bones serves as the basis for finite element analysis (FEA). The FEA simulations are performed offline in Ansys to evaluate knee joint kinematics under different conditions and surgical release types.

doi:10.6342/NTU202503673

Simulated surgical interventions. such as varying lengths of lateral or medial retinacular release, are applied to the digital twin to determine the biomechanical impacts of each surgical release scenario. The resulting data is intended to guide the surgeon in planning the optimal release length for real-world procedures. Post-operative outcomes will be fed back into the system to iteratively refine the digital twin—with the intention of improving its predictive accuracy over time through parameter adaptation. A summary table for the digital twin system is provided in Table 3-1.

Table 3-1. Digital twin system summary table

Subsystem	**Input**	**Process**	**Output**
X-ray acquisition	AP, ML, and Merchant view	Manual landmarking	2D landmarks
2.5D reconstruction	2D landmarks	SBR method	2.5D points
SSM deformation	2.5D points + SSM	TPS deformation	3D mesh
FEA	3D mesh + ligament data	FE model simulation	Patellar tracking
Feedback	Simulated and post-op kinematic data	Adaptive update	Refined digital twin

The current implementation of the digital twin system focuses on a single patient-specific model. The process involved the use of an MRI-segmented STL mesh of a patient to be used for FEA. This FE model allowed for detailed, in-depth analysis of patellar kinematics under different knee conditions, i.e., healthy knee and different degrees of

doi:10.6342/NTU202503673

ligament tightness, as well as different surgical release scenarios. The goal was to understand the mechanisms of the knee under different ligament tightness conditions and its responses to surgical release in a controlled environment. The MRI-segmented FE model served as the ground truth for defining normal patellar tracking and knee joint kinematics. The objective definition of normal patellar tracking aided training the predictive models for malalignment prediction and kinematic responses post-surgery. It is emphasized that the current FE model used and the predictive models are patient-specific and not generalizable but serves as a proof-of-concept. In future research, accumulating multi-patient data is desired for greater accuracy and generalizability by making the digital twin system scalable.

doi:10.6342/NTU202503673

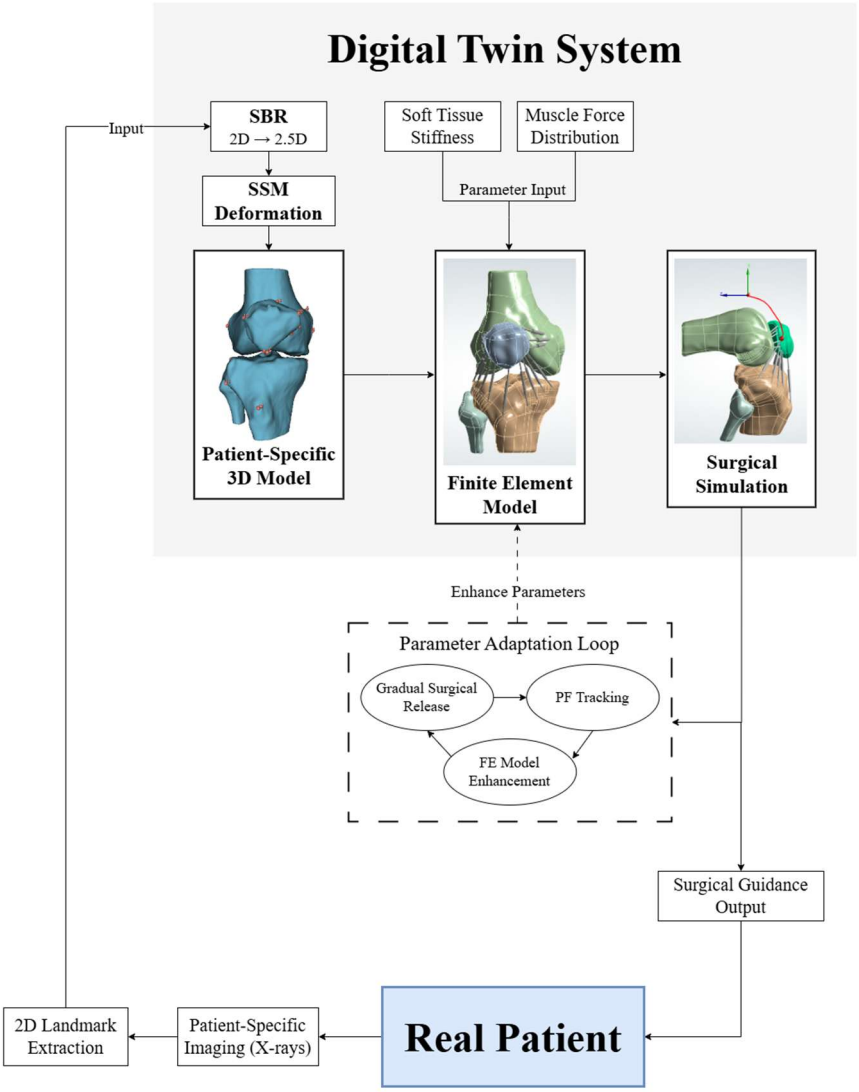

Figure 3-1. Digital twin design for patient-specific knee modeling and surgical simulation. Images used courtesy of ANSYS, Inc.

3.2 Data

The X-ray images used in this study were acquired using a C-arm fluoroscope under standard clinical imaging protocols. These images serve as the basis for extracting 2D anatomical landmarks in the digital twin pipeline. A statistical shape model (SSM) was constructed using 22 datasets. This included five computed tomography (CT) scans and

doi:10.6342/NTU202503673

two magnetic resonance imaging (MRI) scans obtained from publicly available open-source repositories [78]. The MRI datasets were acquired using a T2-weighted protocol, consisting of 192 slices with a slice thickness of 0.5 mm. The in-plane resolution was 320 × 320 pixels, with a pixel spacing of 0.46875 × 0.46875 mm. The CT datasets consisted of 310 slices with a slice thickness of 0.75 mm, an in-plane resolution of 512 × 512 pixels, and a pixel spacing of 0.390625 × 0.390625 mm. The remaining 15 datasets were provided by an orthopedic surgeon for this study. Figure 3-2 shows all the segmented knee joint models from the various dataset sources. One CT segmented knee joint model was discarded due to poor quality CT data.

doi:10.6342/NTU202503673

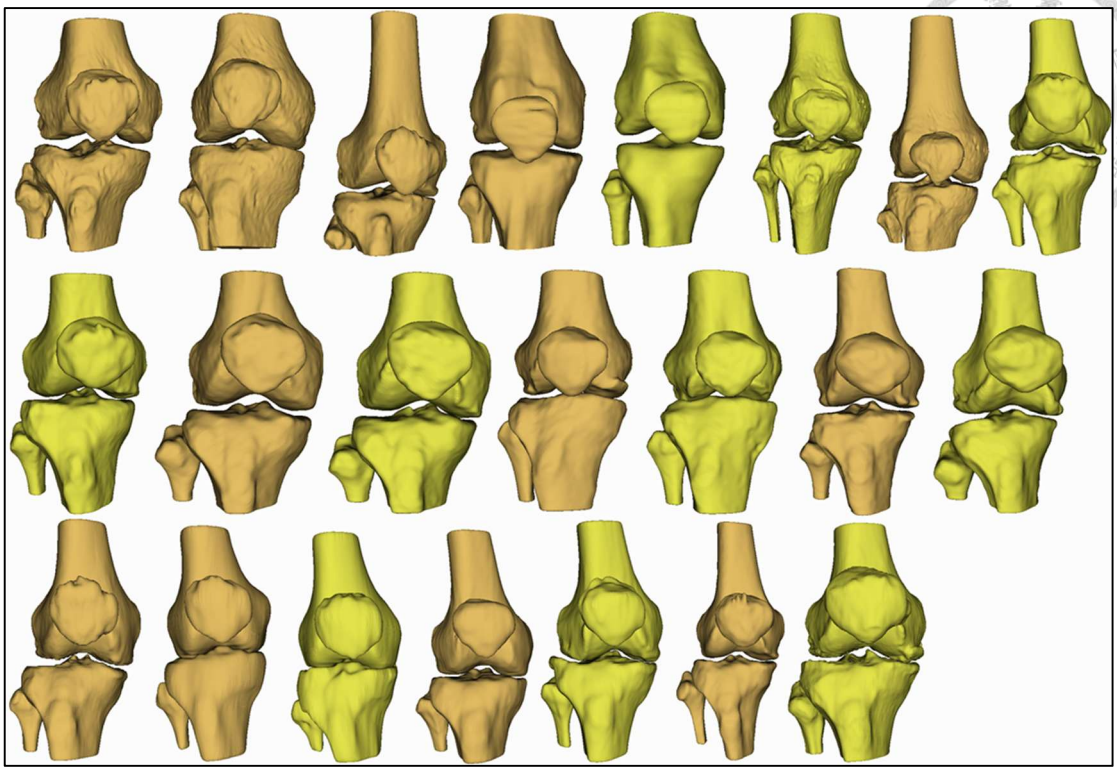

Figure 3-2. Segmented knee joint models used for this study.

3.3 Subset-Based Registration

The proposed method consists of five steps: (1) data input and preprocessing, (2) landmark subset matching, (3) SVD-based rigid registration, (4) landmark projection and correction, and (5) new landmark generation. SBR is the computational approach used to align an incomplete set of 2D anatomical landmarks to a complete 3D reference landmark set and subsequently generate new estimated landmark coordinates based on observed transformations.

The complete 3D landmark set of the SSM consists of landmarks, $\boldsymbol{s}_i$, each defined by a unique identifier, $I(\boldsymbol{s}_i)$, which is its anatomical landmark name, and its spatial coordinates:

doi:10.6342/NTU202503673

$$\boldsymbol{S} = \{\boldsymbol{s}_1, \boldsymbol{s}_2, \dots \ , \boldsymbol{s}_N\}, \qquad \boldsymbol{s}_i = (x_i, y_i, z_i).$$

Similarly, each target subset $\boldsymbol{T}^{(k)}$ extracted from X-ray images contain a fraction of the full landmark set:

$$\boldsymbol{T}^{(k)} = \{\boldsymbol{t}_j \mid \boldsymbol{t}_j \in \boldsymbol{S}\}, \qquad \boldsymbol{T}^{(k)} \subseteq \boldsymbol{S},$$

where *k* indexes different subsets.

For each subset, $\boldsymbol{T}^{(k)}$, the corresponding landmarks in $\boldsymbol{S}$ will be extracted:

$$\boldsymbol{S}^{(k)} = \{\boldsymbol{s}_j \mid I(\boldsymbol{s}_j) = I(\boldsymbol{t}_j),\ \boldsymbol{t}_j \in \boldsymbol{T}^{(k)}\},$$

where $\boldsymbol{S}^{(k)}$ and $\boldsymbol{T}^{(k)}$ have an equal number of elements to ensure one-to-one correspondence between matched landmarks. The number of matched landmarks is denoted $M_k = |\boldsymbol{T}^{(k)}| = |\boldsymbol{S}^{(k)}|$.

To align $\boldsymbol{S}$ with $\boldsymbol{T}^{(k)}$, the subset of $\boldsymbol{S}$ corresponding to the available landmarks in $\boldsymbol{T}^{(k)}$ is denoted as $\boldsymbol{S}_c^{(k)}$, while $\boldsymbol{T}_c^{(k)}$ is the corresponding target points. The centroid of each set is then computed as:

$$\bar{\boldsymbol{s}}^{(k)} = \frac{1}{M_k}\sum_{i=1}^{M_k} \boldsymbol{s}_i\,, \qquad \bar{\boldsymbol{t}}^{(k)} = \frac{1}{M_k}\sum_{j=1}^{M_k} \boldsymbol{t}_i.$$

Subtracting the centroids to position the points at the origin:

$$\boldsymbol{S}_c^{(k)} = \{\boldsymbol{s}_i - \bar{\boldsymbol{s}}^{(k)}\}, \qquad \boldsymbol{T}_c^{(k)} = \{\boldsymbol{t}_j - \bar{\boldsymbol{t}}^{(k)}\}.$$

The covariance matrix is then:

doi:10.6342/NTU202503673

$$\boldsymbol{H} = \left(\boldsymbol{S}_c^{(k)}\right)^T \boldsymbol{T}_c^{(k)}.$$

Applying singular value decomposition (SVD) to obtain:

$$\boldsymbol{H} = \boldsymbol{U}\boldsymbol{\Sigma}\boldsymbol{V}^T.$$

The optimal rotation matrix is given by:

$$\boldsymbol{R} = \boldsymbol{V}\boldsymbol{U}^T.$$

If $\det \boldsymbol{R} < 0$, then $\boldsymbol{V}$ is modified to ensure a proper rotation.

The optimal translation vector is computed as:

$$\boldsymbol{t} = \bar{\boldsymbol{t}}^{(k)} - \boldsymbol{R}\bar{\boldsymbol{s}}^{(k)}.$$

The transformed source landmarks are given by:

$$\boldsymbol{s}_{aligned}^{(k)} = \boldsymbol{R}\boldsymbol{s}_i + \boldsymbol{t}, \qquad \forall\ i \in \{1, \dots, M_k\}.$$

After registration, a new set of points is generated. The relative displacement between matched source and target points is obtained by:

$$\Delta \boldsymbol{s}_j = \boldsymbol{t}_j - \boldsymbol{s}_{aligned,j}^{(k)}.$$

where $\Delta \boldsymbol{s}_j$ is the displacement vector between matched points.

A new projected point is then defined as:

$$\boldsymbol{s}_{new,j}^{(k)} = \boldsymbol{s}_j + \left(\Delta \boldsymbol{s}_j\right)_x \hat{\boldsymbol{\imath}} + \left(\Delta \boldsymbol{s}_j\right)_y \hat{\boldsymbol{\jmath}},$$

doi:10.6342/NTU202503673

where the z-coordinate of $\boldsymbol{s}_j$ remains unchanged.

For unmatched landmarks in the target set, the source coordinates are retained, ensuring a complete set of new landmark points. The final ordered set of transformed landmarks is saved in a CSV file, maintaining the original indexing structure from the source dataset.

The SBR method is applied on the sagittal and coronal X-ray views obtained from a C-arm fluoroscope during the cadaver study—discussed in more detail in the latter portion of this chapter. Identifiable anatomical landmark points were annotated. Ambiguous landmark points were not annotated and were handled appropriately by the SBR algorithm. Figure 3-3 shows the 3D SSM landmarks subset rigidly registered to the 2D sagittal X-ray landmark points. Similarly, Figure 3-4 shows the SSM landmarks registered to the coronal X-ray landmarks. These points from different views are then processed accordingly to yield 2.5D points for SSM deformation using thin-plate splines—this process is discussed in more detail in the following subsections. The SBR method does not expect total alignment between matched points. Instead, it assumes that the relative differences arising from the SBR method shows unique anatomical variation between the patient-specific imaging (X-ray) and the mean shape (SSM). Therefore, RMSE is not calculated.

doi:10.6342/NTU202503673

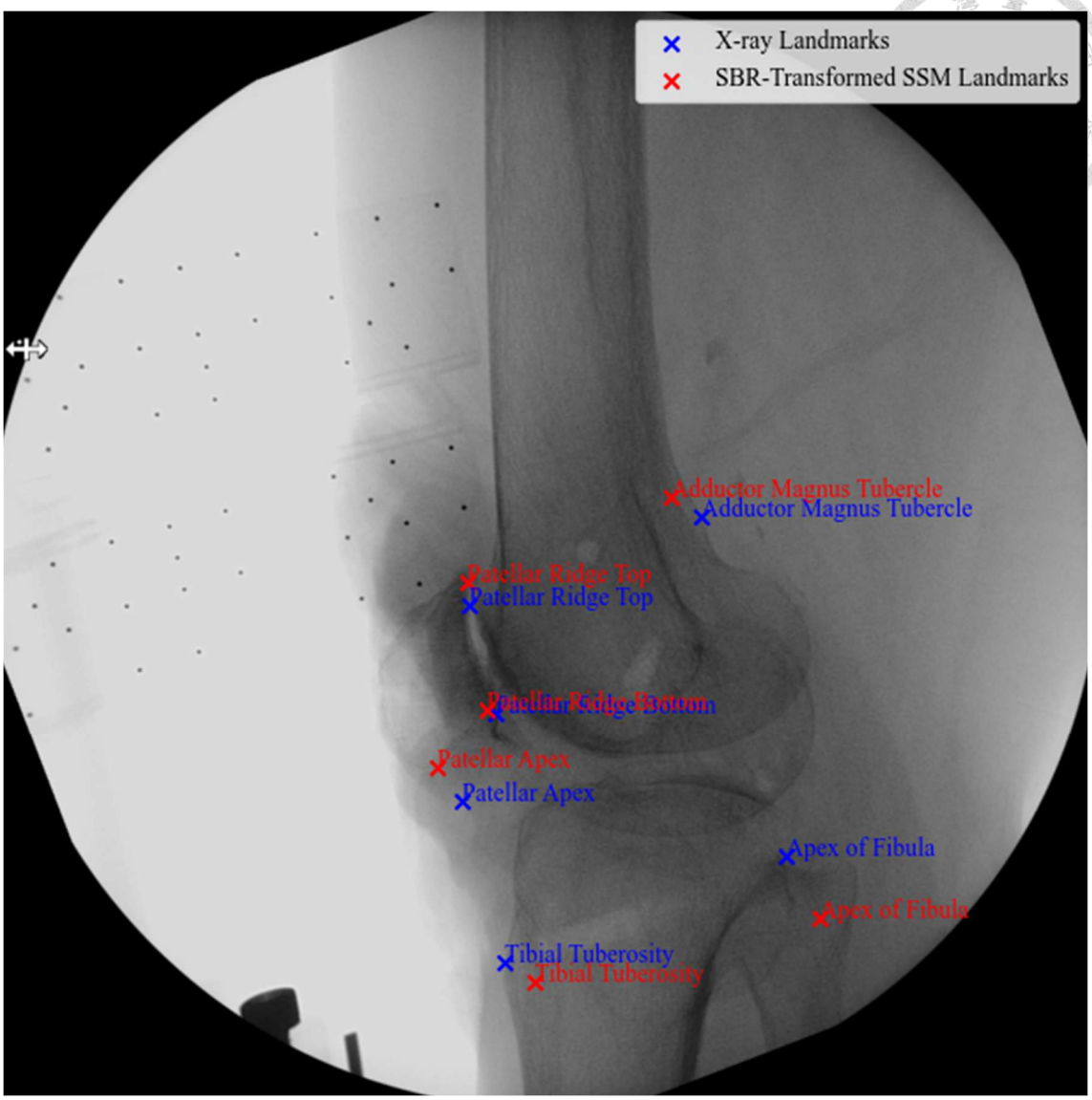

Figure 3-3. 3D SSM landmarks subset rigidly registered to 2D sagittal X-ray landmarks.

doi:10.6342/NTU202503673

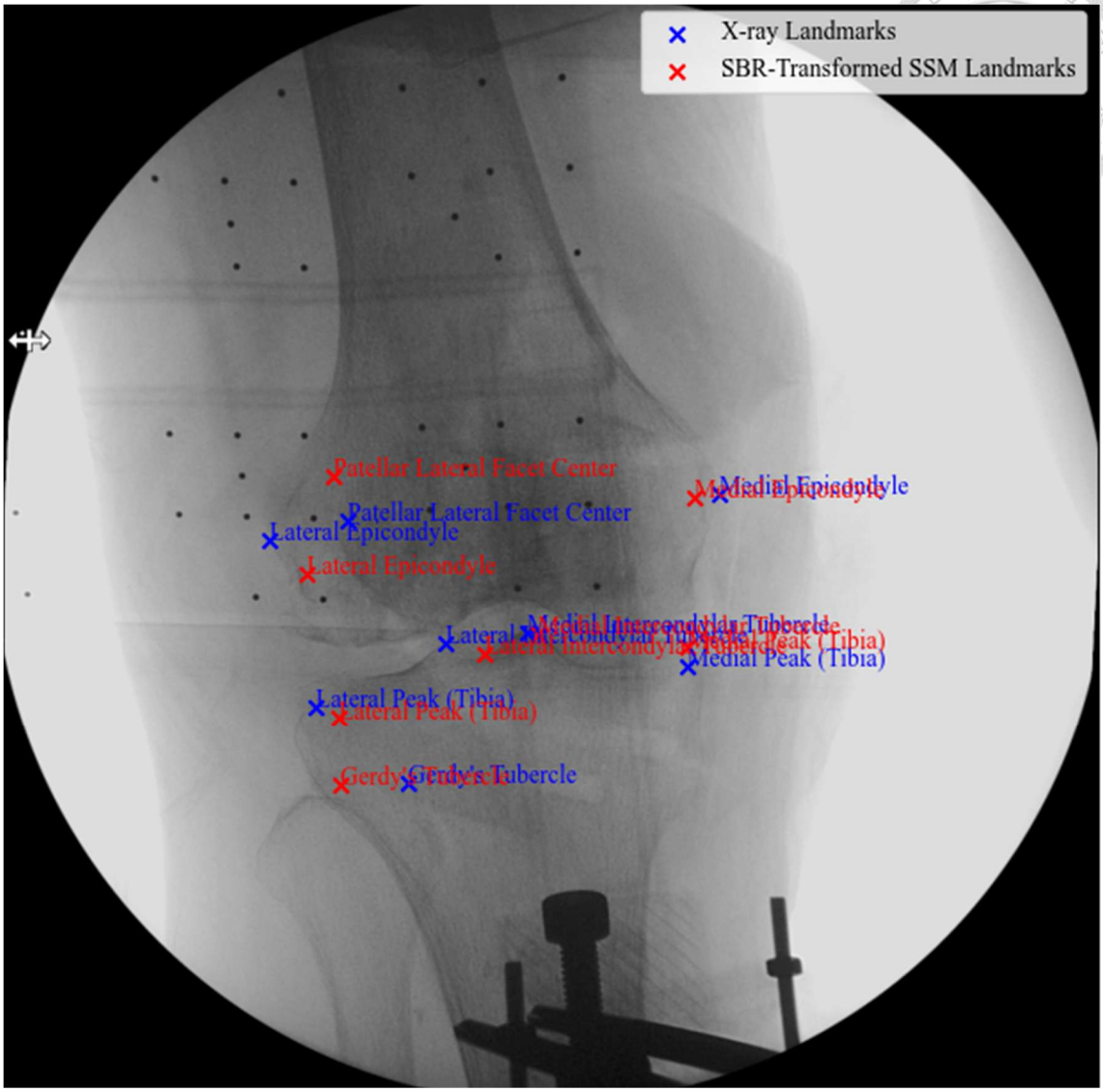

Figure 3-4. 3D SSM landmarks subset rigidly registered to 2D coronal X-ray landmarks.

The SBR method serves as a novel process in performing 2D-3D shape reconstruction by replacing conventional use and training of neural networks. The creation of a neural network is complex. The desired application of the neural network in 2D-3D shape reconstruction for clinical use requires a more sophisticated architecture, further making its creation more challenging. Such design and creation of a neural network are beyond

doi:10.6342/NTU202503673

the scope of this study. Furthermore, large datasets are required to train a neural network. Therefore, the SBR method simplifies the 2D-3D shape reconstruction process by eliminating the necessity of fully automated algorithms. However, SBR method is not as accurate as a neural network—inter-patient variability of anatomical landmark identification is a significant limitation of SBR.

3.4 Statistical Shape Model Development

Let a set of 3D shapes be represented by a collection of N landmark points. The shape of each object is defined by the ordered set of landmarks:

$$\boldsymbol{X} = \begin{bmatrix} x_1 & y_1 & z_1 \\ x_2 & y_2 & z_2 \\ \vdots & \vdots & \vdots \\ x_N & y_N & z_N \end{bmatrix} \in \mathbb{R}^{N\times 3}.$$

A dataset of M such shapes is denoted as $\{\boldsymbol{X}^{(i)}\}_{i=1}^{M}$, where $\boldsymbol{X}^{(i)}$ is the i-th shape.

To remove translation, each shape is centered by subtracting the centroid:

$$\bar{\boldsymbol{x}}^{(i)} = \frac{1}{N}\sum_{j=1}^{N} \boldsymbol{x}_j^{(i)}, \qquad \boldsymbol{X}_c^{(i)} = \boldsymbol{X}^{(i)} - \bar{\boldsymbol{x}}^{(i)},$$

where $\bar{\boldsymbol{x}}_j^{(i)} = (x_j, y_j, z_j)$ is the j-th landmark of shape i, and $\bar{\boldsymbol{x}}^{(i)} \in \mathbb{R}^{1\times 3}$ is the centroid.

To remove rotation and scale the shapes are iteratively aligned using Procrustes analysis, minimizing the pairwise distance between shapes:

doi:10.6342/NTU202503673

$$d\left(\boldsymbol{X}^{(i)}, \boldsymbol{X}^{(j)}\right) = \left\| s\boldsymbol{R}\boldsymbol{X}^{(i)} - \boldsymbol{X}^{(j)} \right\|^2,$$

where s is a uniform scale factor and $\boldsymbol{R}$ is an optional rotation matrix obtained via SVD. After alignment, the mean shape, $\boldsymbol{X}_{mean}$, is obtained by:

$$\boldsymbol{X}_{mean} = \frac{1}{M}\sum_{i=1}^{M} \boldsymbol{X}^{(i)}.$$

Shape variations are captured by performing PCA on the dataset. Each shape deviation from the mean is represented as:

$$\Delta\boldsymbol{X}^{(i)} = \boldsymbol{X}^{(i)} - \boldsymbol{X}_{mean}.$$

The covariance matrix of these shape deviations is obtained by:

$$\boldsymbol{C} = \frac{1}{M}\sum_{i=1}^{M} \Delta\boldsymbol{X}^{(i)}\left(\Delta\boldsymbol{X}^{(i)}\right)^T.$$

Eigenvalue decomposition is then performed:

$$\boldsymbol{C}\boldsymbol{P} = \boldsymbol{P}\boldsymbol{\Lambda},$$

where $\boldsymbol{P} \in \mathbb{R}^{3N\times K}$ contains the principal component eigenvectors, K, and Λ is the diagonal matrix of eigenvalues. A new shape $\boldsymbol{X}$ can be approximated using a subset of principal components:

$$\widehat{\boldsymbol{X}} \approx \boldsymbol{X}_{mean} + \boldsymbol{P}\boldsymbol{b},$$

where $\boldsymbol{b} \in \mathbb{R}^{K\times 1}$ is the vector of deformation coefficients. The number of principal

doi:10.6342/NTU202503673

components retained is selected based on the cumulative variance explained by the model. This statistical shape model serves as the basis for deformation analysis, where a new shape is fitted to the model by estimating its deformation coefficients.

A total of 21 anatomical landmark points were used to create the SSM. Due to the small number of landmark points used, point correspondence was easily achieved through manual methods. However, the small number of points also prevents faithful reconstruction to a mesh surface. Therefore, the SSM is represented by the segmented model closest to the mean.

3.5 SBR-Driven SSM Deformation

2D-3D shape reconstruction was performed by deforming the SSM to obtain a patient-specific 3D model. The process uses the SBR method and is a modification on the PCA visualization in a SlicerMorph extension in 3D Slicer, GPA.

To reconstruct a new deformed shape, the mean shape, denoted as $\boldsymbol{X}_{mean} \in \mathbb{R}^{N\times 3}$, is represented as a set of vertices in 3D space. $\boldsymbol{X}_{mean}$ is flattened first into a one-dimensional vector, s_{mean}, by concatenating the coordinates of all points sequentially to facilitate mathematical operations. The flattening process is consistent as it stacks all vertices into a single vector in s_{mean}:

$$s_{mean} = flatten(\boldsymbol{X}_{mean}) \in \mathbb{R}^{N\times 3},$$

doi:10.6342/NTU202503673

where the coordinates of all N landmarks are stacked sequentially as $(x_1, y_1, z_1, \ldots, x_N, y_N, z_N)^T$.

A linear combination of shape modes from Principal Component Analysis (PCA) is used to generate a new deformed shape that is patient-specific. The weighted combination of $\boldsymbol{P}$ and $\boldsymbol{b}$ added to the mean shape vector, s_{mean}, creates the deformed mean shape vector, $s_{deformed}$, and is defined by:

$$s_{deformed} = s_{mean} + \boldsymbol{P}\boldsymbol{b},$$

where $\boldsymbol{P} \in \mathbb{R}^{3N \times K}$ is a matrix where each column corresponds to a principal component, K, and $\boldsymbol{b} \in \mathbb{R}^{K \times 1}$ is a vector corresponding to shape coefficients estimated by solving the least squares problem, $\boldsymbol{b} = \arg\min_b \|\boldsymbol{P}\boldsymbol{b} - (\boldsymbol{s}_{new} - \boldsymbol{s}_{mean})\|_2^2$, which yields, $\boldsymbol{b} = (\boldsymbol{P}^T\boldsymbol{P})^{-1}\boldsymbol{P}^T(\boldsymbol{s}_{new} - \boldsymbol{s}_{mean})$. The process of finding the deformed mean shape vector ensures that the mean shape is best fit according to the patient-specific data by deforming it along the principal components obtained in the SSM.

The deformed mean shape vector, $\boldsymbol{s}_{deformed}$, is then reshaped into its 3D form

$$\boldsymbol{X}_{deformed} = reshape(s_{deformed}) \in \mathbb{R}^{N \times 3},$$

where $\boldsymbol{X}_{deformed}$ is an $N \times 3$ matrix and N represents the number of landmarks. Displacement vectors, $\boldsymbol{D}$, are calculated as the difference between the deformed shape and the mean shape:

doi:10.6342/NTU202503673

$$\boldsymbol{D} = \boldsymbol{X}_{deformed} - \boldsymbol{X}_{mean}.$$

These displacement vectors represent how each landmark in the mean shape moves to reach its deformed position.

To estimate a smooth deformation field across the entire shape—beyond the discrete landmarks—a thin plate spline (TPS) interpolator was constructed. In 3D Slicer, TPS interpolation is used to visualize the deformations of principal components. However, the software is limited to showing two principal component deformations at a time. Complicated deformations, particularly for representation of patient-specific geometries, requiring multiple principal components are thus unachievable using 3D Slicer on its own.

The TPS function:

$$f: \mathbb{R}^3 \to \mathbb{R},$$

is designed to fit the known displacement vectors, $\boldsymbol{D}$, at the landmarks, $\boldsymbol{X}_{mean}$, while ensuring a smooth deformation surface. The TPS kernel used is:

$$\phi(r) = r^2 \log r,$$

where *r* is the Euclidean distance between source points.

Once the TPS function f is constructed, and using the TPS kernel, the interpolator computes a smooth mapping from the mean shape to the deformed shape. Evaluating the interpolator at the mean shape again yields the predicted displacements:

doi:10.6342/NTU202503673

$$\widehat{\boldsymbol{D}} = f(\boldsymbol{X}_{mean}).$$

Finally, the predicted displacements, $\widehat{\boldsymbol{D}}$, are added to the mean shape. Therefore, the output is a reconstructed, patient-specific 3D shape model:

$$\widehat{\boldsymbol{X}} = \boldsymbol{X}_{mean} + \widehat{\boldsymbol{D}}.$$

The deformed mean shape, $\widehat{\boldsymbol{X}}$, is the best estimate of the knee joint of the patient.

3.6 Finite Element Model

The finite element (FE) simulations in this study were conducted using ANSYS 2020 Academic Multiphysics Campus MBD4A Solution Research, a version of Ansys software intended for academic use. This software was used strictly for educational purposes. No commercial use was involved in accordance with the terms of use of Ansys.

3.6.1 Model Geometry

The SBR-based SSM deformation pipeline has been developed for generating patient-specific 3D reconstructions of knee joint geometry. The generated patient-specific model was then used for the FE model. All the bones in the knee joint (femur, tibia, patella, fibula) were treated as rigid bodies. Simulating dynamic, deformable bodies is computationally expensive in finite element analysis. The bones were assumed to be rigid to simplify the assumptions of the FE model, thereby reducing computational costs of each simulation. Furthermore, CT or MRI scans typically provide surface meshes of the

doi:10.6342/NTU202503673

bones after segmentation rather than their volumetric data. Volumetric information is also not directly accessible from X-rays, which is a significant aspect with regards to the inputs of the digital twin system. Incorporating deformable bodies entails simulation of stresses and strains which would not only complicate the analysis, but also exceeds the scope of this study. Additionally, this study is more focused on patellar tracking during normal knee flexion. The primary concern is the relative motion of the patella governed by the contours of the articular geometries and the passive and active structures that stabilize the patellar tracking. Under normal knee joint flexion-extension it is not expected to handle significant physiological loads that contribute to geometry deformation. Therefore, through the assumption that the bones are relatively rigid, analysis is significantly optimized without negatively affecting accuracy.

3.6.2 Joint Contact and Soft Tissue Approximation

The fibula was bound to the tibia via fixed joint connection. A general type joint connections were applied to the tibiofemoral (tibia and femur) and the patellofemoral (patella and femur) joints to allow 6DOF motion. Frictionless contact was established between the articular surfaces of the patella and the femur. The mesh-based rigid body dynamics (RBD) contact detection was selected to prevent penetration between the tibiofemoral and patellofemoral contact areas during flexion. The mesh-based contact

doi:10.6342/NTU202503673

detection is also able to handle finer geometry details between contact areas.

Furthermore, to simulate the presence of soft tissue such as articular cartilages and menisci, a pinball radius was implemented to the patellofemoral and tibiofemoral joints. The pinball radius increases the contact detection of two articular surfaces by defining a virtual zone of influence around the contact surfaces of each body. Extending the zone of influence causes early detection of contact between the two contact surfaces while preventing interpenetration between the geometries. In this study, the pinball radius acts as the substitute for the tibiofemoral and patellofemoral articular cartilages and the menisci.

The pinball radius of the patellofemoral joint is 6 mm, while the pinball radius of the tibiofemoral joint is 5 mm. These distances were arbitrarily set and approximated according to the initial distances between the bones at their initial position at full extension. Therefore, the spatial occupancy of the soft tissues will be simulated by enforcing a set distance between the bones without adding the geometries of the soft tissues. It has also been observed that implementing a pinball radius between the contact regions significantly decreased the solution time.

3.6.3 Ligament Modeling

The tibiofemoral ligaments were omitted in this study to focus on patellar tracking

doi:10.6342/NTU202503673

kinematics and to achieve a more efficient solving time. Thus, the ligaments included are only the relevant ligaments of the patellofemoral joint. The biomechanics of the ligaments, in that they follow a nonlinear, tension-only spring-like behavior, as well as the complete ligament assembly setup was adapted from the MBS knee joint setup by Marra et al [2]. In this study, the ligament bundles were simulated as nonlinear, tension-only springs. This nonlinear behavior is governed by:

$$F = \begin{cases} k(\varepsilon - \varepsilon_0), & if \ \ \varepsilon > \varepsilon_0 \\ 0, & otherwise \end{cases}$$

where ε is the current strain, ε_0 is the reference strain, and k is the stiffness derived from literature [2]. The following bundles are used along with the corresponding number of spring elements for each: the medial patellofemoral ligament (MPFL) bundle consists of three spring elements designated as superior, middle, and inferior; the lateral epicondylopatellar ligament (LEPL) bundle is represented by two spring elements designated as superior and inferior; the lateral transverse ligament (LTL) bundle is represented by three spring elements designated as superior, middle, and inferior; and the patellar ligament (PL) is represented by a single spring element. The stiffness and reference strain parameters were derived from literature data [2]. The medial and lateral patellar retinacula are also represented as spring elements to simplify the biomechanics of the structures. Each patellar retinaculum is represented by four spring elements.

doi:10.6342/NTU202503673

Surgical incision will be simulated by removing one side of the patellar retinaculum from the model. The total stiffness of each patellar retinaculum is 2 N/mm, which is adapted from a similar study but with different patellar retinacular insertion and origin sites [79]. Small damping was introduced to all the spring elements to maintain stability during knee flexion. The patellar ligament stiffness must be significantly high (2000 N/mm) [2]. However, this causes instability with the solver and is computationally expensive. Thus, the longitudinal stiffness was reduced to 200 N/mm in order to prevent deformation of the patellar ligament while ensuring the convergence of the solver. There was no muscle wrapping or ligament wrapping feature implemented. The springs tend to pass through the bone models instead of wrapping around them. The parameter values are summarized in Table 3-2.

Table 3-2. Baseline parameter values of the ligaments. Adapted from [2].

Ligaments	**Spring Length (mm)**	**Stiffness (N/mm)**	**Reference Strain**
sMPFL	68.728	28.683	0.12
mMPFL	66.296	30.168	0.08
iMPFL	62.947	31.773	0.08
sLEPL	62.477	16.006	0.06
iLEPL	58.884	16.983	0.06
sLTL	55.718	17.948	0.06
mLTL	54.627	18.306	0.06
iLTL	51.353	19.473	0.06
PL	48.602	200	—
Medial Retinaculum	—	2	—

doi:10.6342/NTU202503673

3.6.4 Muscles Representation

Muscle forces are assumed to exert a constant force throughout the knee joint motion. The quadriceps and hamstrings muscles were represented as a bundle of vector forces based on their physiological lines of action. The approach simplifies muscle force representation and ignores factors such as dynamic line of action changes and muscle wrapping. This strategy isolates primary effects on patella kinematics by making the muscle forces as control variables.

The location and orientation of the quadriceps forces were based from the study by Farahmand et al [80]. A load of 175 N force was divided among the quadriceps muscles. The distribution of force was determined according to their normalized physiological cross-sectional area (PCSA) of each muscle. The quadriceps muscles used and their force distribution are the following: the rectus femoris (RF) contributes 12.5% of the total force; the vastus intermedius (VI) contributes 16.67%; the vastus lateralis (VL) contributes 33.33%; the vastus lateralis obliquus (VLO) contributes 8.33%; the vastus medialis (VM) contributes 20.83%; and the vastus medialis obliquus (VMO) contributes 8.33%. The finite element model with the ligament assembly are shown in Figure 3-5.

doi:10.6342/NTU202503673

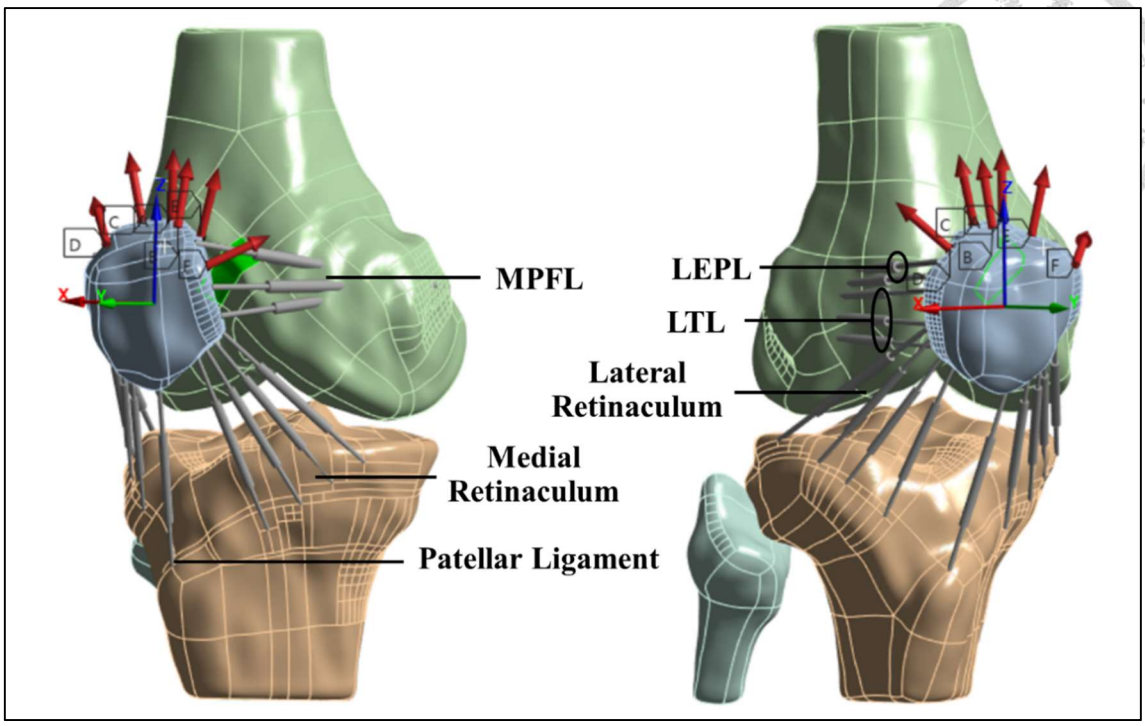

Figure 3-5. Finite element model setup showing the ligaments as spring elements.

Images used courtesy of ANSYS, Inc.

The knee joint was made to move using simplified hamstrings simulated by remote forces. The simplified hamstrings assembly consists of the biceps femoris (BF) and the semimembranous (SM) muscles. The orientation of the two hamstring muscles was adapted from the study by Aalbersberg et al [81]. Accurate representation of the hamstrings such as simulating a dynamically changing muscle vector orientation and muscle-specific force loading are deemed impractical. Further inhibiting factors include the simplified assumptions of the FE model and the hamstrings not being the primary focus of the FE analysis of the digital twin. The force load of both the BF and SM muscles is 222 N each. This force magnitude was chosen to be sufficient to overcome the pulling

doi:10.6342/NTU202503673

force exerted by the quadriceps and the entire patellofemoral ligament assembly. The force components of the BF muscle are: $F_x = -75.93N$, $F_y = -111.00N$, $F_z = 180.66N$; while the force components of the SM muscle are: $F_x = 38.55N$, $F_y = -127.33N$, $F_z = 179.09N$. Figure 3-6 shows the orientations of the BF muscle (lateral side) and the SM muscle (medial side) used in this study.

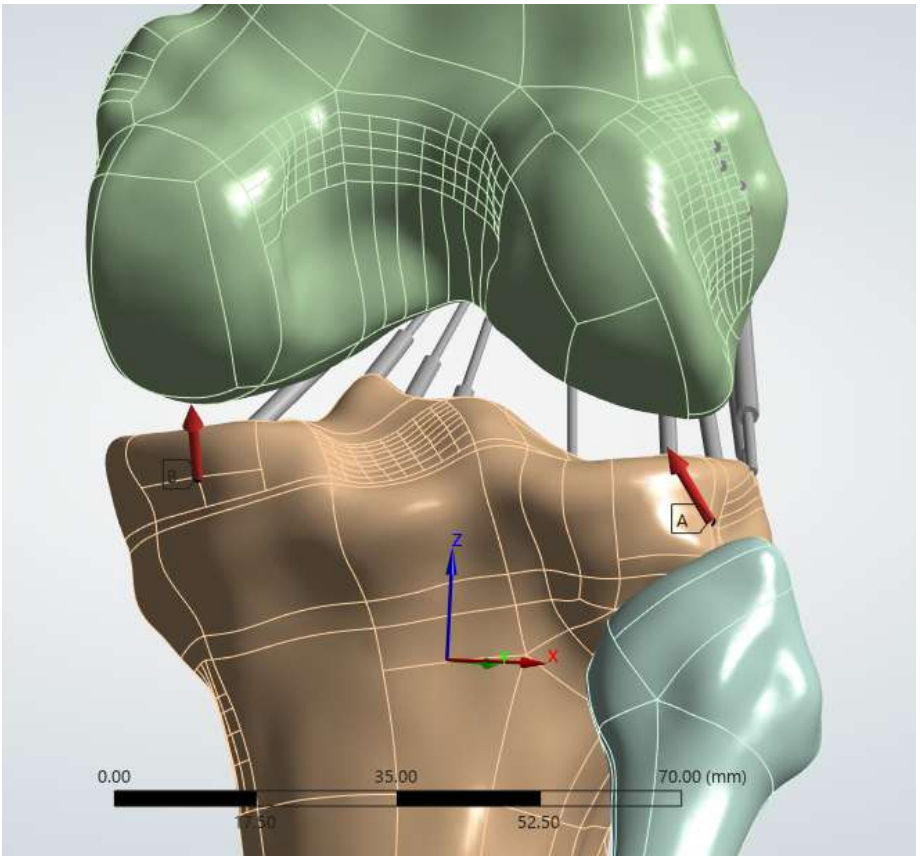

Figure 3-6. Simplified hamstrings as vector-oriented remote forces (red arrows). Medial side: BF; lateral side: SM. Images used courtesy of ANSYS, Inc.

3.6.5 Solver Configuration

The analysis settings included a minimum time step of 10^{-7} s and a maximum time

doi:10.6342/NTU202503673

step of 0.5 s. For the MRI-segmented model used as the FE model, the knee flexion degree of 109.8° is achievable by a step end time of 430 ms. A maximum knee flexion angle of approximately 110° was deemed satisfactory for this study. To ensure stability, the time integration method used was MJ Time Stepping. Additionally, both the correction and assembly types were configured to use the "With Inertia Matrix." It is found that using this configuration for the correction and assembly types resulted in a more stable solution and helps ensure convergence.

3.6.6 Normal Patellar Tracking Definition

Inter-patient normal patellar tracking is highly variable [10]. In this study, the patient-specific knee is healthy, showing no signs of patellar malalignment or dislocation. The parameter values for the ligament assembly and muscle force loads used for the model were typical values of normal knees. Therefore, the baseline knee kinematics simulated using the MRI-segmented geometry and default parameter values are defined as normal patellar tracking, specific only to this patient. Definition of normal patellar tracking acts as the control configuration. The balanced state of all forces acting on the patella and knee joint is reflected by the baseline knee kinematics. In future applications, the deployment of the digital twin shall redefine normal, patient-specific patellar tracking by correcting the abnormal patellar shift and tilt observed in the Merchant view X-ray.

doi:10.6342/NTU202503673

Deviations from the baseline patellar tracking are simulated by modifying the parameter values: ligament stiffness, muscle force loads, and removing passive structures (i.e., the ligaments and retinacula). The patellar tracking is considered pathological once the parameter variation leads to the resulting patellar shift or tilt reaching pathological thresholds. Patellar shift is considered pathological once it exceeds 3 mm. Patellar tilt is considered pathological once it exceeds 20° [7].

3.6.7 Simulation of Deviations from Normal Patellar Tracking and Surgical Release

For this study, lateral retinacular tightening was modeled by increasing the stiffness of the lateral ligaments to four times their normal values. For the medial side, the stiffness values of the medial ligaments were reduced to 0.55 times their normal values. These parameter value changes are arbitrarily chosen. Lateral retinacular release was simulated by progressively removing a percentage of the spring elements in the lateral retinaculum bundle. Kinematic response before and after surgical incision of the LPFL, MPFL, and medial patellar retinaculum was also investigated by performing different combinations of release on these structures. The release direction is varied from superior-to-inferior direction to inferior-to-superior direction. A full release on both medial and lateral side was intentionally avoided to prevent an excessive imbalance between the medial and

doi:10.6342/NTU202503673

lateral patellar forces. A full medial and lateral release would also result in a total loss of passive structures contributing to patellar tracking stability.

3.7 Predictive Models

3.7.1 Data Preparation

A Python-based framework was developed to generate a comprehensive set of stiffness parameter profiles and surgical release profiles. The baseline model includes spring stiffness and damping values for medial and lateral passive structures that stabilize the patella. These soft tissue structures include the medial and lateral retinacula, the medial patellofemoral ligament (MPFL), and the lateral patellofemoral ligament (MPFL)—which is further separated into the lateral epicondylopatellar ligament (LEPL) and the lateral transverse ligament (LTL). The default parameter values of these simulated ligaments—of which the values are obtained from literature data—are established as the baseline values that result in normal patellar tracking. To model variability in mechanical properties, parameter scaling procedure was conducted where the medial ligament parameters were scaled between 0.05 to 1.0 times their normal values. Conversely, the lateral ligament parameters were scaled between 1.0 and 5.0 times their normal values. The scaling increments used were 0.1 and 0.25, the former was used to generate more complex datasets while the latter was used as initial proof-of-concept testing by generating sparser datasets. A Cartesian product was used to generate unique

doi:10.6342/NTU202503673

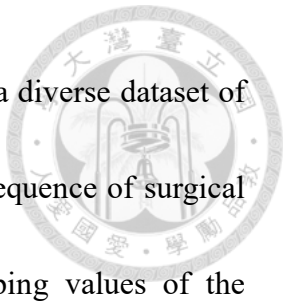

combinations of the medial and lateral scaling factors. The result is a diverse dataset of stiffness profiles, stored in CSV files. For each stiffness profile, a sequence of surgical release was simulated by reducing the spring stiffness and damping values of the ligaments of interest to zero. The ligament stiffness deactivation mimics surgical release. The sequence of surgical release is consistent across all stiffness profiles to reduce dataset heterogeneity. The release (ligament spring stiffness and damping deactivation) order is as follows: Lateral Patellar Retinaculum 4, Lateral Patellar Retinaculum 3, Lateral Patellar Retinaculum 2, Lateral Patellar Retinaculum 1, iLTL, mLTL, sLTL, iLEPL, Medial Patellar Retinaculum 4, Medial Patellar Retinaculum 3, Medial Patellar Retinaculum 2, Medial Patellar Retinaculum 1, and iMPFL. For each step in the surgical release sequence, a new profile was generated and stored in a CSV file. The stiffness profiles and surgical release profiles were then used in the FE simulations to generate datasets for model training on patellar shift and tilt data at a given knee angle. The generated datasets were split into 20% testing and 80% training using a fixed seed for reproducibility.

3.7.2 Malalignment Predictor Model

As part of the parameter adaptation feature of the digital twin system, two predictive models were developed. The first model is the “Malalignment Predictor Model.” The model uses an XGBoost algorithm and is suited for large datasets [82]. The current

doi:10.6342/NTU202503673

malalignment predictor model is trained on a dataset of 1192 different ligament parameter stiffness profiles—datasets containing different scaling of medial and lateral ligament stiffness. The training datasets were further split into training and validation sets in this model to enable early stopping. Early stopping rounds value was set to 10, while the boosting iteration number was 500. The hyperparameters used for the XGBoost model are summarized in Table 3-3. The values used in Table 3-3 are arbitrarily chosen.

Table 3-3. XGBoost hyperparameter values.

Parameter	**Value**
Learning rate	0.05
Max tree depth	6
Subsample ratio	0.9
Column sampling ratio per tree	0.9
L1 regularization coefficient	0.1
L2 regularization coefficient	1.0
Random seed	42

The malalignment predictor model is able to predict patellar shift and tilt at a given knee angle based on the stiffness profile. It is important to note that this model is not trained on full release on both medial and lateral sides, as it is deemed impractical to perform full release on an actual patient.

For the practical use of the malalignment predictor model within the digital twin system, the model first takes an initial guess of the stiffness profile of a patient. If the predicted patellar shift and tilt do not match the X-ray of the patient, the stiffness profile

doi:10.6342/NTU202503673

is iteratively refined and the process is repeated as necessary. Once the similarities between the predictions and the patient X-ray are satisfactory, the stiffness profile is determined to be patient-specific. The obtained patient-specific stiffness profile will be used as inputs for the surgical release predictor model by modifying it with an initial guess of surgical release.

3.7.3 Surgical Release Predictor Model

The second model is the "Surgical Release Predictor Model." The model also uses an XGBoost algorithm. The current surgical release predictor model is trained on 3284 surgical release scenarios by inputs of surgical release profiles. The hyperparameters used in this model is the same as the values found in Table 3-3. The surgical release predictor model is able to predict patellar shift and tilt after surgical release correction at a given knee angle.

For the practical use of the surgical release predictor model within the digital twin system, the input uses the initial guess of the surgical release profile, obtained as the modified output of the malalignment predictor model by deactivating ligaments to simulate release. The result predicts postoperative patellar shift and tilt at a given knee angle. If the predicted outcomes do not meet desired correction criteria, the surgical release profile is iteratively refined. Once the desired post-operative state has been achieved, the recommended surgical release profile is obtained.

doi:10.6342/NTU202503673

3.7.4 Model Limitations and Assumptions

The main objective of this study is to analyze the effects of lateral release on patellar tracking. Accordingly, the predictive models assume that the primary contributor to pathological patellar shift and tilt are caused by ligament tightness. Other contributors to patellar shift and tilt (e.g., bone morphology, muscle loading conditions, contact mechanics, ligament insertion site, etc.) were held constant.

The models used in this study are trained on arbitrarily set ligament stiffness values of a set range of scale that aims to represent tightness and laxity. It is difficult to measure the in-vivo ligament material properties to acquire a large dataset for model training. To the best of the knowledge of the researchers, there is also no publicly available dataset for ligament material properties especially for ligament tightness. Therefore, the scale of the ligament tightness (higher stiffness) or laxity (lower stiffness) used in this study were designed to reflect realistic tightness or laxity based on relative and not absolute tissue properties.

The limited size and diversity of the model dataset may not be generalizable to other knee geometries, age groups, or pathology severities. Given the limited dataset diversity, extrapolation outside the training data may result in unreliable predictions. The current state of the models also cannot predict pathological patellar shift and tilt. The knee

doi:10.6342/NTU202503673

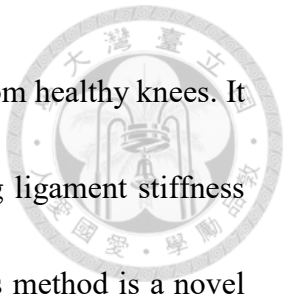

geometry and muscle loading conditions, among other factors, are from healthy knees. It is difficult to simulate pathological conditions by simply modifying ligament stiffness properties while using healthy knee parameter values. However, this method is a novel proof of concept and a promising initial step to understanding the complex biomechanics of surgical release using machine learning.

3.7.5 Predictive Model Implementation

This section demonstrates the application of the trained predictive models to a real clinical case. Ligament tightness was simulated by increasing the stiffness of the lateral ligaments by four times the baseline values. Ligament laxity was then simulated by reducing the stiffness of the medial ligaments by 0.55 times the baseline values. The scaling values are completely arbitrary. Laxity was simulated to enhance lateralization of the patellar shift and tilt brought upon by the increased lateral forces.

The malalignment predictor model was used first to predict the stiffness parameters of the ligaments that have contributed to the abnormal patellar shift and tilt. Next, the surgical release predictor model will then simulate the patellar tracking response to various ligament releases. The goal is to identify a minimal surgical release configuration that corrects patellar tracking to baseline values. Iterative refinement using a greedy search algorithm was used to achieve the stiffness and surgical release profiles.

doi:10.6342/NTU202503673

3.8 Cadaver Study

3.8.1 Cadaver Experiment Setup

The operating room (O.R.) setup is shown in Figure 3-6. An orthopedic surgeon supervised the cadaver experiment. The cadaver patient was positioned supine on the operating table. A computer screen was placed across the table from the surgeon. The infrared (IR) camera was placed adjacent to the computer screen to avoid obstruction of marker movements during the procedure.

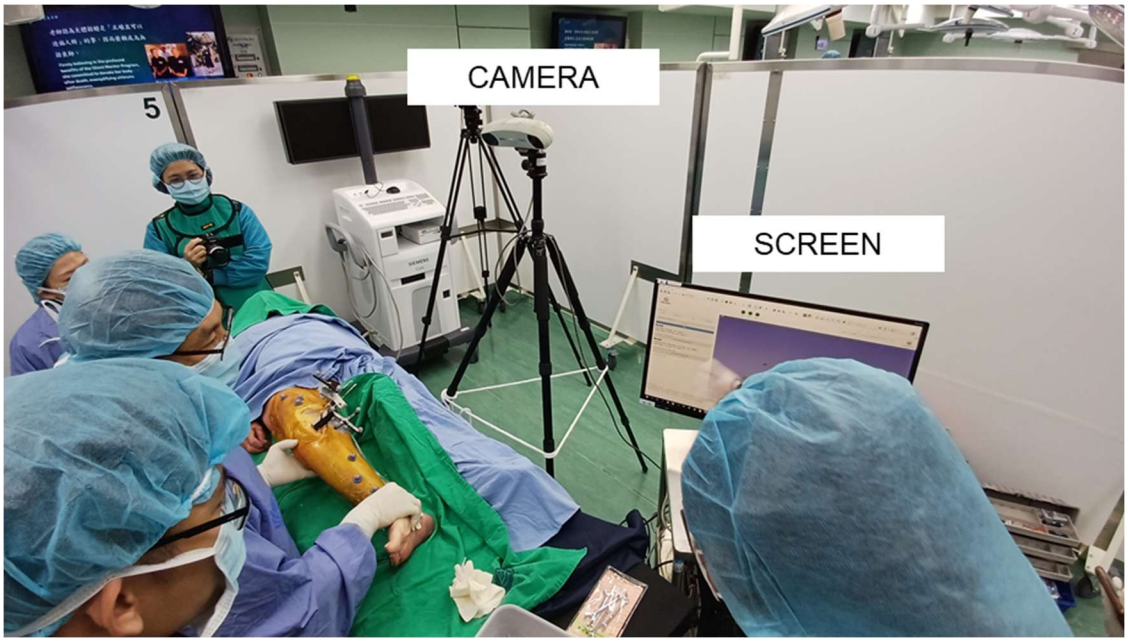

Figure 3-6. O.R. setup for cadaveric study of patellar kinematics.

The detailed experimental setup for the cadaver experiment is shown in Figure 3-7. The experiment used an NDI Polaris infrared motion tracker to capture bone movements. Bone markers were rigidly fixed onto the femur, tibia, and patella for accurate tracking.

doi:10.6342/NTU202503673

The bone markers also provide body-fixed reference frames for the point clouds and the probe tracker. The placement of each bone marker is labeled in Figure 3-29. The probe tracker was used to acquire point cloud data from bone anatomical landmark points and contours.

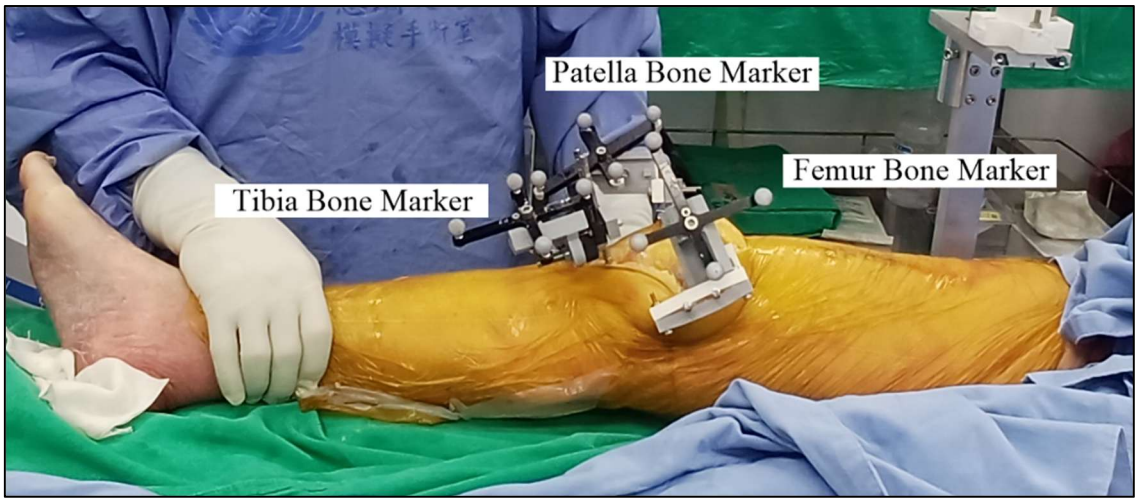

Figure 3-7. Experimental setup for cadaveric study of patellar kinematics.

3.8.2 Surgical Release

3.8.2.1 Objectives

Full lateral and full medial release were performed prior to gathering point cloud data. Notably, the knee joint of the patient is osteoarthritic, as per the observation of the supervising orthopedic surgeon during point cloud acquisition. However, no abnormalities with the patella lateral displacement was observed. No prior tests (e.g., Merchant view X-ray) was conducted to verify normal patellar tilt. No specific observations on patellar tilt abnormalities were documented. Therefore, the patient is

doi:10.6342/NTU202503673

assumed to have normal patellar tracking. Despite the observed normal patellar tracking, surgical release was performed. The primary goal was to record and analyze the effect of soft tissue releases, specifically lateral release and combined medial and lateral release, on patellar kinematics The experimental data will also serve as a validation benchmark for the FE models developed in this study.

3.8.2.2 Order of Procedures

Full lateral release was performed first, in accordance with the surgical plan and decision made by the supervising orthopedic surgeon. Figure 3-8 shows the initiation of the lateral release procedure. Incision was made on the entire soft-tissue structures supporting the lateral side. The completion of the lateral release was confirmed by visual inspection of the lack of restraining soft-tissue structures. Then, full medial release was performed using a similar procedure to simulate combined release scenario.

doi:10.6342/NTU202503673

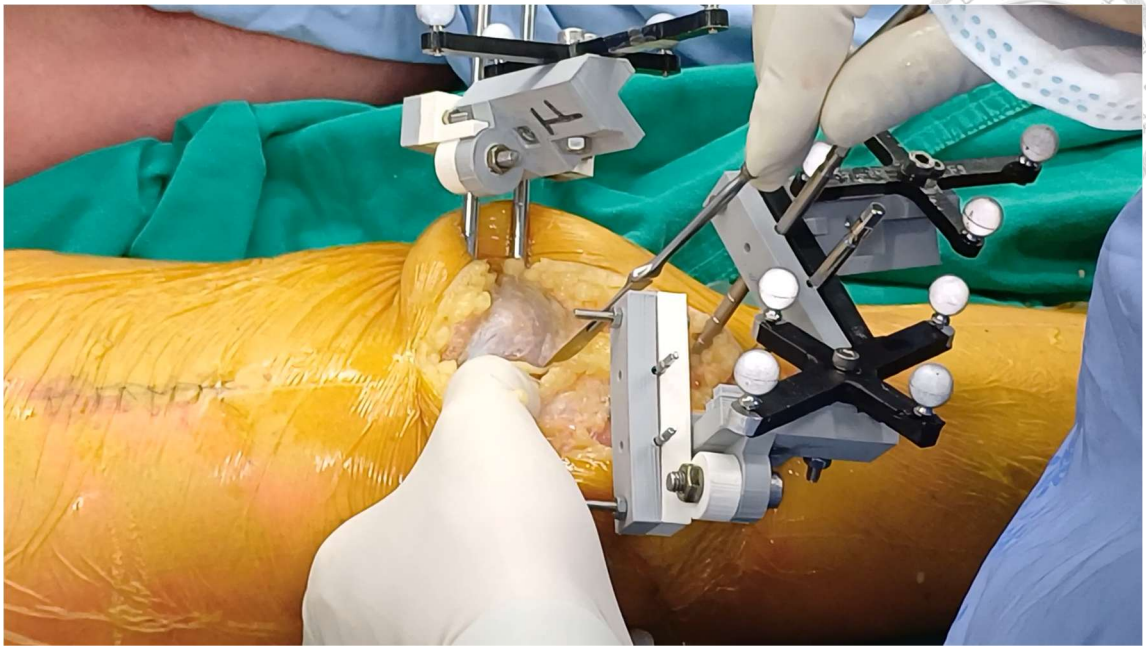

Figure 3-8. Initiation of the lateral release procedure.

3.8.2.3 Measurement Limitations

Unfortunately, incision length was not able to be measured to determine its effects on patellar shift and tilt correction. Similarly, gradual release of the lateral and medial sides of the knee joint was not performed to determine the effects of incision length variation and its kinematic response. These limitations were due to time constraints during the experiment. As a result, experimental validation of the finite element simulations could not be assessed. However, the surgical simulations with the finite element model could not be fully performed through a single cadaver specimen. Additionally, comparisons between experimental (cadaver) data and simulated (finite element model) results would require multiple cadaver specimens before definitive conclusions can be made.

doi:10.6342/NTU202503673

3.8.2.4 Kinematic Data Collection

For each surgical condition—before release, after lateral release, and after combined medial and lateral release—three passive motion trials were conducted. The same supervising surgeon manipulated the knee joint for passive flexion-extension and circumduction motions. Kinematic data was recorded during these motions by digitizing the 3D positions of the bone markers. Three trials of kinematic data recording were performed for each surgical release condition: before release, full lateral release, and combined medial and lateral release.

3.8.2.5 Preparation for Digitization of Exposed Bony Surfaces

After performing both lateral and medial release and the knee joint kinematics were recorded, the knee joint was further incised and soft tissues were retracted to fully expose the distal femur, proximal tibia, and patella. This procedure prepared the knee joint for point cloud data acquisition. Care was taken to minimize soft tissue distortion and cause unnecessary damage to the knee joint.

3.8.3 Point Cloud Data Acquisition

Point cloud data acquisition was performed on the femur, tibia, and the patella. An optically tracked probe was used to digitize the anatomical landmarks and surface contours of the bones. The purpose of the data acquisition was to provide sufficient

doi:10.6342/NTU202503673

information on the morphology of each bone. Using this 3D information, it is possible to determine the relative spatial position of each bone with respect to its corresponding bone marker reference frame. These positions and the point cloud data were then used to define the anatomical coordinate systems of each bone, which can then be used for biomechanical visualization and analysis.

3.8.3.1 Equipment and Tracking Setup

A handheld, digitization probe tracker with passive reflective markers was used with an optical motion capture system (NDI Polaris) to capture the 3D coordinates of the anatomical landmarks and bone contours. The probe tracker was calibrated before the digitization using standard calibration procedures to determine the tip offset. The optical tracking system feedback on the probe tip location was in real-time throughout data acquisition. A custom module was created in 3D Slicer for the real-time feedback and visualization of the point cloud digitization process. A computer monitor was used for the 3D visualization of the module during point cloud digitization. The experimental setup for the point cloud data acquisition was registered to a fiducial marker that acted as the common global coordinate system.

3.8.3.2 Digitization Technique

Specific points and regions were targeted to provide sufficient geometric information

doi:10.6342/NTU202503673

for registration and subsequent analysis. The technique for gathering anatomical landmarks used relatively stationary probe tracker palpations. This method allowed refinement of probe tracker location to ensure the probe tip accurately corresponds to the anatomical landmark point of interest, particularly for landmark points with limited accessibility (e.g., femoral epicondyles). For surface contours, the probe tracker digitized the contours via continuous painting or sweeping motions across bony surfaces of interest. Depending on the bone surface curvature and accessibility, the sweeping direction was varied to best capture the morphological information.

3.8.3.3 Femur Data Acquisition

For the femur, anatomical landmarks included the medial and lateral epicondyles, the center of the femoral notch, and the anterior femoral cortex. Contour acquisition consisted of surface painting along the medial and lateral borders of the medial and lateral femoral condyles, mediolateral painting over the surfaces of the condyles, mediolateral arch painting over the roof of the femoral notch, and proximodistal painting across the intercondylar notch.

3.8.3.4 Tibia Data Acquisition

For the tibia, anatomical landmark points were acquired at the most medial and most lateral aspects of the tibial condyles, which were approximated and palpated due to

doi:10.6342/NTU202503673

limited direct visibility. Surface painting was performed over the medial and lateral tibial condyles, the medial and lateral tibial plateau regions (also palpated), the tibial spine (specifically the medial and lateral intercondylar tubercles), and the anterior margin of the tibia.

3.8.3.5 Patella Data Acquisition

For the patella, anatomical landmarks at the superior (superior pole) and inferior (inferior pole) aspects were digitized. Surface painting was used to capture the medial and lateral articular facets and to trace the outer margin along the borders of the entire patellar ridge.

3.8.3.6 Ensuring Digitization Accuracy and Surface Coverage

All digitization was performed by the supervising orthopedic surgeon to ensure accurate probe placement. Multiple digitization attempts were made when ambiguous measurements were observed. Real-time 3D visualization using a monitor and the custom 3D Slicer module ensured surface contour coverage and consistency.

3.8.4 Coordinate Transformations

From the optical tracking system setup of the point cloud acquisition procedure, the coordinate frames are defined as the following:

doi:10.6342/NTU202503673

1. **FM (fiducial marker)**: the global coordinate system from the perspective of the optical tracker;
2. **BM**: rigid body marker reference frames attached to each bone (BMF for femur marker, BMT for tibia marker, and BMP for patella marker);
3. **pACS**: the anatomical coordinate system of the patella; and,
4. **PR**: the probe tracker reference frame.

For all measurements, the handheld probe tracker (PR) initially recorded all points relative to the global frame (FM), therefore the raw point cloud data are related registered to FM. Due to manual handling of the knee throughout data acquisition and inter-frame motion, positional inaccuracies (coordinate drift) were recorded in the raw data. To account for this motion, a coordinate transformation procedure was applied to the raw point cloud data. Transformations were applied to express the point cloud data in the local coordinate systems defined by their respective bone markers (BM). This procedure allowed each set of points to be accurately realigned with the corresponding bone geometry, independent of inter-frame movement or drift during acquisition. The transformations are described by:

$$ {}^{BM}_{PR}T = ({}^{FM}_{BM}T)^{-1} \cdot {}^{FM}_{PR}T \quad (1) $$

Equation (1) ensures the point clouds are realigned consistently to their bone markers. A visual representation of the point cloud coordinate transformation process is provided in

doi:10.6342/NTU202503673

Figure 3-9.

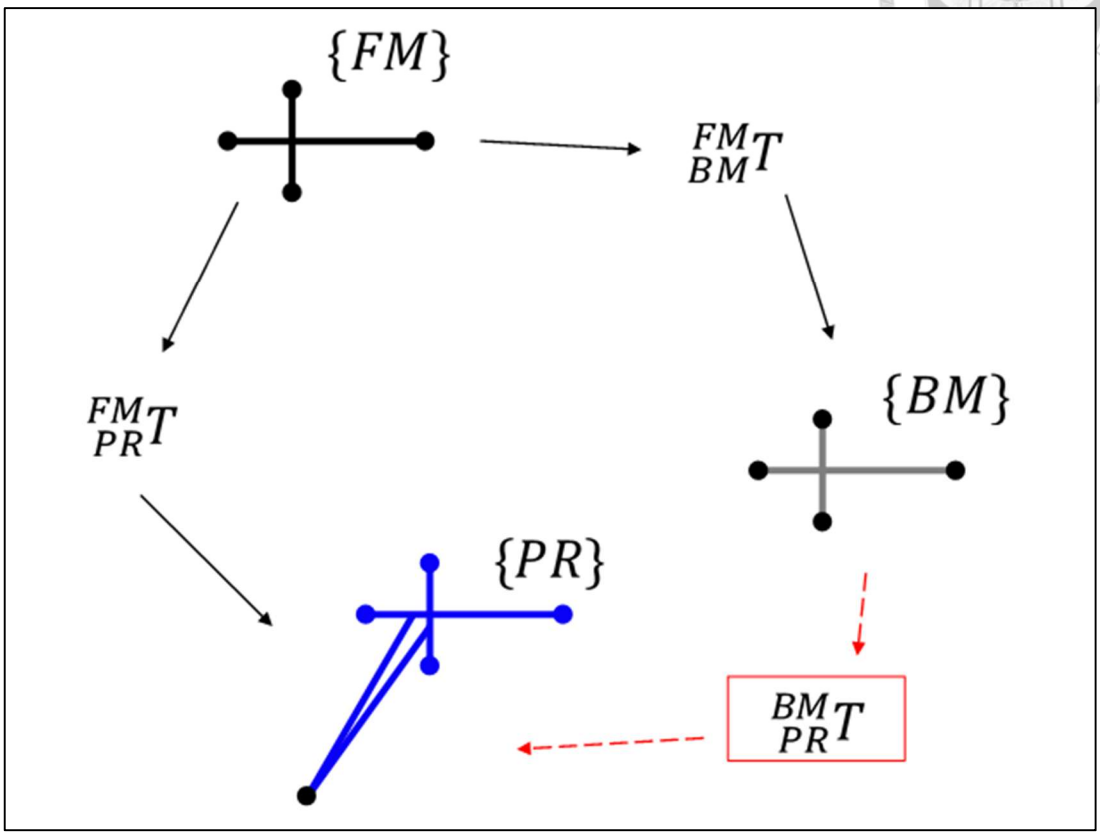

Figure 3-9. Schematic representation of the coordinate transformation process. The probe tracker acquires point cloud data relative to the fiducial marker frame (FM). Coordinate transformations are then applied to express the point cloud data in the local reference frame of the bone marker (BM).

3.8.4.1 Patella Data Acquisition Challenges

During the patella point cloud collection, the patella was positioned in an inverted orientation to gather the morphological features of its posterior side. The patella inversion was necessary because the anterior side of the bone was impossible to access for point cloud data collection. The soft tissue on the anterior side of the patella must be left untouched to prevent unnecessary damage to the knee. Furthermore, exposing the anterior

doi:10.6342/NTU202503673

side of the patella is impractical as it prevents recording normal patella kinematics.

While the patella was in an inverted orientation, the optical tracker system lost sight of the patella bone marker (BMP) since the bone marker was attached to the anterior surface of the patella. This mistake was discovered retrospectively after the experiment had concluded. Figure 3-10 is a visualization of the loss of the BMP during the experiment.

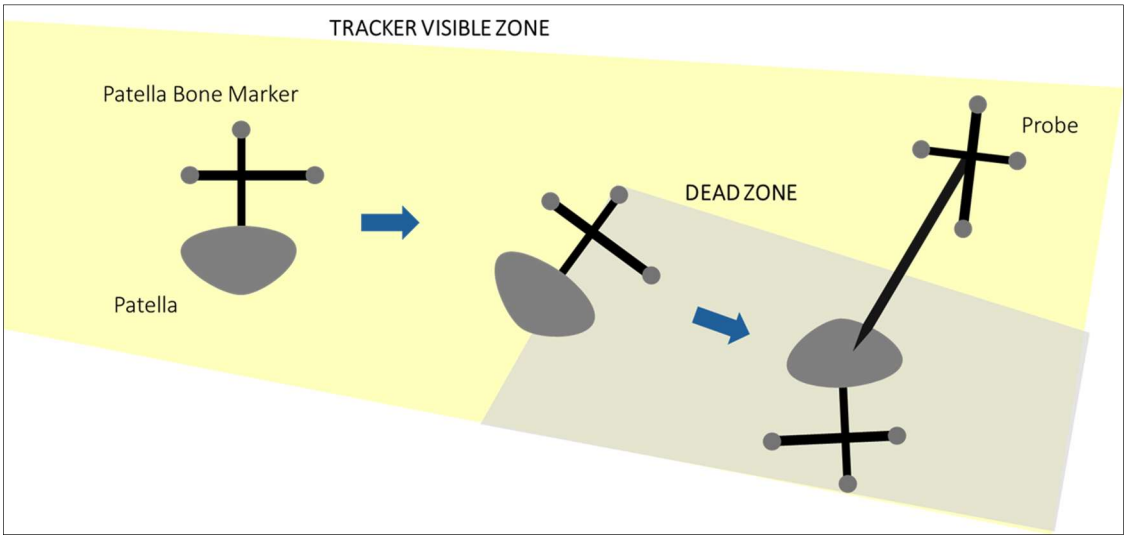

Figure 3-10. Error in point cloud data gathering procedure resulting in loss of BMP.

Obstruction of the BMP from the field of view of the optical tracker is a critical issue, as the patella point cloud cannot be localized in the BMP frame as the anchor of the patella ACS frame (pACS). As a consequence, it is impossible to determine the distance of BMP from pACS. The relative distance between the BMP and pACS determines the position of the patella when it is returned to the knee joint after point cloud data collection. Therefore, to salvage the data and enable patellar tracking analysis, transformation chains were used to define the patellar position and orientation relative to the femur bone marker

doi:10.6342/NTU202503673

frame (BMF). These transformations allow the determination of the patellar pose during knee joint motion despite loss of BMP tracking during point cloud data collection. The transformation chains are defined as follows:

$$ {}^{BMF}_{BMP}T = ({}^{FM}_{BMF}T)^{-1} \cdot {}^{FM}_{BMP}T \tag{2} $$

$$ {}^{BMF}_{pACS}T = {}^{BMF}_{BMP}T \cdot {}^{BMP}_{pACS}T \tag{3} $$

3.8.4.2 Handling Marker Loss and Its Impact on Patellar Kinematics

BMP was lost during point cloud data collection. But the transformation that relates pACS to BMP is assumed to be the last known location of the BMP before it was lost. Thus, in equation (2), the transformation relates BMP to BMF, in which BMF serves as the indirect anchor of BMP. Equation (3) then relates pACS to BMF. This transformation allows locating pACS within BMF, thereby indirectly referencing pACS through BMF, which serves as the indirect anchor for the lost BMP frame. The resulting patellar location after using equations (2) and (3) appears to be anatomically displaced from the knee joint as a consequence of the assumed relationship of pACS to BMP. However, the patellar motion relative to the knee joint now follows normal patellar motion despite dislocation. Thus, insights from the patellar kinematics can be obtained from the datasets.

3.8.5 ACS Determination

Establishing a patellar coordinate system ensures an objective basis for consistent

doi:10.6342/NTU202503673

measurements of mediolateral displacement [9]. The anatomical coordinate system (ACS) of each bone was determined using the acquired point clouds for the anatomical landmarks and surface contours. Different ACS determination strategies were implemented depending on the data acquired. However, the ACS created for each bone follows the convention established by Grood and Suntay, which is the widely used ACS convention [83].

3.8.5.1 Femur ACS

The point cloud data of the femur were clustered closely together and showed no significant outliers. Therefore, no preprocessing was necessary to be performed. The femur ACS was determined as follows. First, the average of the medial (lateral) point cloud was obtained. The existing point closest to the medial (lateral) average is selected as the medial (lateral) epicondyle point. The origin can now be defined as the centerpoint between the medial and lateral epicondylar points. Then, the individual axes can be defined. The x-axis is defined as the line passing through the medial epicondyle point, the origin, and the lateral epicondyle point. The z-axis is defined as the line passing through the origin and the hip center. The hip center is approximated by using the least-squares sphere fitting method. The definition of the hip center is described in more detail in the following subsection. The angle formed by the femoral x- and z-axes is 90.599°. Finally, the y-axis is defined as the cross product of the x- and z-axes. The orientation of the x-

doi:10.6342/NTU202503673

axis is positive from the origin to the lateral epicondyle point. The orientation of the y-axis is positive from the origin pointing towards the anterior side of the femur. The orientation of the z-axis is positive from the origin pointing towards the hip center (Figure 3-11).

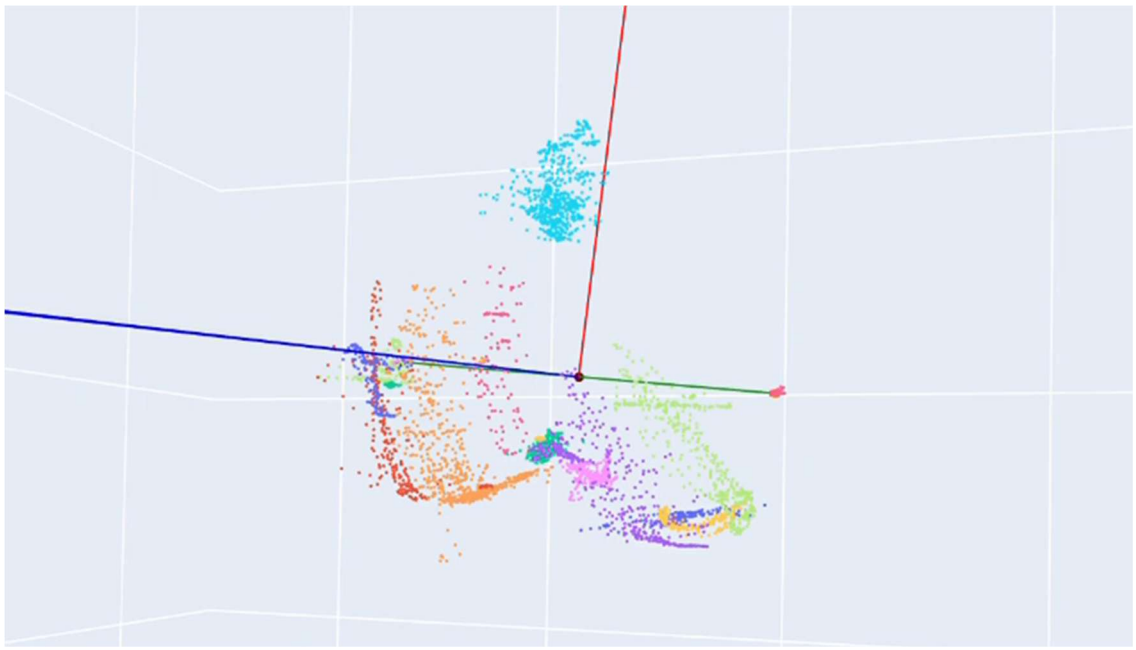

Figure 3-11. Femur ACS. Green: x-axis; Blue: y-axis; Red: z-axis.

3.8.5.2 Tibia ACS

The tibia ACS is defined as follows. Similar to the strategy in the femur ACS x-axis determination, the average point of the medial (lateral) tibial plateau was obtained first. A z-score filter was used to remove the outliers. Then, the existing point closest to the medial (lateral) average point is considered the center of the medial (lateral) tibial plateau. The origin is then defined as the centerpoint between the two central points of the tibial

doi:10.6342/NTU202503673

plateaus. The x-axis is defined as the line passing through the medial tibial plateau center, the origin, and the lateral tibial plateau center. Under conventional methods, the z-axis must be defined after the x-axis. The tibial z-axis is defined by connecting the origin and the centerpoint between the tibia malleoli. However, the malleoli point cloud data was not collected for the tibia ACS. Therefore, the y-axis is defined next due to the absence of malleoli data. The tibial y-axis is defined as the line passing from the origin to the point on the tibial spine point cloud that is most perpendicular to the x-axis. The angle formed by the tibial x- and y-axes is 89.051°. This value is considered as orthogonal for this study. Finally, the z-axis is defined as the cross product of the x- and y-axes. The orientation of the x-axis is positive from the origin to the lateral tibial plateau center. The orientation of the y-axis is positive from the origin pointing towards the anterior side of the tibia. The tibial z-axis is defined as the line extending from a point inferior to the tibial origin upward towards the origin, perpendicular to the plane formed by the x- and y-axes. The positive direction of the z-axis points proximally, toward the tibial origin. (Figure 3-12).

doi:10.6342/NTU202503673

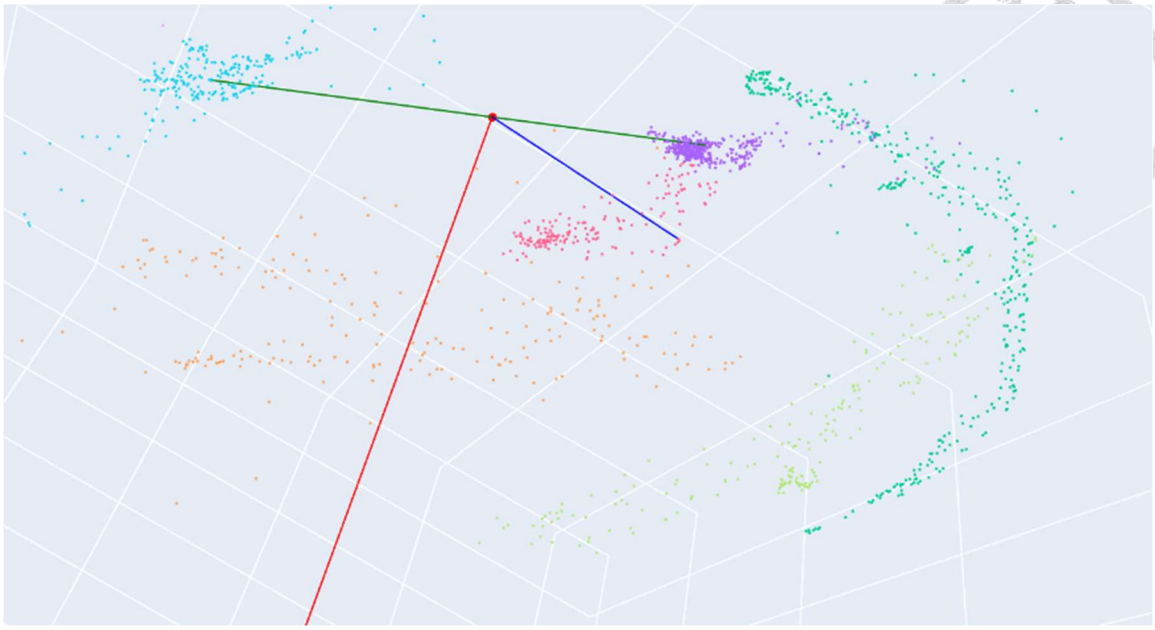

Figure 3-12. Tibia ACS. Green: x-axis; Blue: y-axis; Red: z-axis.

3.8.5.3 Patella ACS

Lastly, the patella ACS is defined as follows. Only two landmark points were obtained during the experiment, the superior and inferior poles of the patella. The anatomic landmark and surface contour point clouds for the patella have more outliers than those of the femur and tibia. A density-based spatial clustering of applications with noise (DBSCAN) clustering algorithm from Scikit-learn was used to remove the numerous outliers of the patella [84]. For the superior patella point cloud outliers, the DBSCAN parameters used were: ϵ = 0.5 and 15 minimum samples. For the inferior patella point cloud outliers, the DBSCAN parameters used were: ϵ = 0.95 and 25 minimum samples. These were arbitrarily chosen parameter values that yielded the most desirable outlier filtering. Upon finding the existing point closest to the mean of the superior and inferior

doi:10.6342/NTU202503673

poles, a line was passed through these points to establish the z-axis. The method of finding the patella z-axis is similar to the method used for defining the x-axes of the femur and tibia. Then, the x-axis is defined as the line passing from the origin to a point in the outer margin of the patella that is most perpendicular to the z-axis. The angle formed by the patellar x- and z-axes is 90.006°. The y-axis is then defined as the cross product of the x- and z-axes. The orientation of the x-axis is positive from the origin towards the lateral side of the patella. The orientation of the y-axis is positive from the origin towards to the anterior surface of the patella. The orientation of the z-axis is positive from the origin towards the superior pole of the patella (Figure 3-13).

doi:10.6342/NTU202503673

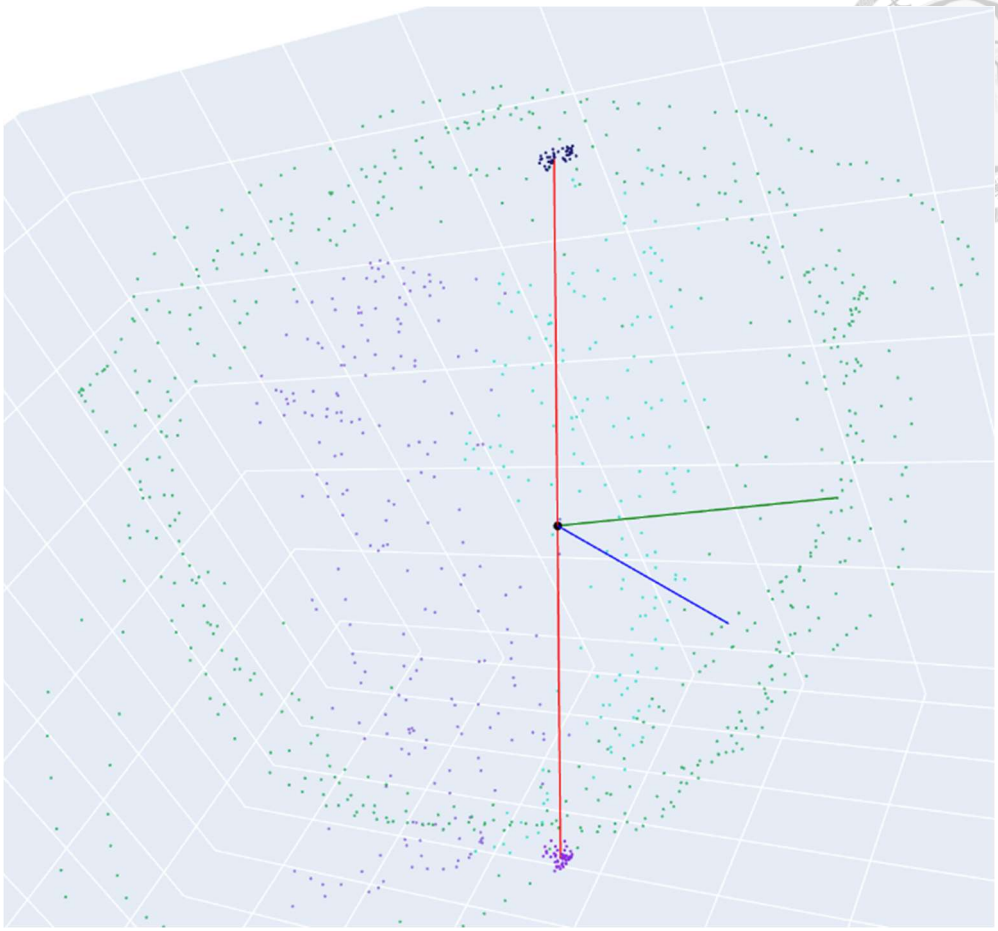

Figure 3-13. Patella ACS. Green: x-axis; Blue: y-axis; Red: z-axis.

3.8.6 Hip Joint Center Approximation

The hip joint center (HJC) was estimated using a least-squares sphere fitting method. The principle of this method assumes that the femoral head follows a ball-joint motion in the pelvis. The joint center is then estimated as the center of the best-fit sphere from the gathered motion data. Using the optical tracking system, the knee was passively moved to full flexion and extension combined with circumduction. The 3D positions of the femur bone marker were recorded over time. A best-fit sphere was attached to the trajectory data and a least-squares optimization algorithm was used to find the center of the best-fit

doi:10.6342/NTU202503673

sphere. This method is widely used for determining the hip joint center [85]. Figure 3-14 shows the motion data points, the best-fit sphere, and the calculated HJC coordinates. The HJC is in the fiducial marker reference frame (FM) due to being obtained using the motion data of the femur bone marker. Therefore, transformations must be made to bring the HJC into alignment with the femur ACS which is in the femur bone marker reference frame (BMF). The transformation ensures that the HJC is located at an anatomical point rather than floating above the body.

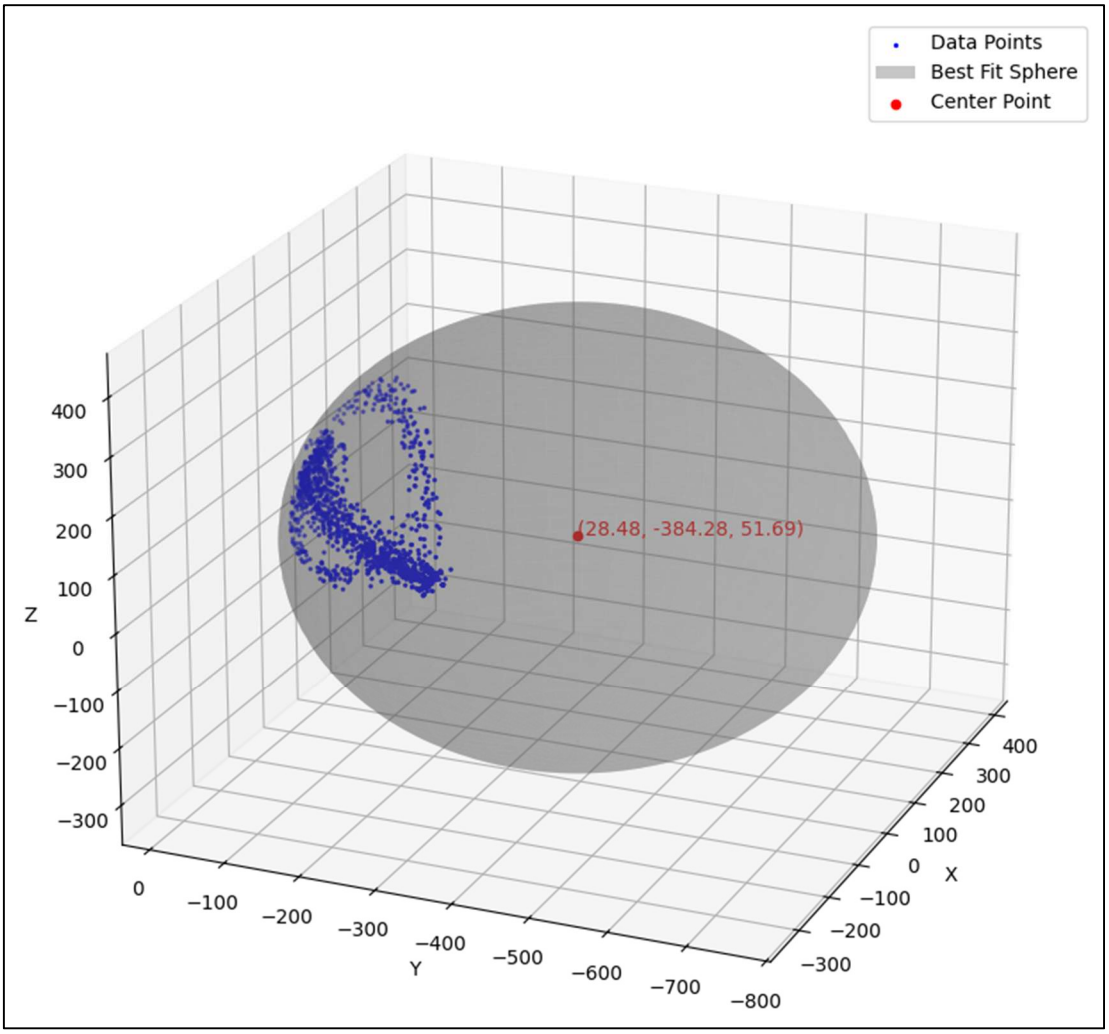

Figure 3-14. Hip joint center approximation using least-squares sphere fitting method.

doi:10.6342/NTU202503673

Chapter 4: Results and Discussion

4.1 SSM Variance Explanation and Model Interpretation

The statistical shape model (SSM) was constructed using principal component analysis (PCA) on a training set of anatomically segmented femur, tibia, and patella shapes. The cumulative explained variance plot (Figure 4-1) shows that 90% of the total shape variability can be captured using the first 10 principal components (PCs). This indicates that only half of the total number of PCs are necessary to approximate the essential anatomical variability present in the dataset. Such dimensionality reduction allows for efficient model use in downstream tasks like shape deformation and registration.

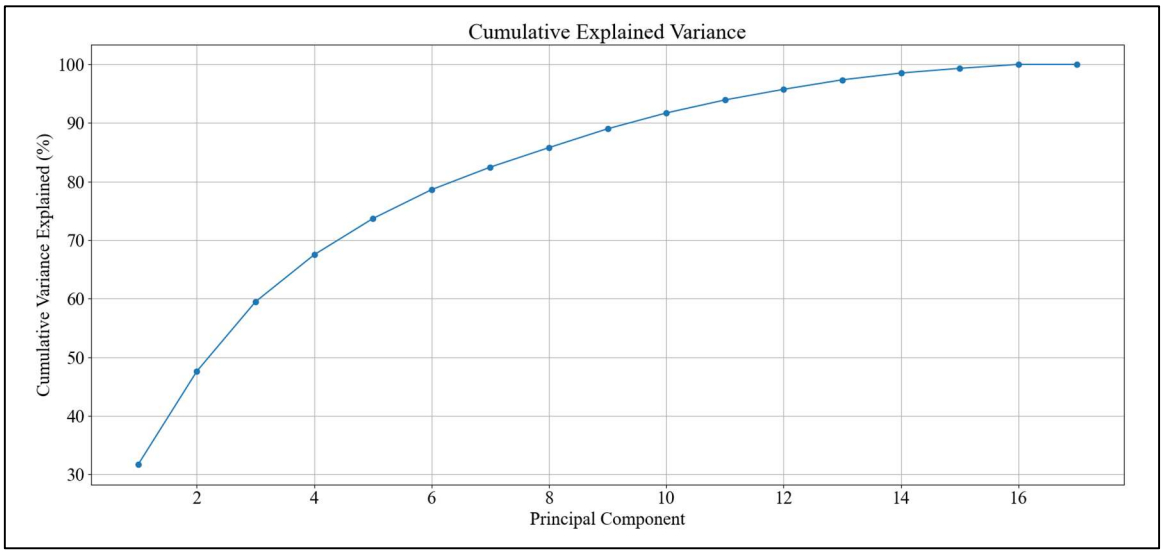

Figure 4-1. PCA cumulative explained variance plot.

To visualize the learned anatomical variation, the mean shape and the first five principal components of the SSM are shown in Figure 4-2. These five PCs account for

doi:10.6342/NTU202503673

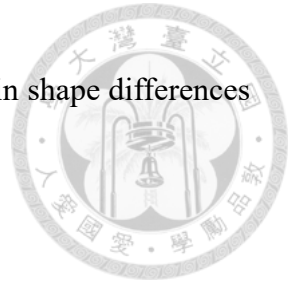

approximately 70% of the total variance, capturing dominant trends in shape differences across subjects.

1. PC1 appears to represent overall size and scaling of the entire knee joint. Uniform scaling can be seen while lowering and raising the PC1 values.

2. PC2 affects relative size variation between bone segments. Specifically, lower PC2 values scales the patella smaller while enlarging the rest of the bone segments. Raising PC2 values higher enlarges the patella while shrinking the tibia and fibula. The femur width here is thinner but the entire femur is elongated.

3. PC3 affects the ROI of the knee joint, influencing the spatial extent of the knee joint represented by the model. Lower PC3 values shows a more localized ROI of the knee joint, while larger PC3 values expand the ROI. This is the result of the non-uniform ROI used in the training shapes.

4. PC4 represents skewness, lower PC4 values introduces negative horizontal skew, while higher PC3 introduces positive horizontal skew.

5. PC5 introduces anisotropic scaling, which affects the aspect ratio of the knee joint. Lower PC5 values compress the knee joint along the mediolateral axis, while higher PC5 values elongates the knee joint along the proximodistal axis.

doi:10.6342/NTU202503673

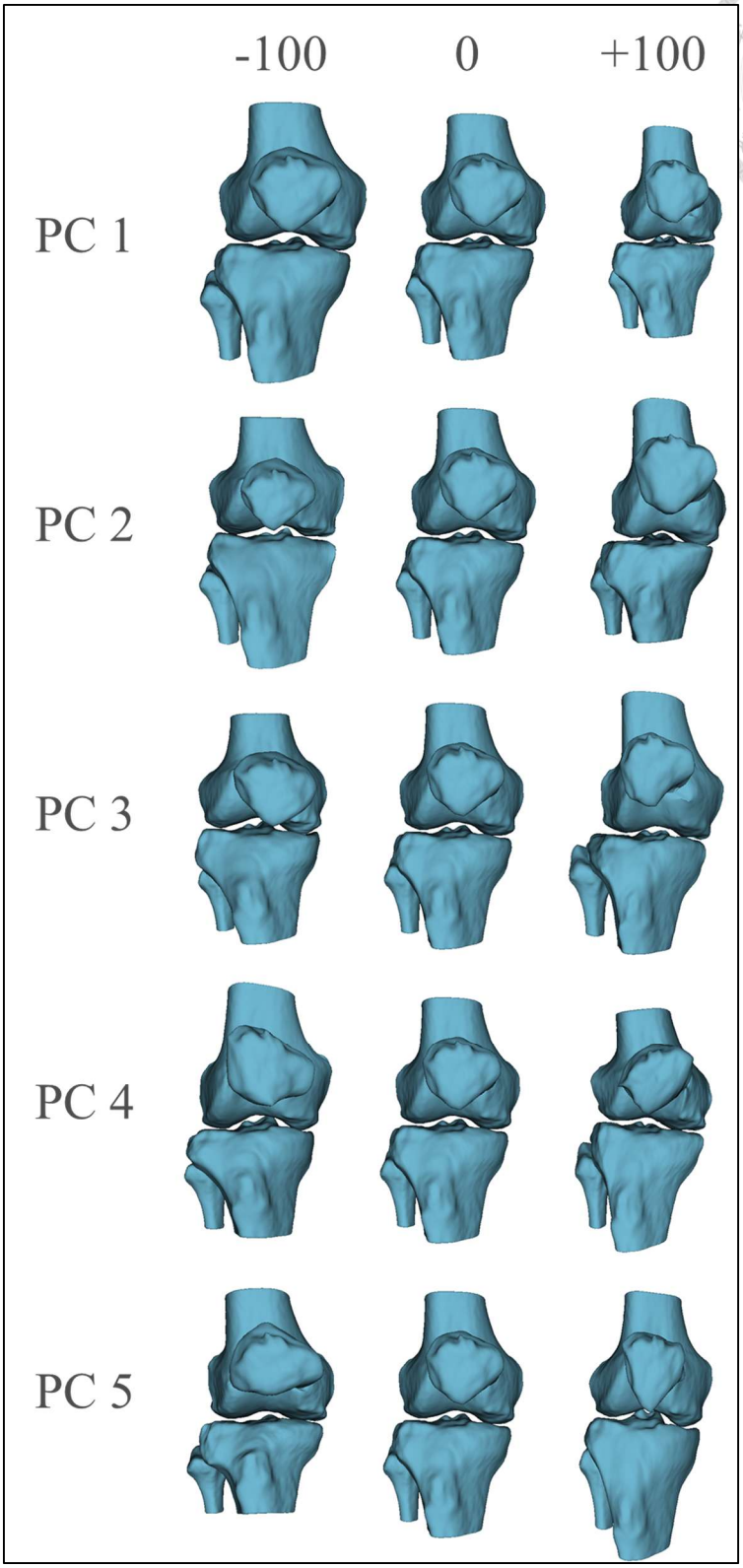

Figure 4-2. Statistical shape model showing the mean and variation of the first five principal component values.

doi:10.6342/NTU202503673

4.2 Quantitative and Qualitative Evaluation of SBR-Driven Shape Reconstruction

The SBR-Based SSM deformation pipeline was applied to a cadaver model without altering the finite element model input, demonstrating its direct applicability in biomechanical simulations (Fig. 4-3). This proves that the SBR method can be used even in the absence of volumetric imaging, using only 2D inputs. While the error margins may limit use in high-precision navigation, the results are sufficient for applications like finite element simulation, where geometry-driven contact mechanics and ligament attachment site approximations are more influential than sub-millimeter shape accuracy.

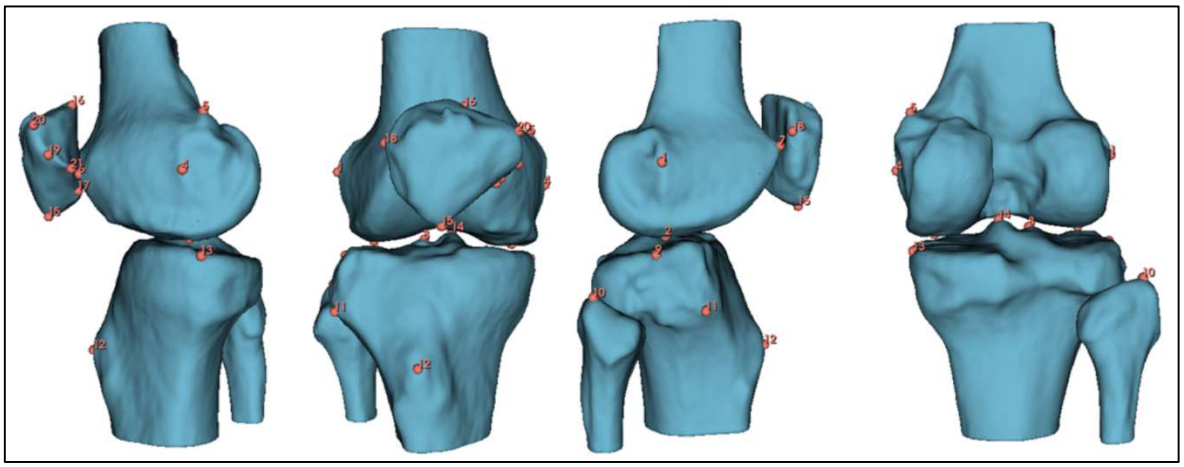

Figure 4-3. Deformed SSM and anatomical landmarks fitted to cadaver model based on SBR method using X-ray input.

To qualitatively assess the subset-based registration (SBR) and the SSM deformation methods, a 3D patient-specific model was reconstructed from 2D landmarks derived from CT projections. The deformed SSM output was visually compared against the ground truth

doi:10.6342/NTU202503673

3D CT segmentation using rigid registration performed with ALPACA (Automated Landmarking through Pointcloud Alignment and Correspondence Analysis), a module within the SlicerMorph extension of 3D Slicer. The overlay shows a high degree of anatomical correspondence in major bone contours and surface boundaries, particularly in the femoral condyles and patellar region (Figure 4-4).

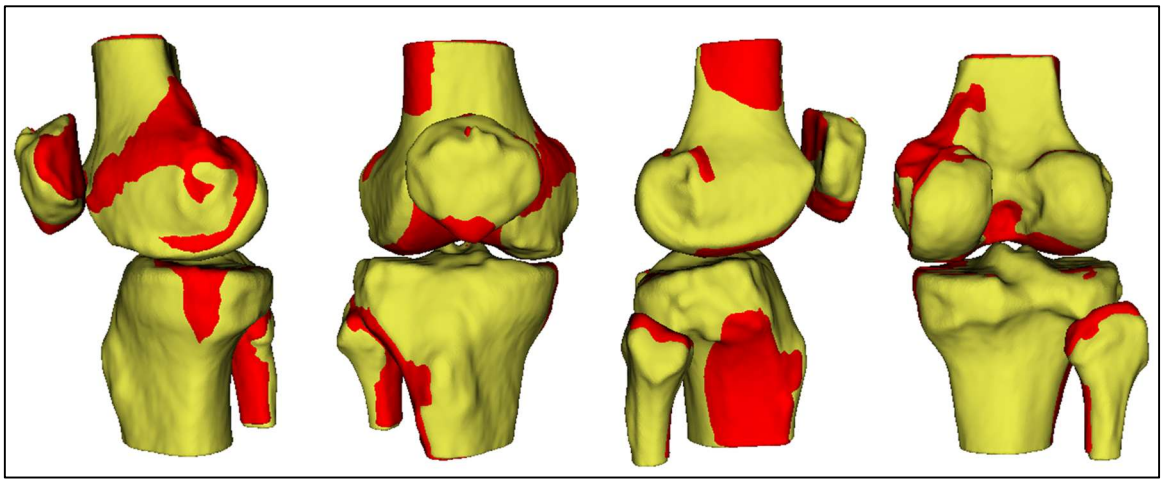

Figure 4-4. Overlay visualization of CT-segmented knee model (ground truth) and SSM-deformed model.

To quantitatively evaluate the accuracy of the SBR pipeline, two metrics were used: (1) mean surface distance between the deformed model and the CT-segmented ground truth, and (2) root mean square error (RMSE) of anatomical landmark positions. After rigid model registration, the mean surface distance between the SSM-deformed model and the CT segmentation was 4.37 mm. This indicates a reasonable surface alignment (Table 4-1). Fiducial registration of anatomical landmarks showed an RMSE of 3.29 mm, suggesting the SBR method achieves sub-5 mm landmark localization accuracy. The CT-based

doi:10.6342/NTU202503673

evaluation confirms that the proposed 2D–3D reconstruction pipeline using SBR and SSM deformation can accurately deform the SSM to obtain patient-specific anatomy.

Table 4-1. Summary of evaluation metrics for SBR method.

Metric	Value
Mean surface distance (mm)	4.37
Landmark points RMSE (mm)	3.29

While the SBR-driven 3D reconstruction was successfully validated qualitatively and quantitatively, it was not integrated in to the FE model during this study due to timeline and computational constraints. The dynamic FE model was developed and refined early in this study and required extensive tuning and stability testing. The 2D-3D shape reconstruction pipeline using the SBR method was completed at a later stage as an innovation. Integrating this model obtained from the novel shape reconstruction into the FE system would require a re-validation of the entire model pipeline. This was considered beyond the feasible timeline of the current work. Despite not being integrated, both the FE model and the SBR-driven 3D reconstruction pipeline are individually validated and serve as the foundation of the digital twin system.

4.3 Simulation Results: Patellar Kinematics

4.3.1 FE Model: Baseline Patellar Tracking of a Normal Knee

As defined earlier in Section 2.2.5, there is a significant inter-patient variability in

doi:10.6342/NTU202503673

patellar tracking [10]. Due to this variability, it is difficult to define a universal, normal patellar tracking trajectory. Therefore, for this study, a normal or healthy patellar tracking is defined as the trajectory measured using the baseline parameter values that represent healthy knees.

For patellar shift (Figure 4-5(a)), early degrees of knee flexion (below 20°) shows medial shift, reversing direction towards the lateral side from 8°. The lateral shift increases until 40° knee flexion, after which a return to medial shift was observed until 75° knee flexion. Beyond this point, the patellar shift becomes relatively stable and plateaus until the end of the knee flexion. In patients with healthy knees, it is common to observe a decrease in patella shift, i.e., a shift towards the medial side, when knee flexion angle is between 0°-30°, then increase at 90° [14]. This increase at 90° knee flexion was not observed for the FE model.

Next, for patella flexion (Figure 4-5(b)), the trajectory is linear with the knee flexion, lagging 70% behind similar to observed patterns in other studies [10]. For patella rotation (Figure 4-5(c)), medial rotation is observed until 10° knee flexion, which is a turning point and the patella rotates laterally until 25° knee flexion. This variability in patella rotation is observed throughout knee flexion, indicating a mobile patella. There are no observed patterns from other studies on patella rotation [10]. Next, for patellar tilt (Figure 4-5(d)), a slight medial tilt is observed until 10° knee flexion, where the patellar tilts

doi:10.6342/NTU202503673

laterally until 60° knee flexion. Beyond this point, the patellar tilt varies from medial to lateral until the end of knee flexion. The patella engages with the trochlear groove at around 15° knee flexion, denoted by a relatively stable trajectory starting from this knee angle.

The variation observed in patellar tilt is likely caused by the geometry of the knee model and the simplified contact mechanics. There is also a recorded 12° internal tibia rotation which may have also contributed to the patellar tracking. This tibia rotation is similar to observed measurements in other studies [31]. The sharp spikes observed in the patellar tracking trajectories are the FE model attempting to stabilize which manifested as abrupt changes at the beginning of the data.

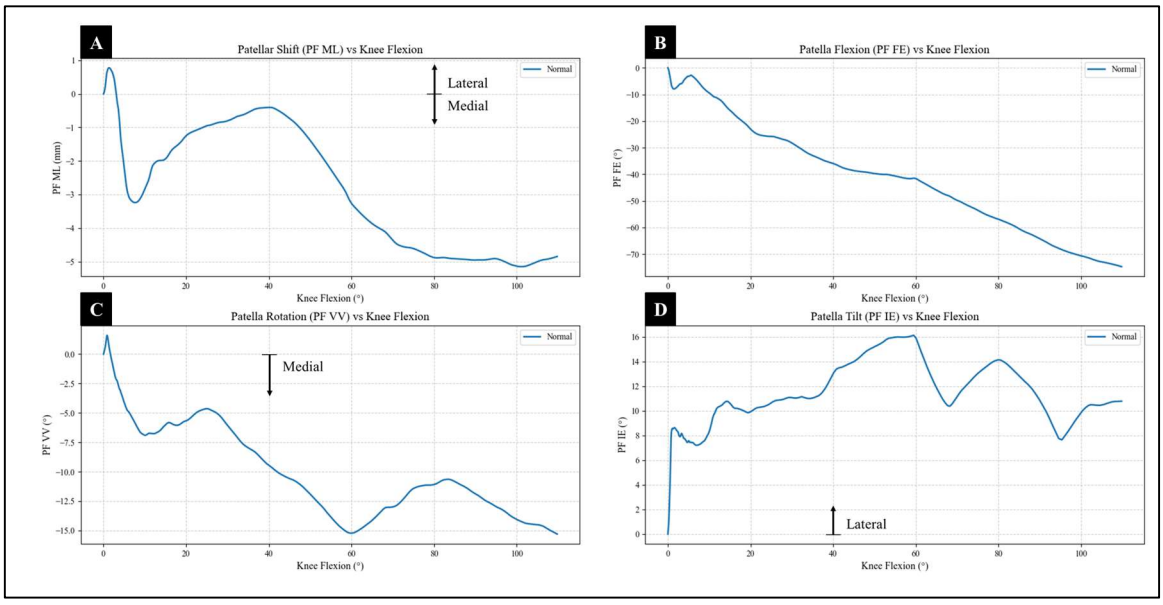

Figure 4-5. Patellar tracking of a normal knee.

This degree of patella mobility can be attributed to the lack of soft tissue wrapping

doi:10.6342/NTU202503673

implementation for structures such as ligaments and muscles. The patella behavior may have deviated from an actual knee joint due to the simplification of ligament wrapping. Another possible factor is the simplification of contact detection. Simplifying cartilages and menisci structures were integral in this study to ensure a personalized model. However, the patella trajectory results from this study are still found to be comparable to other patellar tracking studies. Overall, despite the simplified assumptions used for the FE model, the patellar tracking for a normal knee is comparable to other studies. Therefore, the patellar tracking measurements for this study are competent.

4.3.2 FE Model: Effect of Ligament Tightness on Patellar Kinematics

Using the modified baseline parameter values indicated in Section 3.6.7, i.e., lateral ligaments stiffness increased four times and medial ligaments stiffness reduced 0.55 times the baseline values, the measured patellar tracking trajectories are shown in Figure 4-6. The values in Figure 4-6 did not reach pathological thresholds, particularly for patellar shift and tilt. However, significant deviations from the normal patellar tracking trajectories have been observed.

Patellar shift and tilt are the primary focus of analysis for changes in patellar tracking. For patellar shift (Figure 4-6(a)), The patella is prevented from moving laterally throughout the knee flexion. The patella is observed in Figure 4-6(a) to consistently shift medially. The lateral ligaments exert restraining forces that prevent lateralization of

doi:10.6342/NTU202503673

patellar shift [86]. Tighter lateral restraining forces explain the reduced lateral shift of the patella. The weaker medial restraints may have contributed to reduced medial stability, therefore the patella is shifting more medially than the normal baseline trajectory. Similarly, for patellar tilt (Figure 4-6(d)), the tighter lateral ligaments suppress the medial tilt of the patella. Figure 4-3(d) shows less variability in patellar tilt throughout knee flexion. Changes in patella flexion (Figure 4-6(b)) and patella rotation (Figure 4-6(c)) are not of particular interest for this study.

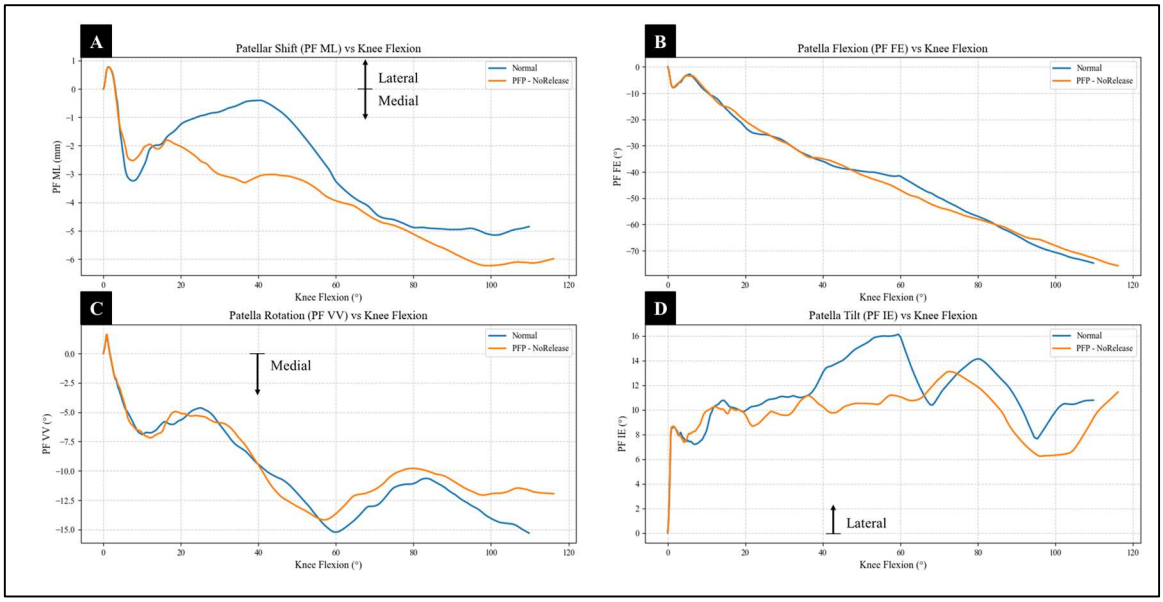

Figure 4-6. Patellar tracking of a knee with tight ligaments.

4.3.3 FE Model: Evaluation of Surgical Release Scenarios

This section will discuss the different effects of various surgical release scenarios simulated using the FE model, focusing on identifying the most effective surgical release scenario that corrects patellar tracking. Each surgical release scenario will comprise of

doi:10.6342/NTU202503673

the graphs of the patellar tracking measurements containing kinematic data of patellar shift (mediolateral displacement), flexion (x-axis rotation), rotation (y-axis rotation), and tilt (z-axis rotation) under different conditions: normal (healthy), preoperative (characterized by tight ligaments, labeled as "PFP" for patellofemoral pain in the figures), and the different degrees of surgical release. Not all unique release types and combinations of compounded release types were investigated in this study. The scope was intentionally limited to avoid straying from the main objective of this study. The only reason various releases and release combinations were explored was to observe potential differences and to visualize findings from SHAP and XGBoost feature importance analyses in Section 4.5.3.

4.3.3.1 Qualitative Evaluation

This subsubsection discusses the kinematic response of medial retinacular (MR) release in the superior to inferior direction with a full lateral retinacular (LR) release for a compounded release scenario. This surgical release scenario was also deemed the best in correcting patellar shift and tilt from a qualitative analysis perspective. For patellar shift (Figure 4-7(a)), the effects of performing full LR release has been discussed in Section 4.3.3.1. Introducing a minimal (25%) MR release with a full LR release shows a patellar shift trajectory that is closer in alignment with the normal patella shift trajectory until about 60° knee flexion, which shows the postoperative shift trajectory is slightly

doi:10.6342/NTU202503673

more lateral than the normal trajectory. Notably, larger releases (>25%) shows closer alignment with the preoperative patellar shift trajectory, indicating over-correction.

For patellar tilt (Figure 4-7(d)), a restoration of patellar tilt mobility can be observed after performing 25% MR release with a full LR release. However, the earlier stages of knee flexion (0°-20°) show that the patellar tilt trajectory is unstable, varying quickly from lateral to medial tilt until it engages with the trochlear groove. After which, the patella tilt shows to have significant medial tilt before moving laterally at 60°. Similar to the analysis for patellar shift, the trajectories for larger MR releases show closer alignment with the preoperative patellar tilt trajectory, further emphasizing effects of over-correction or failure of correction. The postoperative analysis for both patellar shift and tilt suggest the need for calibrating the extent of MR release to avoid patellar tilt instability.

From the SHAP and XGBoost analysis in Section 4.5.3, the superior regions of the MR have significant influences in predicting changes to patellar shift and tilt after surgical release. This influence can be observed by a significant change to the patellar shift and tilt trajectories in Figure 4-7 after only 25% MR release. The sudden over-constrained effect to patellar tracking at larger releases indicate nonlinearity in the relationship between the extent of MR release and patellar tracking. Suggesting that targeted release on ligaments that have significant influence in correcting patellar shift and tilt may

doi:10.6342/NTU202503673

improve surgical outcomes, and larger releases introduces over-constraint.

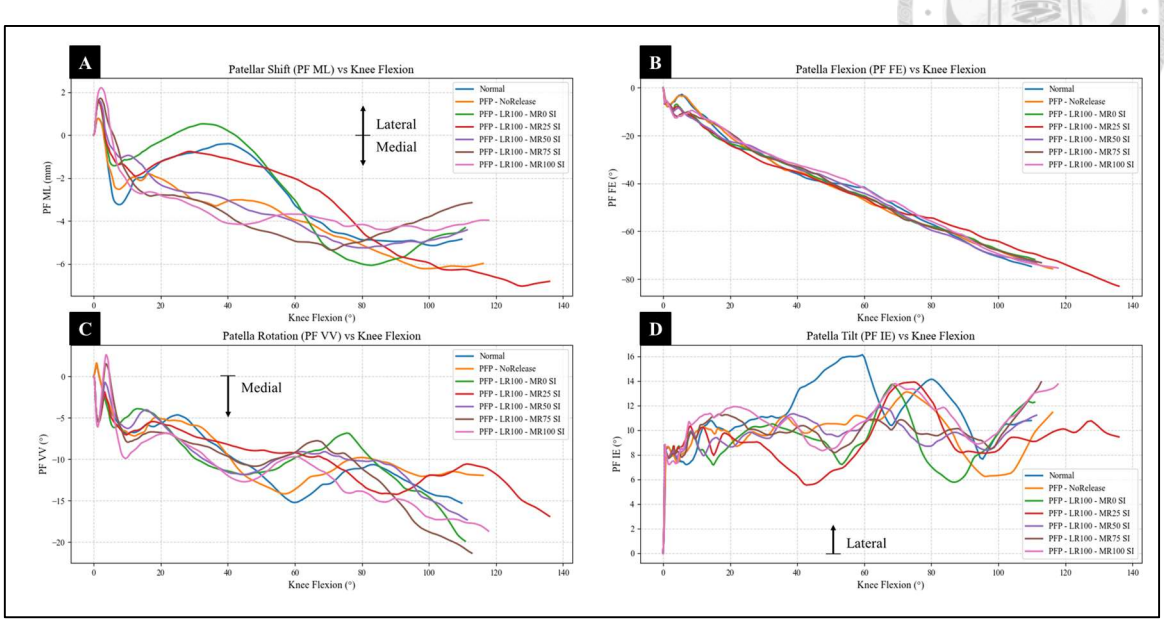

Figure 4-7. Stepwise surgical release of the medial retinaculum (MR) from 0% to 100% in the superior-to-inferior (SI) direction with a full LR release. Each increment represents a unique surgical scenario used in the simulation.

Qualitative assessments of patellar tilt and shift in this surgical release scenario are shown in Figures 4-8 and 4-9. For Figure 4-8, the patellar tilt after 25% MR release and a full LR release shows slight patella alta (high-riding). The patella in this scenario is tilted more medially than other scenarios. From a visual inspection, none of the scenarios closely resemble the normal patellar tilt, indicating poor effectiveness of performing a combined MR release in the SI direction with a full LR release. For Figure 4-9, the patellar shift trajectory for the 25% MR release scenario appears to be the most mobile among all scenarios. As seen in Figure 4-8, this may indicate instability due to the scenario resulting in patella alta. Therefore, while the 25% MR release provides increased patellar

doi:10.6342/NTU202503673

shift and tilt mobility, patellar stability and alignment are compromised. This suggests that this approach may have potentially limited clinical utility, as it can introduce over-release and instability.

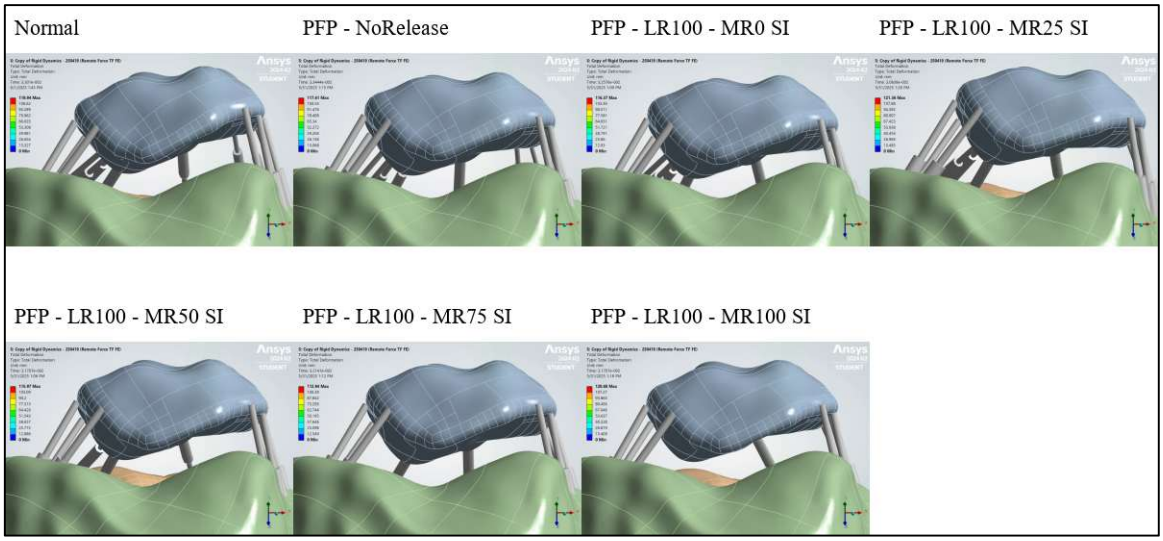

Figure 4-8. Axial (superoinferior) views of the patella at ~60° knee flexion showing tilt orientation in normal, preoperative (PFP), and MR release scenarios (released in SI direction) with a full LR release. Images used courtesy of ANSYS, Inc.

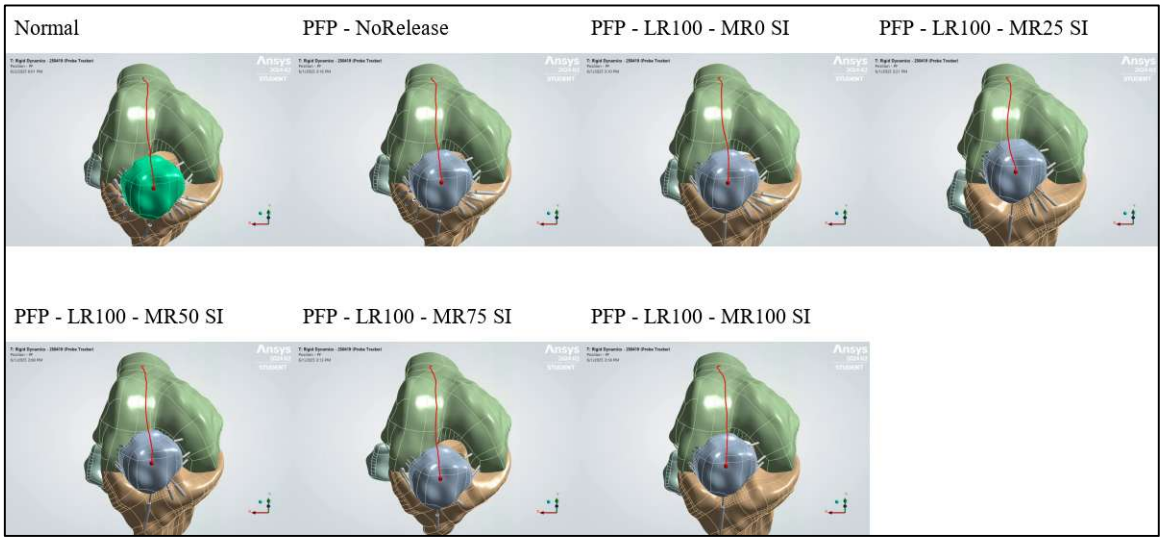

Figure 4-9. Anteroposterior (AP) views of the patella showing shift trajectory traces

doi:10.6342/NTU202503673

from 0° to 110° knee flexion for normal, preoperative (PFP), and MR release cases (released in SI direction) with a full LR release. Images used courtesy of ANSYS, Inc.

4.3.3.2 Quantitative Evaluation

Figure 4-10 shows the static evaluation of the effectiveness of each surgical release scenario performed in the FE simulations, ranked according to their effectiveness scores. The scoring system is determined by the Euclidean distance between the normal and postoperative patellar shift and tilt values at approximately 60° knee flexion. Specifically, the effectiveness score is given by:

$$\boldsymbol{effectiveness\ \ score} = \sqrt{\Delta shift^2 + \Delta tilt^2}.$$

Thus, a lower value represents better results. This evaluation determines correction of patellar malalignment. From the figure, it shows that 75% LR release in the SI direction yields the most effective surgical release scenario. This result is in contrast with the findings from the qualitative analysis of each surgical release scenario, where it was found that partial MR release (25-50% release) with a full LR release yielded the most effective postoperative patellar tracking. Furthermore, this surgical release scenario is ranked lower. Upon inspecting the ranking of the progression of MR release, it shows that there is nonlinearity with the effects of each percentage released. This phenomenon shows that the biomechanical response of the patella is different throughout the progression of ligament release. Overall, these results show only one aspect of the correction of each surgical release scenario. These results are useful for quick reference of the effectiveness of a surgical release scenario by evaluating the patellar shift and tilt correction at 60° knee flexion with the diagnostic X-ray taken also at this knee flexion angle. However, these results are insufficient in evaluating the long-term stability of the knee such as patellar

doi:10.6342/NTU202503673

tracking throughout the entire range of knee flexion.

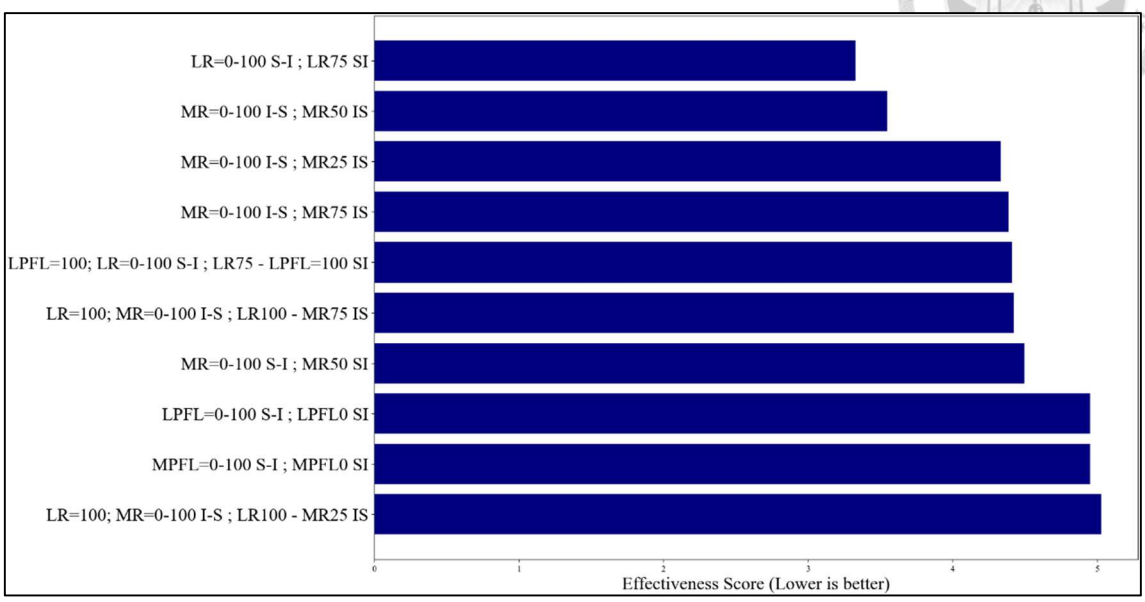

Figure 4-10. Ranked postoperative effectiveness scores for patellar alignment at 60° flexion.

Table 4-2 shows the dynamic evaluation of the effectiveness of each surgical release scenario performed in the FE simulations, ranked according to their total scores. The scoring system used to evaluate the quantitative effectiveness of the surgical scenarios is given by:

$$\boldsymbol{Total\ Score} = w_1 \cdot MSE_{shift} + w_2 \cdot MSE_{Tilt} + w_3 \cdot STD_{Shif} + w_4 \cdot STD_{Tilt},$$

where w_i represent the weights which balance the short-term correction—restoration of patellar alignment at 60° knee flexion, determined by MSE—with long-term stability—stability of patellar tracking throughout knee flexion, determined by STD. The system used for determining the total score is arbitrary and not clinically validated; these values serve as comparative analysis of the various possible surgical release strategies. This evaluation determines correction of patellar tracking. The first two scenarios have completely similar total score values, likely due to a diminishing returns of effectiveness

doi:10.6342/NTU202503673

for this type of surgical release scenario (see Appendix A-7). The similarities of results may have also arisen from the FE model geometry not being able to differentiate more complex differences in biomechanical response due to progressive ligament release. Compared to the static evaluation of the surgical release scenarios, the progressive release of LPFL leads to better patellar tracking than LR release, which is ranked lower in this analysis. The surgical release scenario deemed the most effective from the qualitative analysis has moderate effectiveness according to the quantitative dynamic evaluation. Overall, the significance of these results show that long-term stability of the patella must also be considered with the patellar malalignment correction at a static knee flexion angle.

Table 4-2. Ranked surgical release scenarios by total dynamic score.

Rank	Scenario	MSE_{Shift}	MSE_{Tilt}	STD_{Shift}	STD_{Tilt}	Total Score
1	LPFL=0-100 S-I	0.8326	2.3641	1.8092	2.8712	5.5369
2	LPFL100 ; MPFL100 SI	0.8326	2.3641	1.8092	2.8712	5.5369
3	MPFL33 S-I	0.8326	2.3641	1.8092	2.8712	5.5369
4	LR25 IS	0.6906	5.3726	2.2226	2.1555	8.2523
5	MR25 IS	1.3499	4.6562	2.0963	2.7459	8.4274
6	LR25 SI	0.5385	5.5078	2.3461	2.5545	8.4967
7	MR25 SI	0.8527	5.4777	2.0486	2.9216	8.8157
8	LR100 ; MR25 IS	2.0462	4.5569	2.1430	2.3060	8.8276
9	LR100 ; MR75 IS	2.7781	4.5960	2.2141	2.4035	9.6830
10	MR50 IS	1.4592	5.6526	1.8580	3.3665	9.7241

4.4 Cadaver Study: Patellar Tracking

As previously discussed in Section 3.8.2, the purpose of this cadaver study was to understand the effects of surgical release on patellar kinematics. Additionally, the

doi:10.6342/NTU202503673

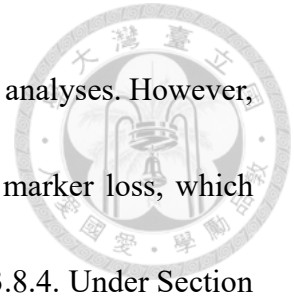

experimental data serves as a validation benchmark for the FE model analyses. However, the cadaver study faced significant challenges due to patella bone marker loss, which required data reconstruction and estimation as discussed in Section 3.8.4. Under Section 3.8.4, it was described how the raw patella point cloud data were initially unusable due to the missing patella bone marker, which resulted in a loss of anchor for the point cloud data obtained. Transformations were used to estimate the patella position relative to the femur. This process introduced several assumptions and is recognized to have negatively affected accuracy.

Figure 4-11 shows the patellar tracking kinematics obtained from the cadaver study, showing three different surgical release scenarios: no release, lateral release, and combined medial and lateral release. The release made on each side were full releases and the extent of each release was not able to be recorded. For patellar shift (Figure 4-11(a)), tracking shows poor resemblance to normal patellar shift tracking results previously reported in other studies (Section 2.2.5), as well as the retrieved results from the FE model in this study (Section 4.3). Due to the loss of the patella bone marker data, the interpretation of these results is speculative and an approximation to salvage the dataset. Consequently, these results are neither optimal or comparable to the quality and reliability of the other results presented in this study.

It was previously discussed in 2.2.5 that the patellar flexion typically shows a lag of

doi:10.6342/NTU202503673

60-70% behind the knee flexion angle. In the cadaver study, patellar flexion (Figure 4-11(b)) is recorded to lag by 30-50% in the no release condition; by 60-75% following lateral release; and by 17-47% following combined lateral and medial release. These values suggest inconsistencies, particularly for the no release and full release cases. A likely cause is variation in the anatomical coordinate systems used for measuring patellofemoral rotation. Eventually, this caused errors in measurements of relative angles. Additionally, the estimation-based reconstruction of the patellar anatomical coordinate system introduced spatial artifacts. This, however, was expected since the transformation to salvage the missing data did not result in a successful and complete restoration of the correct patellar position. These assumptions led to the presence of artifacts.

For patellar rotation (Figure 4-1(c)), it can be observed that the no release and the lateral release conditions were similar, with the lateral release resulting in a slightly more lateralized patellar rotation trajectory throughout the knee flexion cycle. Interestingly, the full release scenario resulted in a reversed rotation trajectory. The patella rotation trajectory changed to a medially rotated orientation. This phenomenon may be the result of destabilization after releasing the passive stabilizing structures on both sides of the patella. Interestingly, all of the patellar rotation trajectories in Section 4.3 shows a medially oriented patellar rotation, regardless of ligament tightness or surgical release performed.

doi:10.6342/NTU202503673

For patellar tilt (Figure 4-11(d)), tracking in the no release condition closely resembled normal trajectories found in literature (Section 2.2.5). However, it appears that the patellar engagement with the trochlear groove is delayed significantly, occurring only after 80° knee flexion. From the FE models patellar engagement usually occurs at around 60° knee flexion. Following lateral release, the patellar tilt trajectory is different from what was observed in the full lateral release scenario from the FE model analysis in Appendix A-3. The delayed engagement may also be a consequence of variation in the anatomical coordinate systems. In the full (combined medial and lateral) release condition, the patellar tilt shows high tilting motions, indicating excessive freedom and a possible risk of subluxation. These findings suggest that a full bilateral release may fully destabilize the knee joint, aligning with the observations made from the FE model analysis in this study as well as other clinical studies.

doi:10.6342/NTU202503673

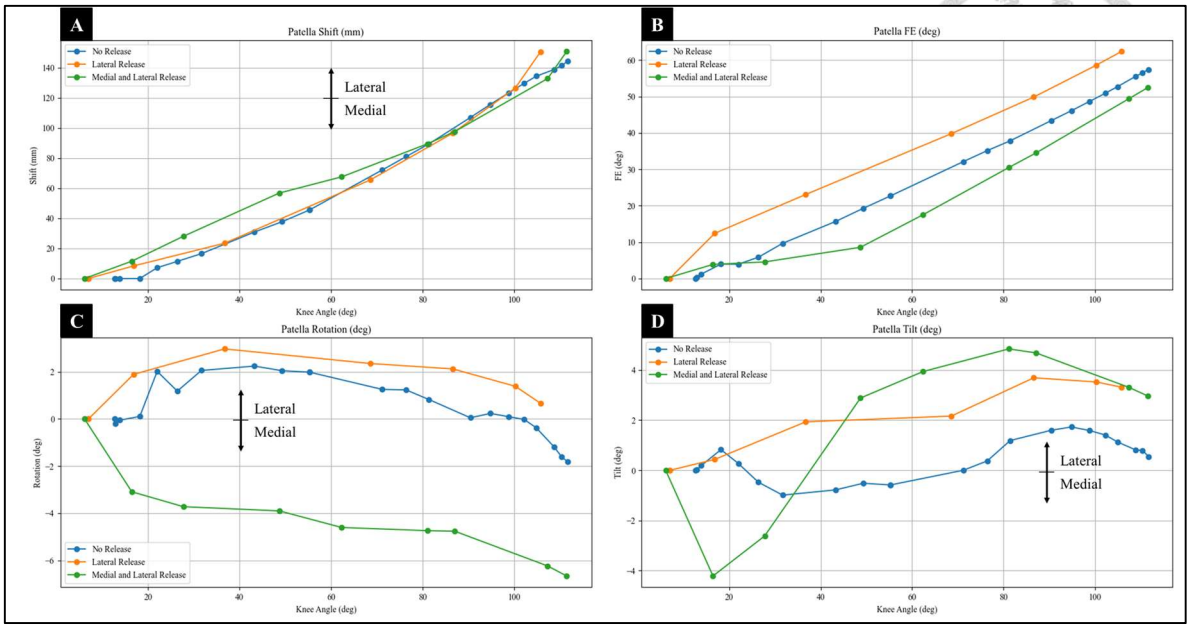

Figure 4-11. Patellar tracking kinematics from the cadaver study under three surgical conditions: no release, lateral release, and combined medial–lateral release. The kinematic parameters shown include patellar shift, flexion, rotation, and tilt over the knee flexion cycle.

Several factors affected the reliability of the results from this cadaver study. The loss of the patella bone marker introduced nontrivial assumptions during data recovery and estimation. The transformation assumptions may not completely represent the true alignment from the cadaveric knee anatomy. The transformation also resulted in inter-frame shifts. Therefore, although conventional methods were used to define each anatomical coordinate systems, the transformations may have reduced comparability. Moreover, it is unclear if patellar maltracking features were present, regardless if they were pathological or not since the cadaver specimen did not show any symptoms.

doi:10.6342/NTU202503673

4.5 Machine Learning Model Results

4.5.1 Performance Evaluation: Malalignment Predictor Model

To objectively analyze the performance of the malalignment predictor model and the surgical release predictor model, evaluation metrics were calculated. The evaluation metrics of the malalignment predictor model are shown in Tables 4-3 and 4-4. For Table 4-3, the errors are relatively small—below 1 mm. The small error values indicate that the shift values predicted do not vary widely. However, these values may be conservative or biased towards a small range. Furthermore, these metrics point towards model underfitting due to the R^2 metric having a value of only 0.16 in predicting patellar shift. The low R^2 corresponds to a lower predictive ability of the model. The low value also shows that while the predictions are not random, the predictions are far from ideal.

For Table 4-4, the higher errors indicate that the patellar tilt data is more difficult to predict using the parameters given in the stiffness profiles. Specifically, the higher MAE may point to systematic bias that exist in the predictions. A moderate value of R^2 shows that the model is able to capture some trend with the nonlinear data but is not sufficient to predict significant variance, especially at higher tilt values. Furthermore, a value of only 0.3775 for R^2 in predicting patellar tilt, while better, still explains less than 40% of the variation. These evaluation metrics show that while the model captures some nonlinear variations, the model is missing critical factors.

doi:10.6342/NTU202503673

Table 4-3. Performance metrics of the malalignment predictor model for patellar shift prediction.

Metric	Value
MSE	0.7353 mm
RMSE	0.8575 mm
MAE	0.6628 mm
R^2	0.16

Table 4-4. Performance metrics of the malalignment predictor model for patellar tilt prediction.

Metric	Value
MSE	4.7101°
RMSE	2.1703°
MAE	1.5864°
R^2	0.3775

To visualize the predictive accuracy of the malalignment predictor model, predicted versus actual plots were generated (Figures 4-12 and 4-13). Furthermore, these diagnostic plots analyze if the model overestimates or underestimates predictions, and assess the model performance at high or low values. For Figure 4-12, clustering can be observed at the -4 to -3 range in the x-axis. This clustering shows accuracy for mid-range values. Fig, 10 shows multiple points scattered away from the 45° line, indicating this model lacks generalizability. The clustering of the points in the middle values also point to the model having poor dynamic response to input, especially at extreme values.

doi:10.6342/NTU202503673

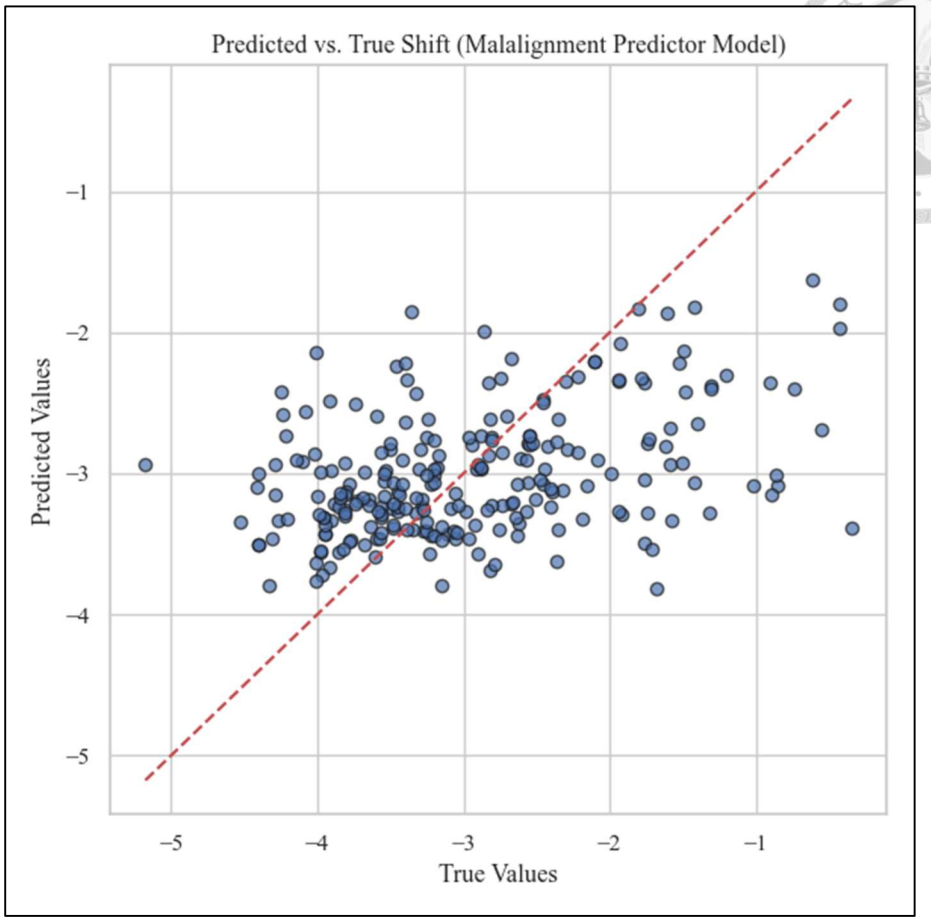

Figure 4-12. Predicted versus true value plot of the malalignment predictor model for patellar shift.

For Figure 4-13, moderate alignment with the 45° line can be observed in the 8-16 range in the x-axis. The plot shows the points are offset to the right—systematic bias. The model underestimates higher tilt values. Outliers can be seen at extreme values indicates the model has limited learning from these cases.

doi:10.6342/NTU202503673

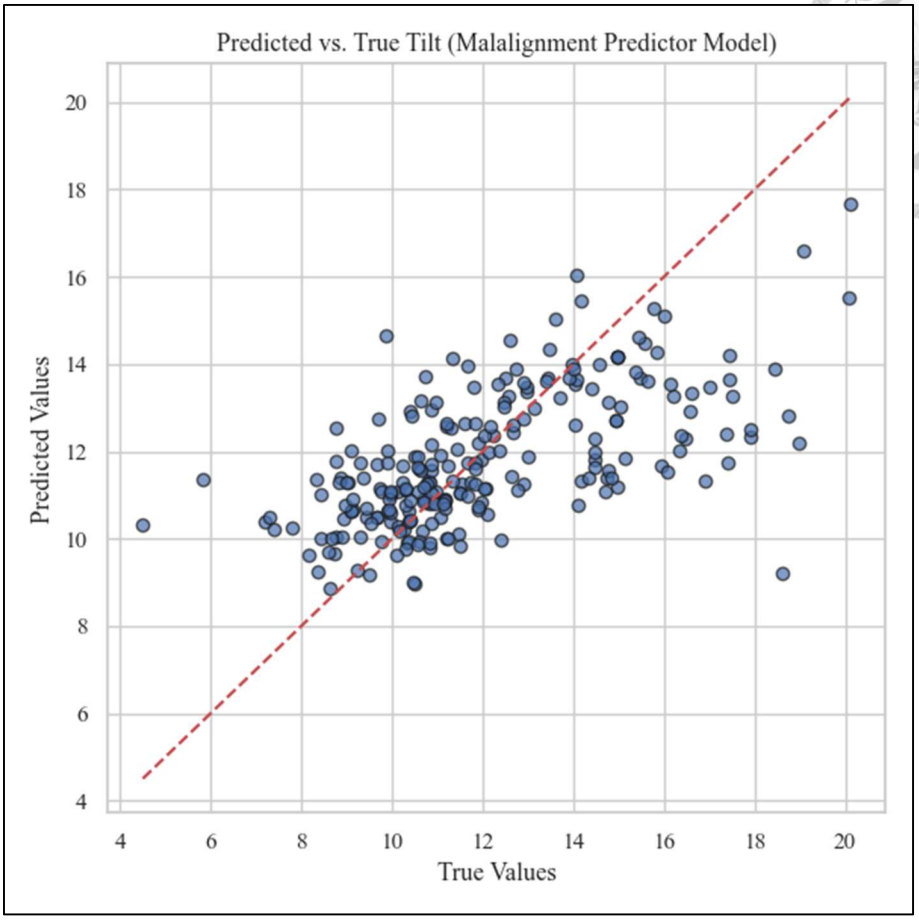

Figure 4-13. Predicted versus true value plot of the malalignment predictor model for patellar tilt.

Figures 4-14 and 4-15 shows the residual plots for the malalignment predictor model. These residual plots determine homoscedasticity, whether the error is consistent for all predictions. Ideally, the residuals must be randomly scattered as close to the zero line as possible. Pattern forming indicates systematic errors and that the model is missing nonlinear relationships in the data. Larger residuals indicate the model may not be reliable in those areas. For Figure 4-14, good concentration especially near -3.5 to -3.0 in the predicted axis, but the residuals spread by values of 2 in the residual axis. The residuals

doi:10.6342/NTU202503673

show some bias but are not catastrophic. Figure 4-15 shows the narrow prediction range of the malalignment predictor model for patellar shift.

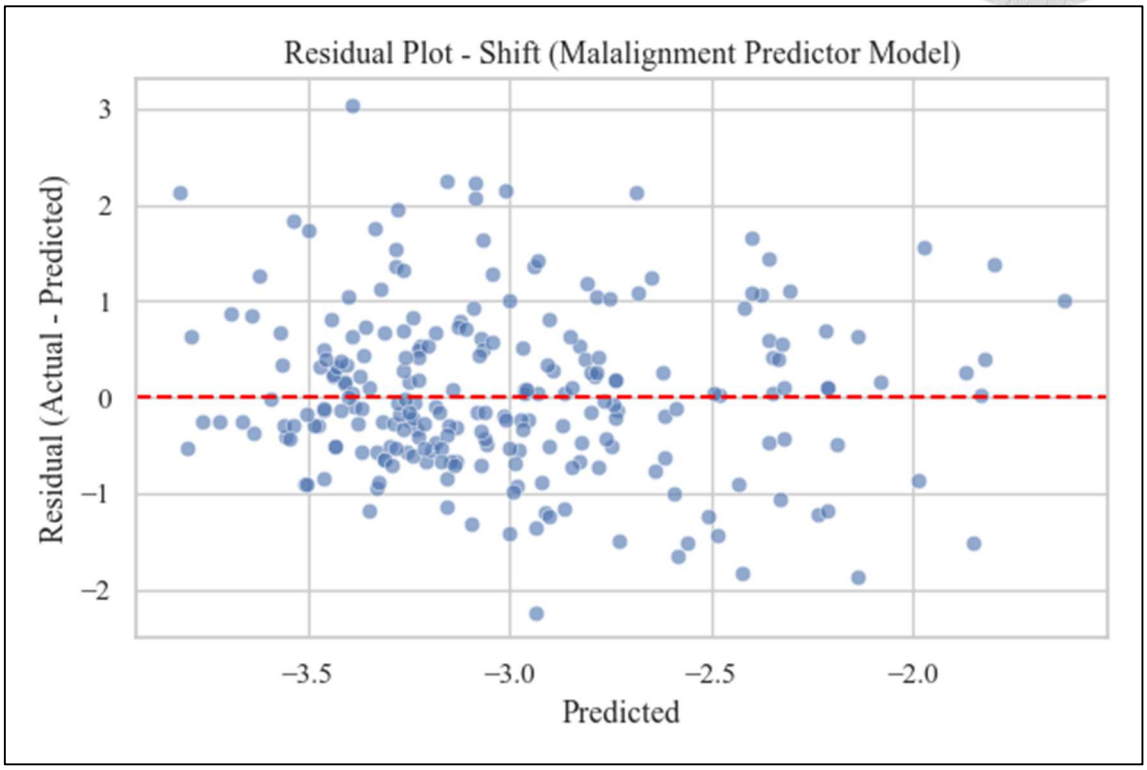

Figure 4-14. Residual plot of the malalignment predictor model for patellar shift.

For Figure 4-15, tight clustering around the zero line with higher systematic bias than Figure 4-14, indicating some heteroscedasticity in which the error variance increases with predicted patellar tilt. The tightest clustering can be observed in the 10-14 range of the predicted axis, showing that the model performs well for middle values.

doi:10.6342/NTU202503673

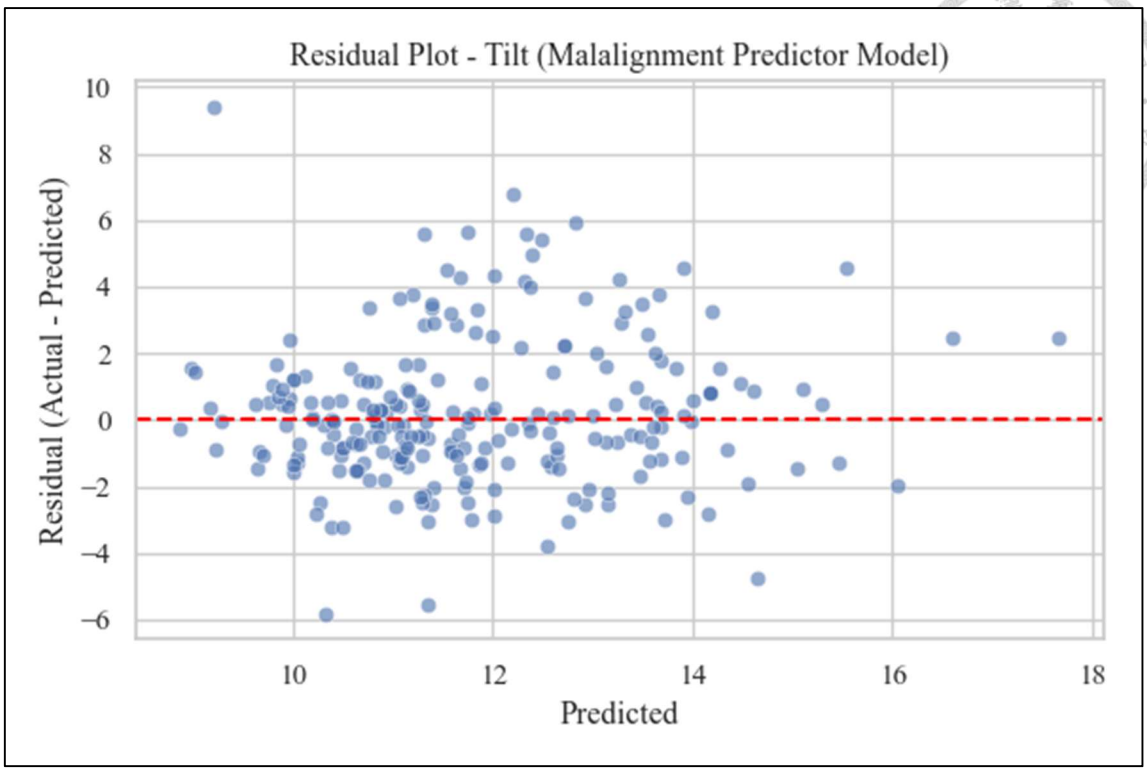

Figure 4-15. Residual plot of the malalignment predictor model for patellar tilt.

4.5.2 Performance Evaluation: Surgical Release Predictor Model

The evaluation metrics of the surgical release predictor model are shown in Tables 6 and 7. For Table 4-5, the errors are relatively low—about 1 mm. Despite the higher MSE, a lower MAE than the malalignment predictor model suggests this model has more consistent predictive capabilities and less large deviations. For Table 4-6, the R^2 is the highest. The surgical release predictor model for patellar tilt prediction is strongest in terms of variance explained. The XGBoost algorithm used in this model therefore was able to capture the nonlinear kinematic response of surgical release on patellar tilt. Furthermore, the generalization of the model can be considered good despite the higher error than the predictions for patellar shift. In both models, this suggests patellar tilt is

doi:10.6342/NTU202503673

more difficult to predict than patellar shift. Compared with the malalignment predictor model, the R^2 values of this model are higher in both the patellar shift and tilt predictions, indicating that the surgical release predictor model better captures the variability of patellar shift after surgical release.

Table 4-5. Performance metrics of the surgical release predictor model for patellar shift prediction.

Metric	**Value**
MSE	1.2438 mm
RMSE	1.1153 mm
MAE	0.6199 mm
R^2	0.6188

Table 4-6. Performance metrics of the surgical release predictor model for patellar tilt prediction.

Metric	**Value**
MSE	7.6403°
RMSE	2.7641°
MAE	1.6838°
R^2	0.6618

Figures 4-16 and 4-17 visualizes the predictive accuracy of the surgical release predictor model. Figure 4-16 shows tight clustering about the 45° line at around -6 to -2 indicates strong prediction accuracy. There are outliers in the -2 to 6 range but most of the points are tightly clustered and aligned to the 45° line.

doi:10.6342/NTU202503673

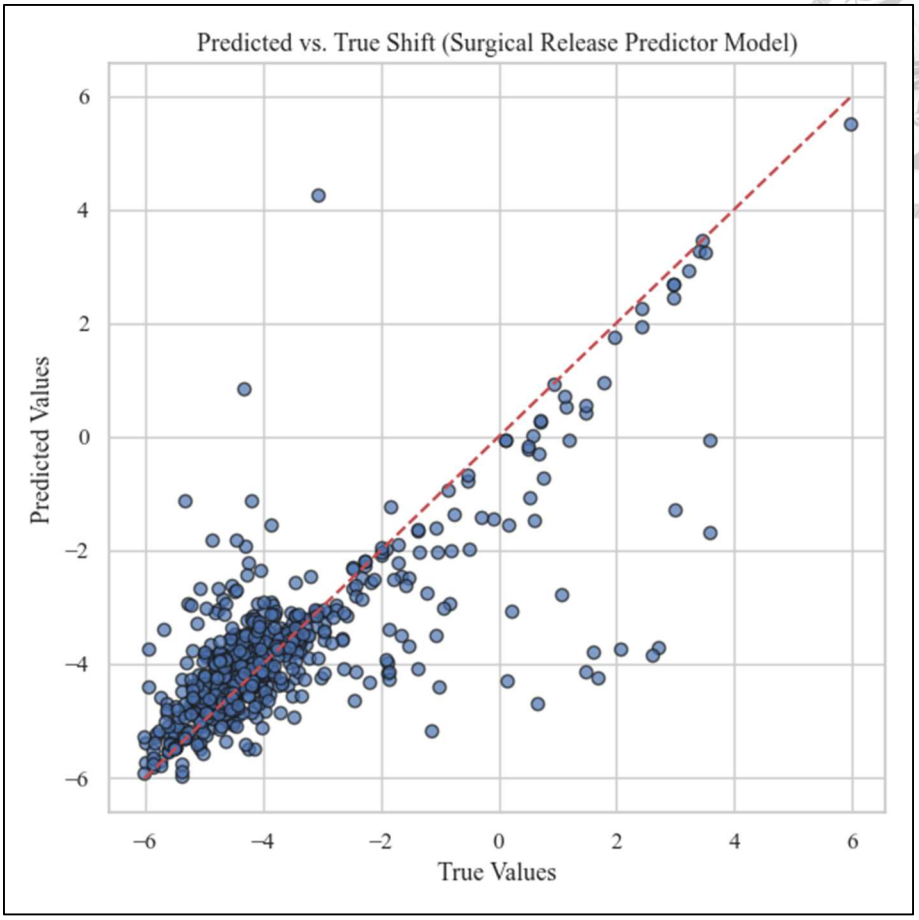

Figure 4-16. Predicted versus true value plot of the surgical release predictor model for patellar shift.

For Figure 4-17, excellent clustering can be observed near the 45° line within the 0 to 20 range. Outliers at higher values indicate that the model encountered difficulties generalizing at these ranges. The figures show that the surgical release predictor model is able to capture the nonlinearity of the patellar kinematic response to ligament stiffness variations and surgical release.

doi:10.6342/NTU202503673

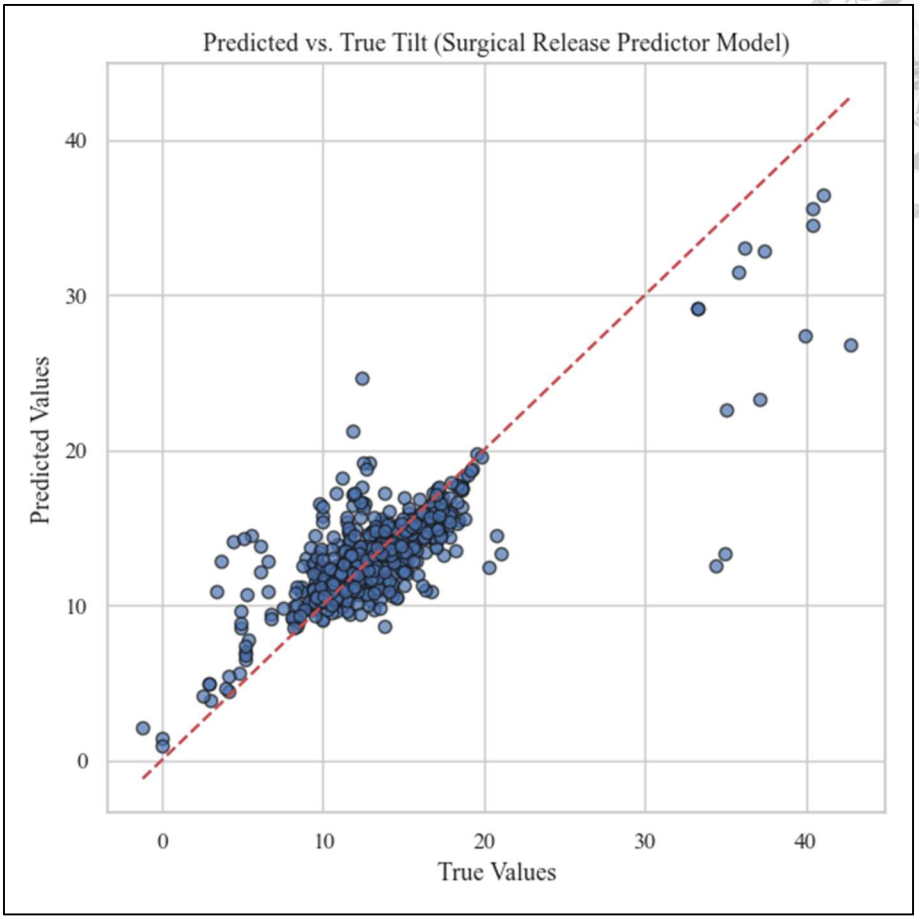

Figure 4-17. Predicted versus true value plot of the surgical release predictor model for patellar tilt.

Figures 4-18 and 4-19 show the residual plots of the surgical release predictor model. For Figure 4-18, tight clustering can be observed in the -6 to -2 range in the predicted axis. However, there is a wide spread in around the -2 value in the predicted axis, this may point to extrapolation error from the model. While there are some outliers, they do not dominate, indicating stable and generalizable predictions.

doi:10.6342/NTU202503673

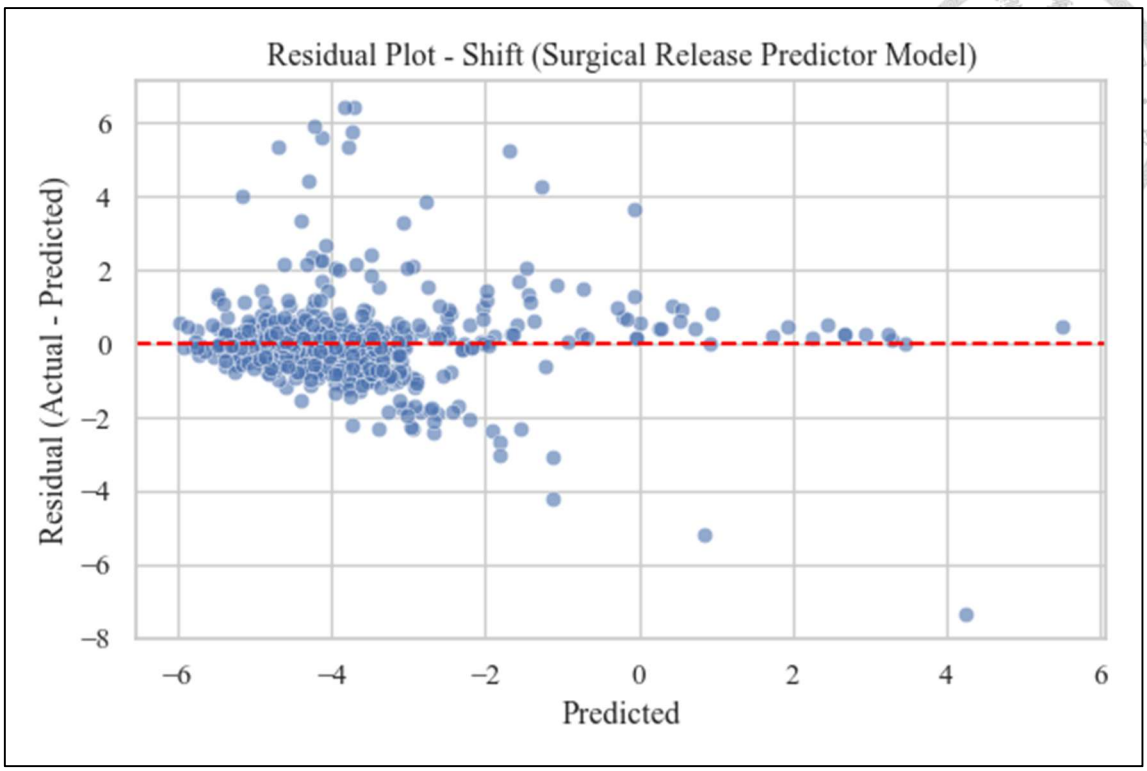

Figure 4-18. Residual plot of the surgical release predictor model for patellar shift.

For Figure 4-19, most of the points are tightly clustered in the 10-20 range in the predicted axis. For most predictions, the model has low residuals. The location of the outliers shows that the model struggles with over- or under-prediction at extreme values. The analysis of Figure 4-19 shows patellar tilt predictions in the surgical release predictor model have more consistency than previous residual plots.

doi:10.6342/NTU202503673

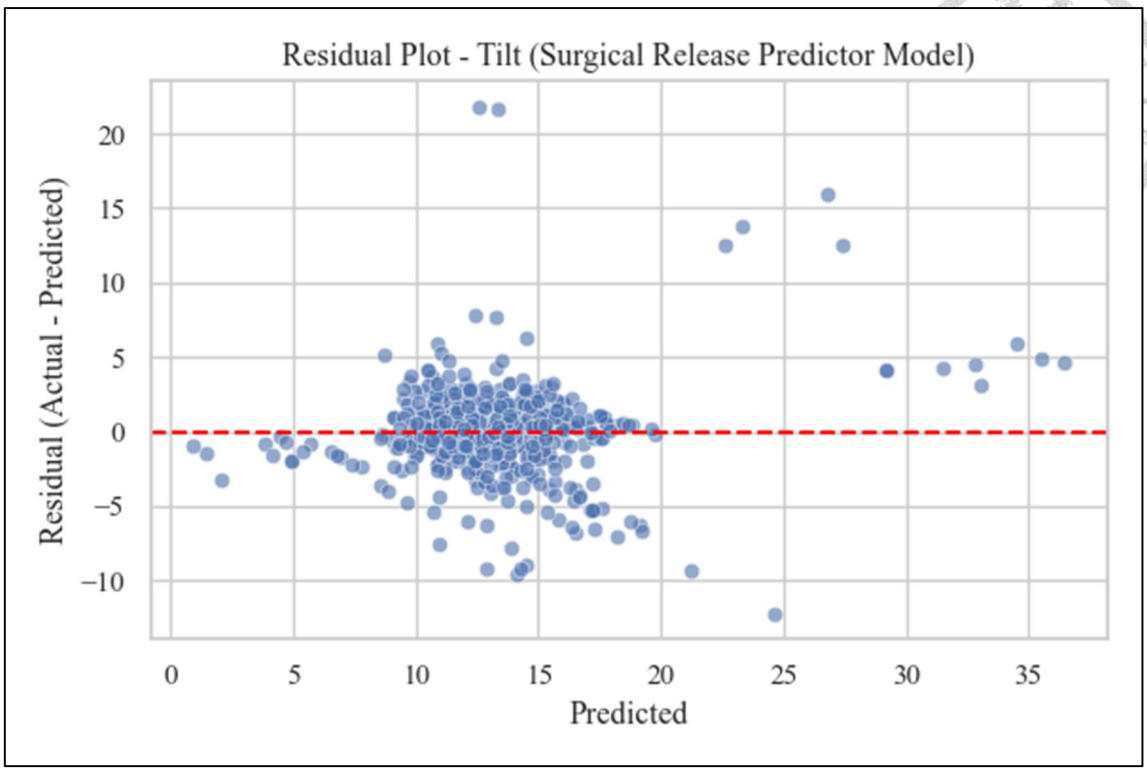

Figure 4-19. Residual plot of the surgical release predictor model for patellar tilt.

The boxplots in Figures 4-20 and 4-21 show the absolute prediction errors of both models, malalignment predictor model and surgical release model, grouped by bins of knee angle. In both models, the surgical release predictor model has better performance than the malalignment predictor model in terms of absolute error in predictions, smaller error ranges, and lower absolute values. The surgical release predictor model has better generalization and does not suffer from underfitting like in the malalignment predictor model

doi:10.6342/NTU202503673

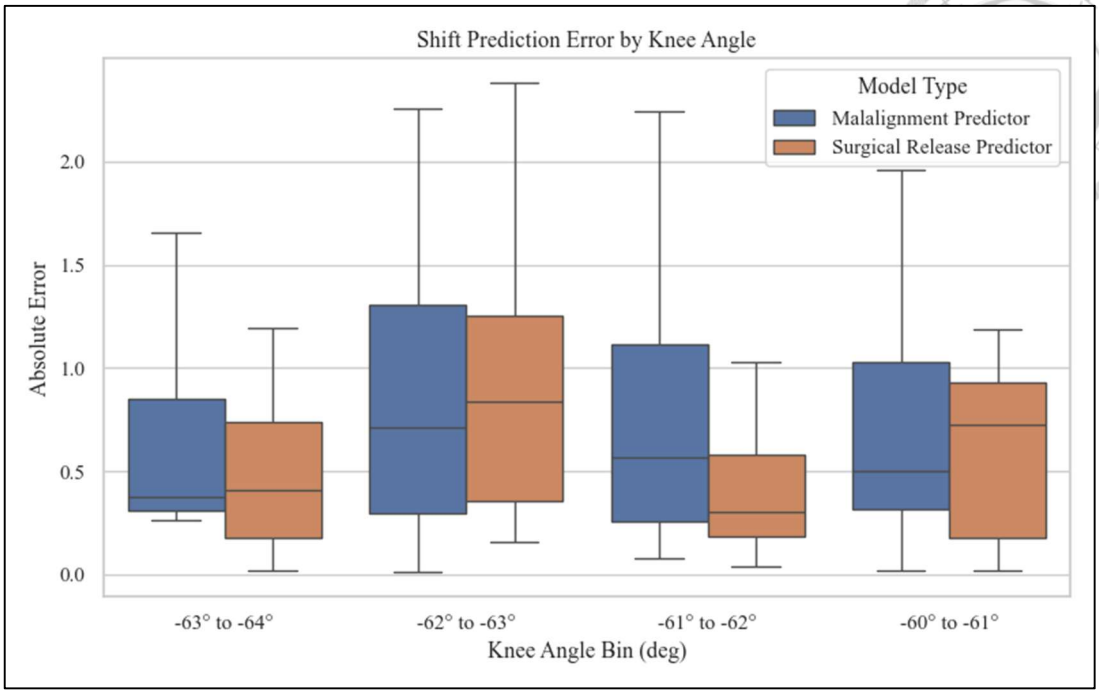

Figure 4-20. Comparison of both models for absolute error in patellar shift predictions across various knee angles.

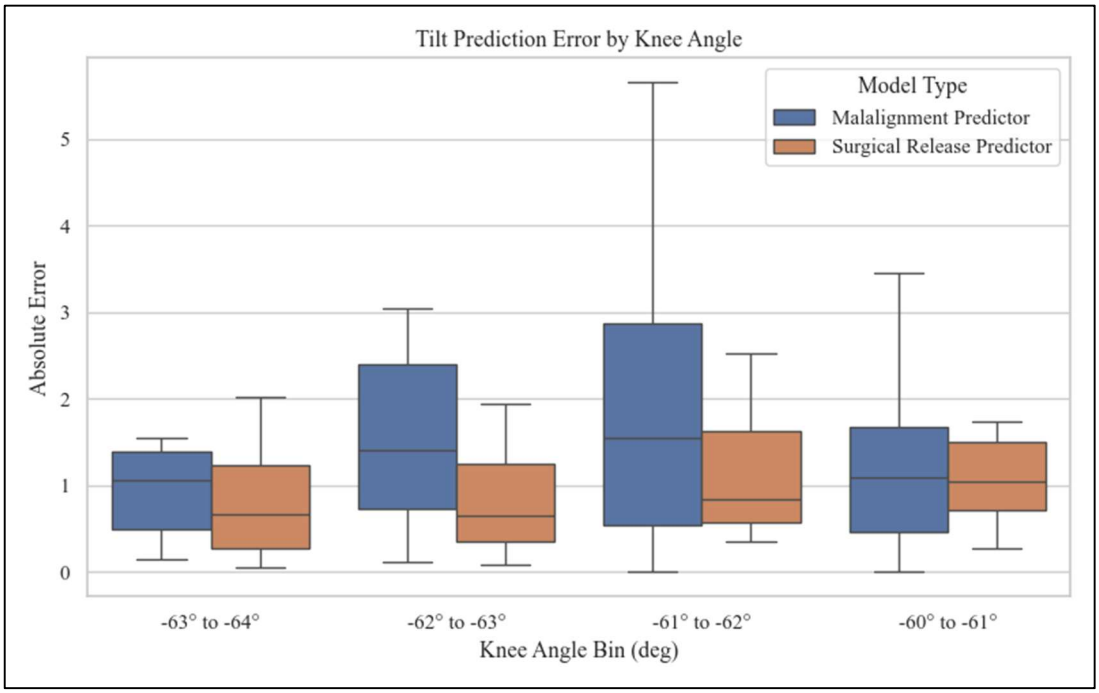

Figure 4-21. Comparison of both models for absolute error in patellar tilt predictions across various knee angles.

doi:10.6342/NTU202503673

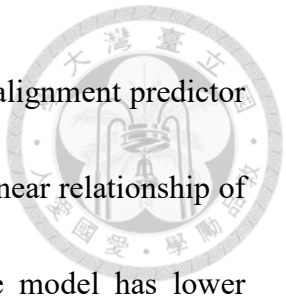

Overall, the surgical release predictor model outperforms the malalignment predictor model. The surgical release predictor model better captures the nonlinear relationship of the data containing kinematic response after surgical release. The model has lower systematic bias, better generalization, and is more consistent with the predictions.

4.5.3 SHAP and Feature Importance Interpretation

The SHapley Additive exPlanations (SHAP) analysis and XGBoost feature importance analysis shows how much each parameter contributes to the prediction and how frequently a parameter is used to split data across decision trees, respectively. Specifically, SHAP analysis interprets causal influence of parameters while XGBoost feature importance assists with model diagnostics but is misleading without SHAP context. Figures 4-22 to 4-29 show the SHAP summary bar plots and XGBoost feature importances plot for the malalignment predictor model. For Figure 4-23, the ligament sLEPL is the most impactful parameter for patellar shift in the model with sMPFL as a secondary, most impactful parameter. This indicates that these two ligaments have the greatest contributions to patellar stability against lateral translation or shift. For Figure 4-25, XGBoost may be underestimating the importance of the parameters as seen by the low importance scores. The underestimation caused a disagreement with the SHAP analysis for patellar shift.

For Figure 4-24, the ligaments sLEPL and sMPFL are the most impactful for predicting

doi:10.6342/NTU202503673

tilt, indicating that cutting these ligaments will introduce an increased lateral tilt. The ligament, Medial Retinaculum 1, also contributes to lateral tilt but with a lesser magnitude. For Figure 4-26, sLTL and iLEPL rank high as being frequently used in XGBoost splits but are not ranked the same in SHAP (Figure 4-24). This shows that these ligaments help create separate subgroups but are not as strong in affecting patellar tilt. Notably, sLEPL appears in SHAP and the feature importance plot, indicating trustworthiness in the ligament influence.

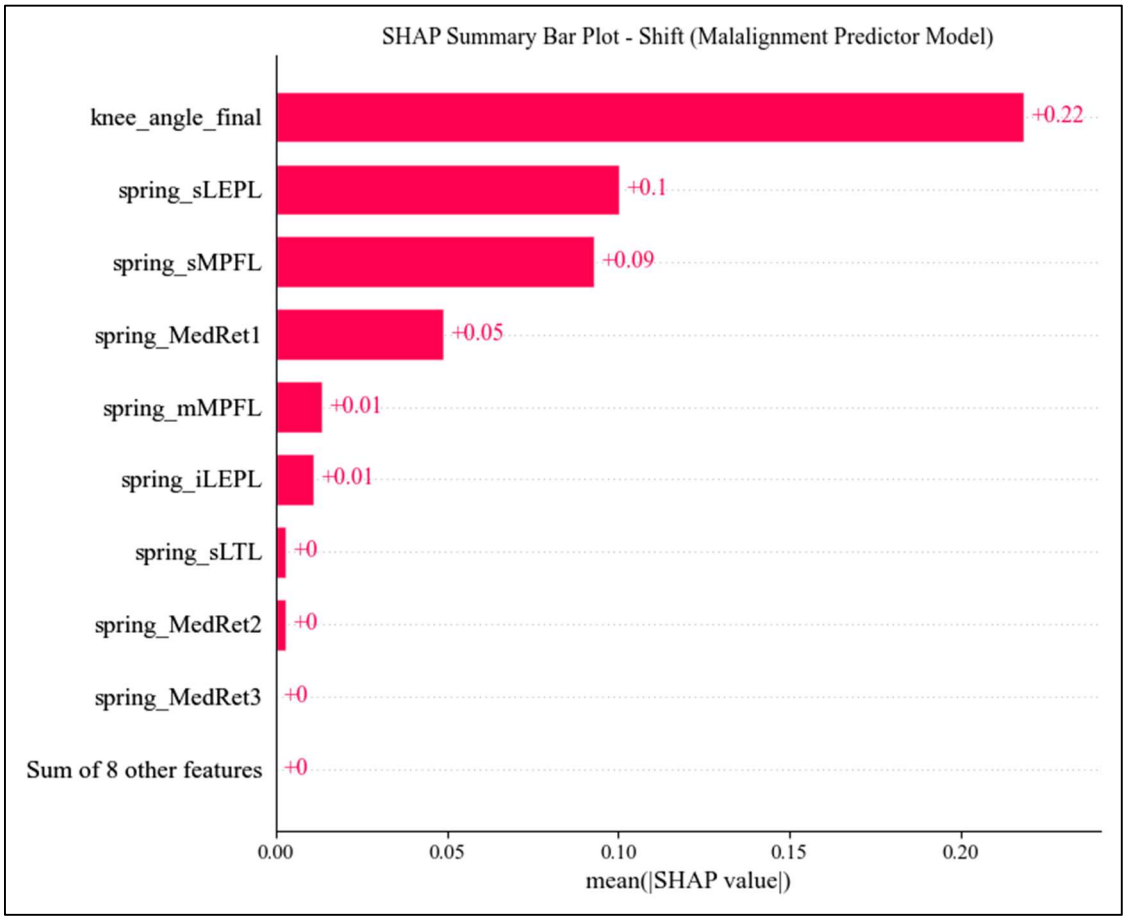

Figure 4-22. SHAP summary bar plot of the malalignment predictor model for patellar shift.

doi:10.6342/NTU202503673

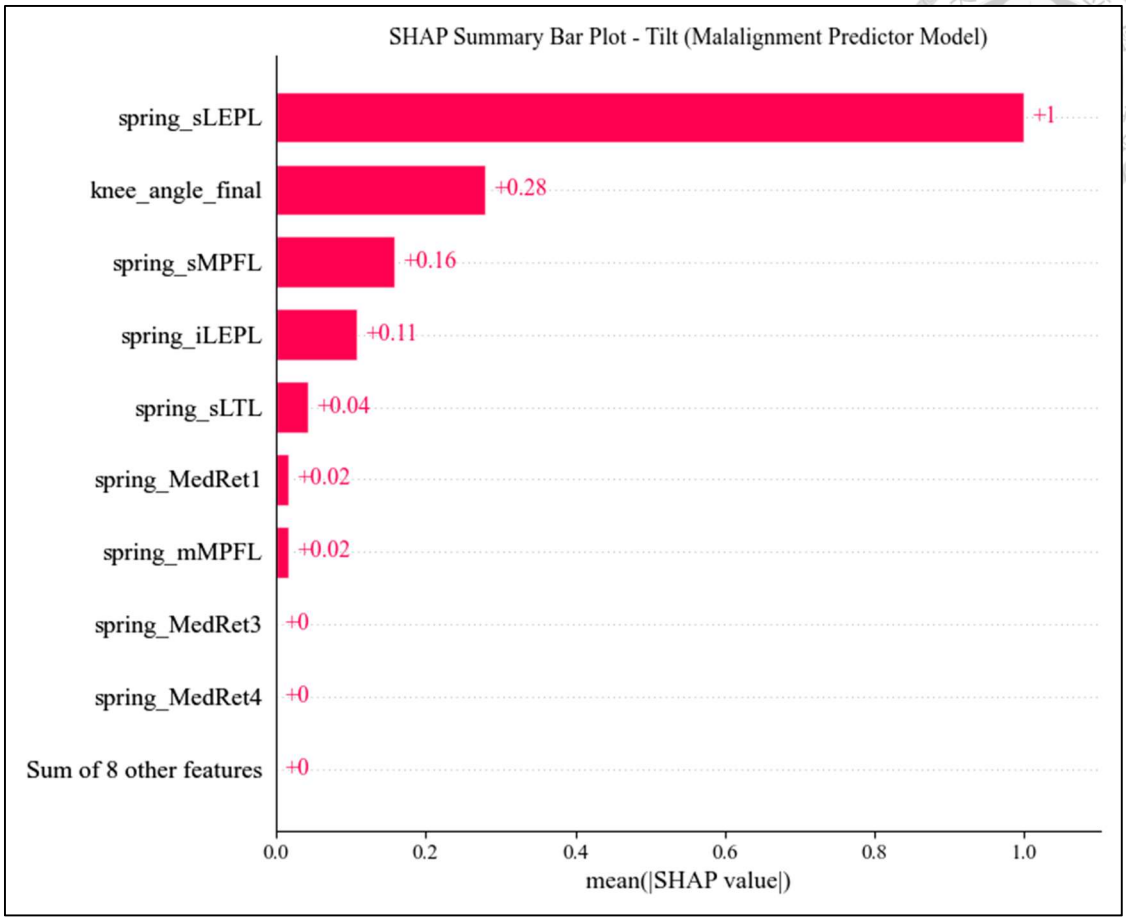

Figure 4-23. SHAP summary bar plot of the malalignment predictor model for patellar tilt.

doi:10.6342/NTU202503673

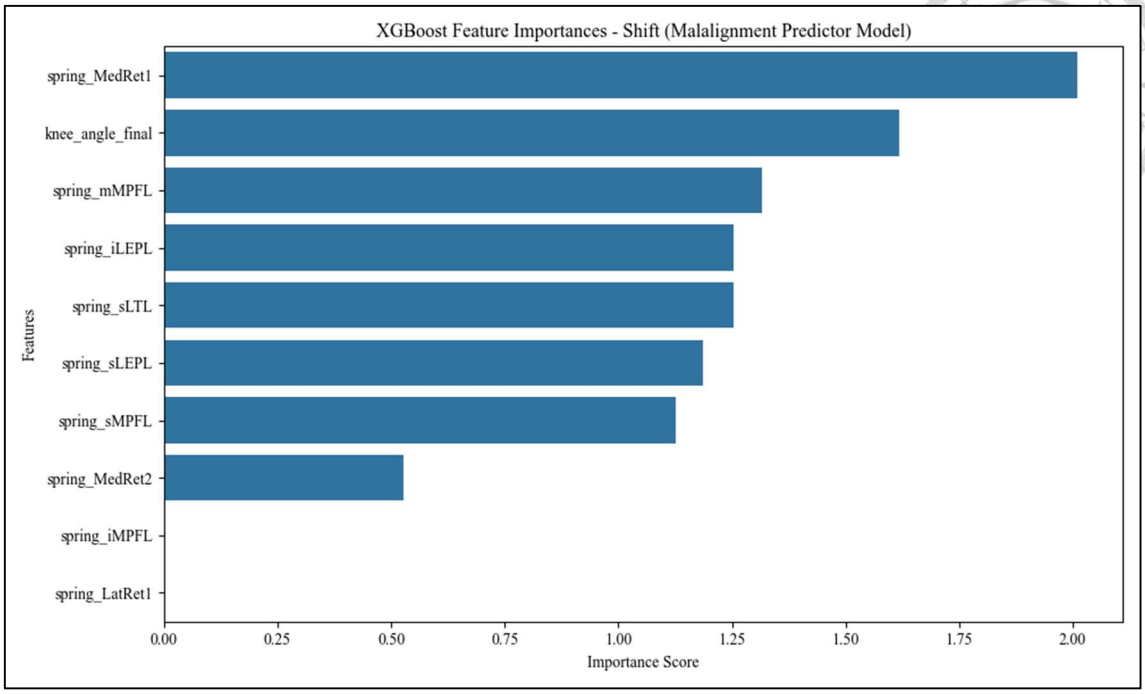

Figure 4-24. XGBoost feature importances plot of the malalignment predictor model for patellar shift.

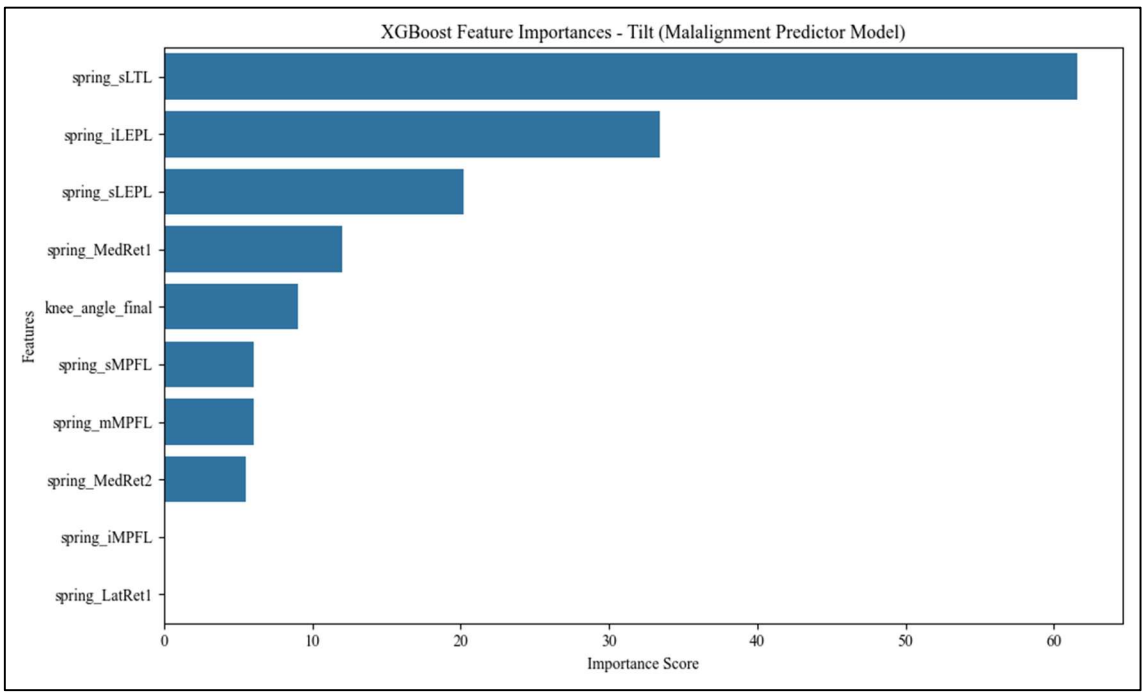

Figure 4-25. XGBoost feature importances plot of the malalignment predictor model for patellar tilt.

doi:10.6342/NTU202503673

Figures 4-27 to 4-30 show the SHAP summary bar plots and XGBoost feature importances plot for the surgical release predictor model. For Figure 4-27, the ligament, Medial Retinaculum 4, has more weight than Medial Retinaculum 1 in this model. Similar to the malalignment predictor model, sLEPL and iLEPL are one of the most important parameters in the model. For Figure 4-30, the SHAP analysis trend matches well; Medial Retinaculum 4 and 3 are key parameters influencing surgical release conditions.

For Figure 4-28, sLEPL and iLEPL are now the dominating parameters while Medial Retinaculum 4 and 3 still have a high influence. For Figure 4-30, iLEPL is ranked high in the feature importance plot, indicating a reliable influence of the parameter. Conversely, sLTL can be seen as the highest in this plot but does not appear so in the SHAP summary bar plot in Figure 4-28. This may point to the importance of the parameter being model-specific instead of a general biomechanical significance.

doi:10.6342/NTU202503673

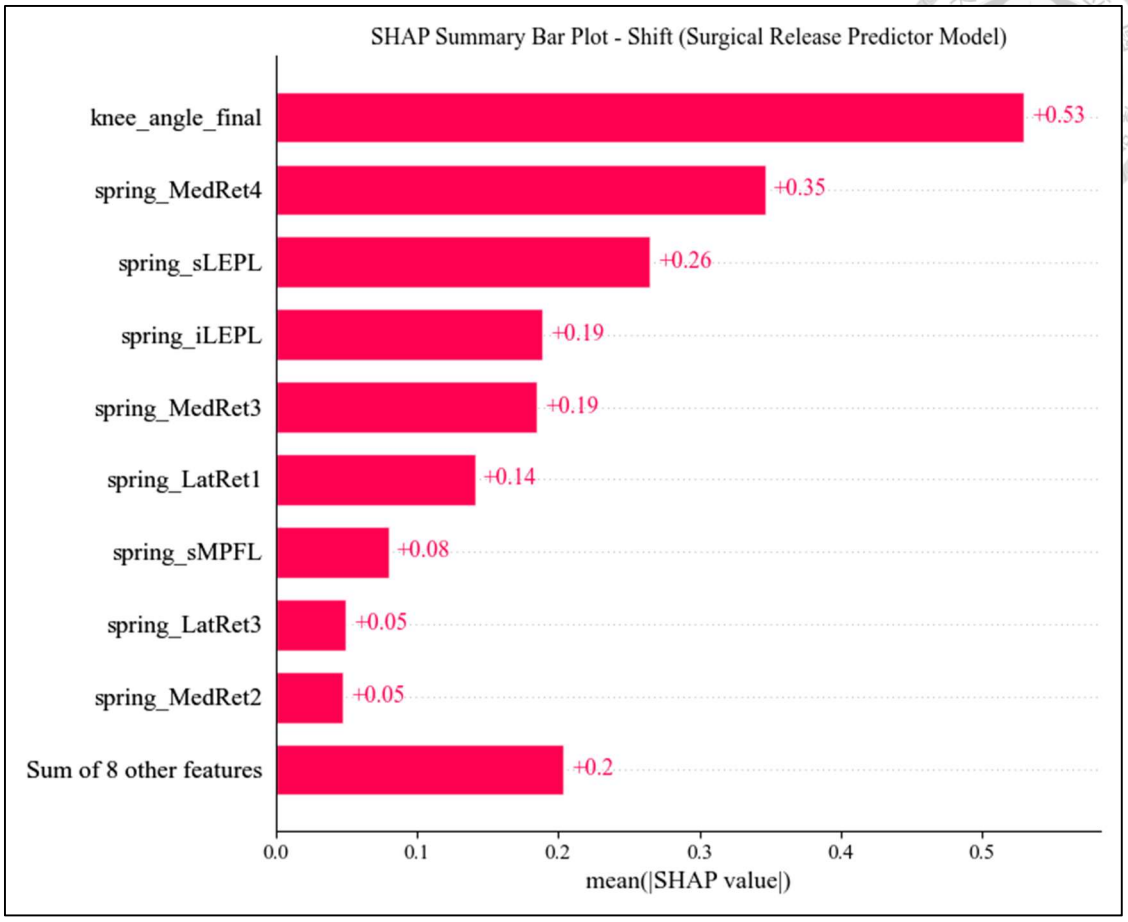

Figure 4-27. SHAP summary bar plot of the surgical release predictor model for patellar shift.

doi:10.6342/NTU202503673

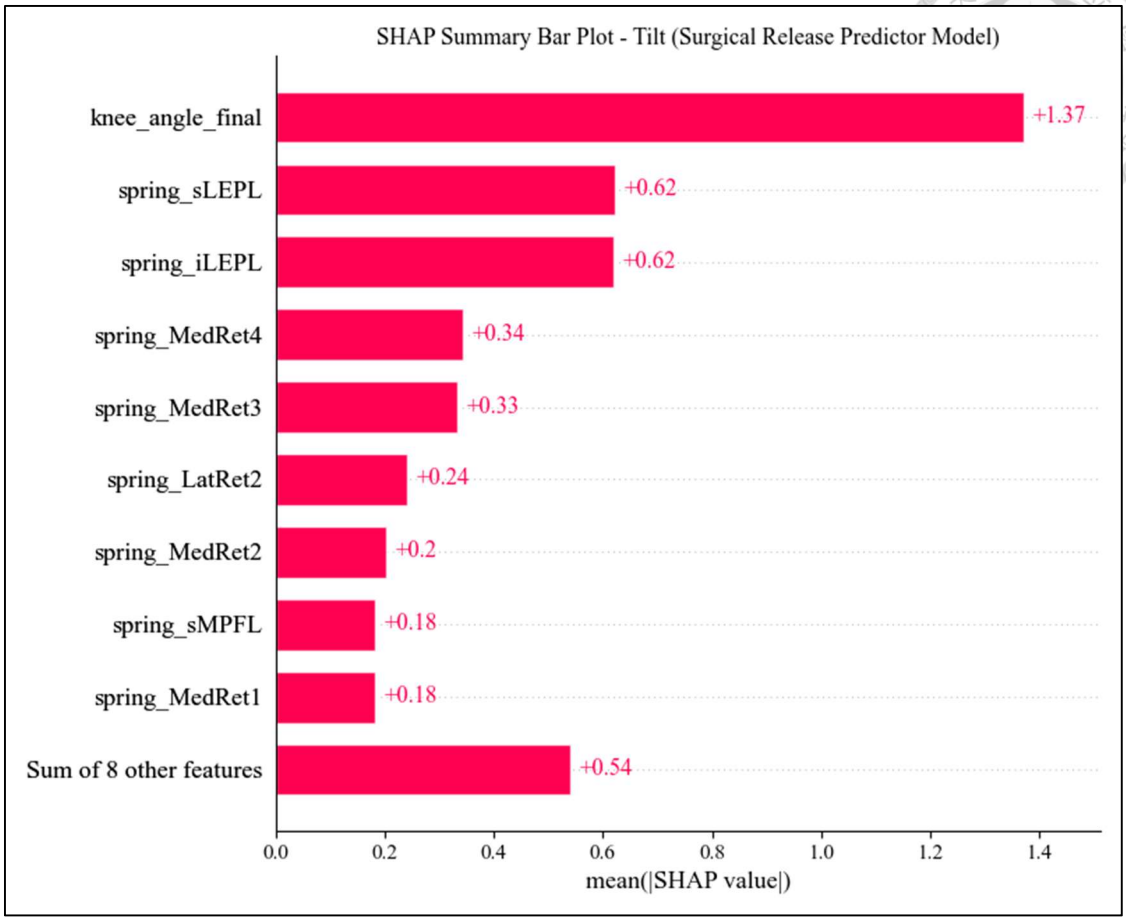

Figure 4-28. SHAP summary bar plot of the surgical release predictor model for patellar tilt.

doi:10.6342/NTU202503673

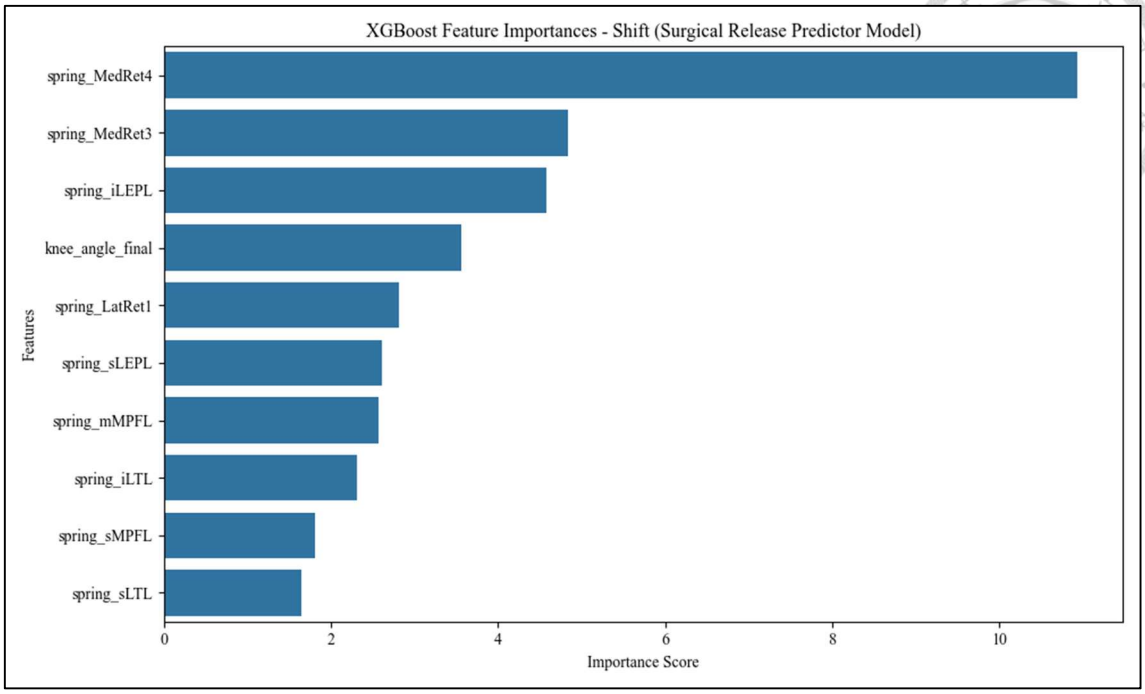

Figure 4-29. XGBoost feature importances plot of the surgical release predictor model for patellar shift.

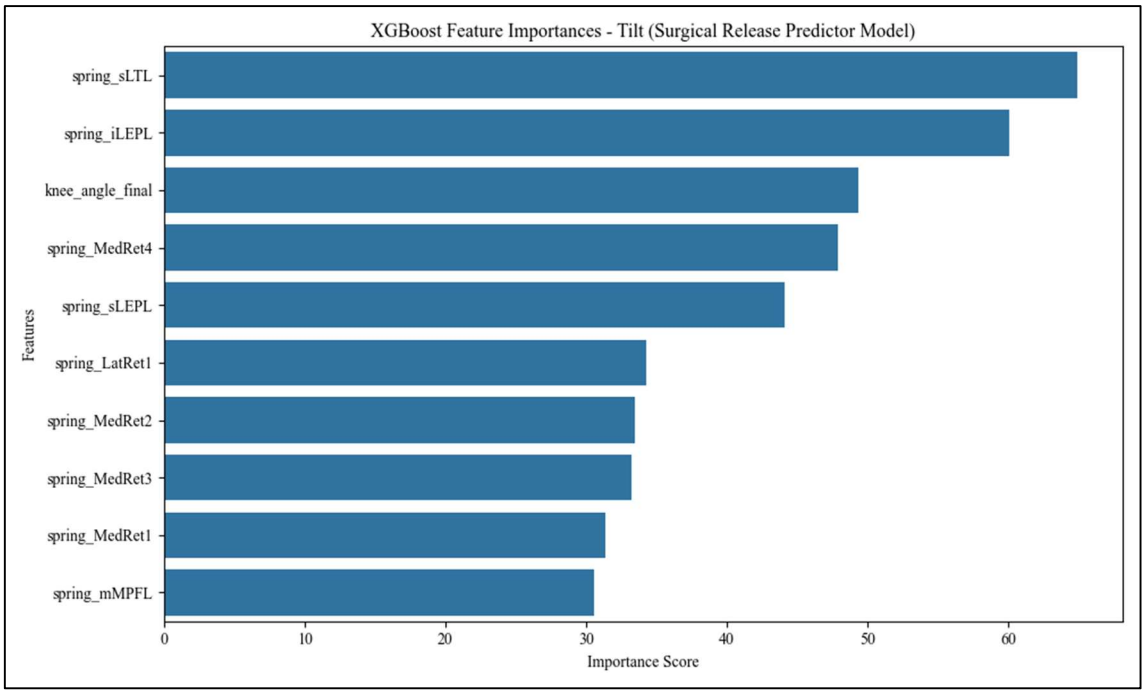

Figure 4-30. XGBoost feature importances plot of the surgical release predictor model for patellar tilt.

doi:10.6342/NTU202503673

Table 4-7 shows the comparison and summary of the key ligament contributions across both the malalignment predictor model and the surgical release predictor model.

Table 4-7. Summary of ligament feature importance across models based on SHAP and XGBoost analyses.

Ligament	Malalignment Predictor Model	Surgical Release Predictor Model	Interpretation
Superior LEPL (sLEPL)	Important in both SHAP and XGBoost analyses	Important in both SHAP and XGBoost analyses	Consistently one of the most influential features
Inferior LEPL (iLEPL)	Important in XGBoost only	Important in both SHAP and XGBoost analyses	Strong influence observed after ligament release
Superior MPFL (sMPFL)	Important in SHAP analysis	Not identified as important	Notable only in the intact condition
Medial Retinaculum 1	Minor importance in both SHAP and XGBoost	Not identified as important	Local influence in the intact condition
Medial Retinaculum 3	Not identified as important	Important in both SHAP and XGBoost analyses	Significant role in post-cut kinematic response
Superior LTL (sLTL)	Important in XGBoost only	Important in XGBoost only	Likely contributing to model decision boundaries

4.5.4 Model-Based Personalization and Surgical Planning for Patellar Malalignment

From the patellar shift and tilt malalignment case caused by tight ligaments in Section 4.3.2, this clinical case presents a simulated patient with a patellar shift of -3.96 mm and

doi:10.6342/NTU202503673

a patellar tilt of 11.02° at knee flexion angle of 60°. This malalignment case is in comparison with a normal (healthy) patellar shift of -3.27 mm and patellar tilt of 15.92° at the same knee flexion angle. There is notable medialization of patellar tilt and slightly medial patellar shift. This malalignment case is not considered pathological, as was discussed in Section 4.3.2.

Using the malalignment predictor model described in Section 3.7, a patient-specific stiffness profile was identified that likely caused the patellar malalignment (Table 4-8). The predicted patient-specific profile shows minor weakening of the superior medial patellofemoral ligament (sMPFL) from 28.68 N/mm to 27.00 N/mm, the middle medial patellofemoral ligament (mMPFL), from 30.17 N/mm to 27.72 N/mm, and the most inferior medial retinaculum (Medial Retinaculum 1), from 0.5 N/mm to 0.43 N/mm. Conversely, the model also predicts tightening of the lateral ligaments. A significant increase in the stiffness of the inferior lateral epicondylopatellar ligament (iLEPL) has been observed: from 16.98 N/mm to 42.19 N/mm. A lesser increase in stiffness is then observed for the following other ligaments: the superior lateral epicondylopatellar ligament (sLEPL), which increased from 16.01 N/mm to 24.22 N/mm, and the superior lateral transverse ligament (sLTL), which increased from 17.95 N/mm to 22.14 N/mm.

doi:10.6342/NTU202503673

Table 4-8. Comparison of ligament spring stiffness profiles across baseline (healthy knee), patient-specific malaligned condition, and the model-recommended surgical release. Values represent spring stiffness in N/mm. Springs highlighted in bold under the surgical release column indicate ligaments selected for release by the model.

Ligament Spring	Baseline (Healthy)	Patient-Specific (Malaligned)	Recommended Surgical Release
sMPFL	28.68	27.00	**0.00**
mMPFL	30.17	27.72	27.72
iMPFL	31.77	31.77	31.77
sLEPL	16.01	24.22	24.22
iLEPL	16.98	42.19	**0.00**
sLTL	17.95	22.14	22.14
mLTL	18.31	18.31	18.31
iLTL	19.47	19.47	19.47
Lateral Retinaculum 1–4	0.5 (each)	0.5 (each)	0.5 (each)
Medial Retinaculum 1	0.5	0.43	**0.00**
Medial Retinaculum 2–4	0.5 (each)	0.5 (each)	0.5 (each)

The malalignment predictor model estimates a patellar shift of -3.29 mm and a patellar shift of 12.33° from the patient-specific stiffness model in Table 4-8. The predicted patellar shift measurement has an absolute deviation of 0.67 mm (16.92% error) compared to the target clinical measurements, while the predicted patellar tilt measurement has an absolute deviation of 1.31° (11.89% error). The surgical release predictor model recommends the following ligaments for release: sMPFL, iLEPL, and Medial Retinaculum 1. The resulting patellar shift and tilt predicted by this model are -4.27 mm and 13.59°, respectively. This corresponds to a patellar shift absolute deviation

doi:10.6342/NTU202503673

of 1.00 mm (30.58% error) and patellar tilt absolute deviation of 2.33° (14.64% error). These results are summarized in Table 4-9.

Table 4-9. Summary of Model Predictions and Deviations from Target Clinical Measurements.

Model	Predicted Shift (mm)	Shift Error	Predicted Tilt (°)	Tilt Error	Recommended Ligaments for Release
Malalignment Predictor	–3.29	0.67 mm (16.92%)	12.33	1.31° (11.89%)	—
Surgical Release Predictor	–4.27	1.00 mm (30.58%)	13.59	2.33° (14.64%)	sMPFL, iLEPL, Medial Retinaculum 1

The limitations of the predictive models were previously discussed in Section 4.5.1. Although their predictive ability can still be improved, the models, as part of the digital twin framework, are functional proofs of concept that demonstrate the clinical utility of model-based personalization and decision support during patellar malalignment or maltracking correction.

4.6 Supporting Results: Point Cloud Transformations

4.6.1 Transformed Femur Point Cloud

The raw point cloud data were reconstructed using the transformations post-experiment. Verification of the point cloud transformation results were performed by visual inspection. Figure 4-31 shows the result of the transformation process for the raw

doi:10.6342/NTU202503673

femur point cloud data. The different colors of the point clouds refer to individual files which store one anatomical landmark or bony contour point cloud. The raw femur point cloud data shows the effects of coordinate slide, resulting in shifted anatomical landmarks and contour data. Reconstruction reveals the recognizable geometry of the distal femur in the inferosuperior (IS) view. Reconstruction also shows the outliers collected during the experiment.

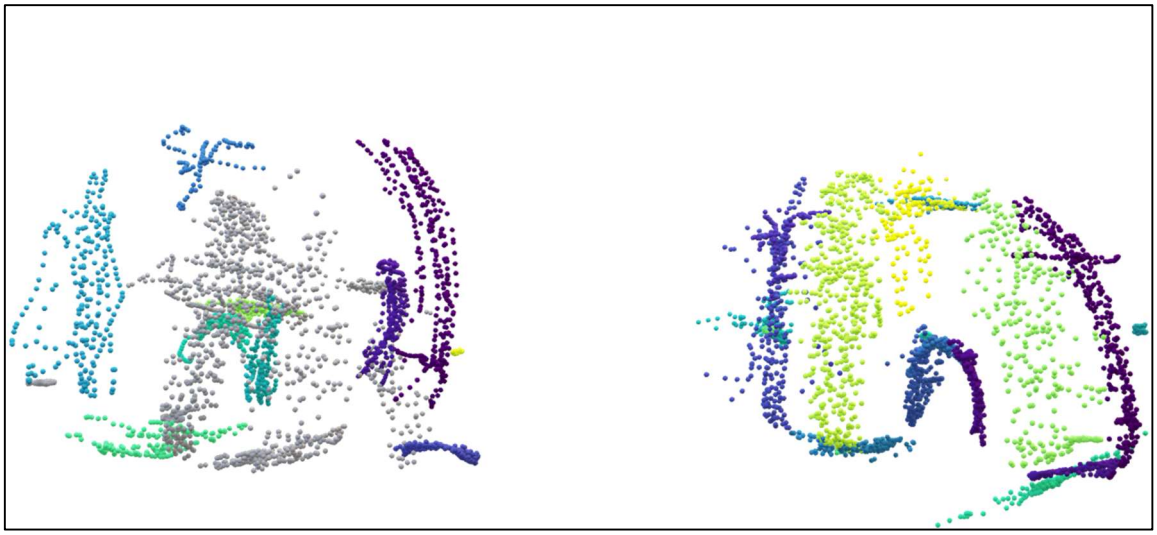

Figure 4-31. Transformed femur point cloud. *Left*: raw femur point cloud. *Right*: reconstructed femur point cloud.

4.6.2 Transformed Tibia Point Cloud

The collected point cloud data for the tibia are predominantly located at the proximal surface, therefore 3D information of the tibia morphology are from the tibia surface within a single plane. In Figure 4-32, the raw tibia point cloud appears that the bony contour data are in different planes not level with one another. This phenomenon is

doi:10.6342/NTU202503673

corrected after reconstruction. However, due to the tibia point cloud data containing mostly surface data, it is difficult to recognize the tibia geometry. Outlier data is also observable as the scattered points and the contour point cloud that are significantly far from the clustered point cloud data post-reconstruction. These outliers are further processed and removed during the determination of anatomical coordinate systems.

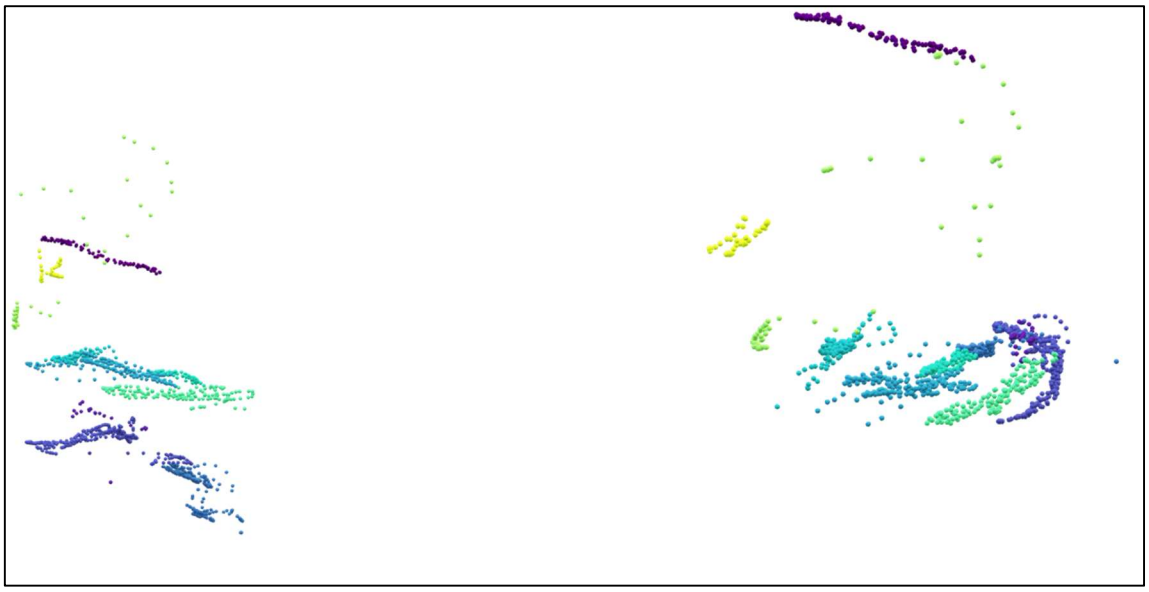

Figure 4-32. Transformed tibia point cloud. *Left*: raw tibia point cloud. *Right*: reconstructed tibia point cloud.

4.6.3 Transformed Patella Point Cloud

Figure 4-33 shows the transformed patella point cloud. Reconstruction of the patella point cloud shows correction of the patella margin contour—the outer border of the patella—and the point clouds corresponding to the facets of the patella are now enclosed within the contours of the patella margin. The recorded patella point cloud also shows

doi:10.6342/NTU202503673

numerous outliers, particularly in the patella margin contour point cloud. These unwanted data will be removed later during the process of defining the anatomical coordinate system.

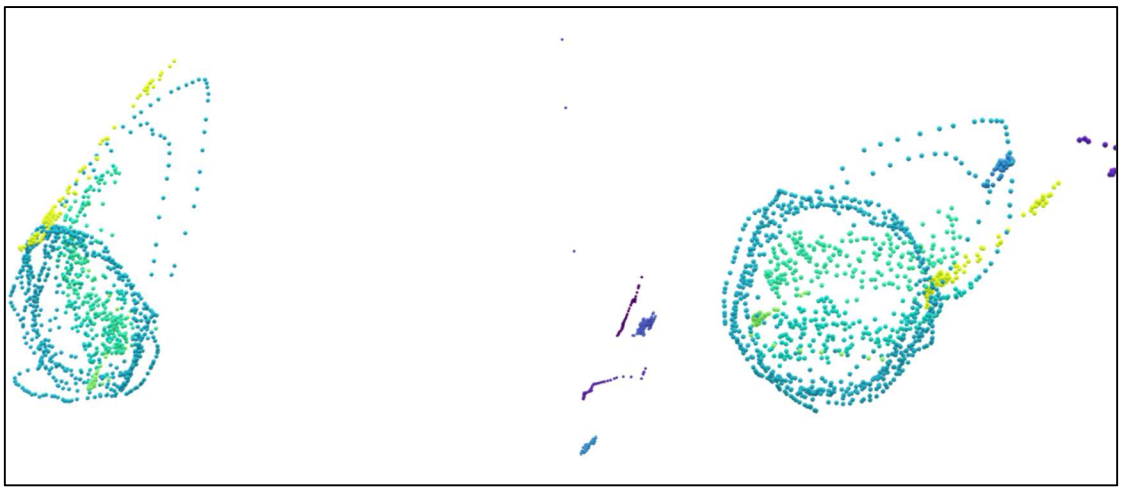

Figure 4-33. Transformed patella point cloud. *Left*: raw patella point cloud. *Right*: reconstructed patella point cloud.

doi:10.6342/NTU202503673

Chapter 5: Conclusions

5.1 Conclusions

This study proposed and validated a patient-specific digital twin framework for simulating patellar tracking and providing decision support during surgical interventions for patellar malalignment and maltracking. The digital twin system integrates multiple computational techniques and some novel: subset-based registration (SBR) method, statistical shape modeling (SSM), SBR-driven SSM deformation, finite element (FE) modeling and surgical simulation, and machine learning models. These techniques reconstruct knee joint anatomy, simulate surgical intervention, and predict optimal surgical strategies.

A novel 2D-3D shape reconstruction technique was developed, the SBR-driven SSM deformation. Using limited 2D fluoroscopy X-rays as inputs, the novel reconstruction technique enables the generation of 3D anatomical models. This method was validated on cadaver data and is geometrically compatible with the FE model pipeline, with regard to the structure, mesh quality, and individual anatomical realism. The 2D-3D shape reconstruction technique developed in this study is feasible for surgical planning workflows without requiring CT imaging. This reduces patient exposure to unnecessary radiation.

A comprehensive FE model of the knee joint was also developed. The FE model was

doi:10.6342/NTU202503673

specifically tuned for dynamic simulations that enable realistic modeling of knee joint kinematics and ligament release scenarios. The parameters used were selected to be as generalizable as possible when patient-specific data cannot be obtained. Different surgical release scenarios were investigated. Specific release combinations that best corrected patellar shift and tilt were identified. From a qualitative analysis perspective, a partial medial retinacular (MR) release of around 25%-50% in the superior-to-inferior (SI) direction was the most effective patellar shift correction, especially when combined with lateral retinacular (LR) release. For correcting patellar tilt, partial MR release (25%) in the SI direction is also the most effective in restoring patellar tilt mobility without introducing lateral instability. From a quantitative analysis perspective, 75% LR release in the SI direction yielded the best patellar malalignment correction, while partial (25%) LPFL release yielded the best patellar tracking correction. Within the specific context of this study, targeted release of the ligaments is more important in correcting patellar shift and tilt tracking to avoid over-release and introducing postoperative complications.

To complement the FE model and enable rapid predictions, two supervised machine learning models were developed: the malalignment predictor and the surgical release predictor. The former estimates patellar alignment based on ligament stiffness profiles, while the latter estimates postoperative patellar alignment outcomes. The SHAP and XGBoost feature importance analyses identified the pivotal role in patellar stability of the

doi:10.6342/NTU202503673

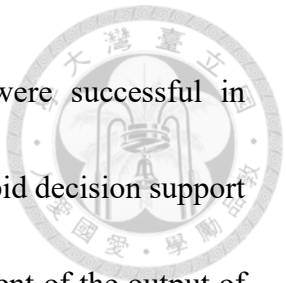

sLEPL and iLEPL (contextual). The machine learning models were successful in delineating key ligament features impacting patellar alignment for rapid decision support regarding targeted release. This was further supported by the alignment of the output of the predictive models with clinical observations. It is also acknowledged that model parameters and outcomes are patient-specific, which may limit the generalizability of the currently obtained results of the FE model and the machine learning models.

The cadaver study provided an opportunity to observe the effects of surgical release on patellar kinematics. The study served as an initial benchmark reference for the FE model surgical simulations. Quantitative reliability was significantly compromised due to patella bone marker loss. The qualitative comparisons, such as for the postoperative patellar tracking after full bilateral (medial and lateral) release scenario, were constrained due to data estimation following the bone marker loss. This loss of bone marker data required data recovery measures, which were transformations to reconstruct data by approximation. This introduced nontrivial assumptions that affected anatomical accuracy and inter-frame measurement consistency. As a consequence, caution must be applied when interpreting the cadaver study results, which may not be comparable to the FE simulation or literature benchmarks.

In summary, the proposed digital twin framework exhibits significant potential in guiding patellofemoral surgical interventions such as lateral release. The digital twin has

doi:10.6342/NTU202503673

the capability to simulate and quantify the patellofemoral kinematic response following various release strategies, establishing a foundation for more personalized and data-driven lateral release surgical planning. This proposed system can enhance surgical outcomes while reducing postoperative complications in treating patellar maltracking.

5.2 Recommendations

5.2.1 Clinical Data Integration

For better predictions by the digital twin, large datasets of intraoperative and postoperative patellar kinematics must be acquired to support real-time parameter adaptation capabilities of the digital twin system. This can also improve the generalizability of the model by using actual patient data compared to simply acquiring data from FE simulations.

5.2.2 Improved Anatomical Fidelity

The SBR method and the SBR-driven SSM reconstruction pipeline should be enhanced for better representation of individual knee joint anatomy. This is to increase the application of the pipeline for high-precision cases. It is also possible to replace this method with existing state-of-the-art 2D-3D shape reconstruction methods to comply with the current standards used by the scientific community.

doi:10.6342/NTU202503673

5.2.3 Model Generalizability

Future work must aim for the FE model to be able to work with multiple different patient anatomies. The FE model system must be further validated against more clinical cases to enhance its clinical relevance.

5.2.4 Experimental Study Robustness

The mistakes reported in this study regarding the cadaver study emphasize the need to establish more robust cadaver experiment protocols to serve as an experimental benchmark for the digital twin system.

5.2.5 Automation and Clinical UI

The current digital twin requires extensive manual intervention, which may be difficult during clinical deployment, such as in a surgical scenario. Automating the pipeline and developing a user interface would significantly improve the usability of the digital twin system for surgical planning and simulation.

doi:10.6342/NTU202503673

References

[1] Matz, J., B. A. Lanting, and J. L. Howard. 2019. Understanding the patellofemoral joint in total knee arthroplasty. Can. J. Surg. 62(1): 57–65.

[2] Grelsamer, R. P., and C. H. Weinstein. 2001. Applied biomechanics of the patella. Clin. Orthop. Relat. Res. 389: 9–14.

[3] Feller, J. A., A. A. Amis, J. T. Andrish, E. A. Arendt, P. J. Erasmus, and C. M. Powers. 2007. Surgical biomechanics of the patellofemoral joint. Arthroscopy 23(5): 542–553.

[4] Berton, A., G. Salvatore, A. Orsi, J. Egan, J. DeAngelis, A. Ramappa, U. G. Longo, A. Nazarian, and V. Denaro. 2022. Lateral retinacular release in concordance with medial patellofemoral ligament reconstruction in patients with recurrent patellar instability: A computational model. The Knee 39: 308–318.

[5] Thomeer, L. T., Y. C. Lin, and M. G. Pandy. 2020. Load distribution at the patellofemoral joint during walking. Ann. Biomed. Eng. 48(10): 2821–2835.

[6] Felli, L., S. Lovisolo, A. G. Capello, F. Chiarlone, M. Formica, and M. Alessio-Mazzola. 2019. Arthroscopic lateral retinacular release and modified Goldthwait technique for patellar instability. Arthrosc. Tech. 8(11): e1295–e1299.

[7] Wu, C. 2023. Patellar malalignment: A common disorder associated with knee pain. Biomed. J. 46(5): 100658.

[8] Moatshe, G., T. R. Cram, J. Chahla, M. E. Cinque, J. A. Godin, and R. F. LaPrade. 2017. Medial patellar instability: Treatment and outcomes. Orthop. J. Sports Med. 5(4): 1–7.

[9] Wheatley, M. G., M. J. Rainbow, and A. L. Clouthier. 2020. Patellofemoral mechanics: a review of pathomechanics and research approaches. Curr. Rev. Musculoskelet. Med. 13(3): 326–337.

[10] Yu, Z., J. Yao, X. Wang, X. Xin, K. Zhang, H. Cai, and B. Yang. 2019. Research methods and progress of patellofemoral joint kinematics: A review. Journal of Healthcare Engineering. 2019(1): 9159267.

[11] Greiwe, R. M., C. Saifi, C. S. Ahmad, and T. R. Gardner. 2010. Anatomy and biomechanics of patellar instability. Operative Tech. in Sports Med. 18(2): 62–67.

[12] Smith, P. N., K. M. Refshauge, and J. M. Scarvell. 2003. Development of the concepts of knee kinematics. Arch. Phys. Med. Rehabil. 84(12): 1895–1902.

[13] Panni, A. S., M. Tartarone, A. Patricola, E. W. Paxton, and D. C. Fithian. 2005. Long-term results of lateral retinacular release. Arthroscopy 21(5): 526–531.

[14] Pohlig, F., U. Lenze, F. W. Lenze, I. Lazic, A. Haug, S. Hinterwimmer, and R. von Eisenhart-Rothe. 2022. Arthroscopic lateral retinacular release improves patello-

doi:10.6342/NTU202503673

femoral and femoro-tibial kinematics in patients with isolated lateral retinacular tightness. Knee Surgery, Sports Traumatology, Arthroscopy 30(3): 791–799.

[15] Thompson, P., and A. J. Metcalfe. 2019. Current concepts in the surgical management of patellar instability. The Knee 26(6): 1171–1181.

[16] Frosch, K. H., and A. Schmeling. 2016. A new classification system of patellar instability and patellar maltracking. Arch. Orthop. Trauma Surg. 136(4): 485–497.

[17] Bjelland, Ø., B. Rasheed, H. G. Schaathun, M. D. Pedersen, M. Steinert, A. I. Hellevik, and R. T. Bye. 2022. Toward a digital twin for arthroscopic knee surgery: A systematic review. IEEE Access. 10: 45029–45052.

[18] Dean, M. C., J. F. Oeding, P. Diniz, R. Seil, K. Samuelsson, and ESSKA Artificial Intelligence Working Group. 2024. Leveraging digital twins for improved orthopaedic evaluation and treatment. Journal of Experimental Orthopaedics 11(4): e70084.

[19] Sun, T., J. Wang, M. Suo, X. Liu, H. Huang, J. Zhang, and Z. Li. 2023. The digital twin: A potential solution for the personalized diagnosis and treatment of musculoskeletal system diseases. Bioengineering 10(6): 627.

[20] Sun, T., X. He, and Z. Li. 2023. Digital twin in healthcare: Recent updates and challenges. Digital Health 9(0): 20552076221149651.

[21] Sahal, R., S. H. Alsamhi, and K. N. Brown. 2022. Personal digital twin: A close look into the present and a step towards the future of personalised healthcare industry. Sensors 22(15): 5918.

[22] Zheng, G., and W. Yu. 2017. Statistical shape and deformation models based 2D–3D reconstruction. Statistical Shape and Deformation Analysis 1(0): 329–349.

[23] Vasiliadis, A. V., Giovanoulis, V., Maris, A., Chytas, D., Katakalos, K., Paraskevas, G., ... and Vassiou, A. (2024). Finite element analysis of the knee joint: a computational tool to analyze the combined behavior after treatment of torn ligaments and menisci in the human knee joint. SICOT-J, 10, 45.

[24] Kheir, N., Salvatore, G., Berton, A., Orsi, A., Egan, J., Mohamadi, A., ... and Nazarian, A. (2022). Lateral release associated with MPFL reconstruction in patients with acute patellar dislocation. BMC Musculoskeletal Disorders, 23(1), 139.

[25] Schindler, O. S., and W. N. Scott. 2011. Basic kinematics and biomechanics of the patello-femoral joint. Part 1: The native patella. Acta Orthop. Belg. 77(4): 421–426.

[26] Grelsamer, R. P., and J. R. Klein. 1998. The biomechanics of the patellofemoral joint. J. Orthop. Sports Phys. Ther. 28(5): 286–298.

[27] Migliorini, F., N. Maffulli, J. Eschweiler, V. Quack, M. Tingart, and A. Driessen. 2021. Lateral retinacular release combined with MPFL reconstruction for patellofemoral instability: A systematic review. Arch. Orthop. Trauma Surg. 141: 283–292.Pohlig, F., Lenze, U., Lenze, F. W., Lazic, I., Haug, A., Hinterwimmer, S., ... and von Eisenhart-Rothe, R. (2022). Arthroscopic lateral retinacular release improves

doi:10.6342/NTU202503673

patello-femoral and femoro-tibial kinematics in patients with isolated lateral retinacular tightness. Knee Surgery, Sports Traumatology, Arthroscopy, 30(3), 791-799.

[28] Siljander, B., Tompkins, M., and Martinez-Cano, J. P. (2022). A review of the lateral patellofemoral joint: Anatomy, biomechanics, and surgical procedures. JAAOS Global Research & Reviews, 6(7), e21.

[29] Wang, C. L., Chen, J. B., and Li, T. (2021). Outcome and experience of arthroscopic lateral retinacular release combined with lateral patelloplasty in the management of excessive lateral pressure syndrome. Journal of Orthopaedic Surgery and Research, 16, 1-7.

[30] Fonseca, L. P. R. M. D., E. H. Kawatake, and A. D. C. Pochini. 2017. Lateral patellar retinacular release: Changes over the last ten years. Rev. Bras. Ortop. 52: 442–449.

[31] Nagamine, R., T. Otani, S. E. White, D. S. McCarthy, and L. A. Whiteside. 1995. Patellar tracking measurement in the normal knee. J. Orthop. Res. 13(1): 115–122.

[32] Amis, A. A., W. Senavongse, and A. M. Bull. 2006. Patellofemoral kinematics during knee flexion-extension: an in vitro study. J. Orthop. Res. 24(12): 2201–2211.

[33] MacIntyre, N. J., N. A. Hill, R. A. Fellows, R. E. Ellis, and D. R. Wilson. 2006. Patellofemoral joint kinematics in individuals with and without patellofemoral pain syndrome. JBJS 88(12): 2596–2605.

[34] Pal, S., T. F. Besier, G. S. Beaupre, M. Fredericson, S. L. Delp, and G. E. Gold. 2013. Patellar maltracking is prevalent among patellofemoral pain subjects with patella alta: an upright, weightbearing MRI study. J. Orthop. Res. 31(3): 448–457.

[35] Pal, S., C. E. Draper, M. Fredericson, G. E. Gold, S. L. Delp, G. S. Beaupre, and T. F. Besier. 2011. Patellar maltracking correlates with vastus medialis activation delay in patellofemoral pain patients. Am. J. Sports Med. 39(3): 590–598.Greiwe, R. M., Saifi, C., Ahmad, C. S., and Gardner, T. R. (2010). Anatomy and biomechanics of patellar instability. Operative Techniques in Sports Medicine, 18(2), 62-67.

[36] LLopis, E., and M. Padrón. 2007. Anterior knee pain. Eur. J. Radiol. 62(1): 27–43.

[37] Petersen, W., A. Ellermann, A. Gösele-Koppenburg, R. Best, I. V. Rembitzki, G. P. Brüggemann, and C. Liebau. 2014. Patellofemoral pain syndrome. Knee Surg. Sports Traumatol. Arthrosc. 22(10): 2264–2274.

[38] Dixit, S., J. P. Difiori, M. Burton, and B. Mines. 2007. Management of patellofemoral pain syndrome. Am. Fam. Physician. 75(2): 194–202.

[39] Gaitonde, D. Y., A. Ericksen, and R. C. Robbins. 2019. Patellofemoral pain syndrome. Am. Fam. Physician. 99(2): 88–94.

[40] Mizuno, Y., M. Kumagai, S. M. Mattessich, J. J. Elias, N. Ramrattan, A. J. Cosgarea, and E. Y. Chao. 2001. Q-angle influences tibiofemoral and patellofemoral kinematics. J. Orthop. Res. 19(5): 834–840.

doi:10.6342/NTU202503673

[41] Dejour, H., Walch, G., Nove-Josserand, L., and Guier, C. H. (1994). Factors of patellar instability: an anatomic radiographic study. Knee Surgery, Sports Traumatology, Arthroscopy, 2, 19-26.

[42] Ricchetti, E. T., S. Mehta, B. J. Sennett, and G. R. Huffman. 2007. Comparison of lateral release versus lateral release with medial soft-tissue realignment for the treatment of recurrent patellar instability: A systematic review. Arthroscopy 23(5): 463–468.

[43] Small, N. C. 1989. An analysis of complications in lateral retinacular release procedures. Arthroscopy 5(4): 282–286.

[44] Li, M., Z. Shao, Q. Liu, and G. Cui. 2023. Lateral retinacular release for treatment of excessive lateral pressure syndrome: The capsule-uncut immaculate (CUI) technique. Arthrosc. Tech. 12(11): e1991–e1996.

[45] Hinckel, B. B., and E. A. Arendt. 2015. Lateral retinaculum lengthening or release. Oper. Tech. Sports Med. 23(2): 100–106.

[46] Christoforakis, J., A. M. J. Bull, R. K. Strachan, R. Shymkiw, W. Senavongse, and A. A. Amis. 2006. Effects of lateral retinacular release on the lateral stability of the patella. Knee Surg. Sports Traumatol. Arthrosc. 14: 273–277.

[47] Tjoumakaris, F. P., B. Forsythe, and J. P. Bradley. 2010. Patellofemoral instability in athletes: Treatment via modified Fulkerson osteotomy and lateral release. Am. J. Sports Med. 38(5): 992–999.

[48] Marra, M. A., V. Vanheule, R. Fluit, B. H. Koopman, J. Rasmussen, N. Verdonschot, and M. S. Andersen. 2015. A subject-specific musculoskeletal modeling framework to predict in vivo mechanics of total knee arthroplasty. J. Biomech. Eng. 137(2): 020904.

[49] Rooks, N. B., T. F. Besier, and M. T. Schneider. 2022. A parameter sensitivity analysis on multiple finite element knee joint models. Front. Bioeng. Biotechnol. 10: 841882.

[50] Yan, M., T. Liang, H. Zhao, Y. Bi, T. Wang, T. Yu, and Y. Zhang. 2024. Model properties and clinical application in the finite element analysis of knee joint: A review. Orthop. Surg. 16(2): 289–302.

[51] Haut Donahue, T. L., M. L. Hull, M. M. Rashid, and C. R. Jacobs. 2002. A finite element model of the human knee joint for the study of tibio-femoral contact. J. Biomech. Eng. 124(3): 273–280.

[52] Beidokhti, H. N., D. Janssen, S. van de Groes, J. Hazrati, T. Van den Boogaard, and N. Verdonschot. 2017. The influence of ligament modelling strategies on the predictive capability of finite element models of the human knee joint. J. Biomech. 65: 1–11.

doi:10.6342/NTU202503673

[53] Li, F., D. Sun, Y. Song, Z. Zhou, D. Wang, X. Cen, and Y. Gu. 2025. Dynamic simulation of knee joint mechanics: Individualized multi-moment finite element modelling of patellar tendon stress during landing. J. Biomech. 112730.

[54] Zhang, X., J. Duan, W. Sun, T. Xu, and S. K. Jha. 2021. A three-stage cutting simulation system based on mass-spring model. Computer Modeling in Engineering & Sciences 127(1): 117–133.

[55] Chanthasopeephan, T., J. P. Desai, and A. C. Lau. 2007. Modeling soft-tissue deformation prior to cutting for surgical simulation: Finite element analysis and study of cutting parameters. IEEE Trans. Biomed. Eng. 54(3): 349–359.

[56] Zhang, X., W. Zhang, W. Sun, H. Wu, and A. Song. 2022. A real-time cutting model based on finite element and order reduction. Comput. Syst. Sci. Eng. 43(1): 1–10.

[57] Du, S., Y. Hu, M. Li, M. Shen, Z. Wang, and Y. Lei. 2025. Modelling and simulation of energy cutting tool for soft tissue using a novel extended finite element method. Int. J. Med. Robot. Comput. Assist. Surg. 21(2): e70052.

[58] Theilen, E., A. Rörich, T. Lange, S. Bendak, C. Huber, H. Schmal, and J. Georgii. 2023. Validation of a finite element simulation for predicting individual knee joint kinematics. IEEE Open J. Eng. Med. Biol. 5: 125–132.

[59] Diniz, P., Grimm, B., Garcia, F., Fayad, J., Ley, C., Mouton, C., ... and Seil, R. (2025). Digital twin systems for musculoskeletal applications: A current concepts review. Knee Surgery, Sports Traumatology, Arthroscopy.

[60] Ahmadian, H., P. Mageswaran, B. A. Walter, D. M. Blakaj, E. C. Bourekas, E. Mendel, and S. Soghrati. 2022. Toward an artificial intelligence-assisted framework for reconstructing the digital twin of vertebra and predicting its fracture response. International Journal for Numerical Methods in Biomedical Engineering 38(6): e3601.

[61] Michaud, F., A. Luaces, F. Mouzo, and J. Cuadrado. 2024. Use of patellofemoral digital twins for patellar tracking and treatment prediction: comparison of 3D models and contact detection algorithms. Frontiers in Bioengineering and Biotechnology 12(0): 1347720.

[62] Aubert, K., A. Germaneau, M. Rochette, W. Ye, M. Severyns, M. Billot, and T. Vendeuvre. 2021. Development of digital twins to optimize trauma surgery and postoperative management: A case study focusing on tibial plateau fracture. Frontiers in Bioengineering and Biotechnology 9(0): 722275.

[63] Okegbile, S. D., J. Cai, D. Niyato, and C. Yi. 2022. Human digital twin for personalized healthcare: Vision, architecture and future directions. IEEE Network 37(2): 262–269.

[64] Chen, J., C. Yi, S. D. Okegbile, J. Cai, and X. Shen. 2023. Networking architecture and key supporting technologies for human digital twin in personalized healthcare: A comprehensive survey. IEEE Communications Surveys & Tutorials 26(1): 706–746.

doi:10.6342/NTU202503673

[65] Rivera, L. F., M. Jiménez, P. Angara, N. M. Villegas, G. Tamura, and H. A. Müller. 2019. Towards continuous monitoring in personalized healthcare through digital twins. Proc. of the 29th Int. Conf. on Computer Science and Software Engineering 29(0): 329–335.

[66] Akkoul, S., A. Hafiane, O. Rozenbaum, E. Lespessailles, and R. Jennane. 2017. 3D reconstruction of the proximal femur shape from few pairs of X-ray radiographs. Signal Processing: Image Communication 59(0): 65–72.

[67] Cerveri, P., C. Sacco, G. Olgiati, A. Manzotti, and G. Baroni. 2017. 2D/3D reconstruction of the distal femur using statistical shape models addressing personalized surgical instruments in knee arthroplasty: A feasibility analysis. Int. J. Med. Robotics Comput. Assist. Surg. 13(4): e1823.

[68] Reyneke, C. J. F., M. Lüthi, V. Burdin, T. S. Douglas, T. Vetter, and T. E. Mutsvangwa. 2018. Review of 2D/3D reconstruction using statistical shape and intensity models and X-ray image synthesis: Toward a unified framework. IEEE Reviews in Biomedical Engineering 12(0): 269–286.

[69] Heimann, T., and H.-P. Meinzer. 2009. Statistical shape models for 3D medical image segmentation: A review. Med. Image Anal. 13(4): 543–563.

[70] Dalal, P., B. C. Munsell, S. Wang, J. Tang, K. Oliver, H. Ninomiya, and H. Fujita. 2007. A fast 3D correspondence method for statistical shape modeling. IEEE Conf. on Computer Vision and Pattern Recognition. 2007: 1–8.

[71] Nolte, D., S. Xie, and A. M. Bull. 2023. 3D shape reconstruction of the femur from planar X-ray images using statistical shape and appearance models. Biomed. Eng. Online 22(1): 30.

[72] Baka, N., B. L. Kaptein, M. de Bruijne, T. van Walsum, J. E. Giphart, W. J. Niessen, and B. P. Lelieveldt. 2011. 2D–3D shape reconstruction of the distal femur from stereo X-ray imaging using statistical shape models. Med. Image Anal. 15(6): 840–850.

[73] Kurazume, R., K. Nakamura, T. Okada, Y. Sato, N. Sugano, T. Koyama, and T. Hasegawa. 2009. 3D reconstruction of a femoral shape using a parametric model and two 2D fluoroscopic images. Comput. Vis. Image Underst. 113(2): 202–211.

[74] Fotsin, T. J. T., C. Vázquez, T. Cresson, and J. De Guise. 2019. Shape, pose and density statistical model for 3D reconstruction of articulated structures from X-ray images. IEEE Eng. Med. Biol. Soc. (EMBC) 2019: 2748–2751.Cohen, Z. A., Henry, J. H., McCarthy, D. M., Van Mow, C., and Ateshian, G. A. (2003). Computer simulations of patellofemoral joint surgery: patient-specific models for tuberosity transfer. The American journal of sports medicine, 31(1), 87-98.

[75] Cohen, Z. A., J. H. Henry, D. M. McCarthy, C. Van Mow, and G. A. Ateshian. 2003. Computer simulations of patellofemoral joint surgery: Patient-specific models for tuberosity transfer. Am. J. Sports Med. 31(1): 87–98.

doi:10.6342/NTU202503673

[76] Cancienne, J. M., Christian, D. R., Redondo, M. L., Huddleston, H. P., Shewman, E. F., Farr, J., ... and Yanke, A. B. (2019). The biomechanical effects of limited lateral retinacular and capsular release on lateral patellar translation at various flexion angles in cadaveric specimens. Arthroscopy, Sports Medicine, and Rehabilitation, 1(2), e137-e144.

[77] Salvatore, G., Berton, A., Orsi, A., Egan, J., Walley, K. C., Johns, W. L., ... and Nazarian, A. (2022). Lateral release with tibial tuberosity transfer alters patellofemoral biomechanics promoting multidirectional patellar instability. Arthroscopy: The Journal of Arthroscopic & Related Surgery, 38(3), 953-964.

[78] Ali, A. A., S. S. Shalhoub, A. J. Cyr, C. K. Fitzpatrick, L. P. Maletsky, P. J. Rullkoetter, and K. B. Shelburne. 2016. Validation of predicted patellofemoral mechanics in a finite element model of the healthy and cruciate-deficient knee. Journal of Biomechanics. 49(0): 302–309.

[79] Elias, J. J., M. J. Kelly, K. E. Smith, K. A. Gall, and J. Farr. 2016. Dynamic simulation of the effects of graft fixation errors during medial patellofemoral ligament reconstruction. American Journal of Sports Medicine. 4(0): 2325967116665080.

[80] Farahmand, F., W. Senavongse, and A. A. Amis. 1998. Quantitative study of the quadriceps muscles and trochlear groove geometry related to instability of the patellofemoral joint. Journal of Orthopaedic Research. 16(1): 136–143.

[81] Aalbersberg, S., I. Kingma, J. L. Ronsky, R. Frayne, and J. H. van Dieën. 2005. Orientation of tendons in vivo with active and passive knee muscles. Journal of Biomechanics. 38(9): 1780–1788.

[82] Chen, T., and C. Guestrin. 2016. XGBoost: A scalable tree boosting system. In Proceedings of the 22nd ACM SIGKDD International Conference on Knowledge Discovery and Data Mining, pp. 785–794.

[83] Grood, E. S., and W. J. Suntay. 1983. A joint coordinate system for the clinical description of three-dimensional motions: Application to the knee. Journal of Biomechanical Engineering. 105(2): 136–144.

[84] Ester, M., H. P. Kriegel, J. Sander, and X. Xu. 1996. A density-based algorithm for discovering clusters in large spatial databases with noise. In Proceedings of the 2nd International Conference on Knowledge Discovery and Data Mining (KDD) 96(34): 226–231.

[85] Camomilla, V., A. Cereatti, G. Vannozzi, and A. Cappozzo. 2006. An optimized protocol for hip joint centre determination using the functional method. Journal of Biomechanics. 39(6): 1096–1106.

[86] Farahmand, F., M. N. Tahmasbi, and A. A. Amis. 2004. The contribution of the medial retinaculum and quadriceps muscles to patellar lateral stability—an in-vitro study. The Knee 11(2): 89–94.

doi:10.6342/NTU202503673

Appendices

A. FE Model: Surgical Release Scenarios

A.1 Surgical Release Scenario: Incremental LR Release (Superior to Inferior)

This surgical release scenario discusses the kinematic response of lateral retinacular (LR) release in the superior to inferior direction. For patellar shift (Figure A-1(a)), 25% shows a near-identical alignment with the normal patellar shift trajectory. Towards the end of knee flexion starting from 60°, the shift is more medial compared to the normal shift trajectory. Early stages of flexion showing alignment with normal shift trajectory indicate significant improvement to patellar stability during the stages prior to engagement with the trochlear groove. Interestingly, at 50% LR release the postoperative shift trajectory is slightly more medial than the normal shift trajectory. Similarly, larger releases and full (75%-100%) release have more lateral trajectory compared to the normal. This indicates that partial release of the LR results in the most effective return to normal shift trajectory, while larger releases result in over-correction.

For patellar tilt (Figure A-1(d)), the mobility of the patellar tilt is partially restored after 25% LR release. Larger releases from 50% and beyond show no differences between each stepwise release, indicating diminishing returns. Larger releases also show a delayed increase in lateral patellar tilt, showing discrepancy with the normal patellar tilt trajectory. The patella shows to be engaged with the trochlear groove at 40° knee flexion. The

doi:10.6342/NTU202503673

delayed increase in lateral patellar tilt in larger LR release may indicate delayed engagement of the patella. Similar to the patellar shift postoperative outcomes, larger release may be detrimental to improving patellar tilt tracking.

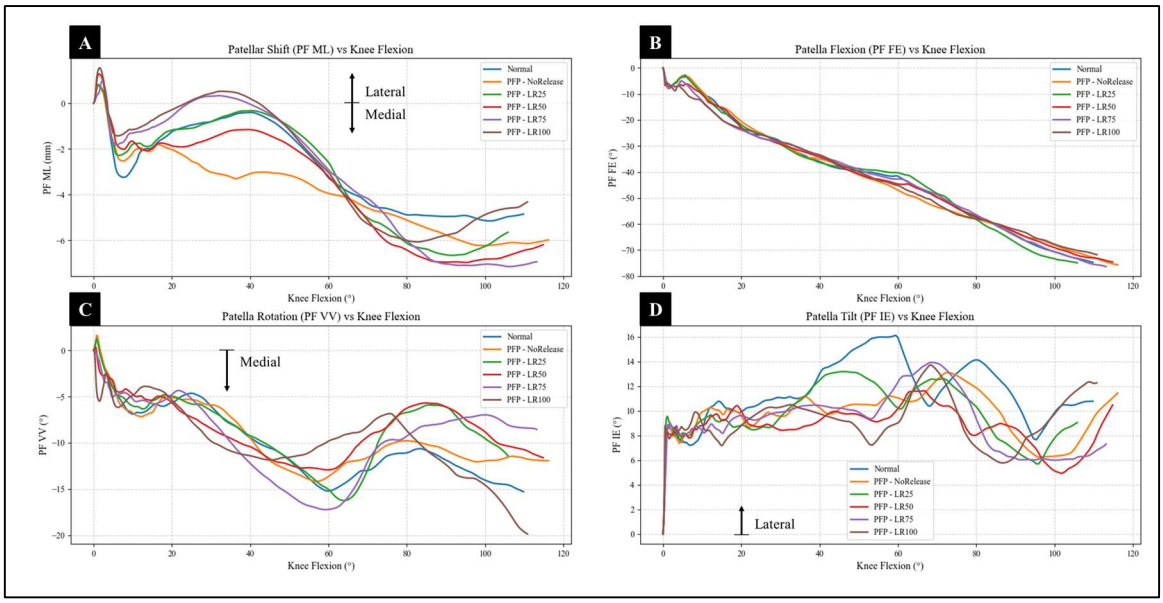

Figure A-1. Stepwise surgical release of the lateral retinaculum (LR) from 0% to 100% in the superior-to-inferior (SI) direction. Each increment represents a unique surgical scenario used in the simulation.

Qualitative assessments of patellar tilt and shift in this surgical release scenario are shown in Figures A-2 and A-3. Figure A-2 shows a good visual alignment between the patellar tilt after 25% LR release and the normal patellar tilt at 60° knee flexion angle. Although a good visual alignment with the normal patellar tilt can also be seen with the 50% and 75% LR release scenarios, Figure A-1 shows that for the entirety of the knee flexion, larger releases do not restore the normal patellar tilt as well as 25% LR release.

doi:10.6342/NTU202503673

Figure A-3 shows that the patellar shift trajectory after 25% LR release shows to have the most mobile trajectory among all surgical outcomes. The larger releases beyond 25% LR release visualizes the delayed lateralization of patellar tilt.

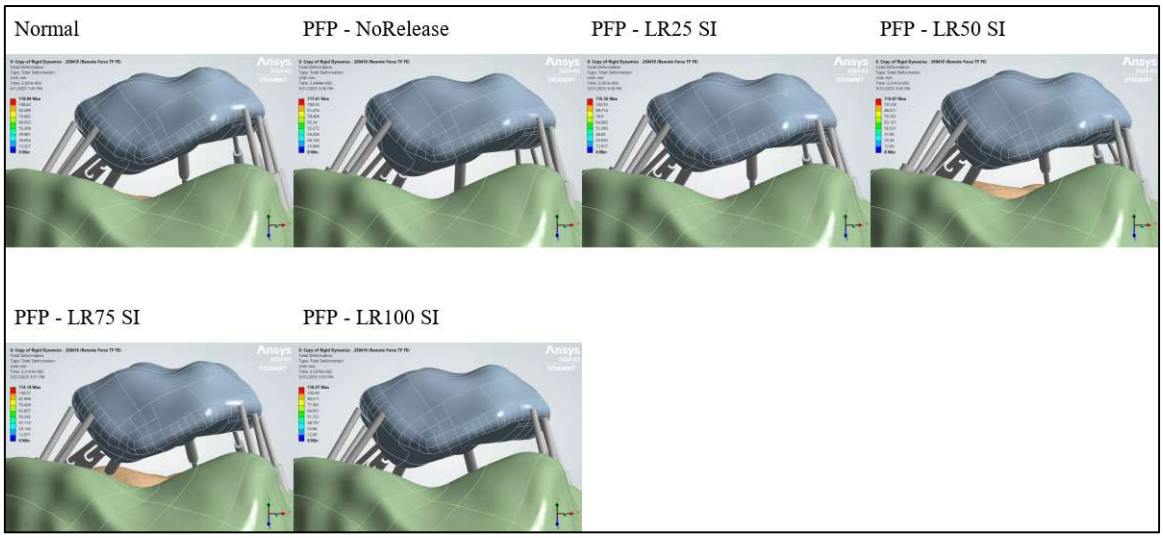

Figure A-2. Axial (superoinferior) views of the patella at ~60° knee flexion showing tilt orientation in normal, preoperative (PFP), and LR release scenarios (released in SI direction). Images used courtesy of ANSYS, Inc.

doi:10.6342/NTU202503673

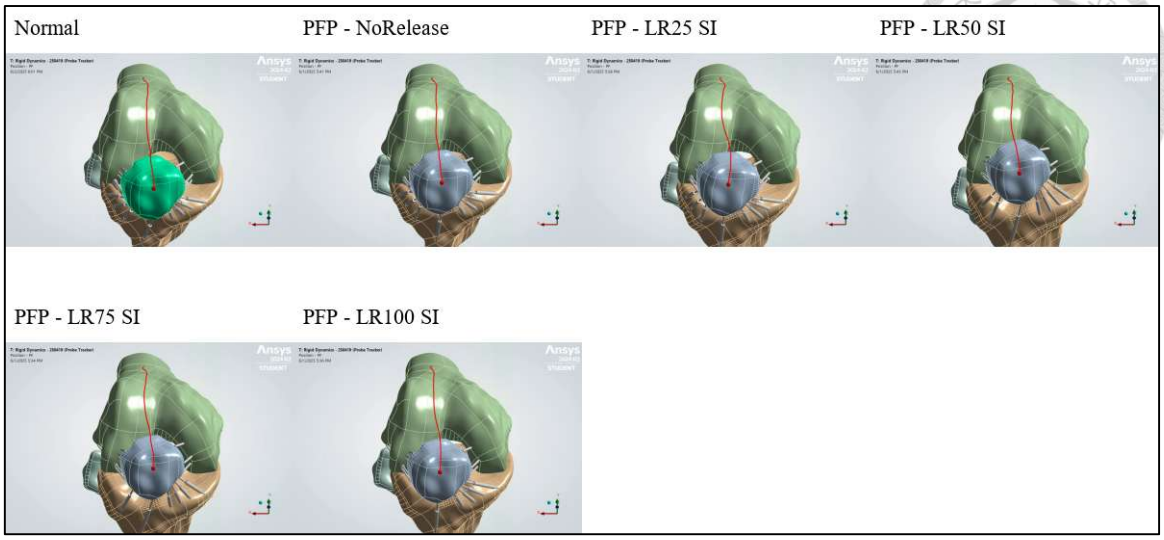

Figure A-3. Anteroposterior (AP) views of the patella showing shift trajectory traces from 0° to 110° knee flexion for normal, preoperative (PFP), and LR release cases (released in SI direction). Images used courtesy of ANSYS, Inc.

A.2 Surgical Release Scenario: Incremental LR Release (Inferior to Superior)

This surgical release scenario discusses the kinematic response of lateral retinacular (LR) release in the inferior to superior (reversed) direction. For patellar shift (Figure A-4(a)), 25%-50% LR releases in the IS direction do not align as well as after 25% LR release in the SI direction. Alignment with the normal patellar shift trajectory can only be observed at 75% release. This indicates that for LR release in the IS direction, return to normal patellar shift trajectories require larger releases.

For patellar tilt (Figure A-4(d)), 25% LR release in the IS direction shows no improvement to patellar tilt trajectory and may even result in worse patellar tilt tracking. At 50% LR release, however, the patellar tilt shows to be more mobile than the normal

doi:10.6342/NTU202503673

patellar tilt trajectory, particularly at knee flexion angle just before 60°. The more mobile patella tilt after LR release indicates a loss of stability. The patellar tilt shows slight improvement in tracking after performing 75% LR release. However, the trajectory in this scenario after 60° becomes even more medial than the normal tilt trajectory. Overall, careful consideration must be applied to balance improving patellar tracking while maintaining stability. Specifically, partial releases may be insufficient to completely restore patellar shift. Larger releases have better improvement to restoring patellar shift but result in a more mobile patella tilt.

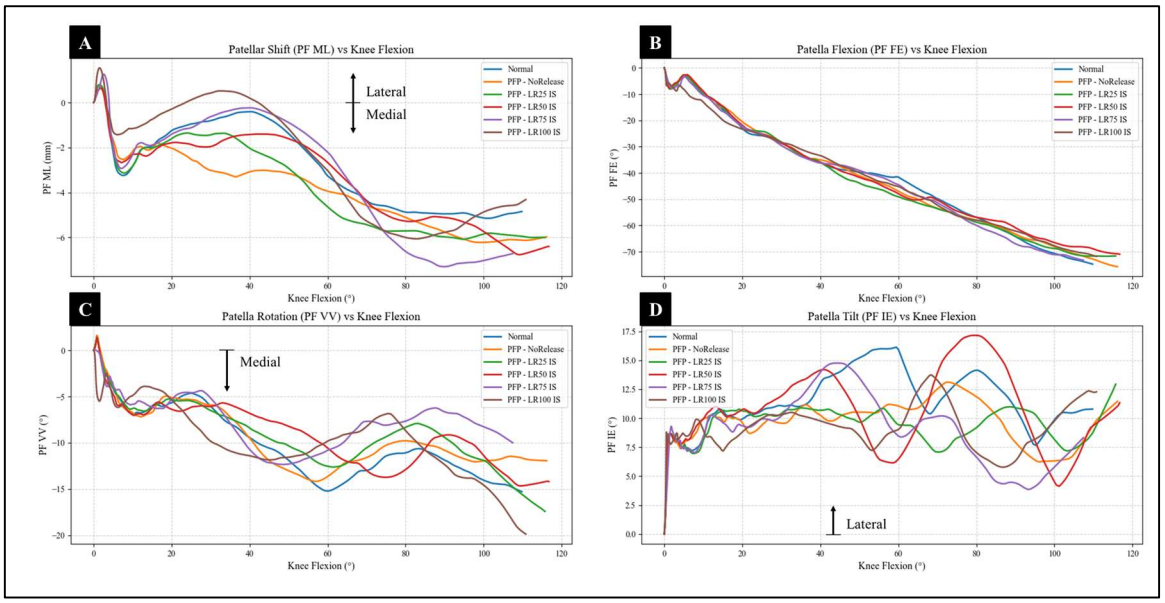

Figure A-4. Stepwise surgical release of the lateral retinaculum (LR) from 0% to 100% in the inferior-to-superior (IS) direction. Each increment represents a unique surgical scenario used in the simulation.

Qualitative assessments of patellar tilt and shift in this surgical release scenario are shown in Figures A-5 and A-6. For Figure A-5, the 25%-75% LR release scenarios in the

doi:10.6342/NTU202503673

IS direction shows that the patellar tilt appears worse compared to performing the same amount of releases in the SI direction. Notably at 75% LR release the patellar is positioned higher on the lateral edge of the trochlear groove, which worsens the patellar tracking. For Figure A-6, minute differences are difficult to identify visually. However, it can be seen that at 25% LR release the patellar shift trajectory is less mobile, while at 75% LR release the trajectory is more mobile. This phenomenon can be seen from Figure A-4.

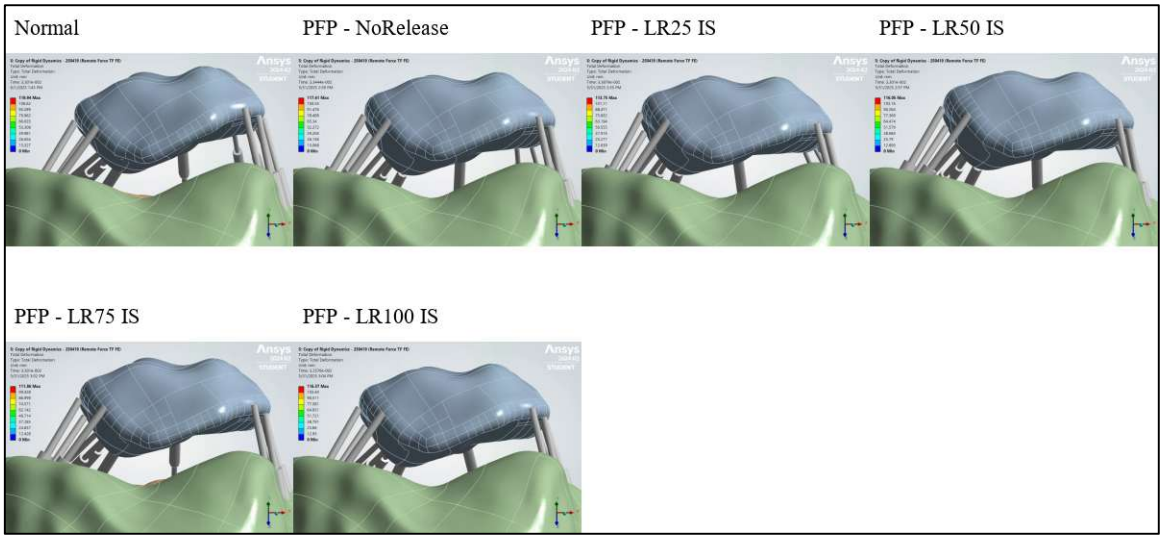

Figure A-5. Axial (superoinferior) views of the patella at ~60° knee flexion showing tilt orientation in normal, preoperative (PFP), and LR release scenarios (released in IS direction). Images used courtesy of ANSYS, Inc.

doi:10.6342/NTU202503673

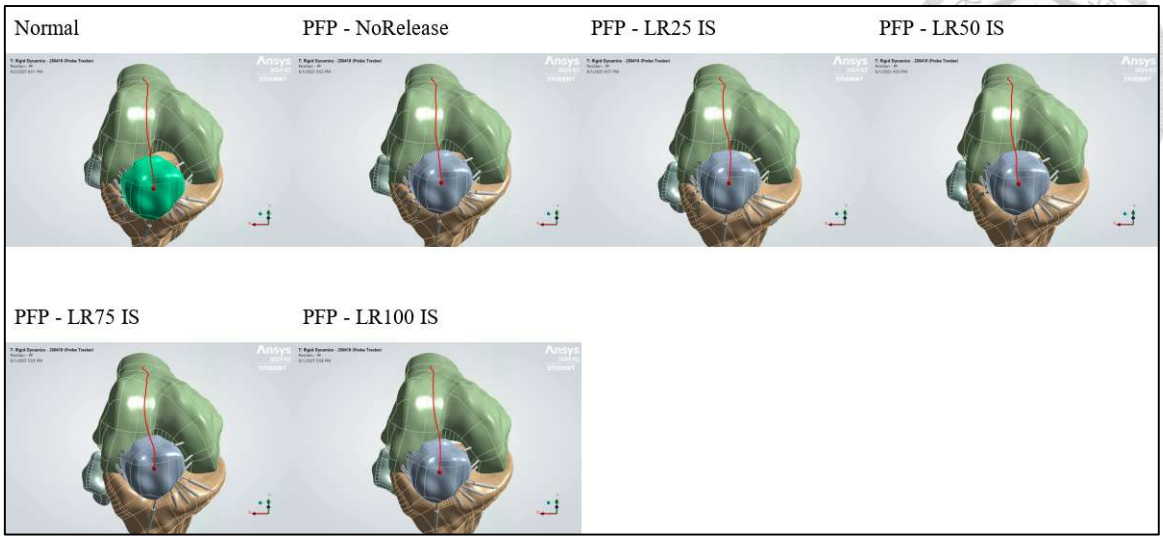

Figure A-6. Anteroposterior (AP) views of the patella showing shift trajectory traces from 0° to 110° knee flexion for normal, preoperative (PFP), and LR release cases (released in IS direction). Images used courtesy of ANSYS, Inc.

A.3 Surgical Release Scenario: Incremental LR Release (Superior to Inferior) with Full LPFL Release

The LPFL ligament bundle comprises of springs that have the highest stiffness in the FE model. This surgical release scenario discusses the kinematic response of lateral retinacular (LR) release in the superior to inferior direction with a full lateral patellofemoral ligament (LPFL) release for a compounded release scenario. Particularly, this surgical release scenario simulates a full lateral release. Beginning with an absent superior region of the lateral ligaments, the extent of the release continued until it reached the most inferior region of the LR, resulting in a full lateral release.

For patellar shift (Figure A-7(a)), the absence of the LPFL bundle, which contains the

doi:10.6342/NTU202503673

ligaments with the highest stiffness, did not result in significant changes compared to preoperative patellar shift trajectory, indicating no improvement. Performing LR release without the LPFL results in improvement with the patellar shift tracking. Even minimal release (25%) resulted in significant improvement and good alignment with the normal patellar shift trajectory. Performing larger to full releases all resulted in good restoration of patellar shift trajectory.

For patellar tilt (Figure A-7(d)), a full release of the LPFL resulted in a good restoration of patellar tilt trajectory, even without performing LR release. Notably, after performing 75% LR release combined with a full LPFL release, the patella tilt loses mobility from 0°-60° knee flexion angles, then rises significantly until 70°. This is the only scenario where this phenomenon can be observed. Other amounts of release appear to prohibit patellar tilt motion throughout knee flexion. Overall, since the LPFL contains the stiffest ligaments, it has significant effects during targeted release. Performing full LPFL release does not improve patellar shift, but partially restores patellar shift trajectory. Combining full LPFL release with LR release always results in improvements in patellar shift, but the patellar tilt trajectory only improved after performing 75% LR release. Comparing the different patellar tilt responses to a full LPFL release with stepwise LR release show that this phenomenon may be unstable, since 25%-50% and full LR releases showed restrained patellar tilt trajectories.

doi:10.6342/NTU202503673

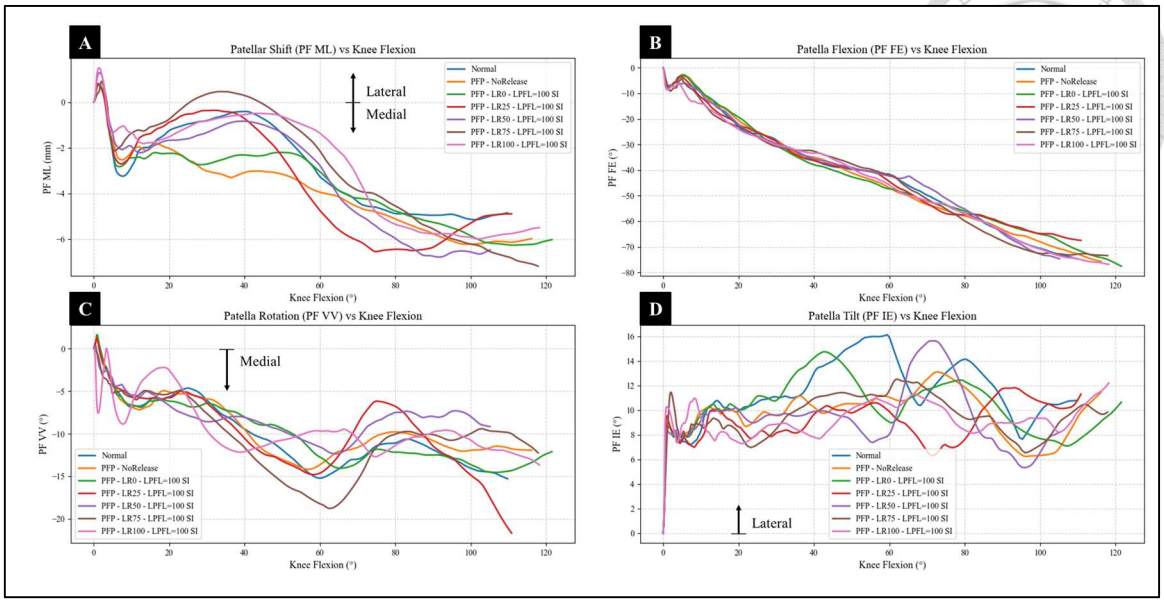

Figure A-7. Stepwise surgical release of the lateral retinaculum (LR) from 0% to 100% in the superior-to-inferior (SI) direction with a full LPFL release. Each increment represents a unique surgical scenario used in the simulation.

Qualitative assessments of patellar tilt and shift in this surgical release scenario are shown in Figures A-8 and A-9. For Figure A-8, a standalone full LPFL release shows no visual improvement to the patellar tilt, supporting the quantitative data from Figure A-7. The same phenomenon can be observed in Figure A-9, showing a patellar shift trajectory with no postoperative improvement. Conversely, after performing 25%-75% LR releases, the correction of patellar tilt shows better visual alignment with the normal patellar tilt. This visual improvement is in comparison with the graphical data from Figure A-7, which show that these scenarios only have partial improvements. It is possible that there are cases where partial improvements can show acceptable visual improvements to patellar tracking. At both full LPFL and LR releases the resulting patellar tilt is more similar to

doi:10.6342/NTU202503673

the preoperative scenario, showing no improvement. A full lateral release also implies a complete loss in lateral stabilizers, which may cause complications postoperatively. For Figure A-9, combining a full LPFL release with any amount of LR release all showed improved patellar shift trajectory, supporting the data in Figure A-7.

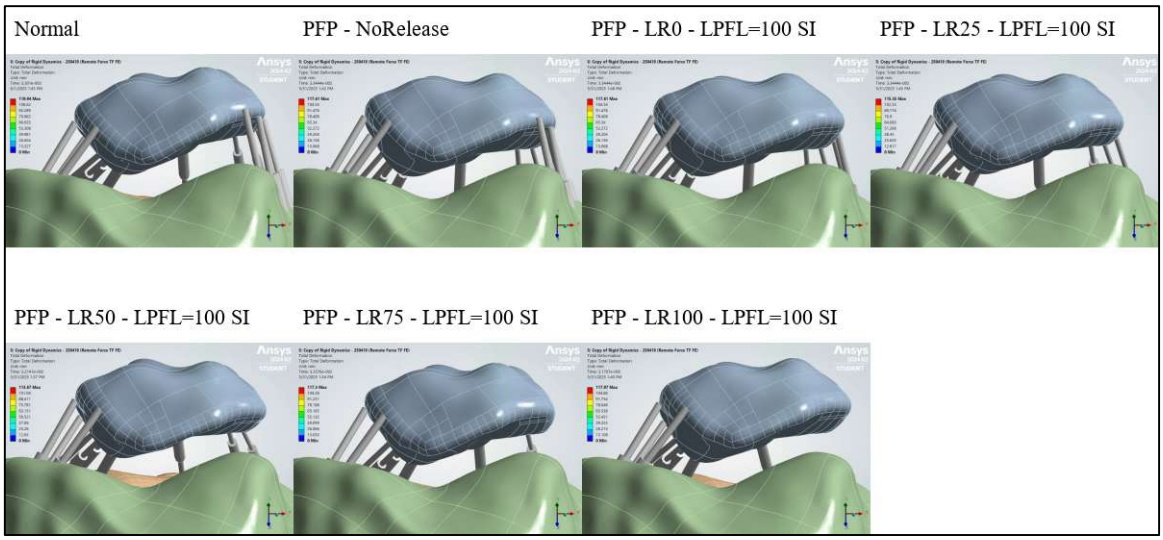

Figure A-8. Axial (superoinferior) views of the patella at ~60° knee flexion showing tilt orientation in normal, preoperative (PFP), and LR release scenarios (released in SI direction) with a full LPFL release. Images used courtesy of ANSYS, Inc.

doi:10.6342/NTU202503673

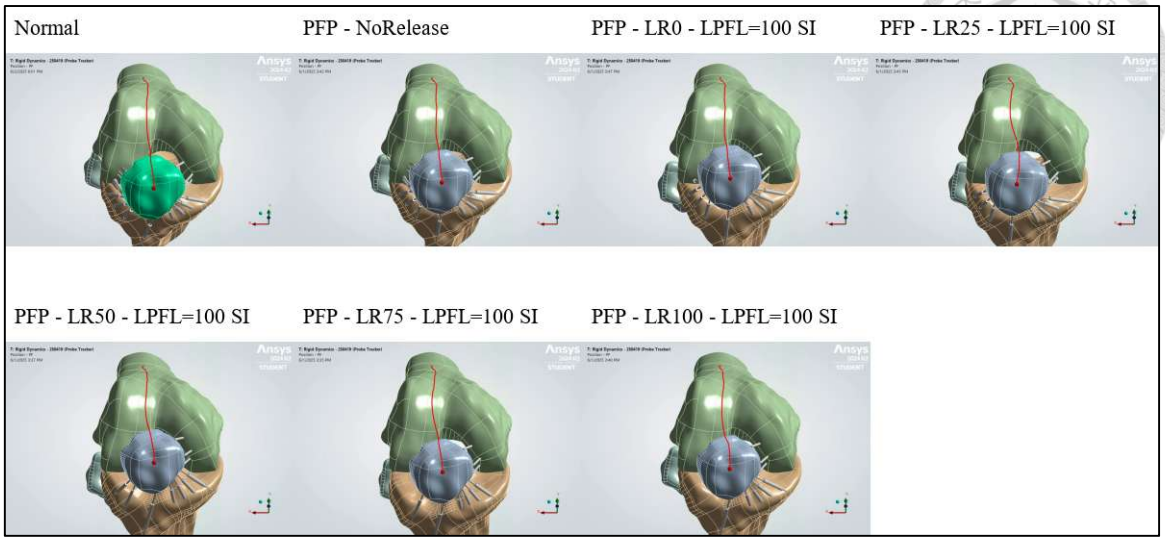

Figure A-9. Anteroposterior (AP) views of the patella showing shift trajectory traces from 0° to 110° knee flexion for normal, preoperative (PFP), and LR release cases (released in SI direction) with a full LPFL release. Images used courtesy of ANSYS, Inc.

A.4 Surgical Release Scenario: Incremental LPFL Release (Superior to Inferior) with Full LR Release

This surgical release scenario discusses the kinematic response of lateral patellofemoral ligament (LPFL) release in the superior to inferior direction with a full lateral retinacular (LR) release for a compounded release scenario. For patellar shift (Figure A-10(a)), introducing a minimal (20%) LPFL release from the superior region shows an over-correction in patellar shift and causes the trajectory to be more lateral than the normal trajectory. Increasing the amount of LPFL release (40%-80%) improves the correction, with 80% LPFL release being slightly more lateral than the normal patellar shift trajectory. This indicates that releasing the superior region of the LPFL leads to a

doi:10.6342/NTU202503673

slightly unstable patella.

For patellar tilt (Figure A-10(d)), it is difficult to denote any significant differences between each amount of LPFL release. The common trend is that the patellar tilt is relatively stable until knee flexion angle of 60° where the patellar tilt increases significantly—the normal patellar tilt trajectory shows earlier engagement with the trochlear groove. This may indicate a delayed patellar engagement with the trochlear groove. Overall, partial release (20%-40%) of the LPFL with a full LR release show optimized patellar stability, providing a balanced approach that corrects shift maltracking without resulting in instability.

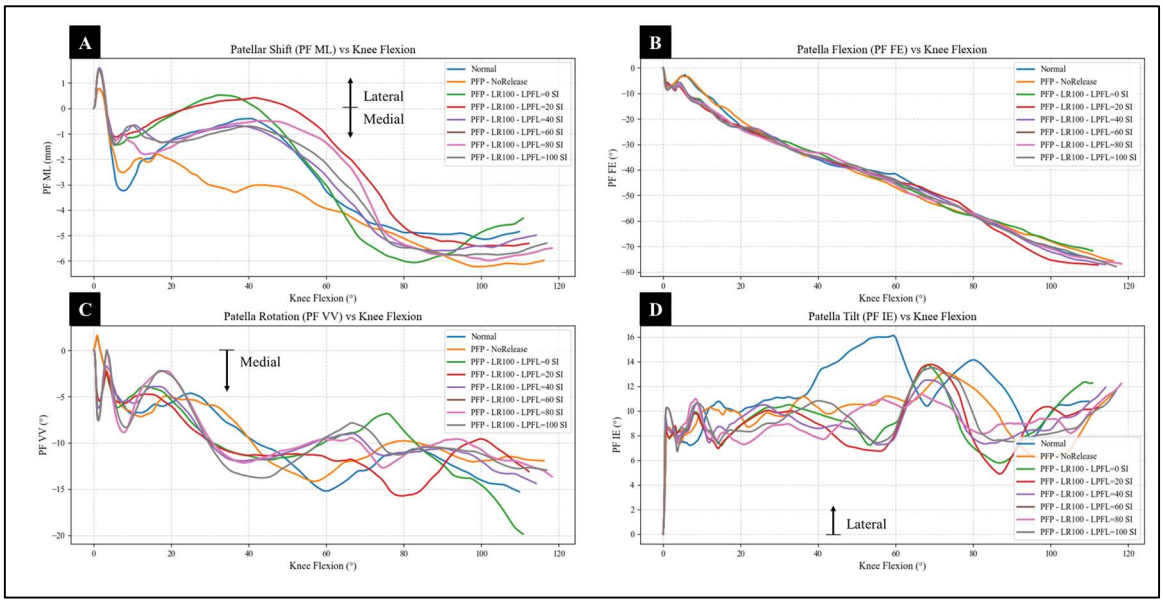

Figure A-10. Stepwise surgical release of the lateral patellofemoral ligament (LPFL) from 0% to 100% in the superior-to-inferior (SI) direction with a full LR release. Each increment represents a unique surgical scenario used in the simulation.

Qualitative assessments of patellar tilt and shift in this surgical release scenario are

doi:10.6342/NTU202503673

shown in Figures A-11 and A-12. For Figure A-11, the best visual alignment with the normal patellar tilt can be observed from the 20% and 40% LPFL release scenarios. This suggests that partial release of the superior regions of the LPFL leads to visual improvements in correcting patellar tilt. For Figure A-12, a partial (20%) LPFL release shows the greatest lateralized patellar shift trajectory for most of the knee flexion, supporting the data from Figure A-10. Alternatively, larger releases (60% LPFL release and beyond) lead to less mobile patellar shift trajectories that are similar with each other.

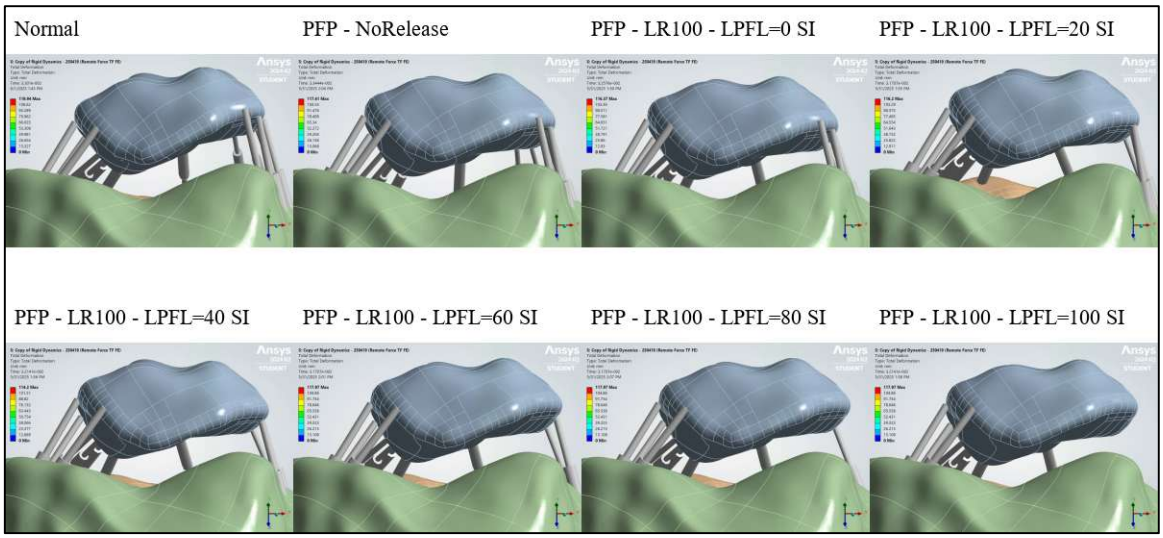

Figure A-11. Axial (superoinferior) views of the patella at ~60° knee flexion showing tilt orientation in normal, preoperative (PFP), and LPFL release scenarios (released in SI direction) with a full LR release. Images used courtesy of ANSYS, Inc.

doi:10.6342/NTU202503673

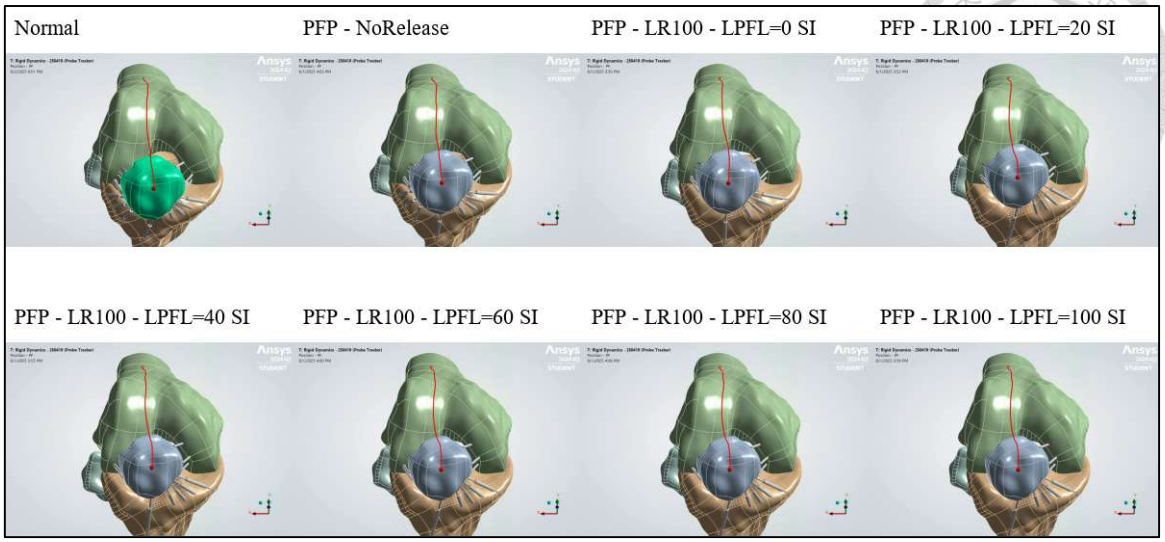

Figure A-12. Anteroposterior (AP) views of the patella showing shift trajectory traces from 0° to 110° knee flexion for normal, preoperative (PFP), and LPFL release cases (released in SI direction) with a full LR release. Images used courtesy of ANSYS, Inc.

A.5 Surgical Release Scenario: Incremental LPFL Release (Inferior to Superior) with Full LR Release

This surgical release scenario discusses the kinematic response of lateral patellofemoral ligament (LPFL) release in the inferior to superior direction with a full lateral retinacular (LR) release for a compounded release scenario. This scenario is similar to Appendix A-3 in that this is a full lateral release scenario in the IS direction. For patellar shift (Figure A-13(a)), the full LR release has been previously discussed in Appendix A-1. Similarly, the full lateral release, i.e., full LR and LPFL releases, has also been discussed in Appendix A-3. Interestingly, combining a full LR release with LPFL release does not result in any change in patella shift response. 20%-60% LPFL release combined

doi:10.6342/NTU202503673

with a full LR release has the same patella shift trajectory as a standalone full LR release. Only after performing 80% of LPFL release yields noticeable changes, which shows an over-correction and a patellar shift trajectory that is more lateral than the normal trajectory.

The similar phenomenon can be observed for patellar tilt (Figure A-13(d)). The patellar tilt trajectory after performing 20%-60% LPFL release with a full LR release has the same trajectory as a standalone full LR release. At 80% LPFL release, the patellar tilt trajectory shows a more mobile patellar tilt compared to the trajectory after a full LR release. This indicates that the LPFL does not contribute to influencing patellar shift and tilt when combined with a full LR release until a substantial (80%) release has been performed. Furthermore, it is suggested that the LPFL has no role in controlling patellar shift and tilt until an almost full lateral release is performed.

doi:10.6342/NTU202503673

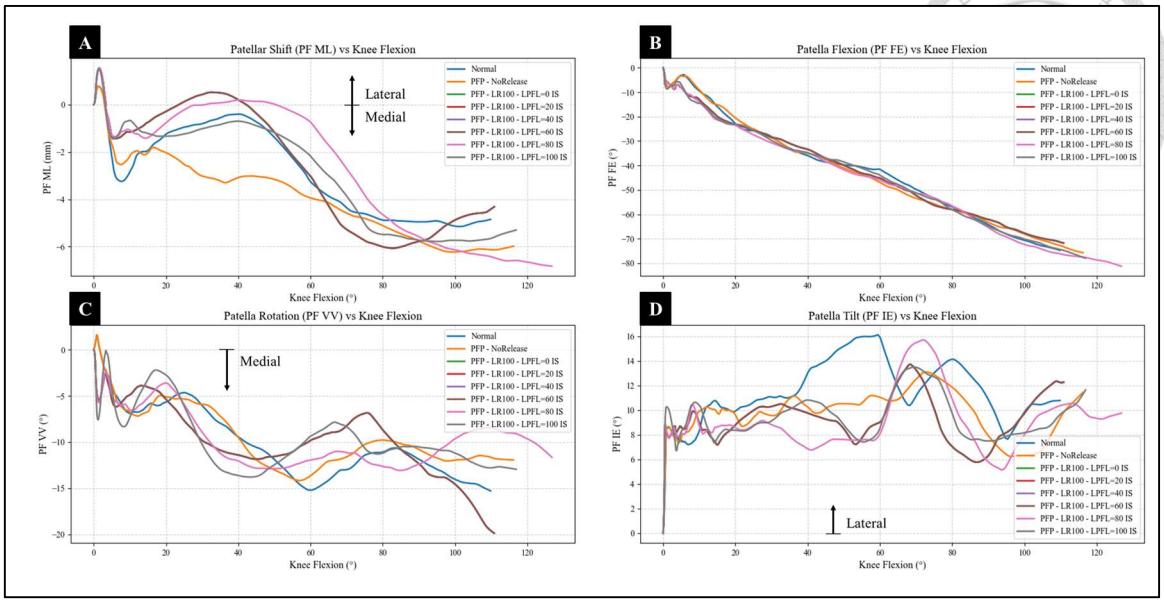

Figure A-13. Stepwise surgical release of the lateral patellofemoral ligament (LPFL) from 0% to 100% in the inferior-to-superior (IS) direction with a full LR release. Each increment represents a unique surgical scenario used in the simulation.

Qualitative assessments of patellar tilt and shift in this surgical release scenario are shown in Figures A-14 and A-15. For Figure A-14, the images of the patellar tilt after performing various amounts of LPFL release with LR release appear indistinguishable from each other. The only exception is the patellar tilt at 80% LPFL and full lateral release scenarios, which show the patella positioned higher at the lateral edge of the trochlear groove. This may lead to further complications postoperatively. In Figure A-15, the patellar shift trajectories are also indistinguishable even after various LPFL release scenarios until 80% LPFL release and full release. The trajectories at these scenarios show being more lateral throughout knee flexion, supporting Figure A-13. Similar to Section 4.3.3.3, a full lateral release does not show improvement to patellar tracking and may

doi:10.6342/NTU202503673

introduce complications.

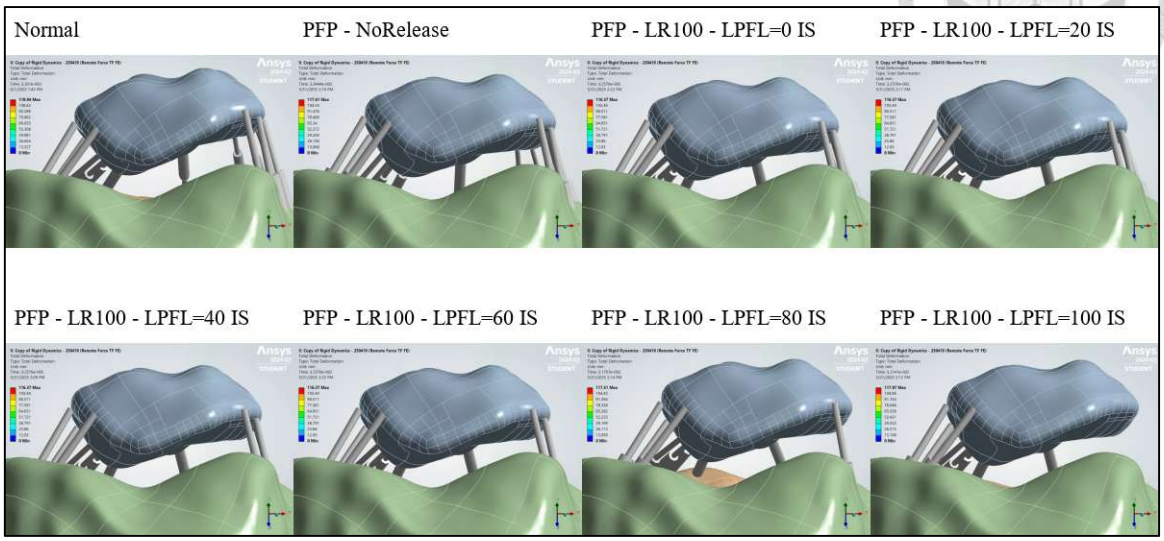

Figure A-14. Axial (superoinferior) views of the patella at ~60° knee flexion showing tilt orientation in normal, preoperative (PFP), and LPFL release scenarios (released in IS direction) with a full LR release. Images used courtesy of ANSYS, Inc.

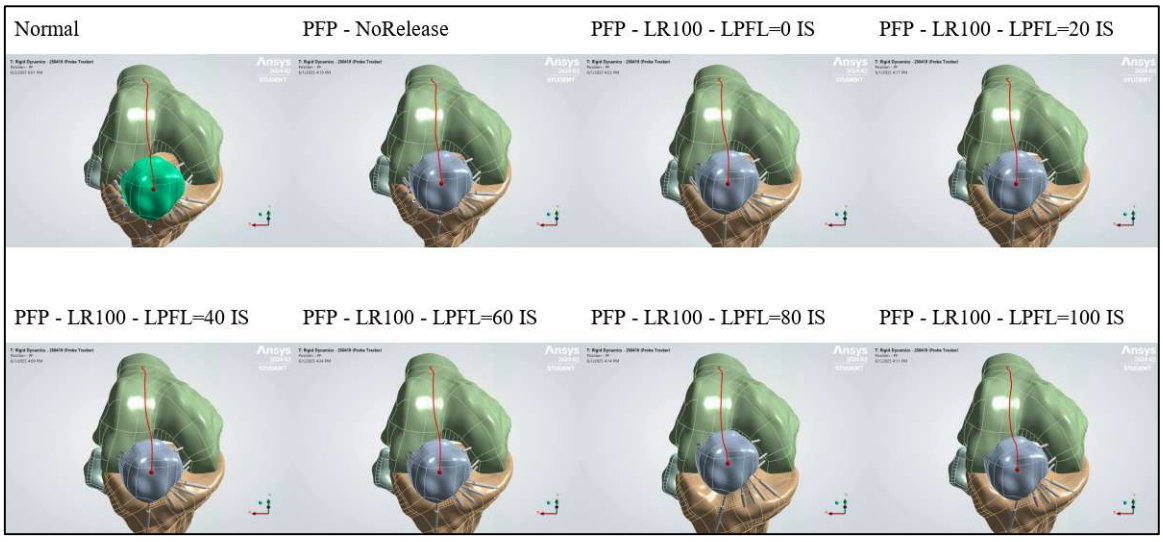

Figure A-15. Anteroposterior (AP) views of the patella showing shift trajectory traces from 0° to 110° knee flexion for normal, preoperative (PFP), and LPFL release cases (released in IS direction) with a full LR release. Images used courtesy of ANSYS, Inc.

doi:10.6342/NTU202503673

A.6 Surgical Release Scenario: Incremental MR Release (Inferior to Superior) with Full LR Release

This surgical release scenario discusses the kinematic response of medial retinacular (MR) release in the inferior to superior direction with a full lateral retinacular (LR) release for a compounded release scenario. This scenario performs the MR release in the opposite direction from what was used in Section 4.3.3.1. For patellar shift (Figure A-16(a)), after performing 25% MR release with a full LR release shows that there is only a slight improvement from the preoperative patellar shift trajectory in the knee flexion angle range 0°-40°. After 40° knee flexion, the patellar shift trajectory appears to be more aligned with the preoperative condition. Increasing the amount of MR release to 50% shows over-correction. The patella shift is now significantly more displaced than the normal patellar shift trajectory. Interestingly, increasing the MR release further to 75% results in a patellar shift trajectory that is more constrained than the preoperative condition.

For patellar tilt (Figure A-16(d)), the effect of various amounts of release on patellar tilt is almost similar to the response observed in Appendix A-1; only partial correction can be observed and larger releases result in instability. The most notable effect on patellar tilt trajectory is performing 75% MR release which, similar to the effect on patellar shift, causes the highest mobility to the patellar tilt. This response may indicate over-correction and an unstable patella.

doi:10.6342/NTU202503673

The variability in patellar shift and tilt responses per amount of release indicates nonlinearity in the kinematic response. Different amounts of release can have disproportionate effects to patellar shift and tilt. The same is true when reversing the direction of release, as the response of the patellar shift and tilt are different from Section 4.3.3.1. From the SHAP and XGBoost analysis in Section 4.5.3, the most inferior medial retinaculum region has a minor influence in predicting changes in patellar shift, but no significant influence in patellar tilt. Therefore, targeting the most inferior MR regions have limited impact in correcting patellar shift, and negligible impact on patellar tilt.

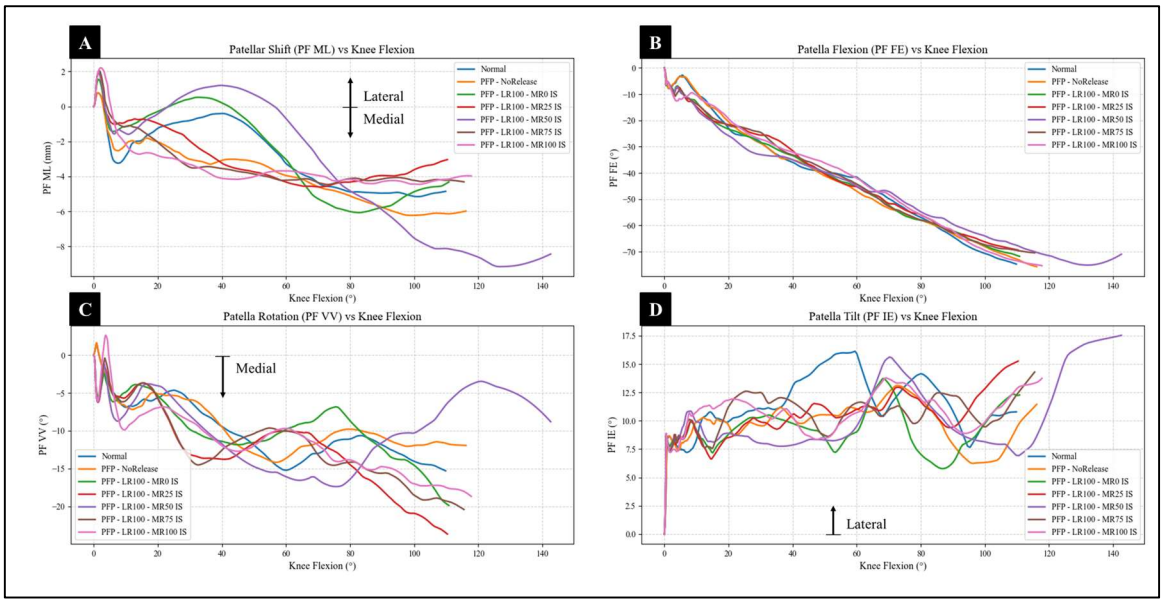

Figure A-16. Stepwise surgical release of the medial retinaculum (MR) from 0% to 100% in the inferior-to-superior (IS) direction with a full LR release. Each increment represents a unique surgical scenario used in the simulation.

Qualitative assessments of patellar tilt and shift in this surgical release scenario are shown in Figures A-17 and A-18. For Figure A-17, the patella after 25% MR release in

doi:10.6342/NTU202503673

the IS direction is no longer positioned high on the lateral edge of the trochlear groove. However, the various amounts of release do not have a visual improvement to restoring patellar tilt. This may be another result of the animations lacking enough frames to display small differences. Observing the 50% MR release scenario, it can be seen that the lateral edge of the patella is highest on the lateral edge of the trochlear groove, supporting the data from Figure A-18 that the patellar tilt in this scenario is the most unstable. However, based on the data in Figure A-16, the different MR release scenarios do not show significant improvement to patellar tilt trajectories either. For Figure A-18, it can be observed that the 50% MR release scenario has the most mobile patellar shift trajectory among all scenarios.

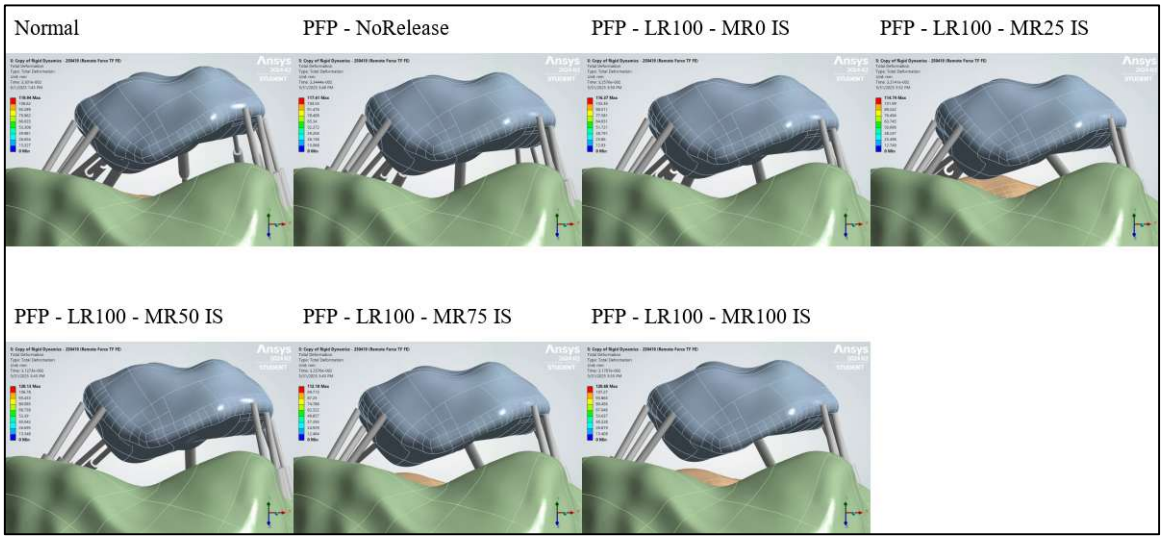

Figure A-17. Axial (superoinferior) views of the patella at ~60° knee flexion showing tilt orientation in normal, preoperative (PFP), and MR release scenarios (released in IS direction) with a full LR release. Images used courtesy of ANSYS, Inc.

doi:10.6342/NTU202503673

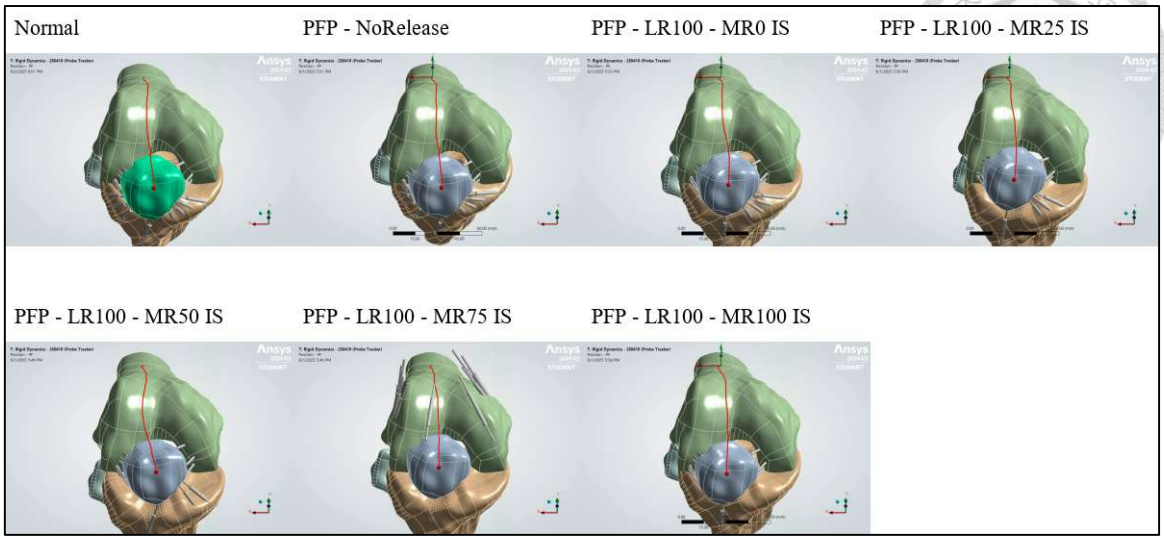

Figure A-18. Anteroposterior (AP) views of the patella showing shift trajectory traces from 0° to 110° knee flexion for normal, preoperative (PFP), and MR release cases (released in IS direction) with a full LR release. Images used courtesy of ANSYS, Inc.

A.7 Surgical Release Scenario: Incremental LPFL Release (Superior to Inferior)

This surgical release scenario discusses the kinematic response of lateral patellofemoral ligament (LPFL) release in the superior to inferior direction. This scenario discusses the isolated influence of the tightest ligament bundle during stepwise release. For patellar shift (Figure A-19(a)) and patellar tilt (Figure A-19(d)), it is difficult to discern from strict visual inspection, but the response to every amount of LPFL release to patellar shift and tilt is the same. Specifically, for patellar shift (Figure A-19(a)), LPFL release results in only a minor improvement to the preoperative patellar shift trajectory. However, for patellar tilt (Figure A-19(d)), there is a notable improvement to the patellar

doi:10.6342/NTU202503673

tilt trajectory.

The SHAP and XGBoost analysis in Section 4.5.3 shows that the most superior region of the LPFL, i.e., the LEPL bundle, is consistently one of the most influential parameters in the FE model. The LEPL bundle in the LPFL have the highest influence in affecting predictions to changes in patellar shift and tilt. However, the LTL bundle, located inferior to the LEPL bundle in the FE model, has no significant influence. This indicates that the LEPL portion of the LPFL bundle has a more critical role in controlling patellar kinematics, particularly tilt, during surgical release. Targeted release on the LPFL bundle, specifically on the LEPL portion, is able to achieve intended patellar tracking correction outcomes, minimizing risks of over-correction.

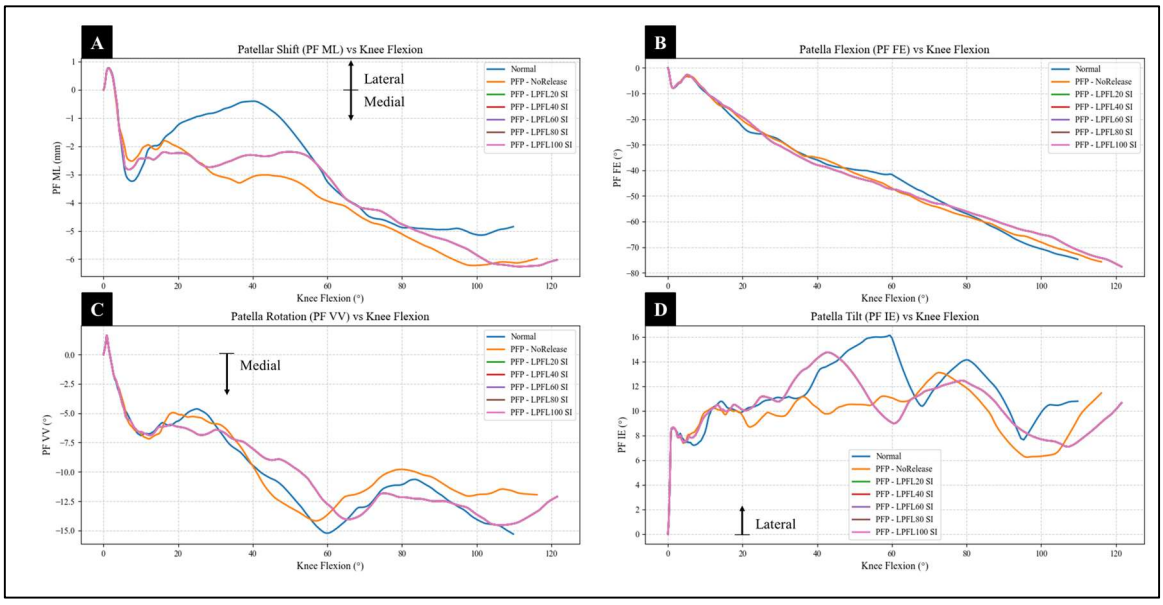

Figure A-19. Stepwise surgical release of the lateral patellofemoral ligament (LPFL) from 0% to 100% in the superior-to-inferior (SI) direction. Each increment represents a unique surgical scenario used in the simulation.

doi:10.6342/NTU202503673

Qualitative assessments of patellar tilt and shift in this surgical release scenario are shown in Figures A-20 and A-21. For Figure A-20, it is difficult to visually inspect differences between preoperative and postoperative patellar tilt at knee flexion angle 60°. As can be seen from Figure A-21, the magnitude of patellar tilt of the postoperative patellar tilt is close to the value of the preoperative patellar tilt. Therefore, from qualitative assessment alone, it is difficult to discern changes. However, the postoperative patellar tilt trajectory shows improved mobility and restoration of normal patellar tilt throughout the entire knee flexion, despite no significant improvement can be seen at 60° knee flexion. From Figure A-21, the improvement to the patellar tilt trajectory is minimal at all amounts of LPFL release.

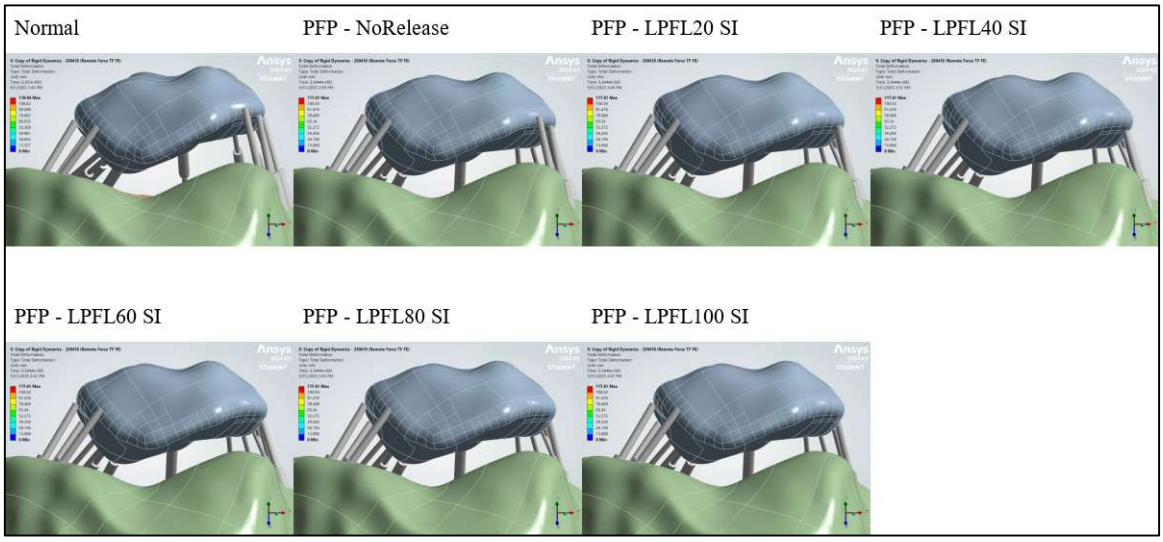

Figure A-20. Axial (superoinferior) views of the patella at ~60° knee flexion showing tilt orientation in normal, preoperative (PFP), and LPFL release scenarios (released in SI direction). Images used courtesy of ANSYS, Inc.

doi:10.6342/NTU202503673

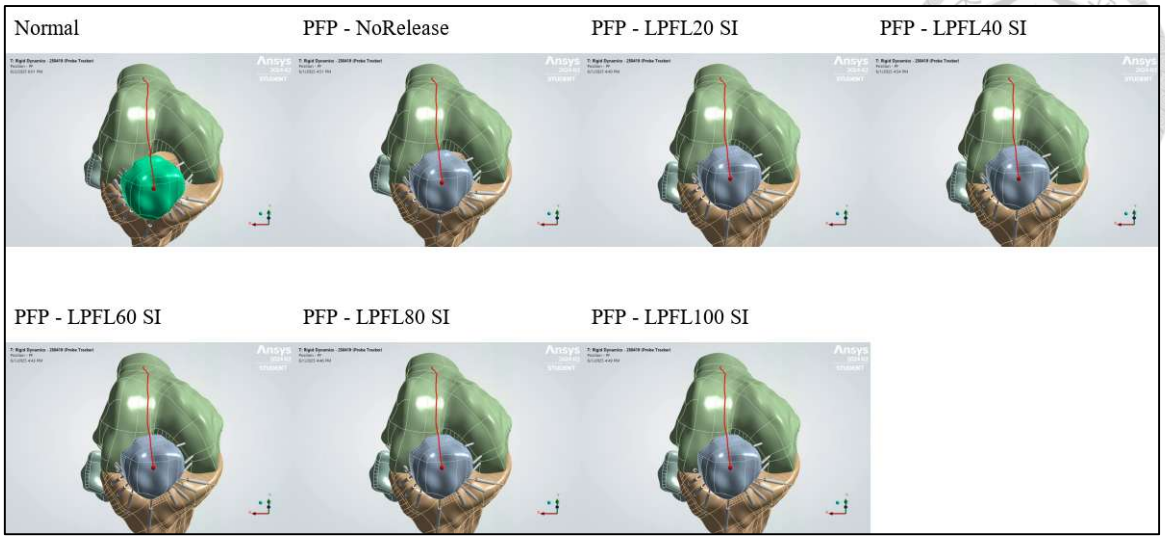

Figure A-21. Anteroposterior (AP) views of the patella showing shift trajectory traces from 0° to 110° knee flexion for normal, preoperative (PFP), and LPFL release cases (released in SI direction). Images used courtesy of ANSYS, Inc.

A.8 Surgical Release Scenario: Incremental MPFL Release (Superior to Inferior) with Full LPFL Release

This surgical release scenario discusses the kinematic response of medial patellofemoral ligament (MPFL) release in the superior to inferior direction with a full lateral patellofemoral ligament (LPFL) release for a compounded release scenario. This scenario discusses the influence of the tightest ligament bundles (LPFL and MPFL) during stepwise release. For patellar shift (Figure A-22(a)) and patellar tilt (Figure A-22(d)), there is no difference from the results from this scenario with the results in 4.4.8. Specifically, even after performing compounded stepwise MPFL release and a full LPFL release, no changes can be detected. This suggests that the combination of MPFL and

doi:10.6342/NTU202503673

LPFL releases in this manner does not have a significant impact in restoring normal patellar shift and tilt kinematics. These findings indicate that the tightest ligament bundles, MPFL and LPFL, may not be necessary for correcting patellar shift and tilt. Only specific parameters with high influence, such as the LEPL portion of the LPFL bundle, should be targeted for release to achieve effective surgical outcomes.

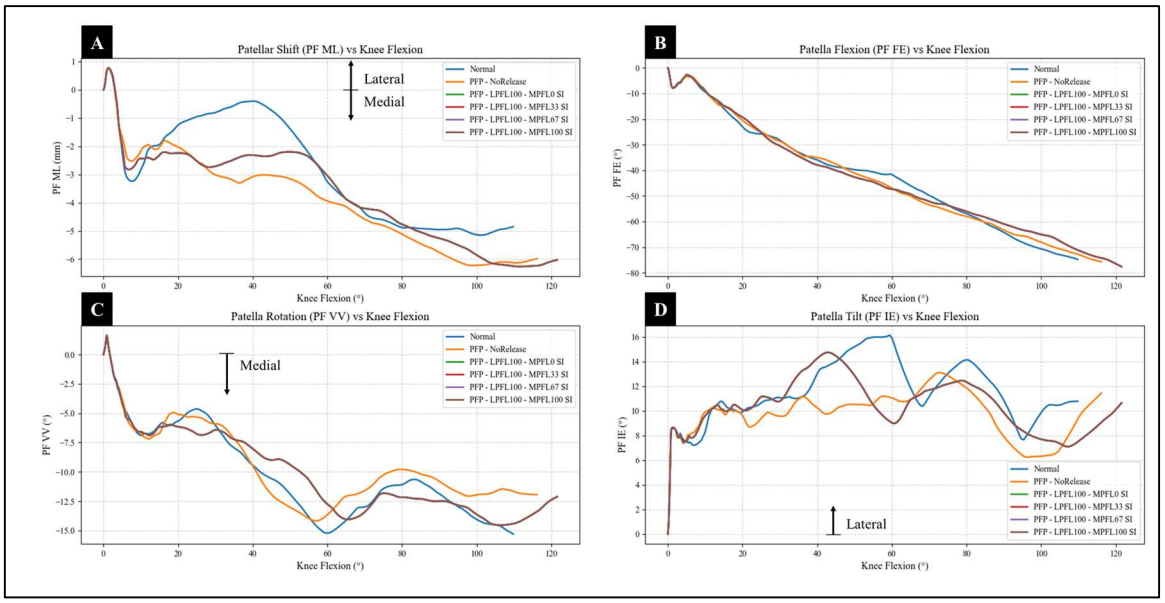

Figure A-22. Stepwise surgical release of the medial patellofemoral ligament (MPFL) from 0% to 100% in the superior-to-inferior (SI) direction with a full LPFL release. Each increment represents a unique surgical scenario used in the simulation.

Qualitative assessments of patellar tilt and shift in this surgical release scenario are shown in Figures A-23 and A-24. The qualitative assessments reflect the analysis from the quantitative data in Figure A-22: the compounded MPFL and LPFL release approach does not produce any significant changes. The misrepresentation of ligament springs seen in the full MPFL and LPFL release scenario is only a display artifact caused by Ansys

doi:10.6342/NTU202503673

and does not indicate any error in the solution itself.

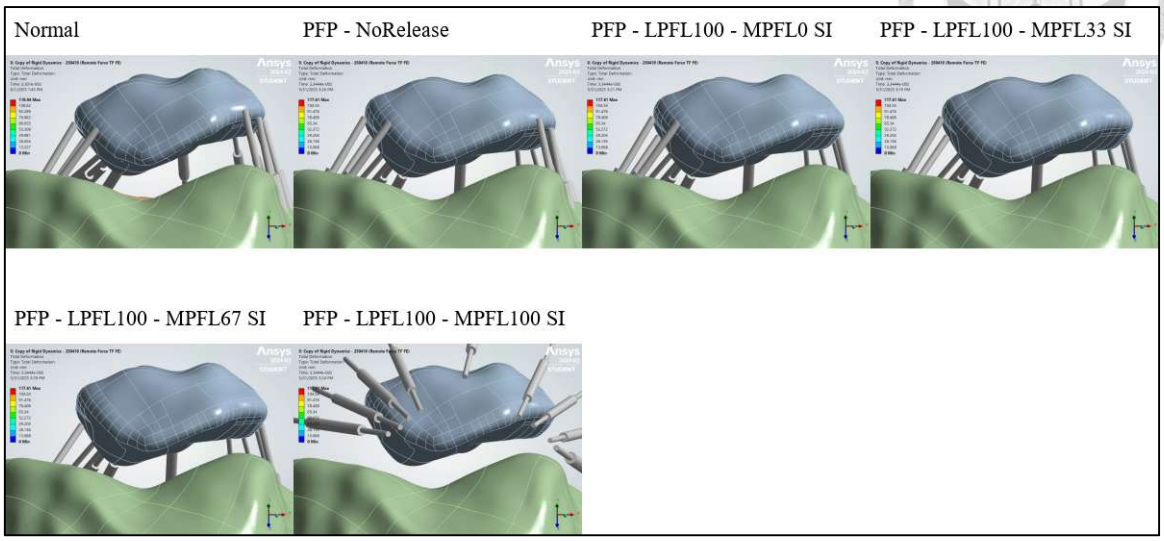

Figure A-23. Axial (superoinferior) views of the patella at ~60° knee flexion showing tilt orientation in normal, preoperative (PFP), and MPFL release scenarios (released in SI direction) with a full LPFL release. Images used courtesy of ANSYS, Inc.

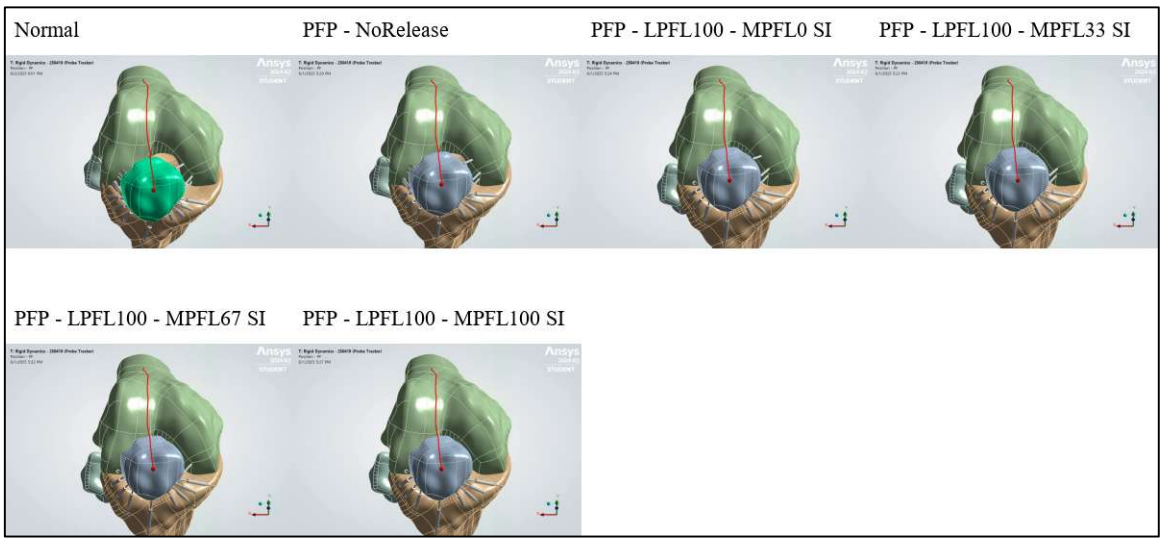

Figure A-24. Anteroposterior (AP) views of the patella showing shift trajectory traces from 0° to 110° knee flexion for normal, preoperative (PFP), and MPFL release cases (released in SI direction) with a full LPFL release. Images used courtesy of ANSYS, Inc.

doi:10.6342/NTU202503673

A.9 Surgical Release Scenario: Incremental MR Release (Superior to Inferior)

For patellar shift (Figure A-25(a)), 25% of medial retinacular (MR) release shows an increase in lateral shift compared to the preoperative trajectory from 20°-60° knee flexion angle range. Towards the end of knee flexion, the trajectory of patellar shift is similar to that of the preoperative trajectory. After 50% MR release, the trajectory from 0°-30° knee flexion is the same as the preoperative trajectory. Within 30°-80° knee flexion, however, the patellar shift trajectory is more medial than preoperative. Then, towards the end of knee flexion, patellar shift becomes more aligned with the normal trajectory. 75% MR release shows better alignment with normal trajectory starting from 60° knee angle. However, early knee flexion shows that this release scenario results in more pronounced medialization of the patellar shift. A full (100%) MR release shows no improvement to restoring patellar shift to normal.

For patellar tilt (Figure A-25(d)), 25% MR release restores the mobility of the patellar tilt. The difference between the postoperative and normal tilt trajectories is that the lateral tilt occurs earlier in the postoperative trajectory. Further degrees of MR release do not result in improvement to restoring normal patellar tilt trajectories. Particularly, further MR releases yield no significant changes between each release. Partial to moderate MR release improves certain aspects of patellar shift and tilt, although it may introduce earlier

doi:10.6342/NTU202503673

lateralization of patellar tilt. Larger and complete release results in diminishing returns and is found to be harmful to restoring normal patellar shift and tilt.

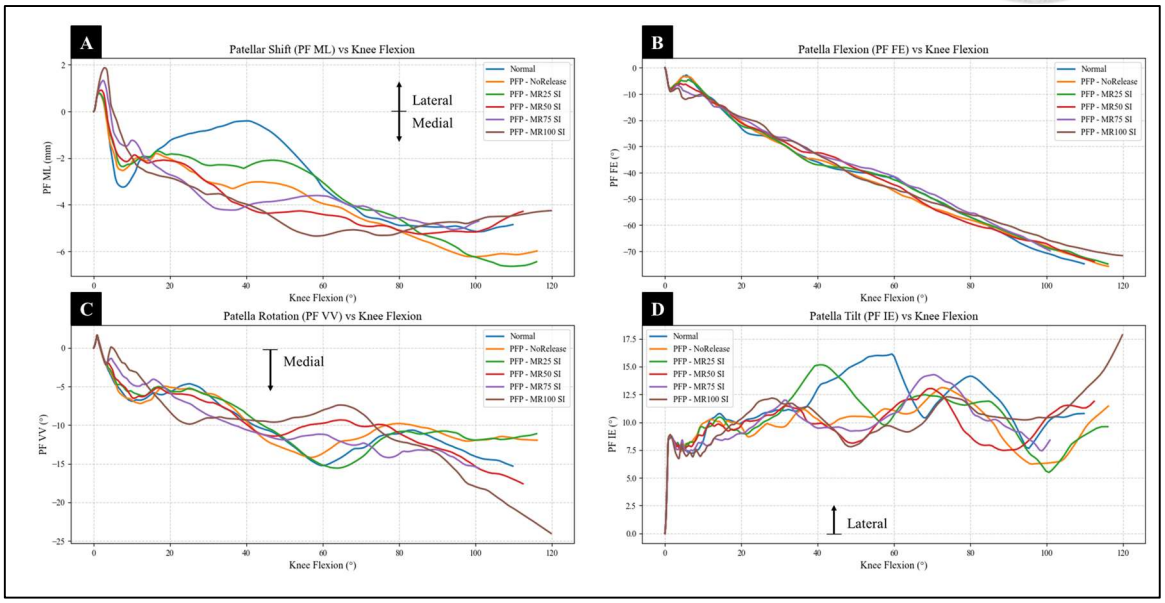

Figure A-25. Stepwise surgical release of the medial retinaculum (MR) from 0% to 100% in the superior-to-inferior (SI) direction. Each increment represents a unique surgical scenario used in the simulation.

Qualitative assessments of patellar tilt and shift in this surgical release scenario are shown in Figures A-26 and A-27. Notably, in Figure A-26, 25% and 100% MR releases show the closest visual alignment with the normal patellar tilt at 60° knee flexion. The image in the 75% MR release scenario shows display artifacts caused by Ansys and do not indicate errors in the solution. The patellar tilt after 25% MR release may have a more favorable correction than indicated by quantitative data. In Figure A-27, it shows that the larger releases have more mobile patellar shift trajectory, indicating loss of stability. Therefore, careful consideration must be given to the extent of MR release, as excessive

doi:10.6342/NTU202503673

release may be more harmful to stability across the entire knee flexion.

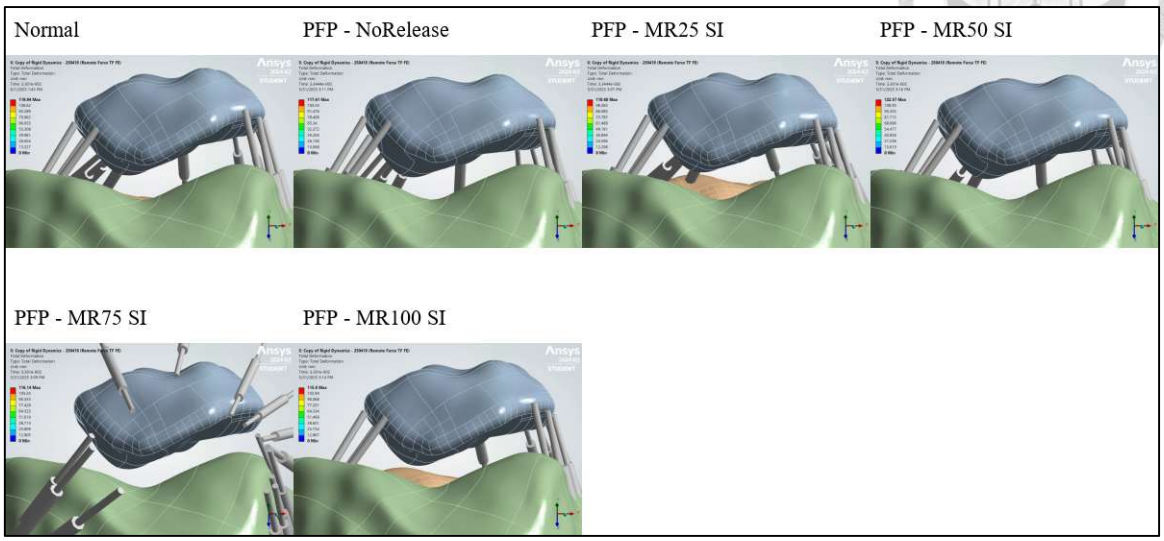

Figure A-26. Axial (superoinferior) views of the patella at ~60° knee flexion showing tilt orientation in normal, preoperative (PFP), and MR release scenarios (released in SI direction). Images used courtesy of ANSYS, Inc.

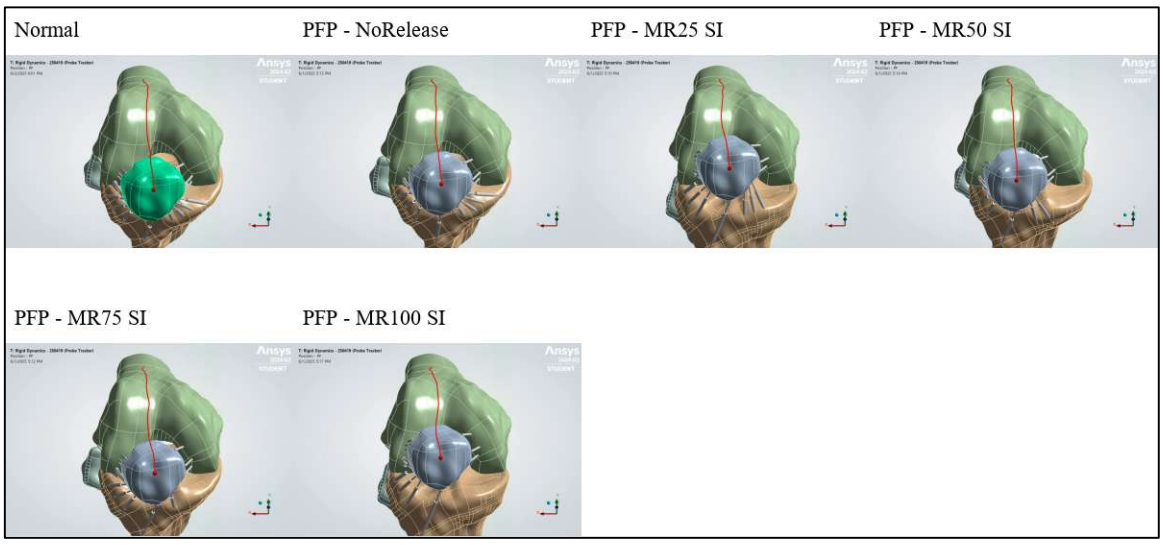

Figure A-27. Anteroposterior (AP) views of the patella showing shift trajectory traces from 0° to 110° knee flexion for normal, preoperative (PFP), and MR release cases (released in SI direction). Images used courtesy of ANSYS, Inc.

doi:10.6342/NTU202503673

A.10 Surgical Release Scenario: Incremental MR Release (Inferior to Superior)

This surgical release scenario discusses the kinematic response of reversing the MR release direction. For patellar shift (Figure A-28(a)), the effects of 25%-75% MR release in the IS direction appear almost sharing the similar trajectory, 75% release shows slightly more medial shift in the 40°-60° knee flexion angle range. For patellar tilt (Figure A-28(d)), partial to halfway MR release restores the mobility of the patellar tilt, however 50% MR release results in a delayed lateral tilt with a greater magnitude compared to the normal trajectory. Increasing the MR release to full does not improve the patellar tilt. Overall, partial release in the IS direction of the MR release shows better capability of restoring patellar tilt mobility compared to MR release in the SI direction.

doi:10.6342/NTU202503673

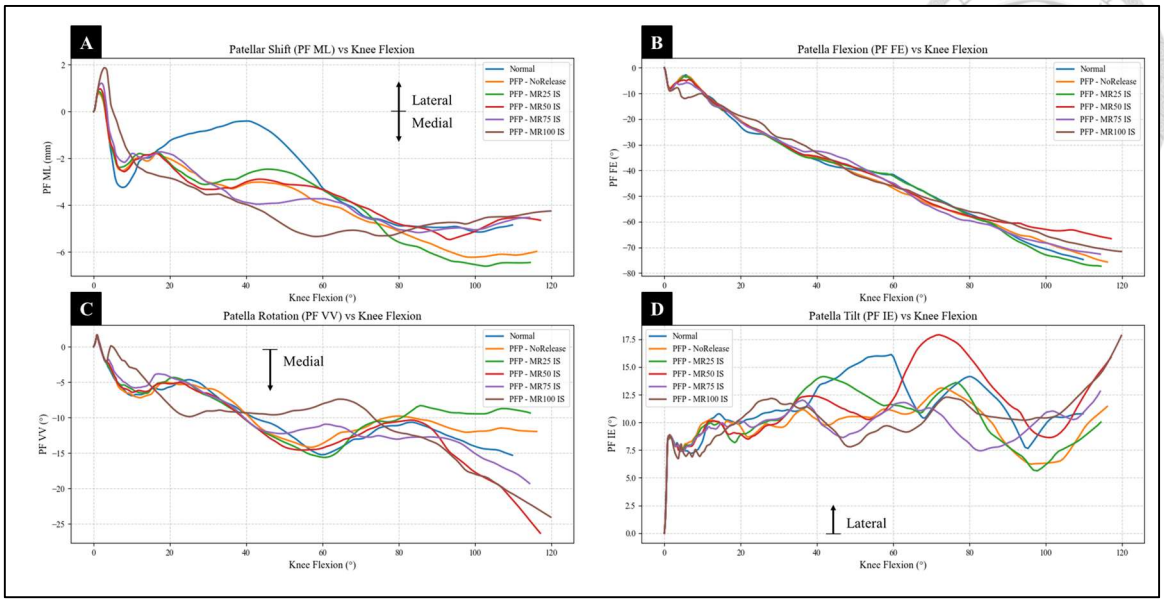

Figure A-28. Stepwise surgical release of the medial retinaculum (MR) from 0% to 100% in the inferior-to-superior (IS) direction. Each increment represents a unique surgical scenario used in the simulation.

Qualitative assessments of patellar tilt and shift in this surgical release scenario are shown in Figures A-29 and A-30. In Figure A-29, the effects of 25%-50% MR release have good visual alignment. Similar to the analysis for Figure A-29, the patellar shift trajectories in Figure A-30 are nearly identical, indicating comparable in patellar shift response to MR release in the IS direction. This highlights that a moderate amount of MR release in the IS direction achieve better improvement to patellar tracking.

doi:10.6342/NTU202503673

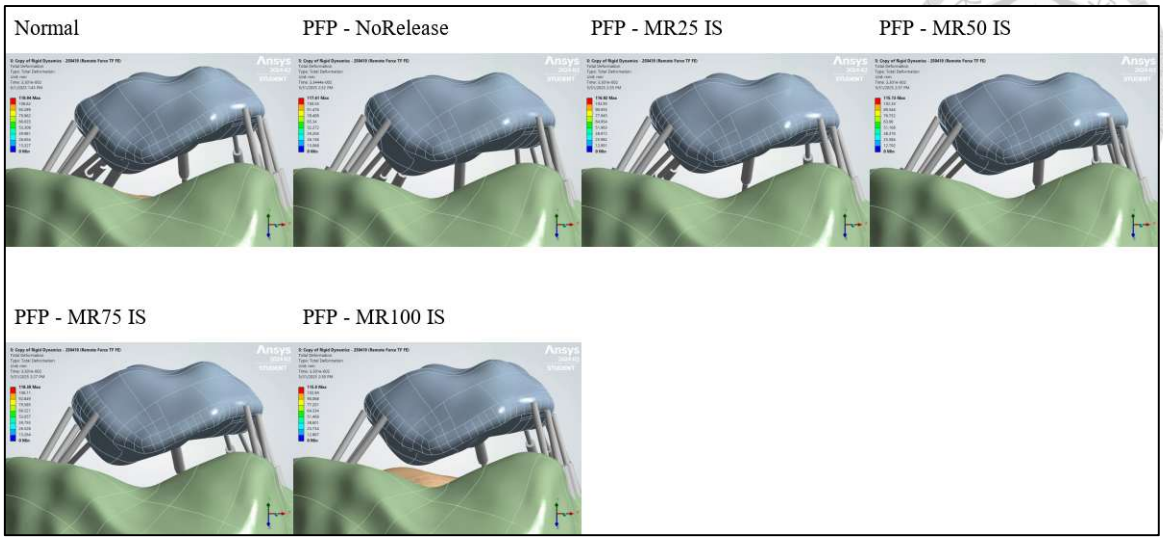

Figure A-29. Axial (superoinferior) views of the patella at ~60° knee flexion showing tilt orientation in normal, preoperative (PFP), and MR release scenarios (released in IS direction). Images used courtesy of ANSYS, Inc.

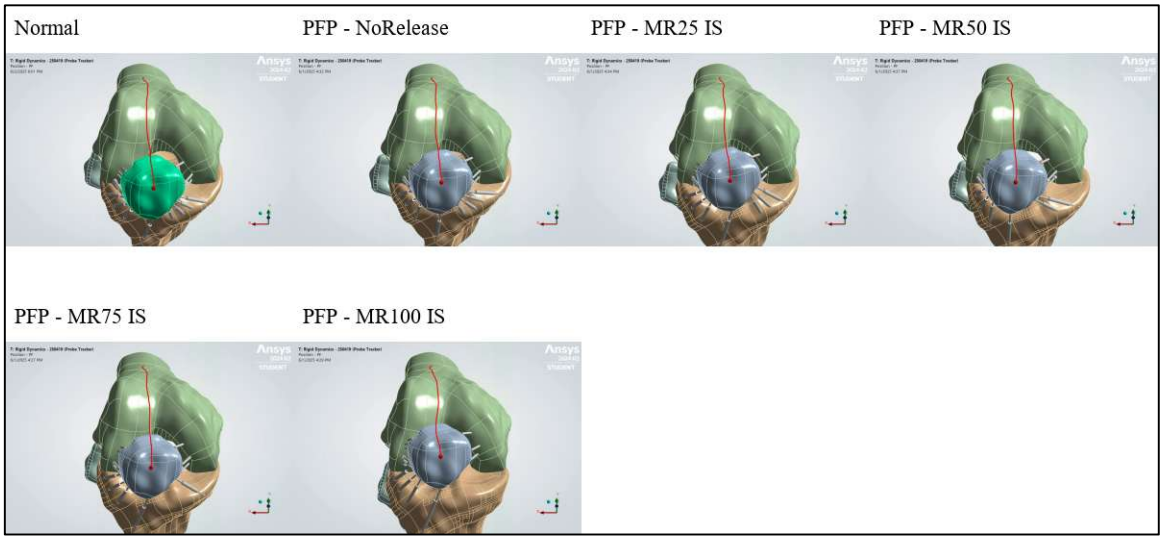

Figure A-30. Anteroposterior (AP) views of the patella showing shift trajectory traces from 0° to 110° knee flexion for normal, preoperative (PFP), and MR release cases (released in IS direction). Images used courtesy of ANSYS, Inc.

doi:10.6342/NTU202503673

A.11 Surgical Release Scenario: Incremental MPFL Release (Superior to Inferior)

Figure A-31 shows the stepwise release of the medial patellofemoral ligament (MPFL). For patellar shift (Figure A-31(a)), there is slight improvement to relieving imbalanced tension in the patella by an observed more lateral shift starting from 30° until the end of knee flexion. For patella tilt (Figure A-31(d)), a significant improvement can be seen to restoring the normal patella tilt trajectory. MPFL release restores a near-complete restoration of patella tilt. However, there is no difference between the trajectories in each release scenario. The identical trajectories indicate that the superior portion of the MPFL has a primary influence in patellar dynamics, while the remaining regions have negligible impact. This result supports the SHAP and XGBoost analysis from Section 4.5.3, where the superior MPFL is identified as one of the most important parameters in influencing patellar stability.

doi:10.6342/NTU202503673

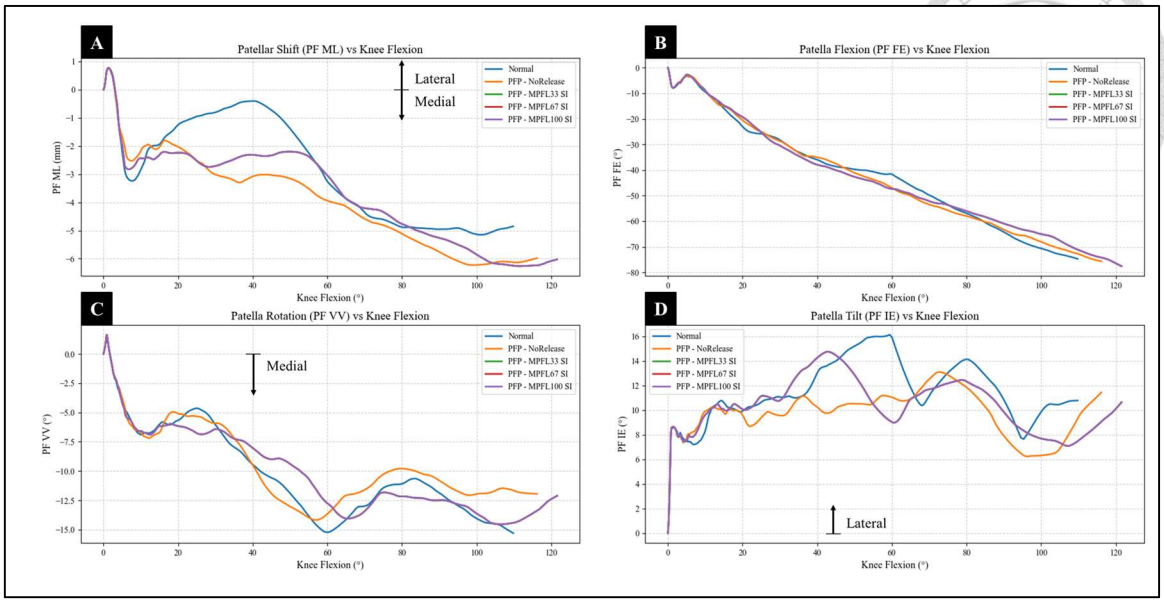

Figure A-31. Stepwise surgical release of the medial patellofemoral ligament (MPFL) from 0% to 100% in the superior-to-inferior (SI) direction. Each increment represents a unique surgical scenario used in the simulation.

Qualitative assessments of patellar tilt and shift in this surgical release scenario are shown in Figures A-32 and A-33. Due to the identical patella shift and tilt trajectories observed in Figure A-31, there is almost no difference between each release scenario. It can also be seen in Figures A-32 and A-33 that there is no notable difference between the release scenarios and the preoperative scenario. This may be caused by the keyframes from the animations being unable to capture minute differences between preoperative and postoperative scenarios (e.g., lack of frames).

doi:10.6342/NTU202503673

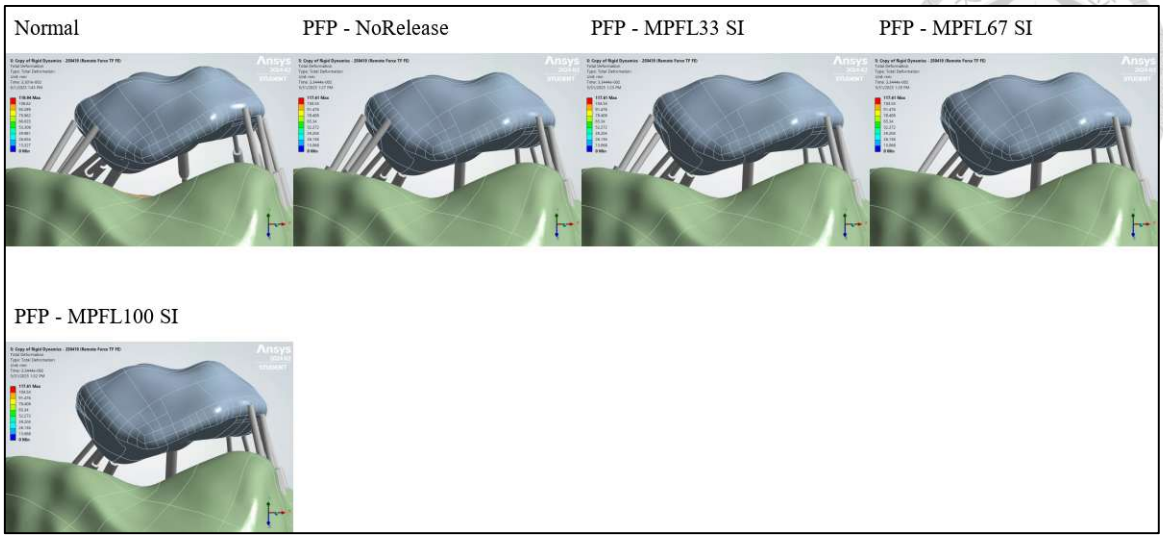

Figure A-32. Axial (superoinferior) views of the patella at ~60° knee flexion showing tilt orientation in normal, preoperative (PFP), and MPFL release scenarios (released in SI direction). Images used courtesy of ANSYS, Inc.

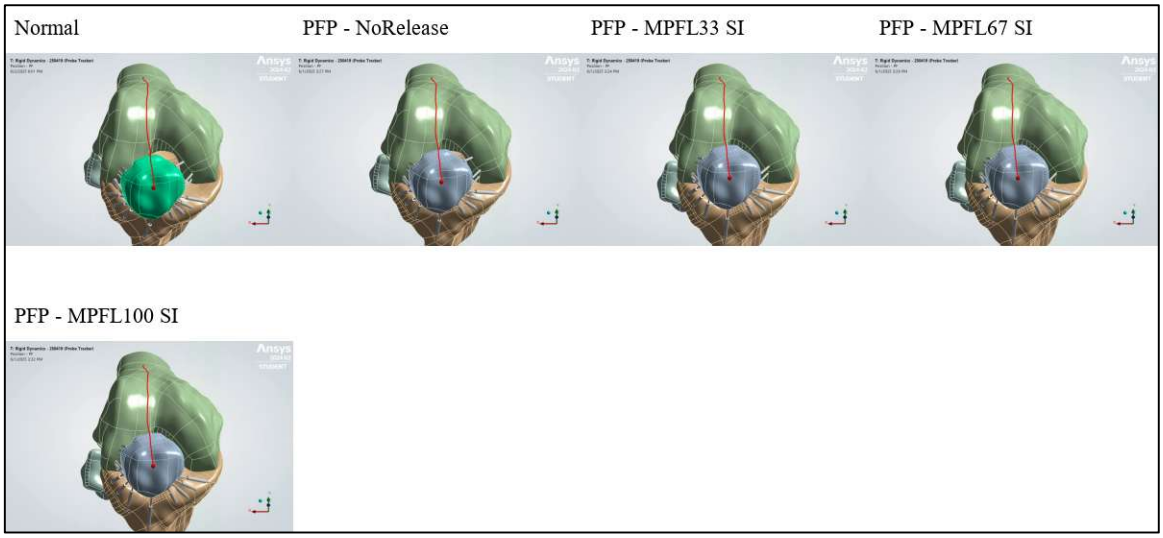

Figure A-33. Anteroposterior (AP) views of the patella showing shift trajectory traces from 0° to 110° knee flexion for normal, preoperative (PFP), and MPFL release cases (released in SI direction). Images used courtesy of ANSYS, Inc.

doi:10.6342/NTU202503673

B. Full Surgical Scenario Static Evaluation Figures

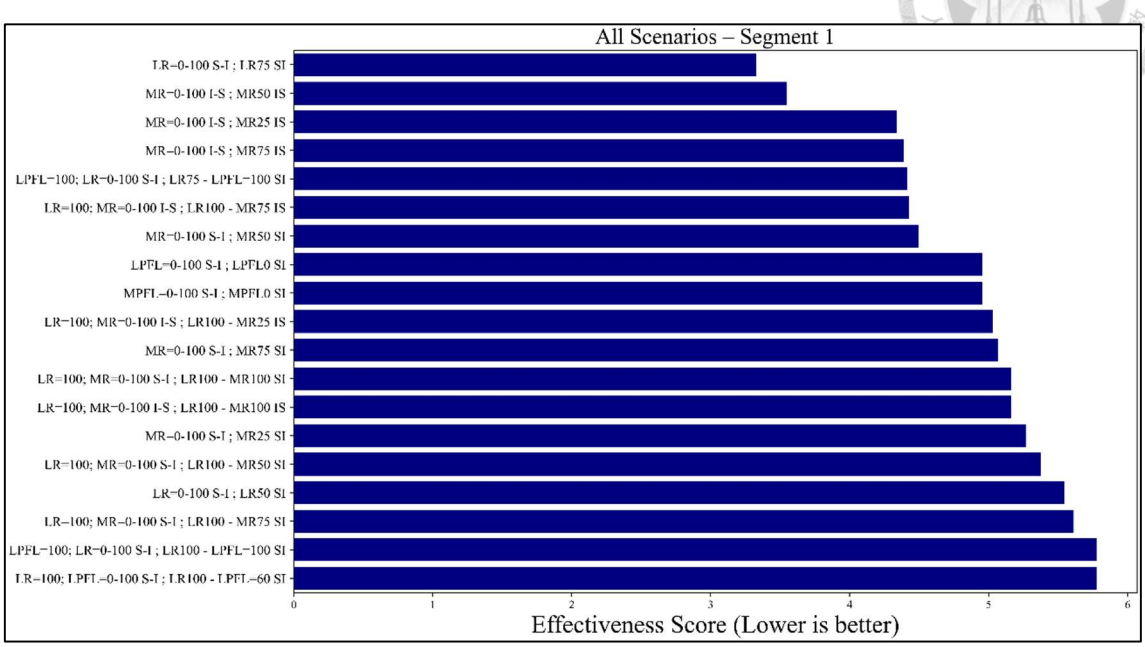

Figure B-1. Ranked postoperative effectiveness scores for static knee at 60° flexion.

Segment 1.

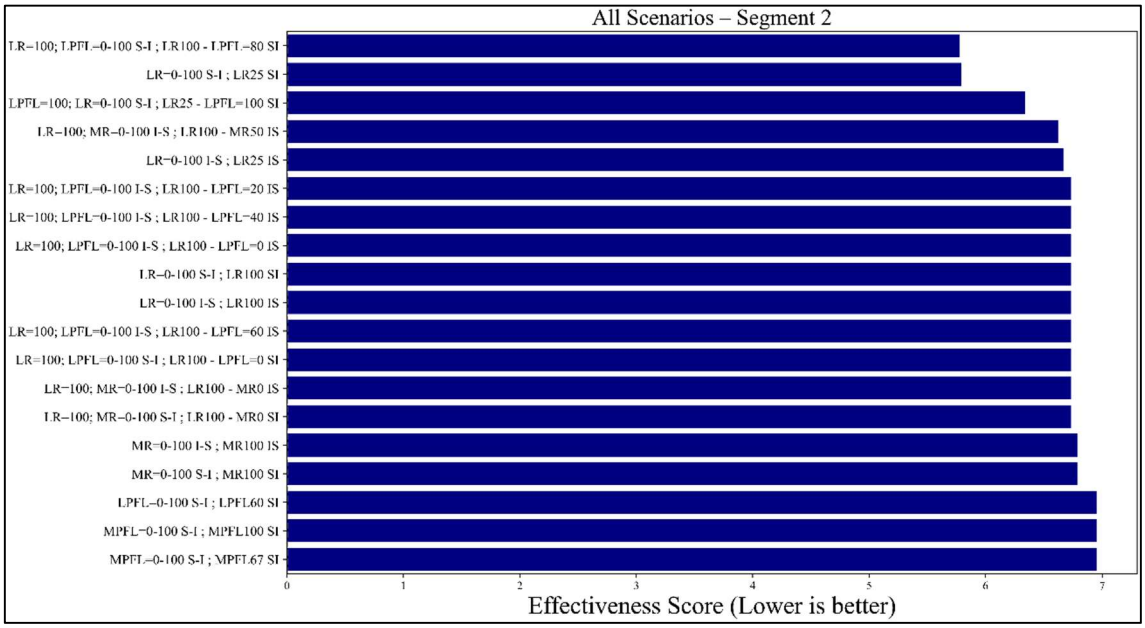

Figure B-2. Ranked postoperative effectiveness scores for static knee at 60° flexion.

Segment 2.

doi:10.6342/NTU202503673

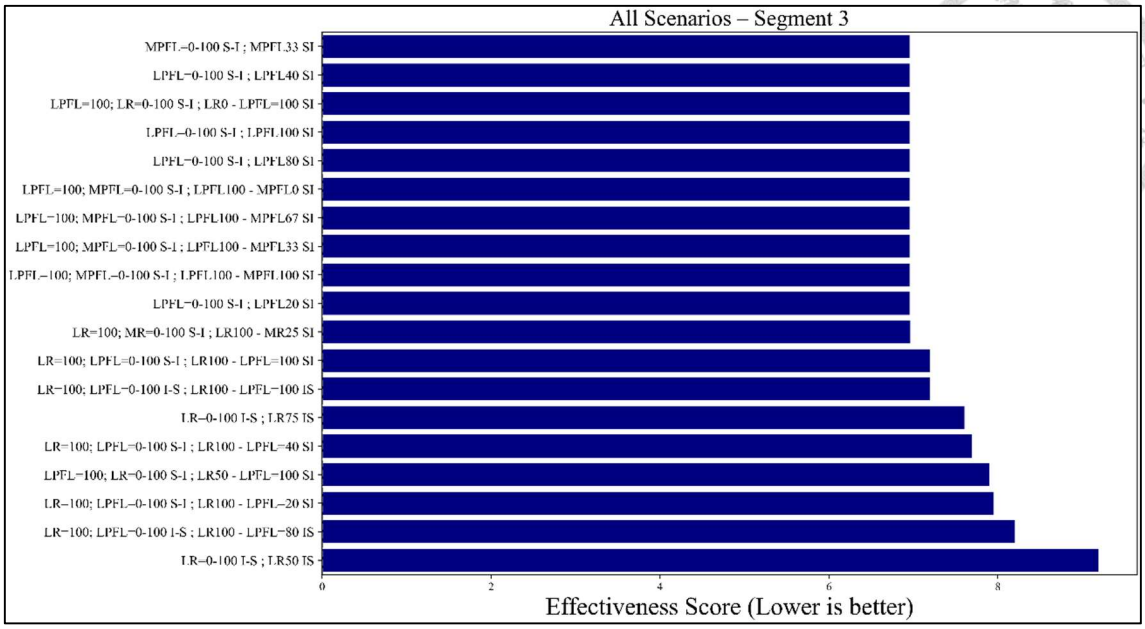

Figure B-3. Ranked postoperative effectiveness scores for static knee at 60° flexion.

Segment 3.

doi:10.6342/NTU202503673

C. Full Surgical Scenario Dynamic Evaluation Table

Table C-1. Complete ranking of surgical release scenarios by total dynamic score.

Strategy	Scenario	MSE_{Shift}	MSE_{Tilt}	STD_{Shift}	STD_{Tilt}	Total Score
LPFL=0-100 S-I	LPFL20 SI	0.8326	2.3641	1.8092	2.8712	5.537
LPFL=0-100 S-I	LPFL40 SI	0.8326	2.3641	1.8092	2.8712	5.537
LPFL=0-100 S-I	LPFL60 SI	0.8326	2.3641	1.8092	2.8712	5.537
LPFL=0-100 S-I	LPFL80 SI	0.8326	2.3641	1.8092	2.8712	5.537
LPFL=100; LR=0-100 S-I	LR0 - LPFL=100 SI	0.8326	2.3641	1.8092	2.8712	5.537
LPFL=0-100 S-I	LPFL100 SI	0.8326	2.3641	1.8092	2.8712	5.537
LPFL=100; MPFL=0-100 S-I	LPFL100 - MPFL100 SI	0.8326	2.3641	1.8092	2.8712	5.537
LPFL=100; MPFL=0-100 S-I	LPFL100 - MPFL0 SI	0.8326	2.3641	1.8092	2.8712	5.537
LPFL=100; MPFL=0-100 S-I	LPFL100 - MPFL67 SI	0.8326	2.3641	1.8092	2.8712	5.537
LPFL=100; MPFL=0-100 S-I	LPFL100 - MPFL33 SI	0.8326	2.3641	1.8092	2.8712	5.537
MPFL=0-100 S-I	MPFL33 SI	0.8326	2.3641	1.8092	2.8712	5.537
MPFL=0-100 S-I	MPFL67 SI	0.8326	2.3641	1.8092	2.8712	5.537
MPFL=0-100 S-I	MPFL100 SI	0.8326	2.3641	1.8092	2.8712	5.537
LR=0-100 I-S	LR25 IS	0.6907	5.3727	2.2226	2.1555	8.2524
MR=0-100 I-S	MR25 IS	1.35	4.6563	2.0964	2.746	8.4275
LR=0-100 S-I	LR25 SI	0.5386	5.5078	2.3461	2.5545	8.4967
MR=0-100 S-I	MR25 SI	0.8527	5.4778	2.0487	2.9217	8.8157
LR=100; MR=0-100 I-S	LR100 - MR25 IS	2.0462	4.5569	2.1431	2.306	8.8277
LPFL=0-100 S-I	LPFL0 SI	1.5319	5.9044	2.0835	2.3187	9.6373

doi:10.6342/NTU202503673

MPFL=0-100 S-I	MPFL0 SI	1.5319	5.9044	2.0835	2.3187	9.6373
LR=100; MR=0-100 I-S	LR100 - MR75 IS	2.7781	4.596	2.2142	2.4035	9.683
MR=0-100 I-S	MR50 IS	1.4592	5.6526	1.8581	3.3665	9.7242
LR=100; MR=0-100 S-I	LR100 - MR50 SI	2.4561	5.3425	2.3253	1.9369	9.9296
LPFL=100; LR=0-100 S-I	LR75 - LPFL=100 SI	0.6357	7.0241	2.3936	2.1998	9.9566
MR=0-100 S-I	MR75 SI	2.729	4.9743	2.1105	2.5583	10.0377
LR=0-100 I-S	LR75 IS	1.558	6.086	2.3698	2.7268	10.1923
MR=0-100 I-S	MR75 IS	1.8179	6.3508	2.05	2.1405	10.264
MR=0-100 S-I	MR100 SI	2.9674	5.2288	2.4458	2.3598	10.599
MR=0-100 I-S	MR100 IS	2.9674	5.2288	2.4458	2.3598	10.599
LR=100; LPFL=0-100 S-I	LR100 - LPFL=100 SI	1.0016	8.0094	2.1181	2.2083	11.1742
LR=100; LPFL=0-100 I-S	LR100 - LPFL=100 IS	1.0016	8.0094	2.1181	2.2083	11.1742
LR=0-100 S-I	LR50 SI	1.1701	7.7917	2.532	1.9725	11.2141
LR=100; MR=0-100 S-I	LR100 - MR100 SI	3.8584	4.9509	2.3773	2.4831	11.2395
LR=100; MR=0-100 I-S	LR100 - MR100 IS	3.8584	4.9509	2.3773	2.4831	11.2395
LPFL=100; LR=0-100 S-I	LR25 - LPFL=100 SI	1.1719	7.8824	2.4359	2.0262	11.2854
LR=0-100 S-I	LR75 SI	1.1727	7.7904	2.736	2.4541	11.5581
MR=0-100 S-I	MR50 SI	2.4771	6.9596	2.0183	2.2987	11.5951
LPFL=100; LR=0-100 S-I	LR100 - LPFL=100 SI	1.396	8.4111	2.0943	1.9148	11.8117
LR=100; LPFL=0-100 S-I	LR100 - LPFL=60 SI	1.396	8.4111	2.0943	1.9148	11.8117
LR=100; LPFL=0-100 S-I	LR100 - LPFL=80 SI	1.396	8.4111	2.0943	1.9148	11.8117

doi:10.6342/NTU202503673

LR=100; MR=0-100 S-I	LR100 - MR75 SI	3.6623	6.0967	2.3728	2.0537	11.9722
LPFL=100; LR=0-100 S-I	LR50 - LPFL=100 SI	0.7825	9.0671	2.4531	2.6707	12.4114
LR=100; LPFL=0-100 S-I	LR100 - LPFL=40 SI	0.8692	9.5569	2.2025	1.9374	12.4961
LR=0-100 S-I	LR100 SI	1.2285	9.1541	2.455	2.2097	12.7151
LR=0-100 I-S	LR100 IS	1.2285	9.1541	2.455	2.2097	12.7151
LR=100; LPFL=0-100 I-S	LR100 - LPFL=20 IS	1.2285	9.1541	2.455	2.2097	12.7151
LR=100; LPFL=0-100 I-S	LR100 - LPFL=0 IS	1.2285	9.1541	2.455	2.2097	12.7151
LR=100; LPFL=0-100 S-I	LR100 - LPFL=0 SI	1.2285	9.1541	2.455	2.2097	12.7151
LR=100; LPFL=0-100 I-S	LR100 - LPFL=40 IS	1.2285	9.1541	2.455	2.2097	12.7151
LR=100; MR=0-100 S-I	LR100 - MR0 SI	1.2285	9.1541	2.455	2.2097	12.7151
LR=100; MR=0-100 I-S	LR100 - MR0 IS	1.2285	9.1541	2.455	2.2097	12.7151
LR=100; LPFL=0-100 I-S	LR100 - LPFL=60 IS	1.2285	9.1541	2.455	2.2097	12.7151
LR=0-100 I-S	LR50 IS	0.4532	9.8652	2.1137	3.3954	13.073
LR=100; MR=0-100 S-I	LR100 - MR25 SI	1.3586	10.4981	2.346	2.3198	14.1896
LR=100; LPFL=0-100 S-I	LR100 - LPFL=20 SI	1.0264	11.344	2.1883	2.2665	14.5978
LR=100; MR=0-100 I-S	LR100 - MR50 IS	3.1708	9.2158	3.1476	2.3849	15.1529
LR=100; LPFL=0-100 I-S	LR100 - LPFL=80 IS	1.2707	12.3207	2.4215	2.5212	16.0628

doi:10.6342/NTU202503673

D. Questions and Suggestions Raised During the Oral Defense

Panelist 1: Dr. Shuo-Suei Hung

1. *Is it possible to simulate an FE model of a knee joint in a position similar to a Merchant view X-ray?*

It is possible. The main concern is not showing the FE model at a certain angle that is similar to a Merchant view X-ray or making the knee dynamically move to that angle. Instead, the issue with the FE model is the lack of features that can simulate accurate behavior of soft tissues, particularly ligament and muscle wrapping. Using simplified assumptions for the soft tissue structures lead to patella tracking behavior that has variance compared to an actual patient.

2. *Based on the surgical release strategies shown, do the incisions need to be specifically performed at the indicated soft tissue area?*

Not necessarily. The FE model uses springs as ligaments. The mechanism for simulating surgical incision is by removing the springs completely. This does not represent performing incision on any specific area.

doi:10.6342/NTU202503673

Panelist 2: Prof. Hsiao-Mei Wu

1. *What makes the digital twin patient-specific?*

There are several methods applied that make the digital twin patient-specific. Unique morphological features of each patient are captured and reconstructed into a 3D model in the custom 2D-3D shape reconstruction pipeline. For the FE model, literature data for the ligament stiffness properties are used as initial guess. Using machine learning, these parameters are modified to adapt to the case of each patient.

2. *What would happen to the patellar tracking results if you use a range for the muscle force magnitude instead of a fixed value? How do you justify the values used?*

Using a range of values for the muscle forces has been considered for application in the past. However, adding muscle forces as a variable will make the scope of the study too broad. Therefore, the main consideration for using a fixed value is to focus on analyzing the effects on biomechanical response of the ligaments. The force vector magnitudes used are based from literature data.

3. *Why did you modify the stiffness parameter of the ligaments? Why did you choose a uniform scaling factor of four for the lateral retinacular tightening?*

It is difficult to measure the actual stiffness parameter values of healthy ligaments. Several methods have been considered for measuring ligament properties. One method

doi:10.6342/NTU202503673

considered was ultrasound elastography. However, this method is not accurate and it was considered impractical to perform ultrasound elastography during surgery to gather in-vivo data on unhealthy ligaments. Therefore, the scaling factor was arbitrarily selected to simulate ligament tightening. A uniform scaling was used for simplicity. The goal was to simulate a hypothetical clinical case where the stiffness parameter of the lateral soft tissues has significantly increased, while the medial soft tissues have significantly decreased in stiffness. Thus resulting in a net force pulling the patella towards the lateral side.

4. *How did you determine the proper values for modifying the parameter values? Which scaling ratio is more appropriate?*

The modified parameter values represent a hypothetical patient with lateral retinacular tightening. The validity of the parameter values was based on its representation of a patient that had abnormal ligament stiffness properties. The tightening of the ligaments was believed by this study to influence patellar malalignment or maltracking. Therefore, these modified values were used as an assumption of an existing patient case that is recommended for surgical intervention.

5. *How did you evaluate the efficiency of the model-inferred surgical release profile? What was the goal?*

doi:10.6342/NTU202503673

The efficiency of the model-inferred predictions is based on the absolute error between the normal, "healthy," and postoperative patellar shift and tilt values. The model-inferred surgical release profile is considered acceptable if the absolute error is less than five units from the reference value.

6. *Similarly, for the FE model simulations, how did you define the best correction for postoperative patellar shift and tilt?*

Initially, a qualitative analysis was performed for both the patellar malalignment and maltracking corrections after surgical release. The criteria were a sufficient return to normal values for both static (patellar kinematics at 60° knee flexion) and dynamic (patellar kinematics during dynamic motion) postoperative values. However, quantitative measures have since been implemented to determine surgical release scenario efficiency on a scientific basis. For patellar malalignment correction, Euclidean distance was considered between the normal and postoperative values. Lower distance values were considered more efficient due to a closer return to normal values. For patellar maltracking correction, an arbitrary scoring system was used to weigh the return to normal patellar tracking values. The standard deviation of the patellar tracking was also considered. This method ensures that the immediate patellar tracking correction is balanced with patellar stability by analyzing high patellar mobility, measured by the standard deviation.

doi:10.6342/NTU202503673

Panelist 3: Prof. Chien-Kai Wang

1. *The work focuses on an inverse problem: proper parameters are required to properly describe the dynamic system. The baseline parameter values used in the thesis needs iteration process to make the model more robust. The mechanical nonlinearity of the system comes from two primary sources: material and geometry. The material properties in the FE model used were linear. Therefore, the nonlinearity originates from the geometry. It is not recommended to perform machine learning analysis on the given knee joint FE model because it is difficult to make predictions.*

The implementation of a machine learning algorithm was used as an initial means of parameter adaptation in order to enhance the personalization of the digital twin. A significant amount of data is required to create meaningful insights on the origins of the model nonlinearity. This study has only made initial steps in achieving this due to the lack of data.

2. *Is it feasible to collect knee motion data of regular to high-intensity exercises from healthy patients, collect X-ray data, create a personalized digital twin per patient to perform FE analysis using parameter values from literature data, then compare the patellar tracking results using literature data with the actual patient's patellar tracking for validation? If this iteration works, it will be possible to perform*

doi:10.6342/NTU202503673

projection to predict reasonable causes of nonlinearity. Successfully completing the inverse problem, performing any kind of forward problems will be possible for Dr. Hung's application. The same approach can then be performed for an abnormal case. Then try to find the correlation between normal and abnormal knees.

The process is feasible. A pipeline must first be designed to efficiently measure all the data required from each individual. Using machine learning or other means of parameter adaptation, the patellar tracking results using literature data can be compared with true values from in-vivo experiments. This process will enhance the robustness of the digital twin system. However, this approach is highly dependent on the quantity of data that can be procured in a given research study timeframe.

3. *Another issue is with the computational cost. For this application, the simulation needs to be in real time.*

The current simulation time is approximately three minutes of solving time. The model has already been simplified without compromising the anatomical accuracy. While the FE model is not available for real time simulations, the solving time is not significantly long. The approach for the FE model is designed for preoperative deployment. The relatively short solving time can even allow intraoperative deployment.

doi:10.6342/NTU202503673

4. Is it possible to measure the muscle forces?

Several methods exist for measuring muscle forces. However, the simpler approach is to acquire sufficient data of the physiological cross-sectional area of the muscles of patients to generate a generalizable model across the population. Since muscle force magnitude can vary, it is recommended to simply use literature data for common magnitude used during simple knee flexion. The distribution of the muscle force will then be the aspect that is unique for each patient, instead of the muscle force magnitude.

doi:10.6342/NTU202503673